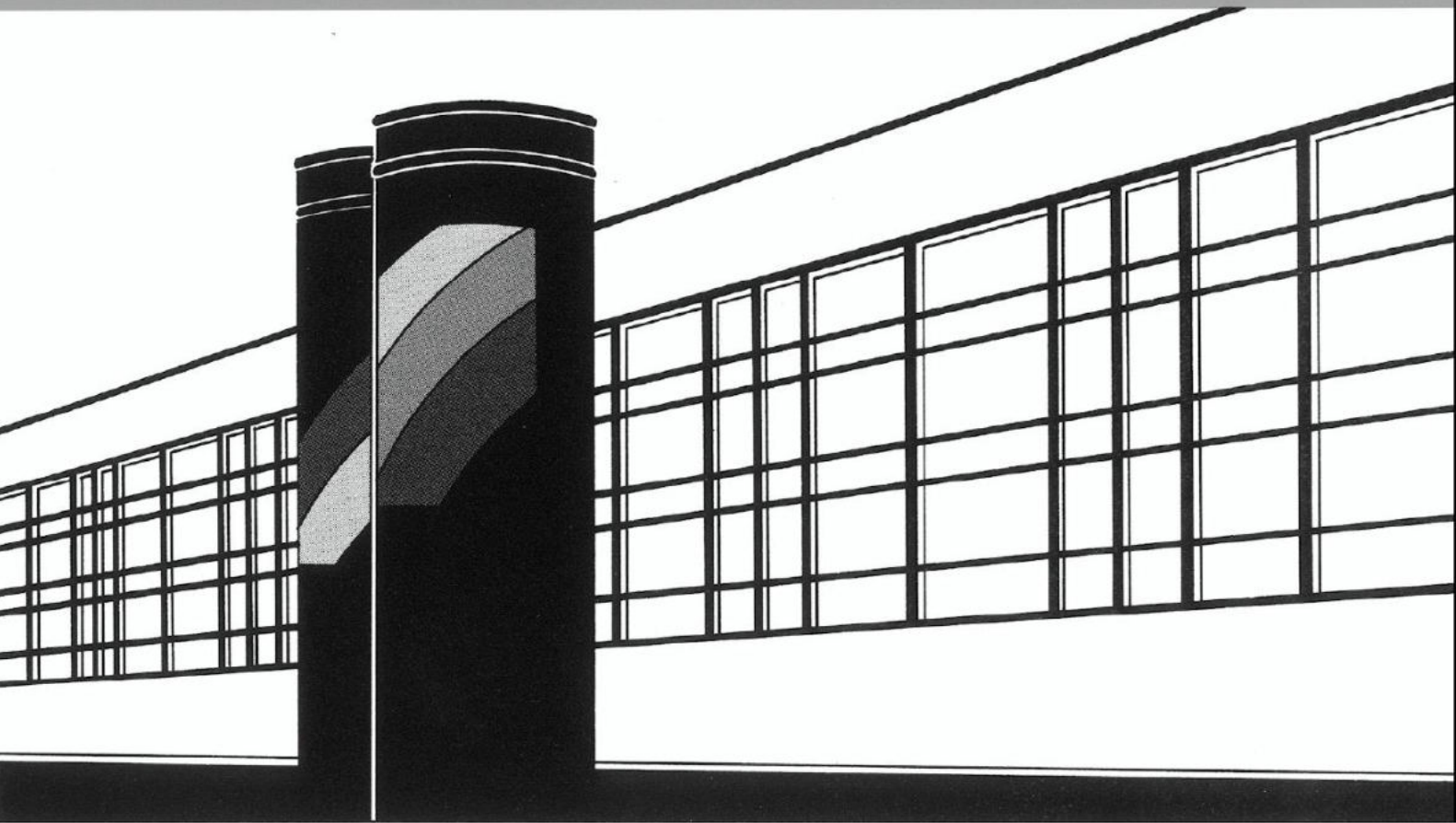


Universität Stuttgart



Institut für Wasser- und Umweltsystemmodellierung

Mitteilungen



Heft 286 Cynthia Michalkowski

Modeling water transport at the interface
between porous GDL and gas distributor of a
PEM fuel cell cathode

Modeling water transport at the interface between porous GDL and gas distributor of a PEM fuel cell cathode

von der Fakultät Bau- und Umweltingenieurwissenschaften der
Universität Stuttgart und dem Stuttgart Center for Simulation Science
zur Erlangung der Würde eines Doktor-Ingenieur (Dr.-Ing.)
genehmigte Abhandlung

vorgelegt von
Cynthia Michalkowski
aus Tübingen, Deutschland

Hauptberichter: Prof. Dr.-Ing. Rainer Helmig
Mitberichter: Dr. Vahid Joekar-Niasar
apl. Prof. Dr.-Ing. Holger Class

Tag der mündlichen Prüfung: 25. Januar 2022

Institut für Wasser- und Umweltsystemmodellierung
der Universität Stuttgart
2022

Heft 286 **Modeling water transport at
the interface between porous
GDL and gas distributor of a
PEM fuel cell cathode**

von
Dr.-Ing.
Cynthia Michalkowski

Eigenverlag des Instituts für Wasser- und Umweltsystemmodellierung
der Universität Stuttgart

D93 Modeling water transport at the interface between porous GDL and gas distributor of a PEM fuel cell cathode

Bibliografische Information der Deutschen Nationalbibliothek

Die Deutsche Nationalbibliothek verzeichnet diese Publikation in der Deutschen Nationalbibliografie; detaillierte bibliografische Daten sind im Internet über <http://www.d-nb.de> abrufbar

Cynthia Michalkowski:

Modeling water transport at the interface between porous GDL and gas distributor of a PEM fuel cell cathode, Universität Stuttgart. - Stuttgart: Institut für Wasser- und Umweltsystemmodellierung, 2022

(Mitteilungen Institut für Wasser- und Umweltsystemmodellierung, Universität Stuttgart: H. 286)

Zugl.: Stuttgart, Univ., Diss., 2022

ISBN 978-3-942036-90-0

NE: Institut für Wasser- und Umweltsystemmodellierung <Stuttgart>: Mitteilungen

Gegen Vervielfältigung und Übersetzung bestehen keine Einwände, es wird lediglich um Quellenangabe gebeten.

Herausgegeben 2022 vom Eigenverlag des Instituts für Wasser- und Umweltsystemmodellierung

Druck: DCC Kästl e.K., Ostfildern

Danksagung

Ich möchte mich im Folgenden bei all jenen bedanken, die mich bei der Anfertigung dieser Arbeit während der letzten Jahre begleitet und unterstützt haben. Dies gilt insbesondere für Rainer Helmig und Veronika Schleper, auf deren Engagement und fachlichen Rat ich mich jederzeit verlassen konnte. Rainers begeisterte Persönlichkeit und positive Einstellung motivieren mich seit dem Studium und werden mich nachhaltig prägen. In Veronika habe ich ein persönliches Vorbild gefunden. Ihre starke und proaktive Art inspirieren mich.

Ich bedanke mich bei meiner Abteilung bei Bosch, die mich als Kollegin auf Augenhöhe aufnahmen und mir für viele interessante fachliche und persönliche Gespräche zur Seite standen. In besonders guter Erinnerung behalte ich meine Zeit im Bosch Doktorandenprogramm. Das beeindruckende Engagement der Doktoranden trotz enger Zeitpläne und die großartigen Veranstaltungen, die wir gemeinsam organisierten, werde ich nie vergessen. Meine Doktorandenzeit wäre ohne den intensiven Zusammenhalt und lustigen Momente nicht Mal halb so schön gewesen.

Mein außergewöhnlicher Dank geht an das Team des Lehrstuhls für Hydromechanik und Hydrosystemmodellierung, das mich von Beginn an in seine Reihen aufnahm und mir nie das Gefühl gab zwischen den Stühlen zu sitzen. Ich habe es sehr genossen, diese großartige Atmosphäre und den außergewöhnlichen Teamgeist zu erleben. Ohne die gegenseitige Unterstützung bei jeglichen Themen und die wunderbaren Kaffeepausen wäre diese Arbeit nicht möglich gewesen. Vielen Dank an alle Kollegen!

Ein herzlicher Dank geht auch an Bernd Flemisch, der sich immer Zeit für meine Herausforderungen zwischen DuMu^x und hpc nahm und mir geduldig Lösungen erklärte. Ich möchte mich auch bei Stefanie Siegert, Beate Spinner, David Werner, Prudence Lawday und Michelle Hartnick für das Meistern bürokratischer und computertechnischer Hürden jedweder Art bedanken.

Herzlichen Dank auch an Holger Class für die Übernahme des Mitberichts und die fachliche Unterstützung. Er hatte immer ein offenes Ohr für meine Fragen. I would like to thank Vahid Joekar-Niasar for writing the report, sharing his knowledge with me and all the fruitful discussions. Thanks to Matthijs de Winter for hosting me in Utrecht and introducing me to the world of microfluidic experiments.

Ich danke der Robert Bosch GmbH und dem Institut für Wasser- und Umweltsystemmodellierung für die Finanzierung meiner Promotion und der Deutschen Forschungsgemeinschaft (DFG) für die Förderung des Sonderforschungsbereichs 1313, in dessen Rahmen diese Arbeit entstanden ist.

Mein besonderer Dank gilt schließlich meinen Eltern und meiner Schwester Carissa, die sich immer geduldig all meine Sorgen anhörten und mir in allen Situationen tatkräftig zur Seite standen. Der größte Dank gebührt meinem Freund Frederik, ohne dessen unermüdliche und liebevolle Unterstützung und aufmunternden Worte die vorliegende Dissertation nicht möglich gewesen wäre.

Contents

List of Figures	V
Nomenclature	XIII
Abstract	XIX
Zusammenfassung	XXIII
1 Introduction	1
1.1 Motivation	1
1.2 Structure of the thesis	9
2 Fundamentals	11
2.1 Terms and definitions	11
2.1.1 Components	12
2.1.2 Scales	13
2.2 Fluid properties	14
2.2.1 Density and viscosity	14
2.2.2 Contact angle and wettability	15
2.2.3 Surface tension and capillary pressure	16
2.3 Thermodynamics basics	17
2.4 Flow regimes	20
2.5 REV scale properties	20
2.6 Pore-scale properties	21
2.6.1 Idealized geometries and shape factor	21
2.7 Displacement and transport processes on the pore scale	23
2.7.1 Displacement processes in the gas diffusion layer on the pore scale	23
2.8 Modeling techniques for flow on the pore scale	25

2.9	Polymer electrolyte membrane (PEM) fuel cell functionality	26
2.9.1	Materials and structures of GDB (or MPL-free GDL) and gas distributor	27
2.9.2	Electro-chemistry in the catalyst layer	29
3	Conceptual and numerical models for the single domains	35
3.1	Pore-network model	38
3.1.1	Governing equations for single-phase flow	39
3.1.2	Governing equations for two-phase flow	40
3.1.3	Numerical model	48
3.1.4	Pore-network generation	49
3.2	Gas distributor channel model	51
3.2.1	Free-flow model	51
3.2.2	REV model	54
4	Boundary and interface configurations	59
4.1	Representation of the catalyst layer and influence of the MPL	60
4.2	Droplets forming in channels of the gas distributor	63
4.2.1	Droplet on a porous surface	64
4.2.2	Simplified model	70
4.2.3	Application to the pore-network approach	75
4.3	Fluidic interaction at the interface between hydrophobic and hydrophilic material	81
4.3.1	Application to pore-network approach	82
4.4	Trapping in mixed-wet pores below land	90
4.4.1	Application to pore-network approach	91
4.5	Effects of wettability, surface roughness and fiber structure	97
5	Coupling approach pore-network with free-flow domain	103
5.1	Assumptions and simplifications to capture the relevant processes at the interface	104
5.2	Total mass balance	105
5.3	Momentum balance	106
5.4	Chemical equilibrium and molar flux conservation	107
5.5	Energy balance and thermal flux conservation	111

6	Coupling approach pore-network (GDL) with REV domain (gas channel)	113
6.1	Assumptions and simplifications of the interface concept	114
6.2	Mass balance gas phase	115
6.3	Momentum balance gas phase	116
6.4	Mass balance liquid phase	116
7	Simulation results of pore-scale flow and transport through GDLs	119
7.1	Structural and flow characteristics of MPL-free GDL representation	119
7.1.1	Pore shape characterization	119
7.1.2	Global capillary pressure-saturation curves	123
7.1.3	Influence of local contact-angle variations	127
7.1.4	Discussion	129
7.2	Single phase investigations of a GDL-gas distributor setup	130
7.2.1	Influence of the channel width on component transport	131
7.2.2	Influence of pressure difference between two gas distributor channels on component transport	133
7.2.3	Discussion	136
8	Simulation results of the uncoupled interface configurations occurring at the interface between GDL and gas distributor	137
8.1	Pore-network model including droplets at the porous surface	137
8.1.1	Formation, growth and detachment of a single droplet	138
8.1.2	Formation, growth and detachment of multiple droplets in a system	144
8.1.3	Formation, growth and detachment of droplets at the surface of a GDL	150
8.1.4	Discussion	153
8.2	Pore-network model including hydrophobic-hydrophilic interaction	155
8.2.1	Fundamental behavior of the interacting pores	155
8.2.2	Investigation of the network response to interaction of several interface pores	159
8.2.3	Application to the interface between GDL and gas distributor	164
8.2.4	Comparison of the pore-network behavior to CFD investigations using ANSYS Fluent	167
8.2.5	Discussion	171

8.3	Pore-network model including trapping in mixed-wet pores below land	173
8.3.1	Proof of concept on simple, regular pore-network	173
8.3.2	Application on GDL representing pore-network	174
8.3.3	Discussion	176
8.4	Uncoupled pore-network representing GDL with three interface configurations representing gas distributor	178
8.4.1	Discussion	180
9	Simulation results of coupled domains models	183
9.1	Coupling pore-network with free flow domain including drop interaction	183
9.1.1	Pore-network coupled with free flow including single droplet interaction	184
9.1.2	Pore-network coupled with free flow including two-droplets interaction	189
9.1.3	Regular lattice network coupled with free flow including multiple-droplets interaction	192
9.1.4	Discussion	196
9.2	Coupling pore-network with REV-model domain including drop interaction	199
9.2.1	Regular lattice network coupled with Darcy flow including single droplet interaction	200
9.2.2	Simple pore-network coupled with Darcy flow including multiple-droplets interaction	203
9.2.3	GDL representation coupled with gas distributor channel . . .	205
9.2.4	Discussion	211
9.3	Comparison of the coupling approaches	213
10	Summary and Outlook	215
10.1	Summary	215
10.2	Outlook	218
	Bibliography	221

List of Figures

1.1	Composition of a PEM fuel cell stack	3
1.2	3D visualization of water configuration at GDL and gas distributor interface	8
1.3	2D visualization of water transport processes from MPL-free GDL to gas distributor	9
2.1	From pore-scale to REV-scale by averaging quantities [1, 2]	14
2.2	Shape of a water droplet on surface	15
2.3	Deformed shape of a water droplet on a hydrophobic surface	16
2.4	Capillary action of water in tube	17
2.5	Visualization of different pore geometries and shape factors	22
2.6	Characterization of fluid displacement patterns	24
2.7	Layered structure of PEM fuel cell	27
2.8	Gas diffusion layer (GDL) generated using GeoDict®	28
2.9	Channel structures	29
2.10	Interface configurations between GDL and gas distributor	29
2.11	Exemplary polarization curve of a PEM fuel cell	31
3.1	Coupled domains for GDL and gas distributor using PNM-FF model and PNM-REV model	36
3.2	Contact angle dependent capillary pressure-saturation relation	43
3.3	Fluid configuration in a throats	44
3.4	Capillary entry pressure	47
3.5	Box scheme for pore-network model	49
3.6	Pore-network extraction process using PoreSpy[3]	50
3.7	Free flow domain Ω^{FF}	51
3.8	Staggered grid for Navier-Stokes discretization	54

3.9	REV domain Ω^{REV}	55
3.10	Discretization of the box method for the REV domain [4]	57
4.1	Overview interface configurations	59
4.2	Lumped boundary condition for MPL and CCL influence	60
4.3	Interface including droplet formation between GDL and gas distributor	63
4.4	Droplet forming on a hydrophobic surface in a gas flow channel	64
4.5	Droplet on the GDL surface with no surrounding gas flow	65
4.6	Droplet on the GDL surface in a gas flow channel	66
4.7	Cassie-Baxter vs. Wenzel state	66
4.8	Deformation of the droplet due to gravitational force cf. [5]	68
4.9	Bond number of a water droplet in air environment dependent on the droplet size	69
4.10	Deformed (left) and undeformed (right) droplet on a surface.	69
4.11	Simplified representation of a droplet on the GDL surface.	70
4.12	Flow profiles around a droplet	71
4.13	Forces acting in and around the deformed droplet	71
4.14	Tangential components of the forces acting on the droplet	72
4.15	States of drop formation, growth and detachment	76
4.16	Droplet on a surface in equilibrium	77
4.17	Stages of droplet growth	78
4.18	Contact angles at stages of droplet growth	78
4.19	$p_c - s_w$ relation for drop interface pore	80
4.20	Hydrophobic-hydrophilic interface configuration	81
4.21	Interface configuration between GDL and gas distributor	82
4.22	Hydrophobic-hydrophilic interaction pore	83
4.23	Fluid configurations of liquid water invasion	83
4.24	Different configurations of water invasion	84
4.25	$p_c - s_w$ relation for a hydrophilic and a hydrophobic domain	85
4.26	Representation of two pores at the interface	86
4.27	Different configurations of water leaving the hydrophobic pore	87
4.28	Different configurations of water leaving the hydrophobic pore with different connections	87
4.29	Mixed-wet configuration at the interface between GDL and gas distributor	90

4.30	Mixed-wet pores below gas distributor land	90
4.31	Primary drainage/filling of a mixed-wet pore	91
4.32	Reconfiguration of the water in the pore body after contact	92
4.33	Emptying of the pore body after contact	93
4.34	Residual water saturation being trapped in the pore body	93
4.35	Residual water saturation being trapped in the pore body	94
4.36	$p_c - s_w$ for the configurations during primary drainage	96
4.37	$p_c - s_w$ for the configurations during secondary drainage	98
4.38	Intermediate wet conditions at surface of fibrous material	100
5.1	Coupling interface between GDL and gas distributor using PNM and FF model	103
5.2	Drop formulation interface PNM-FF	104
5.3	Coupling PNM-FF fluxes for no drop case	109
5.4	Coupling PNM-FF fluxes for drop case	110
6.1	Coupling interface between GDL and gas distributor using PNM and REV model	113
6.2	Coupling PNM-REV using ghost nodes	114
6.3	Coupling PNM-REV at REV scv faces	115
6.4	Coupling PNM-REV local pressures	116
6.5	Coupling PNM-REV detached droplet mass	118
7.1	200 μm cube samples of fibrous MPL-free GDL	120
7.2	Histogram of the inscribed radius	121
7.3	Histogram of the shape factor of the pore throats	122
7.4	200 μm cube samples of fibrous GDB w/o binder	122
7.5	Histogram of the shape factor w/o binder	123
7.6	Sample of a MPL-free GDL or GDB	124
7.7	Global static $P_c - S_w$ relation of MPL-free GDL	125
7.8	Liquid phase saturation in pore-network at $P_c = 5050$ Pa	125
7.9	Invaded pore throats at $P_c = 5050$ Pa	126
7.10	Dependence of the static $p_c - s_w$ relation on throat shape and contact angle	127
7.11	Influence of contact angle distribution on pore-network representing MPL- free GDL or GDB structures	127

7.12	Influence of contact angle distribution on static $P_c - S_w$ relation . . .	128
7.13	Container boundary condition for inflow condition	130
7.14	Simulation setup for single phase investigation on MPL-free GDL or GDB	131
7.15	Water vapor concentration in pore-network with channel width of 1 mm	132
7.16	Oxygen concentration in pore-network with channel width of 1 mm .	132
7.17	Water vapor concentration in pore-network with channel width of 0.5 mm	133
7.18	Oxygen concentration in pore-network with channel width of 1 mm .	134
7.19	Water vapor concentration in pore-network with pressure difference be- tween channels	135
7.20	Oxygen concentration in pore-network with pressure difference between channels	135
8.1	Simulation setup for uncoupled single droplet model	138
8.2	Drop radius comparison 2p REV, 2p PNM and experiment	140
8.3	Setup of the CFD simulation performed using Ansys Fluent R2019. Gas channel with parabolic gas flow velocity inlet and pressure outlet. In the center, water is injected through a throat with a mass flux boundary conditions. The drops form inside the channel and are deformed and detached by the surrounding gas flow.	140
8.4	Droplet detachment lines from different derivation approaches	142
8.5	Bulging menisci model Quesnel et al. [6]	145
8.6	Simulation setup uncoupled multiple-droplet interaction	146
8.7	Drop radii and p_c during two-droplets interaction	147
8.8	Water pressure in the inlet pore of a multi-tube setup	147
8.9	Drop radius and p_c in the inlet pore of a multi-tube setup	148
8.10	Liquid-phase pressure in the inlet pore of the 16 interface pores setup	149
8.11	Liquid-phase pressure in the inlet pore of the 101 interface pores setup	149
8.12	Pore-network representing a MPL-free GDL or GDB structure	151
8.13	Drop radius and p_c of 101 interface pores setup	152
8.14	CFD simulation of receding meniscii in GDL Niblet et al. [7]	152
8.15	Liquid water saturation in the pore-network with drop formation . . .	153
8.16	Simulation setup: hydrophobic-hydrophilic interaction (1 interaction pore)	156
8.17	Liquid phase saturation in interaction pore	157

8.18	Liquid phase saturation and fluxes at t_1	157
8.19	Liquid phase saturation and fluxes at t_2	158
8.20	Liquid phase saturation and fluxes at t_3	158
8.21	Liquid phase saturation and fluxes at t_1	159
8.22	Simulation setup with multiple interface pores	160
8.23	Liquid phase saturation in the interface pore	160
8.24	Liquid phase saturation and fluxes at t_1	161
8.25	Liquid phase saturation and fluxes at t_2	162
8.26	Liquid water saturation in interface pore	163
8.27	Liquid phase saturation and fluxes at t_3	163
8.28	Liquid phase saturation and fluxes at t_4	164
8.29	Pore-network representing MPL-free GDL with hydrophobic-hydrophilic interface	165
8.30	Liquid phase saturation in MPL-free GDL pore-network	166
8.31	Liquid phase saturation in interaction pore	166
8.32	Ansys CFD simulation setup hydrophobic-hydrophilic interaction	168
8.33	Ansys Fluent: Liquid water distribution in hydrophobic pore	169
8.34	Ansys Fluent: Liquid water distribution in hydrophobic pore	169
8.35	Ansys Fluent: Saturation of liquid water in the hydrophobic pore	170
8.36	Simplified simulation setup mixed-wet pore bodies	173
8.37	Liquid water saturation in pore-network with mixed-wet pore bodies	174
8.38	Pore-network representing a MPL-free GDL or GDB sample w/o mixed- wet pores	175
8.39	Influence of mixed-wet pores on static $P_c - S_w$	176
8.40	MPL-free GDL unit cell	178
8.41	Pore-network of MPL-free GDL unit cell	179
8.42	Liquid water saturation in MPL-free GDL sample with gas distributor representation	181
8.43	Drop radius and hydrophobic-hydrophilic interaction at boundary of MPL-free GDL unit cell	182
9.1	Simulation setup for coupled PNM-FF model with single droplet	184
9.2	Water vapor concentration from single droplet at t_1 (coupled PNM-FF)	186
9.3	Water vapor concentration from single droplet at t_2 (coupled PNM-FF)	186
9.4	Water vapor concentration from single droplet at t_3 (coupled PNM-FF)	187

9.5	Droplet radius of single droplet (coupled PNM-FF)	188
9.6	Influence of T and rh on droplet radius of single droplet (coupled PNM-FF)	188
9.7	Simulation setup for coupled PNM-FF model with two droplets . . .	190
9.8	Water vapor concentration from two droplets at t_1 (coupled PNM-FF)	190
9.9	Water vapor concentration from two droplets at t_2 (coupled PNM-FF)	191
9.10	Droplet radii of two droplets (coupled PNM-FF)	191
9.11	Simulation setup for coupled PNM-FF model with multiple droplets .	192
9.12	Water vapor concentration from multiple droplets at t_1 (coupled PNM-FF)	193
9.13	Water saturation in multiple-droplets network at t_1 (coupled PNM-FF)	194
9.14	Water saturation in multiple-droplets network at t_2 (coupled PNM-FF)	194
9.15	Water saturation in multiple-droplets network at t_3 (coupled PNM-FF)	195
9.16	Water saturation in multiple-droplets network at t_4 (coupled PNM-FF)	195
9.17	Water saturation in multiple-droplets network at t_5 (coupled PNM-FF)	196
9.18	Drop radii of multiple droplets (coupled PNM-FF)	196
9.19	Simulation setup for coupled PNM-REV model with single droplet . .	201
9.20	Drop radius comparison coupled(PNM-REV)-uncoupled model	202
9.21	Liquid phase saturation after single drop detachment (coupled PNM-REV)	202
9.22	Drop radius during formation, growth and detachment of single drop (coupled PNM-REV)	203
9.23	Simulation setup for coupled PNM-REV model with multiple droplets	204
9.24	Liquid phase saturation after detachment of multiple droplets (coupled PNM-REV)	206
9.25	Drop radii during formation, growth and detachment of multiple droplets (coupled PNM-REV)	207
9.26	Simulation setup for coupled PNM-REV model applied to GDL-gas distributor interaction	207
9.27	Drop radius evolution at GDL-gas distributor interface (coupled PNM-REV)	209
9.28	Liquid phase saturation in gas distributor at t_1 (coupled PNM-REV)	209
9.29	Liquid phase saturation in gas distributor at t_2 (coupled PNM-REV)	210
9.30	Liquid phase saturation in gas distributor at t_3 (coupled PNM-REV)	210
9.31	Liquid phase saturation in gas distributor at t_4 (coupled PNM-REV)	211

Nomenclature

Selected acronyms

AM arc meniscus

CFD computational fluid dynamics

FC fuel cell

FF free flow model

GDB gas diffusion backend (fibrous part of GDL)

GDL gas diffusion layer (consists of MPL and GDB)

MPL micro porous layer

PEM polymer electrolyte membrane

PNM pore-network model

REV representative elementary volume

VoF volume of fluid

Greek letters

α corner half angle [rad]

β crevice resistance factor [-]

Δt	time step	[s]
η_i	overpotential corresponding to reaction i (anode or cathode reaction)	[V]
Γ^{FF}	interface between Ω^{PNM} and Ω^{FF}	
Γ^{MPL}	interface between black box model for CCL and MPL and Ω^{PNM}	
Γ^{REV}	interface between Ω^{PNM} and Ω^{REV}	
Γ_{box}	face of bulk-model box control volume on coupling interface	
λ	heat conduction factor	[W/(mK)]
μ	dynamic viscosity	[Pa s]
ν	kinematic viscosity	[m ² /s]
Ω^{FF}	free-flow domain	
Ω^{PNM}	pore-network model domain	
Ω^{REV}	REV model bulk porous medium domain	
Φ	porosity	[-]
ϕ^0	equilibrium potential	[V]
ρ_α	density of phase α	[kg/m ³]
σ	interfacial tension	[N/m]
θ	contact angle	[°]

Non-dimensional numbers

Ca	capillary number	$Ca = \frac{\mu_n V_{n,\text{char}}}{\sigma}$
------	------------------	---

M viscosity ratio $M = \frac{\mu_n}{\mu_w}$

Re Reynolds number $Re = \frac{vd_{\text{char}}}{\nu}$

Roman letters

A area $[\text{m}^2]$

A_{ij} cross-sectional area of throat ij $[\text{m}^2]$

$A_{w,n}$ cross-sectional area of the wetting layer in corner n $[-]$

c factor in wall friction term $[-]$

d_{char} characteristic diameter $[\text{m}]$

$D_{(\alpha,i)}^\kappa$ diffusion coefficient of component κ (in phase α) in pore body i $[\text{m}^2/\text{s}]$

F Faraday constant $[\text{sA/mol}]$

G shape factor $[-]$

\mathbf{g} gravitational acceleration $[\text{m/s}^2]$

G_0^\neq free activation enthalpy $[\text{J}]$

H Henry constant $[\text{Pa}]$

h specific enthalpy $[\text{J/kg}]$

I current $[\text{A}]$

i current density $[\text{A/m}^2]$

\mathbf{J}_{diff} diffusive flux vector $[\text{mol/s}]$

\mathbf{K} intrinsic permeability $[\text{m}^2]$

k_{ij}^α	conductance factor of pore throat ij for phase α	$[\text{m}^2/(\text{sPa})]$
k_{rw}, k_{rn}	relative permeability of the wetting (w) and non-wetting (n) phase	$[-]$
l_{ij}	pore throat length	$[\text{m}]$
m	mass	$[\text{kg}]$
M^κ	molar mass of component κ	$[\text{kg}/\text{mol}]$
\dot{N}_κ	production rate (molar flux) of component κ	$[\text{mol}/\text{s}]$
\mathbf{n}	unit normal vector	$[-]$
P	perimeter	$[\text{m}]$
p	pressure	$[\text{Pa}]$
p_{sat}	saturation vapor pressure	$[\text{°C}]$
P_c	capillary pressure on system or REV scale	$[\text{Pa}]$
p_c	pore-local capillary pressure	$[\text{Pa}]$
p_i^α	phase pressure of phase α in pore body i	$[\text{Pa}]$
q	mass source/sink term	$[\text{kg}/\text{s}]$
q^κ	molar source/sink term	$[\text{mol}/\text{s}]$
q^e	energy source/sink term	$[\text{kg}/\text{s}^3]$
q^T	heat source/sink term	$[\text{kg}/\text{s}^3]$
Q_{ij}	volume flow through pore throat ij	$[\text{m}^3/\text{s}]$
R	universal gas constant	$[\text{J}/\text{molK}]$
R_{spec}	specific ohmic resistance	$[\Omega]$

R_i	pore body inscribed radius	[m]
r_{ij}	pore throat inscribed radius	[m]
rh	relative humidity	[-]
S^α	saturation of phase α on system or REV scale	[-]
s^α	pore-local saturation of phase α	[-]
T	temperature	[°C]
t_i	time step	[s]
u	specific internal energy	[J/kg]
U_{OCV}	open circuit voltage	[V]
\mathbf{v}	velocity vector	[m/s]
v	scalar velocity	[m/s]
V_{drop}	drop volume	[m ³]
V_i	volume of pore body i	[m ³]
X^κ	mass fraction of component κ	[-]
x^κ	mole fraction of component κ	[-]
z	number of transferred electrons in reaction	[-]

Sub- and superscripts

α	phase index
κ	component index
air	property referring to air component

gas, g property referring to gas phase

H_2O property referring to water component

i pore body index

ij pore throat index connecting pore body i and j

liq, l property referring to liquid phase

n property referring to non-wetting phase

O_2 property referring to oxygen component

s property referring to solid phase

w property referring to wetting phase

Operators and other symbols

Δ_{ij} difference of property in pore body i and pore body j

$[\cdot]^{\text{FF}}$ free flow interface quantity

$[\cdot]^{\text{PNM}}$ pore-network model interface quantity

$[\cdot]^{\text{REV}}$ REV model interface quantity

Abstract

Operating vehicles with polymer electrolyte membrane (PEM) fuel cells is a promising technology for reducing traffic-related greenhouse gas emissions. In a PEM fuel cell, hydrogen and oxygen react producing water, electric energy, and heat. Oxygen is consumed on the cathode side of the cell, while the excess water must be removed to prevent the so-called flooding (blockage of the transport paths). A sophisticated water management is crucial for improved operating conditions of a PEM fuel cell. Therefore, it is necessary to understand the transport mechanisms of water throughout the cell constituents, where an intelligent use and drainage of the water buffer can be used to enhance the performance of the fuel cell. Pore-scale modeling of gas diffusion layers (GDLs) and the gas distributor has been established as a favorable technique to investigate the ongoing processes.

A particular challenge is the investigation of the interface between the GDL and the gas distributor. Here, multi-phase flow in the porous material of the GDL is combined with the free flow in the gas distributor resulting in strong interaction. Different interface processes occur based on the pore-local structural properties, such as surface wettability and interaction with the gas flow in the gas distributor. At the interface between hydrophobic porous GDL and the hydrophilic side walls of the gas distributor, the fluids interact with the differently wetting surfaces. This results in complex pore-scale transport processes in the pores located at the interface. In the channels of the gas distributor, drops emerging from the porous domain at the interface have a strong influence on the exchange of mass, momentum, and energy between the two flow regimes. Additionally, we also consider transport processes of the gas phase between the GDL and the gas distributor, where no water breakthrough occurs.

Models A dynamic pore-network model is applied to capture the pore-scale flow and transport processes in the GDL beyond capillary equilibrium states. This model lo-

cally resolves pore-scale processes on a simplified but equivalent porous geometry which makes it efficient compared to direct numerical simulations.

We distinguish between the uncoupled pore-network model, which represents the GDL only but captures the interaction with the flow through the gas distributor in a simplified way by newly-developed boundary conditions, and the coupled models. The coupled models combine the pore-network representing the GDL with models describing the flow in the gas distributor. Here, two approaches are investigated: A free flow model solving the (Navier-)Stokes equations and a REV-based formulation. At the interface, conservation of mass, momentum, and energy is fulfilled, and the particular interface processes in the PEM fuel cell cathode are included by distinct pore-scale coupling conditions, which have been developed in this work.

The boundary and coupling conditions at the interface (interface conditions) are described and discussed in detail to capture the relevant processes and ensure thermodynamic consistency.

We take the open-source porous media simulator DuMu^x for the implementation of the interface conditions and the coupled models by using its multi-model coupling facilities. To create a pore-network adequately representing a realistic fibrous GDL structure, the open-source pore-network extractor PoreSpy is used.

Results First, the pore-network properties to represent flow through a fibrous GDL structure are evaluated. It has been found that cubic pore bodies and connecting throats with a cross-sectional shape of an equilateral triangle are well suited to represent the complex porous structure with simplified geometric shapes. Additionally, the influence of contact angle distributions is investigated.

Single-phase (gas) transport simulations are performed on a pore-network representing a GDL sample to evaluate the influence of some properties of the gas distributor, such as channel width and pressure distribution. Pressure differences between the channels of the gas distributor control the resulting concentrations at the reaction layer, while the channel width is only of minor influence in the single-phase case when the total supply of reactant gases is sufficient.

The uncoupled pore-network model allows to investigate the influence of the different interface configurations and to evaluate their general behavior. The different interface conditions are applied separately to pore-networks of different complexity ranging from single interaction pores to the application on realistic GDL sample structures. Finally,

the interface conditions are combined to be applied on a small GDL unit cell example. In particular, the droplet formation, growth, and detachment have a major influence on the exchange processes at the interface between GDL and gas distributor.

Therefore, we focus on droplet related interface processes in the coupled models and, for simplicity, perform isothermal simulations only. Nevertheless, the two-phase multi-component flow in the pore-network coupled with single-phase multi-component free flow (PNM-FF) allows for investigating the interaction between the two domains including evaporation processes and vapor transfer across the interface. We analyze how ambient temperature and relative humidity influence the droplet formation, growth and detachment, and the evaporation from the droplet surface. This model is well suited to investigate the transfer and transport of water vapor from the porous GDL and droplets on the surface to the gas flow in the gas distributor but it does not track the detached droplets in the free-flow domain. The vapor transport is of particular interest for dry conditions in the gas channel, when low liquid water content is expected in the gas distributor as it occurs near the gas inlet of a fuel cell.

At humid conditions, if only small amounts of the water are transferred as vapor while film flow in the gas distributor is relevant, a two-phase pore-network model coupled with a two-phase REV model (PNM-REV) is the better choice. Here, the high humidity in the gas phase results in low evaporation rates but liquid water transfer between the GDL and the gas distributor becomes relevant. The developed PNM-REV coupling model captures droplet formation, growth, and detachment at the interface and the transport of detached droplet in the REV domain using a film-flow formulation. This behavior occurs near the gas outlet in a fuel cell.

Zusammenfassung

Mit Polymer-Elektrolyt-Membran (PEM) Brennstoffzellen betriebene Fahrzeuge sind eine vielversprechende Technik zur Verringerung der durch den Verkehr verursachten Treibhausgasemissionen. In einer PEM-Brennstoffzelle reagieren Wasserstoff und Sauerstoff und erzeugen Wasser, elektrische Energie und Wärme. Der Sauerstoff wird auf der Kathodenseite der Zelle verbraucht, während das überschüssige Wasser entfernt werden muss, um das so genannte Flooding (Verstopfung der Transportwege) zu verhindern. Ein ausgeklügeltes Wassermanagement ist entscheidend für verbesserte Betriebsbedingungen einer PEM-Brennstoffzelle. Daher ist es notwendig, die Mechanismen des Wassertransports durch die Zellbestandteile zu verstehen, wobei eine intelligente Nutzung und Entwässerung des Wasserpuffers zur Verbesserung der Leistung der Brennstoffzelle beitragen kann. Die porenskalige Modellierung von Gasdiffusionsschichten (GDLs) und Gasverteilern hat sich als günstige Methodik zur Untersuchung der ablaufenden Prozesse etabliert.

Eine besondere Herausforderung ist die Untersuchung der Grenzfläche zwischen der GDL und dem Gasverteiler. Hier wird die Mehrphasenströmung im porösen Material der GDL mit der freien Strömung im Gasverteiler kombiniert, was zu starken Wechselwirkungen führt. In Abhängigkeit von den porenlokalen Struktureigenschaften, wie der Oberflächenbenetzbarkeit und der Wechselwirkung mit der Gasströmung im Gasverteiler, treten unterschiedliche Grenzflächenprozesse auf. An der Grenzfläche zwischen hydrophober, poröser GDL und den hydrophilen Seitenwänden des Gasvertailers interagieren die Fluide mit den unterschiedlich benetzenden Oberflächen. Daraus resultieren komplexe, porenskalige Transportprozesse in den Poren an der Grenzfläche. In den Kanälen des Gasvertailers haben Tropfen, die aus dem porösen Bereich an der Grenzfläche austreten, einen starken Einfluss auf den Austausch von Masse, Impuls und Energie zwischen den beiden Strömungsregimen. Zusätzlich betrachten wir auch Transportprozesse der Gasphase zwischen der GDL und dem Gasverteiler, bei denen kein Wasserdurchbruch auftritt.

Modelle Ein dynamisches Porennetzwerkmodell wird angewandt, um die porenskaligen Strömungs- und Transportprozesse in der GDL jenseits von Kapillargleichgewichtszuständen zu erfassen. Dieses Modell löst die porenskaligen Prozesse lokal auf einer vereinfachten, aber äquivalenten porösen Geometrie auf, was es im Vergleich zu direkten numerischen Simulationen effizient macht.

Wir unterscheiden zwischen dem ungekoppelten Porennetzwerkmodell, das nur die GDL abbildet, aber die Wechselwirkung mit der Strömung durch den Gasverteiler in vereinfachter Weise durch neu entwickelte Randbedingungen erfasst, und den gekoppelten Modellen. Die gekoppelten Modelle kombinieren das Porennetzwerk, das die GDL darstellt, mit Modellen, die die Strömung im Gasverteiler beschreiben. Hier werden zwei Ansätze untersucht: Ein Modell für freie Strömungen, das die (Navier-)Stokes-Gleichungen löst, und eine REV-basierte Formulierung. An der Grenzfläche wird die Massen-, Impuls- und Energieerhaltung erfüllt, und die speziellen Grenzflächenprozesse in der PEM-Brennstoffzellenkathode werden durch spezielle Kopplungsbedingungen auf der Porenskala berücksichtigt, die in dieser Dissertation entwickelt worden sind.

Die Rand- und Kopplungsbedingungen an der Grenzfläche (Interface Conditions) werden detailliert beschrieben und diskutiert, um die relevanten Prozesse zu erfassen und die thermodynamische Konsistenz zu gewährleisten.

Wir verwenden den Open-Source-Simulator für poröse Medien DuMu^x für die Implementierung der Grenzflächenbedingungen und der gekoppelten Modelle, indem wir seine Multimodell-Kopplungsmöglichkeiten nutzen.

Um ein Porennetzwerk zu erstellen, das eine realistische faserige GDL-Struktur adäquat repräsentiert, wird der Open-Source-Tool zur Porennetzwerk-Extraktion PoreSpy verwendet.

Ergebnisse Zunächst werden die Porennetzwerkeigenschaften zur Darstellung der Strömung durch eine faserige GDL-Struktur bewertet. Es hat sich gezeigt, dass kubische Porenkörper und verbindende Porenhälse mit der Querschnittsform eines gleichseitigen Dreiecks gut geeignet sind, um die komplexe poröse Struktur mit vereinfachten geometrischen Formen darzustellen. Zusätzlich wird der Einfluss von Kontaktwinkelverteilungen untersucht.

Einphasige (Gasphasen-) Transportsimulationen werden an einem Porennetzwerk durchgeführt, das einen GDL-Ausschnitt darstellt, um den Einfluss einiger Eigenschaften des Gasverters wie Kanalbreite und Druckverteilung zu bewerten. Druckunter-

schiede zwischen den Kanälen des Gasverteilers steuern die resultierenden Konzentrationen an der Reaktionsschicht, während die Kanalbreite im einphasigen Fall nur einen geringen Einfluss hat, wenn die Gesamtversorgung mit Reaktionsgasen ausreichend ist. Das entkoppelte Porennetzwerkmodell erlaubt es, den Einfluss der verschiedenen Grenzflächenkonfigurationen zu untersuchen und ihr allgemeines Verhalten zu bewerten. Die verschiedenen Grenzflächenbedingungen werden separat auf Porennetzwerke unterschiedlicher Komplexität angewandt, von einzelnen Interaktionsporen bis hin zur Anwendung auf realistische GDL-Strukturen. Schließlich werden die Grenzflächenbedingungen zur Anwendung auf eine kleine GDL-Einheitszelle kombiniert. Insbesondere die Bildung, das Wachstum und die Ablösung von Tröpfchen hat einen großen Einfluss auf die Austauschprozesse an der Grenzfläche zwischen GDL und Gasverteiler. Daher konzentrieren wir uns in den gekoppelten Modellen auf die tröpfchenbezogenen Grenzflächenprozesse. Dabei beschränken wir uns auf isotherme Simulationen. Die zweiphasige Mehrkomponentenströmung im Porennetzwerk gekoppelt mit der einphasigen freien Mehrkomponentenströmung (PNM-FF) ermöglicht es jedoch, die Wechselwirkung zwischen den beiden Bereichen zu untersuchen, einschließlich der Verdampfungsprozesse und des Dampftransfers über die Grenzfläche. Wir analysieren, wie die Umgebungstemperatur und die relative Luftfeuchtigkeit die Bildung, das Wachstum und die Ablösung von Tröpfchen sowie die Verdunstung von der Tröpfchenoberfläche beeinflussen. Dieses Modell eignet sich gut zur Untersuchung des Transfers und des Transports von Wasserdampf von der porösen GDL und den Tröpfchen auf der Oberfläche in die Gasströmung im Gasverteiler, aber es berücksichtigt nicht die abgelösten Tröpfchen im freien Strömungsbereich. Der Dampftransport ist besonders interessant bei trockenen Bedingungen im Gaskanal, wenn ein geringer Flüssigwassergehalt im Gasverteiler zu erwarten ist, wie er in der Nähe des Gaseinlasses einer Brennstoffzelle auftritt. Bei feuchten Bedingungen, wenn nur geringe Mengen des Wassers als Dampf übertragen werden, aber die Filmströmung im Gasverteiler relevant ist, ist ein zweiphasiges Porennetzwerkmodell gekoppelt mit einem zweiphasigen REV-Modell (PNM-REV) die bessere Wahl. Hier führt die hohe Feuchtigkeit in der Gasphase zu geringen Verdampfungsraten, aber der Flüssigwassertransfer zwischen GDL und Gasverteiler wird relevant. Das entwickelte PNM-REV-Kopplungsmodell erfasst die Tropfenbildung, das Wachstum und die Ablösung an der Grenzfläche sowie den Transport der abgelösten Tropfen in der REV-Domäne mithilfe einer Filmströmungsformulierung. Dieses Verhalten tritt in der Nähe des Gasauslasses in einer Brennstoffzelle auf.

1 Introduction

1.1 Motivation

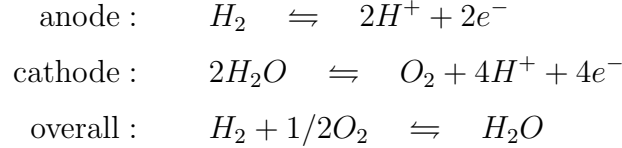
Reducing greenhouse gas emissions is the primary objective of global climate policy. A significant amount of CO₂-emissions is caused by traffic. Therefore, alternative power-train technologies competitive to conventional combustion engines have a high potential and gained more and more attention in the last decade.

Fuel cells operating on hydrogen generate zero emissions [8, 9]. The only exhaust is unused air and water. This is attractive not only for mobility solutions but also for many stationary applications such as auxiliary power units. However, hydrogen is not a readily available fuel and during the synthesis some emissions are generated. Also if methanol is used in a fuel cell instead of hydrogen, some emissions, including carbon dioxide, are released. However, in general, these emissions are lower than those of comparable conventional energy conversion technologies like combustion engines [9, 10].

Fuel-cell types Several different types of fuel cells have been developed in the last decades. They vary in their ranges of operating temperature, start-up times, used fuels, efficiency, and possible power supply. Dependent on the desired application, different fuel-cell properties are important and determine the optimal choice of the fuel-cell type. Two types have been commercially established in recent years. Solid oxide fuel cells (SOFCs) operate at high temperatures between 800°C and 1000°C. SOFC compositions allow the operation with hydrogen and methanol at high efficiency but they need long start up times to heat up before they can run on full power. This type of fuel cell is usually used for stationary applications where variations in power generation rarely occur spontaneously. For automotive applications, other requirements are needed. Here, fast changes in power generation and quick start-up times are required, combined with

an adequate efficiency. Therefore, PEM fuel cells are applied in the mobility sector. PEM stands for Polymer Electrolyte Membrane or Proton Exchange Membrane [11]. PEM fuel cells use a proton-conductive polymer membrane as electrolyte. They operate at lower temperatures ($60 - 100^\circ\text{C}$), have a lower efficiency and require pure hydrogen as fuel but offer quick start-up times and a flexible energy supply under partial load.

Efficiency of PEM fuel cells / hydrogen fuel cells In a PEM fuel cell, hydrogen and oxygen react to water in a two-stage reaction. Hydrogen is fed on the anode side of the membrane and splits into its primary constituents, protons and electrons during the anode reaction. Protons travel through the proton-conductive membrane, while the electrons travel through electrically conductive electrodes, through current collectors, and through the outside electric circuit, where they perform useful work, and return to the cathode side of the membrane. At the cathode catalyst, the electrons meet with the protons that crossed the membrane and with oxygen that is fed on that cathode side of the membrane. During this cathode reaction, water is generated in the electrochemical reaction [11].



The net result of this two-stage reaction is a current of electrons through an external circuit and, therefore, direct electrical current. The maximum amount of electrical energy generated in a PEM fuel cell corresponds to the Gibbs free energy, ΔG , of the reactions described above.

The maximum theoretical efficiency of PEM fuel cells results from the ratio of the Gibbs free energy and the enthalpy of the reaction $\eta = \frac{\Delta G}{\Delta H}$. The Gibbs free energy equation is given by:

$$\Delta G = \Delta H - T\Delta S,$$

with the entropy of reaction $\Delta S = (s_f)_{H_2O} - (s_f)_{H_2} - 1/2(s_f)_{O_2}$ and the temperature T . The enthalpy of the reaction ΔH is the sum of the enthalpy of formation h_f of the reactants and the products of the reaction ($\Delta H = (h_f)_{H_2O} - (h_f)_{H_2} - 1/2(h_f)_{O_2}$). The

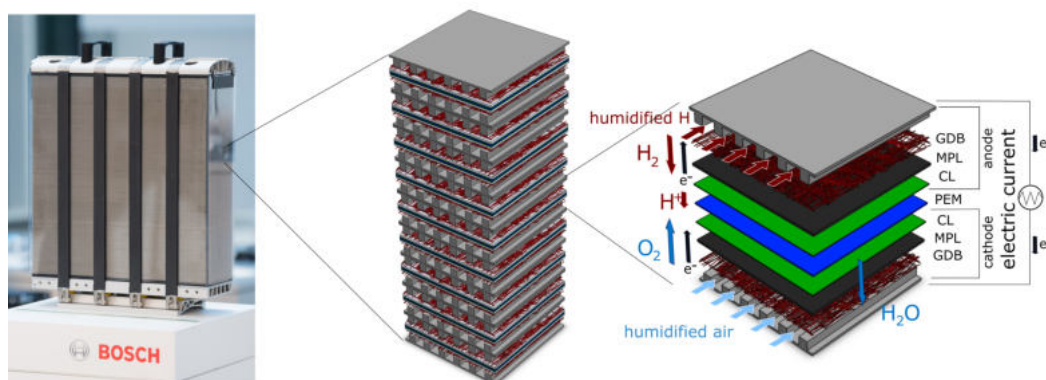


Figure 1.1: Composition of a PEM fuel cell stack: Left: PEM fuel cell stack with roughly 400 cells; center: part of the fuel cell stack with 9 single cells, connected with bipolar plates ; right: detailed view of one cell, showing the different layers and components of one fuel cell.

enthalpy and entropy of formation, h_f and s_f , are temperature dependent values which can be found in thermodynamic data tables [12]. The resulting maximum efficiency of a hydrogen fuel cell is $\eta \approx 83\%$.

However, the practical efficiency of a PEM fuel cell is between 40 and 60% [8, 9, 11]. The losses are caused, among others, by activation losses due to the kinetics of the electrochemical reactions, ohmic losses due to internal electrical and ionic resistance, and mass transport losses, which result from crossover of reactants and difficulties in getting the reactants to reaction sites [9]. A well-known reason for the latter one is the so-called flooding, when liquid water accumulates in the cathode gas diffusion layer (GDL) and transport paths for oxygen are blocked, which results in a lower reaction rate in the catalyst layer. To improve the efficiency of a fuel cell, the choice of appropriate materials and corresponding operating conditions is crucial.

Components of PEM fuel cells Often, the term fuel cell is used for the complete power-supply unit. However, to be exact, this unit has to be called 'fuel-cell stack', while only one single unit in this stack is correctly called 'fuel cell'. In Figure 1.1, the composition of a fuel-cell stack is shown. On the left, an exemplary fuel cell stack, which delivers a power of approximately 120 kW is presented. This fuel-cell stack consists of roughly 400 single cells. In the center of the figure, a section of nine cells is pictured exemplary. The cells are connected at the bipolar plates (grey). A typical fuel cell is schematically represented in explosion view by the layered structure on the

right side in Figure 1.1. Here, an electrolyte (blue) is placed between an anode and a cathode backing layer, consisting of the micro-porous layer (MPL) (black) and gas diffusion backbone (GDB) (red fibrous structure). The combination of MPL and GDB form the gas diffusion layer (GDL). In the literature, often the GDL denotes the fibrous structure only which is, to be precise, only valid for MPL-free GDLs. A thin catalyst layer (green) is placed between the anode or cathode MPL, respectively, and the electrolyte, referred to as the anode or cathode catalyst layer (ACL or CCL). The anode-electrolyte-cathode assembly (MEA - membrane electrolyte assembly) is clamped between two bipolar plates (grey), which house the flow channels for fuel and oxidant feed.

The membrane (electrolyte) is a thin ($< 50 \mu\text{m}$) proton-conductive polymer membrane (typically a perfluorocarbon-sulfonic acid (PFSA) ionomer) [9, 11]. A well-known manufacturer of the membrane is Nafion, and this name is often found in the literature for membrane materials. The key properties of the fuel-cell membrane are protonic conductivity, water transport, low gas permeation, and physical properties such as strength and dimensional stability. All of these properties are directly related to the membrane water content [11].

In the catalyst layers, the electrochemical reactions take place. More precisely, the electrochemical reactions take place on the catalyst surface. Since there are three kinds of species that participate in the electrochemical reactions, namely gases, electrons, and protons, the reactions can take place on a portion of the catalyst surface where all three species have access to [11]. The most common catalyst in PEM fuel cells for both oxygen-reduction and hydrogen-oxidation reactions is platinum. Since it is the catalyst surface area that matters, not the weight, it is important to have small platinum particles (4 nm or smaller) with large surface area finely dispersed on the surface [11]. A combination of membrane and catalyst layers is called the catalyst coated membrane (CCM).

The micro-porous layer (MPL) is usually fabricated by intermixing PTFE with carbon grains [13]. This yields a thin layer located between CL and GDL with pore sizes smaller than $17 \mu\text{m}$ (resulting from measured break through pressures). It is found that the presence of MPLs drastically reduces the GDL water saturation at water breakthrough from ca. 25% to ca. 5% [14, 15], and it is therefore expected that MPLs improve the fuel-cell performance.

The GDB is a fibrous carbon structure coated with PTFE to get hydrophobic surface properties. It must be sufficiently porous to allow flow of both reactant gases and prod-

uct water, but also electrically and thermally conductive through-plane and in-plane [11]. Even though, interfacial or contact resistance is typically more important than bulk conductivity [16]. Additionally, fabrication restrictions for economic reasons occur since the manufacturing process must be suitable for mass production. Therefore usually carbon fiber based materials such as carbon-fiber papers and woven carbon fabrics or cloths are used in commercial applications [16]. The GDL shall establish a homogeneous distribution of the reactants on the CL coming from the gas distributor channels to ensure optimal usage of the catalyst surface for the reactions.

The gas distributor channels are part of the bipolar collector or separator plates, which have several functions in a fuel-cell stack. They connect cells electrically in series, collect produced current, and house the gas channels to distribute the fuel and oxidant along the whole cell. As well, they facilitate water management by removing the excess water from the cell [17]. For an efficient water removal, usually hydrophilic surfaces are chosen which must be corrosion resistant in the fuel-cell environment; yet they must not be made out of 'exotic' and expensive materials. Common materials are coated metals or graphite, which also provide mechanical support for the cells in a PEM fuel cell stack. Various designs for the gas-channel orientation were proposed by researchers including pins, straight channels, serpentine channels, interdigitated channels, and open porous gas distributors. A detailed review of gas-distributor configurations was given by Manso et al. [18]. In this work, straight channels are considered since they are still the most commonly used technique. We focus on the fluid transport and the properties necessary for a potent water management.

Water management in cathodes of PEM fuel cells Water management plays a critical role in PEM fuel-cell performance. The membrane needs high water content to conduct protons effectively, whereas excessive water would block gas pathways and cover catalyst sites, resulting in reactant starvation and cell degradation. As previously described, PEM fuel-cell cathodes consist of several layers with different properties. In this section, insights into water movement through the cathode layers is given. We start in the center of the cell, at the membrane, and follow the excess water through the components on the cathode side.

The proton conductivity of the polymer electrolyte membrane highly depends on its water content. Liquid water is necessary to transport the protons along the polymer chains from the anode to the cathode side. The reactant-gas supplies (H_2 and O_2

stream) are often humidified to prevent dry-out of the membrane. Diffusion and potential gradients are the driving force of water transport in this layer, while pressure gradients play a minor role [19].

In CCL, water is produced during the reaction and it exists in liquid and vapor form [20] as well as in the form of sorbed water in the ionomer of the membrane. Contrary to conditions in the membrane, excessive liquid water formation is not beneficial in the catalyst layer. The reaction's penetration depth is significantly reduced in completely flooded CCLs, which results in inactivity of major parts of the catalyst [20]. These are conflicting requirements for optimal water management. In addition to the cathode reaction, the transformation from liquid water to water vapor is one important function of the CCL, since vapor is easier to be transported out of the cell. A favorable side effect is the resulting evaporative cooling, which converts some of the waste heat of the reaction to latent heat. Nevertheless, not all of the liquid water is transferred to vapor. Actually, the minimum portion of liquid water transferred to the neighboring layers is linked to the produced current density. A detailed explanation is given by Eikerling et al. [20]. It is proposed that for a current density around 2 A/cm^2 , the minimum relative portion of water flux, which is transferred to the GDL in liquid form, is between 0.6 and 0.8. Therefore, liquid water transport plays an important role in the neighboring hydrophobic coated GDL (MPL and GDB). The function of MPL is to enhance electrical and thermal contact between the CL and the GDB, which has a much coarser structure than the CL and would therefore have a less continuous surface. The MPL is a fine porous grain structure with a hydrophobic surface made from carbon grains. Its mechanical strength protects the CCM from the rather stiff fibers of the GDB. The small grain size results in a capillary barrier to liquid water leaving the CCL preventing the MEA from dry out. It is still not well understood how the liquid water passes through the MPL, but it is assumed that water passes through the fine porous layer through larger cracks [21]. The MPL structure is very sensitive and cracks are very likely to occur during the fabrication of the cells. In the GDL, liquid water transport is mainly driven by pressure gradients and capillary forces. Due to the importance of the GDL in PEM fuel cells, a vast amount of papers regarding GDL studies have been published in the literature over the past two decades. For a comprehensive review on the GDL for PEM fuel cells, it is referred to Cindrella et al. [22]. In this work, we focus on (MPL-free) carbon paper GDLs or GDBs. It is often found in literature that the most promising improvements on PEM fuel cell performance can be achieved by optimizing the GDL to enhance its mass transfer ability, such as reactants transport

to the catalyst layers and liquid water removal out of the MEA. Especially, excessive water accumulation leads to so-called flooding of the GDL. Dependent on the operating conditions, a significant amount of the water might be present in liquid form in the GDL. The liquid water then blocks the paths of the oxygen to reach the catalyst layer. The resulting lack of oxygen in the cathode catalyst layer reduces the cell performance. Therefore, the produced water needs to be removed in an efficient way.

This shows, how crucial an appropriate water management in the PEM fuel cell is. However, to alter the water management, the relevant processes in the porous layers and at the shared interfaces need to be understood, inhering the interface between the MPL and GDB, the principal effects in the GDL (liquid and vapor water transport, evaporation and condensation, local wettability changes, effects of pore shapes), the interface driven process at the interface to the gas distributor including wettability change, droplet growth and detachment, and local blockage of pores.

Focus on the water transport processes at the interface between GDL and gas distributor In the past few years, tremendous efforts have been contributed to the understanding of liquid water transport in PEM fuel cells in particular in GDL and gas distributor. In Figure 1.2, the water transport through these two components is visualized presenting the different occurring configurations at the interface between GDL and gas distributor. A detailed and physically based representation, which allows to include many physical processes, is the direct numerical simulation (DNS) [23]. However, in general, two-phase DNS models are not mass conservative at phase interfaces [24]. Additionally, it comes with high computational costs, such that the calculation of representative spatial and temporal dimensions is expensive, not to mention the effort involved in generating the grids in the complex, porous structures. On the other hand, volume-averaged methods, such as representative elementary volume (REV) methods, lack precision for thin porous materials like GDLs [25], even for single-phase flow through GDL representations [26]. For two-phase fluid flow, the problem is further amplified since local patterns cannot be mapped [27]. A promising technique are pore-network models (PNM), which capture pore-scale effects with a reasonable computational effort. Most of the PNMs for GDL modeling found in the literature are stationary or quasi-stationary approaches [28, 29, 30, 31, 32, 33, 34, 35, 36, 37] or use simplified, regular GDL or GDB structures [38, 21]. For these models, it is assumed that the boundary conditions vary slow enough such that the flow pattern can equilibrate

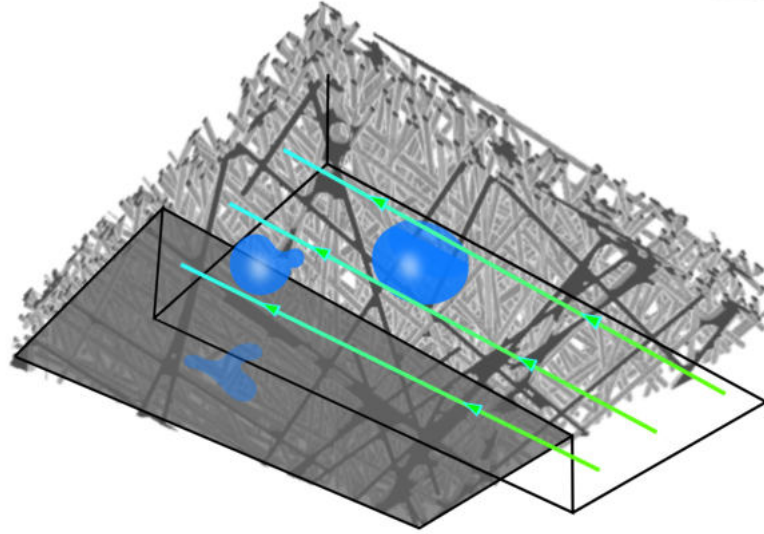


Figure 1.2: Three-dimensional visualization of the liquid water transport from MPL-free GDL to gas distributor including drop formation in the gas channel, mixed-wet interactions between hydrophobic GDL and hydrophilic channel wall and local blockage at channel surface in direct contact with GDL in land parts.

in every time step. But these models are not capable to capture the highly dynamic conditions at the interface between GDL and gas distributor. A particular challenge is the wettability change between the two layers. Different interface configuration can be distinguished, depending on whether water is in contact with the hydrophilic surface of the gas distributor. In this case, the liquid water might interact with the gas flow such that it can be detached from the hydrophobic GDL or it might be trapped by hydrophilic solid structures. Otherwise, if no contact with hydrophilic surfaces occurs at the interface, we consider flow through hydrophobic porous materials and the formation of drops at the interface between free gas flow and porous GDL. It is observed that the flow behavior at the interface has a high influence on the water distribution in the GDL and, accordingly, on the performance of the fuel cell. Therefore, it is crucial to understand the ongoing processes at the interface to improve the efficiency of PEM fuel cells.

In the following, we only consider MPL-free GDLs, such that the term GDL is equivalent to GDB.

In this work, we focus on incorporating the highly dynamic interface conditions at the interface between GDL and gas distributor into a dynamic pore network model that represents flow through realistic MPL-free GDL structures (see Figure 1.3). The

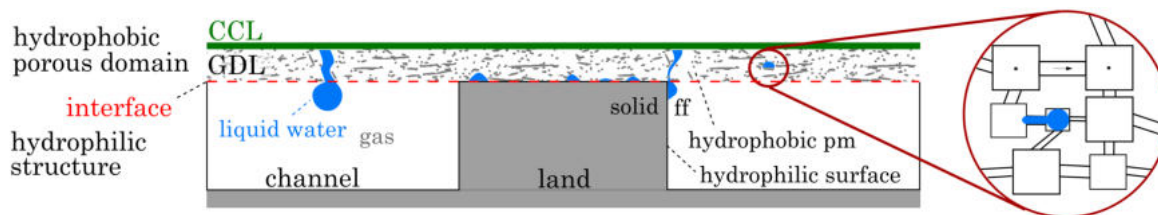


Figure 1.3: Two-dimensional visualization of water transport processes from GDL to gas distributor. The hydrophobic, porous GDL is represented by a pore-network model, which is coupled with the CCL layer and the gas distributor including the different occurring interface configurations.

developed model captures efficiently the two-phase transport in-between the porous, hydrophobic GDL and the hydrophilic gas distributor on the cathode side of a PEM fuel cell.

1.2 Structure of the thesis

In the next chapter, some fundamentals and the modeling concept are explained. Among others, the basic functionality of a PEM fuel cell is explained and an introduction to pore-network modeling and the pore-network generation is given. Of major importance is the description of the interface between the GDL and the gas distributor. In Chapter 3, the conceptual models used for the single domains of interest are presented, followed by the conceptual models for the different occurring interface phenomena between GDL and gas distributor in Chapter 4. In Chapter 5 and 6, we introduce two different coupling approaches to model the interaction of fluid flow in MPL-free GDLs and gas distributors. We distinguish between a coupling approach of a pore-network with a free flow domain (Chapter 5) and one of a pore-network with a REV domain (Chapter 6). The numerical results of the single-domain investigations and coupled models are presented in Chapter 7, 8 and 9, respectively. In Chapter 7, some structural and flow characteristics of the MPL-free GDL are evaluated and single phase investigations are performed on a GDL-gas distributor setup. Chapter 8 presents the simulation results of the uncoupled interface conditions, which are occurring at the interface between GDL and gas distributor. The results of simulations of the coupled domain models are shown in Chapter 9. In the last chapter, the results and potentials are discussed and we conclude with some further perspectives.

2 Fundamentals

In this chapter, the fundamental terms and assumptions are explained, which are relevant for the developed model of the PEM fuel-cell-cathode interfaces. We consider three phases, one solid phase and two fluid phases, a gas phase and a liquid one. The developed model distinguishes two domains separated by an interface, namely the pore-network model representing the MPL-free GDL, and either a free flow or an REV domain for the gas distributor.

The used terms and definitions are explained in Section 2.1. Due to the complex and heterogeneous materials and processes, the fuel-cell layers are considered on the pore-scale. The pore-scale properties are introduced in Section 2.6. We focus on the properties relevant for the water management in a PEM fuel cell. Therefore, the governing principles of the flow on the cathode side of a PEM fuel cell are presented in Section 2.9.

2.1 Terms and definitions

Fluids are substances that continuously deform under shear stress. This deformation means the fluid flows. The properties of the fluids and the fluids' behavior are determined by the behavior on the molecular scale. Nevertheless, modeling fluid flow on the molecular scale is computationally very expensive such that we consider the behavior in an averaged sense to obtain continuous, differentiable functions. With this continuum approach, fluids can be described as phases consisting of components following Gibbs phase rule [1].

Phases

A phase α is a region of space or a thermodynamic system, throughout which all physical properties of a material are essentially uniform and which is physically separated from other phases by an interface. In this thesis, we distinguish between three different phases (gaseous, liquid, solid). A phase might disappear or reappear in the system due to transitions like evaporation, condensation, dissolution, or degassing. Through the same processes, different phases interact and exchange mass, momentum, and energy. The gas phase is always homogeneous since gaseous components are mixed on the molecular scale. In contrast to that, mixtures of liquids are often immiscible or partly miscible so that these mixtures are denoted as heterogeneous or multiphasic mixtures [1].

A phase is called compressible, if its density can change in the system. In this thesis, the liquid phase is assumed as an incompressible phase while the gaseous phase is compressible.

The third phase in the considered systems of this work, the solid matrix of a porous medium, is assumed to be rigid and immobile. The void space of the porous material can be filled with gas and/or liquid fluids.

In the scope of this thesis, we consider two mobile phases, namely liquid and gas, $\alpha \in l, g$, and one immobile solid phase.

2.1.1 Components

A component κ comprises a set of molecules of either single chemical elements (e.g. hydrogen) or molecular compounds (e.g. water or carbondioxide). Often a set of different molecules is cumulated to one linked component, if the behavior of the single substances is not of interest.

Each component is quantified in each phase by its mass fraction X_α^κ or mole fraction x_α^κ . The sum of these fractions within one phase sums to one

$$\sum_{\kappa} X_\alpha^\kappa = \sum_{\kappa} x_\alpha^\kappa = 1.$$

Mass and mole fractions can be converted using the molar mass of the components M^κ :

$$X_\alpha^\kappa = \frac{x_\alpha^\kappa M^\kappa}{\sum_\kappa x_\alpha^\kappa M^\kappa}. \quad (2.1)$$

We distinguish two components in this work, water and air, $\kappa \in w, a$. Both components can be present in both phases. Water vapor can mix with air in the gas phase and air can be dissolved in water in the liquid phase.

2.1.2 Scales

Transport processes in PEM fuel cells occur on different spatial and temporal scales.

Spatial scales Considering a fluid on the molecular scale, the movement and behavior of individual molecules as well as intermolecular interactions are described. The continuum scale results from averaging over a sufficiently large number of molecules. Here, average-based quantities, such as density, viscosity, and surface tension are defined (see Section 2.2).

For the solid phase of the porous medium, we distinguish between the pore scale and the REV scale: On the pore scale, the detailed geometrical description of the local solid and void space within a porous medium are defined (see Section 2.6). If we consider a sufficiently large volume of the porous medium, i.e. the representative elementary volume (REV), its properties may be averaged which gives REV-scale quantities like porosity or permeability [2] (see Section 2.5). Dependent on the quantity of interest, the size of an REV has to be chosen.

An REV must be chosen large enough to smooth out any fluctuating pore-scale properties, while a maximum size should not be exceeded in order to capture REV-scale heterogeneity. In Figure 2.1, the spatial scales are visualized. In this work, we are interested in pore-local effects and take the influence of local variations of the void space in the porous material into account. Therefore, in the following, the pore scale will be the main scale to analyze flow in the porous material.

Temporal scales Flow process in porous media occur on very different time scales. While pore-scale displacement and transport processes, such as Haines jumps [39], may

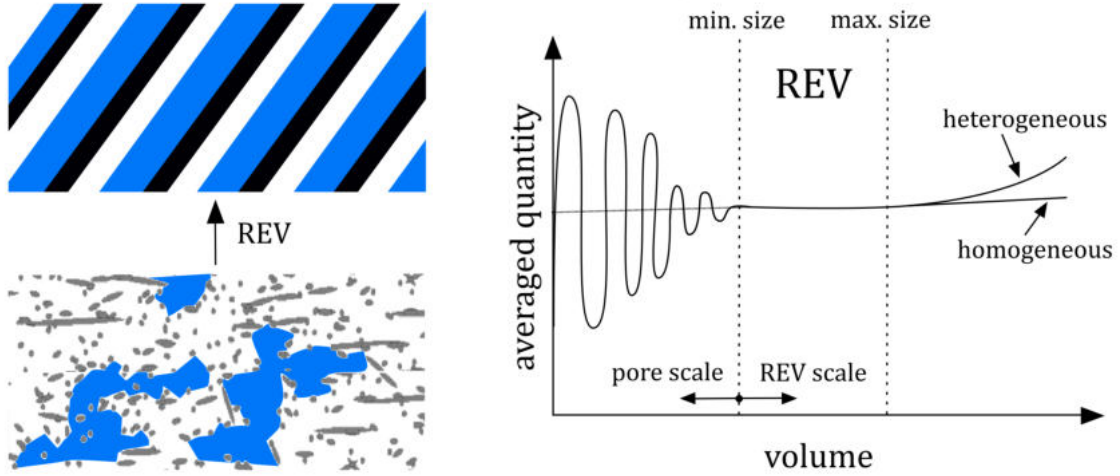


Figure 2.1: From pore-scale to REV-scale by averaging quantities of interest in representative volumes following [2, 1].

occur on temporal scales of the order of milliseconds, phenomena captured on the REV scale are usually much slower, ranging from seconds to years, dependent on the spatial scale of interest. In the field of fuel-cell modeling, considering the water management, computation times ranging from milliseconds to minutes are of interest.

2.2 Fluid properties

In the following some fluid properties are introduced.

2.2.1 Density and viscosity

The phase density and phase viscosity are in general temperature- and pressure-dependent properties. The density ρ of a phase α denotes the ratio of its mass to the volume it occupies:

$$\rho_{\alpha} = \frac{m_{\alpha}}{V_{\alpha}}. \quad (2.2)$$

The dynamic phase viscosity μ_{α} describes the resistance of a fluid to deformation [1].

2.2.2 Contact angle and wettability

Wettability describes the tendency of a fluid to spread on a solid surface to get into a favorable energy state. The wetting phase refers to the phase, which prefers to coat the solid surface, while the non-wetting phase tries to minimize the contact area with the solid. The contact angle is measured at the line where all three phases are in contact and accounts for the local balance of forces described by the Young equation

$$\sigma^{ns} = \sigma^{ws} + \cos \theta \sigma^{nw}, \quad (2.3)$$

with the interfacial tensions σ^{ns} , σ^{ws} and σ^{nw} between the wetting phase, the non-wetting phase, and the solid phase denoted by the superscripts w , n and s , respectively. By convention, the contact angle is measured from the denser phase, such that for a system with air and water, the following terms are established: The contact angle is larger than 90 degrees on a hydrophobic surface and smaller than 90 degrees on a hydrophilic surface.

At the interface between a porous domain and a free flow domain, the capillary forces, surface tension and interfacial tension, cause the invading fluid phase (e.g. liquid in gas phase) to form a droplet on the material surface. A droplet resting on a solid surface and surrounded by a gas forms a characteristic contact angle θ . On a hydrophilic surface ($\theta < 90^\circ$), a water droplet tends to spread on the surface, while on a hydrophobic surface ($\theta > 90^\circ$), a shorter triple-phase contact line is build (see Figure 2.2). The

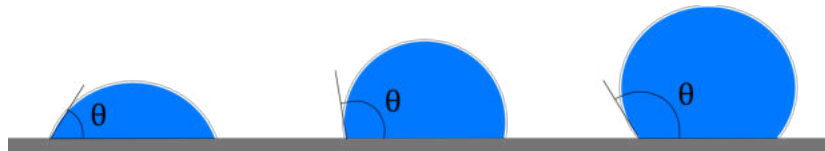


Figure 2.2: Shape of a water droplet on a hydrophilic (left), on a hydrophobic surface (middle) and super-hydrophobic surface (right).

contact angle measured at a resting droplet on a smooth surface is the equilibrium contact angle or static contact angle. If external forces, like a gas stream, are acting on the droplet, which cause a deformation, the contact angle varies before the three-phase contact line starts moving. Once a critical contact angle is reached, the contact line starts moving. In upstream direction, where the contact angle of the droplet is decreasing due to the deformation, the critical angle is called *receding contact angle*. In downstream direction of the gas flow, the critical contact angle which needs to be

overcome before the contact line gets in motion is called *advancing contact angle*. The deformed droplets and the contact angles are visualized in Figure 2.3.

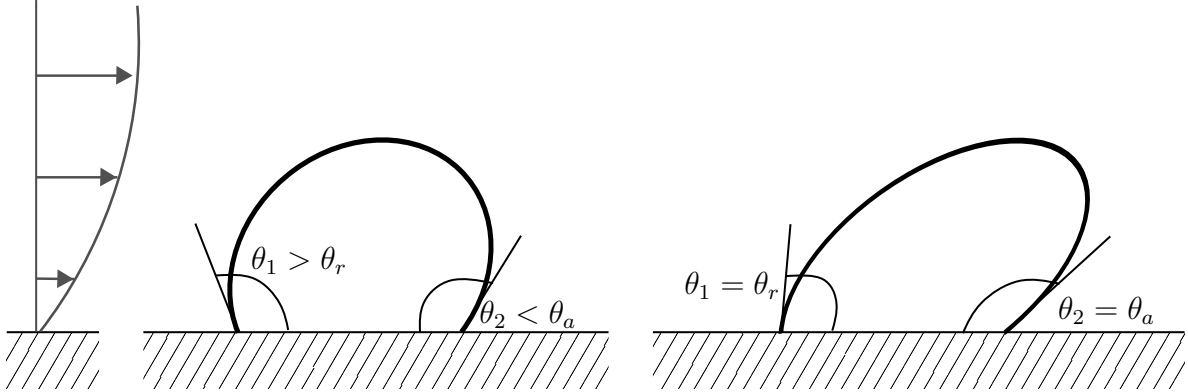


Figure 2.3: Deformed shape of a water droplet on a hydrophobic surface in a gas stream resulting in a drag force on the drop surface. θ_r denotes the receding contact angle and θ_a the advancing contact angle. The angles θ_1 and θ_2 are the actual contact angles in upstream and downstream direction, respectively.

2.2.3 Surface tension and capillary pressure

Fluids tend to minimize their surface area with respect to the volume, which results in a curved interface between two immiscible fluids. This curved interface, e.g. between a gas and a liquid, causes capillary effects. Considering water in a hydrophilic capillary tube, a rise in the water level is observed (left in Figure 2.4). The water is wetting the walls, increasing the area between wall and liquid. As a result, the surface of the liquid curves inside the capillary tube. A similar behavior results from water in a hydrophobic tube, but in this case, the curvature of the interface is opposite, resulting in a decrease of the water level in the tube (right in Figure 2.4). Due to the interfacial tension, the pressure on the concave side of the interface is higher than the one on the convex one. Under equilibrium, the Laplace equation relates the capillary pressure to the curvature radii

$$p_c = \sigma \left(\frac{1}{r_1} + \frac{1}{r_2} \right), \quad (2.4)$$

with the radii of the curved interface r_1 and r_2 , respectively, and the surface tension σ . The term surface tension describes the interfacial tension of a solid or liquid phase with

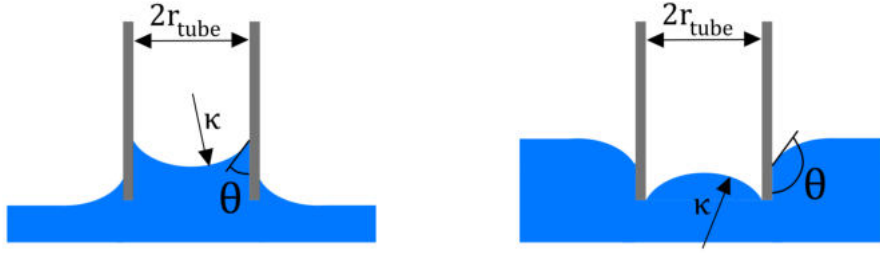


Figure 2.4: Capillary action of water in a hydrophilic tube (left) and in a hydrophobic tube (right).

its pure gas phase. A derivation of the Laplace equation can be found e.g. in [40]. The total curvature of the interface is given by $\kappa = \left(\frac{1}{r_1} + \frac{1}{r_2}\right)$. For spherical geometries, the two radii are equal. Considering a cylindrical tube as presented in Figure 2.4, the curvature κ is related to the tube radius r_{tube} by the equilibrium contact angle θ at the three-phase contact line at the wall ($r_{\text{tube}}/2 = \kappa \cos \theta$).

Following e.g. Hassanizadeh et al. [41], under equilibrium conditions, a balance of interfacial forces results in

$$p_c = p_n - p_w, \quad (2.5)$$

with the phase pressures of the non-wetting phase n and the wetting phase w , respectively.

In this work, we distinguish between the pore-local capillary pressure which describes the phase-pressure difference of the non-wetting phase n and the wetting phase w across a fluid-fluid interface and the global capillary pressure which is applied across a complete domain. It describes the phase pressure difference between in- and outlet for fluids in the computation domain. The pore-local capillary pressure is denoted with a small letter p_c , and for the global capillary pressure, a capital letter is used P_c .

2.3 Thermodynamics basics

In the following, some thermodynamic essentials and relations are described.

Thermodynamic equilibrium The thermodynamic equilibrium is the combination of mechanical, thermal, and chemical equilibrium [1]. The mechanical equilibrium at the interface between two phases implies that all mechanical forces acting at the interface are balanced. Note that, in multi-phase flow in porous media, pressure jumps due to capillary forces occur due to the above discussed surface tension. The thermal equilibrium is achieved when two phases in thermal contact with each other cease to have a net exchange of energy. It follows that if two phases are in thermal equilibrium, their temperatures are locally the same (also at the interface). This means that the thermal equilibrium is fulfilled if the influence of convection is negligible compared to conduction. The chemical equilibrium implies that the phases in the system have the same chemical potentials. The number of present phases is not relevant. Hence the mole fractions in a multi-phase multi-component system are constant if pressure and temperature are constant.

Local equilibrium refers to equilibrium conditions in a volume of fluid-filled porous material that is representing the smallest entity in the model concept (pores on the pore-scale, REV on the REV-scale) [1].

Local thermodynamic equilibrium is usually satisfied, if the processes are sufficiently slow compared to fluid displacement processes. The processes of interest happen at a larger time scale than the equilibration processes. In this work, we assume local thermodynamic equilibrium is always satisfied.

Phase composition and phase change A gas is a structural phase of matter in which the thermal mobility of molecules or atoms is strong enough to permit their free motion, significantly exceeding the cohesive force. This means, gases do not have a free surface. A gas is assumed to be ideal, if its components are not subject to inter-particle interactions. Ideal gases obeys the ideal gas law, a simplified equation of state,

$$pV = nRT, \quad (2.6)$$

with the pressure p , the volume V , the number of moles n , the ideal gas constant $R = 8.314 \text{ J}/(\text{mol K})$ and the temperature T .

Here, we use the ideal gas law as a simple relation between the different state variables. The ideal gas law is valid in the considered fuel-cell application since the occurring pressure is far below the critical pressure but close to atmospheric conditions.

When locally several phases (e.g. a gas and a liquid) coexist in chemical equilibrium, their compositions can be calculated using molar quantities. In an ideal gas mixture, the partial pressure of a component κ is proportional to its mole fraction x_g^κ

$$p_g^\kappa = x_g^\kappa p_g, \quad (2.7)$$

with the gas phase pressure p_g .

According to Dalton's law, the sum of all partial pressures gives the phase pressure

$$\sum_{\kappa} p_g^\kappa = p_g. \quad (2.8)$$

Since we assume the phases to be in chemical equilibrium, the partial pressure of water, the main component in the liquid phase, equals the saturated vapor pressure. For a system of water and air, it holds

$$p_g^w = p_{\text{sat}}^w, \quad (2.9)$$

and the mole fractions of the components water (w) and air (a) can be determined in the gas phase using Eqs. (2.7) and (2.8)

$$x_g^w = \frac{p_{\text{sat}}^w}{p_g} \quad \text{and} \quad x_g^a = 1 - x_g^w. \quad (2.10)$$

The composition in the liquid phase can be determined using Henry's law or Raoult's law, dependent on whether the component κ is the major (solvent) or minor (solute) component within the liquid phase. Henry's law states that the amount of dissolved gas in liquid (x_l^a) is proportional to its partial pressure in the gas phase (p_g^a) divided by the Henry coefficient H_{gl}^a . Therefore, the mole fractions in the liquid phase are given by

$$x_l^a = \frac{p_g^a}{H_{gl}^a} \quad \text{and} \quad x_l^w = 1 - x_l^a. \quad (2.11)$$

Raoult's law combines Eq. (2.7) with Eq. (2.9) to get the solvent's (component with higher concentration) partial pressure

$$p_g^w = x_l^w p_{\text{sat}}^w. \quad (2.12)$$

2.4 Flow regimes

Fluid flow can be characterized using the dimensionless Reynolds number:

$$Re = \frac{v d_{\text{char}}}{\nu}, \quad (2.13)$$

with the velocity v , the characteristic length d_{char} and the kinematic viscosity of the fluid ν .

Considering flow with very low velocities ($Re < 1$), inertial forces can be neglected and one talks about creeping flow. For natural processes in porous media, this is usually a valid assumption. Also the flow regime in gas diffusion layers of PEM fuel cells is usually in this regime.

In the gas distributor, flow velocities are much higher. Here, we consider laminar flow. In this case, inertial effects are relevant.

For very high flow velocities ($Re > 2300$) in the gas channels of the PEM fuel cell, one might reach a transition to the turbulent flow regime. In this case, one observes a high amount of mixing and transfer of kinetic energy from larger to smaller eddies, where it dissipates into heat. However, in this work, only laminar flow in the gas channels and creeping flow in the MPL-free GDL is considered.

2.5 REV scale properties

Porosity A porous medium is a material which includes void spaces (pores) and solid matrix (e.g., fibers or grains). The porosity is the ratio of void space, V_{void} , to the overall volume of the REV, V_{total} , including both, the void space and the solid matrix

$$\Phi = \frac{V_{\text{void}}}{V_{\text{total}}}. \quad (2.14)$$

Saturation The saturation is a measure of how much volume of the void space V_{void} is filled by a given fluid phase α

$$S_{\alpha} := \frac{V_{\alpha}}{V_{\text{void}}}. \quad (2.15)$$

By definition, the sum of all saturations S_α equals one

$$\sum_{\alpha} S_{\alpha} := 1. \quad (2.16)$$

If the void spaces or pores are connected with each other, fluids may flow from one pore to another and the porous medium is called permeable.

Permeability Flow in porous media is highly influenced by the solid matrix. It is impeded by constrictions and the resulting small dimensions of available flow channels between grains or fibers. On the REV-scale, this limitation is taken into account with the help of the permeability K . Its value has to be determined experimentally for a specific porous material and might vary in the different spatial directions such that the permeability becomes a tensor \mathbf{K} . If only one phase is considered, on the REV-scale, flow velocity in a porous medium is proportional to its permeability.

Relative permeability Not only the solid matrix, but also the presence of another fluid influences the REV flow velocity in a porous medium. In pores filled with two fluids, the wetting phase is in contact with the solid walls while the non-wetting phase flows in the center of a pore. This effect is taken into account on the REV-scale by the relative permeability k_r . The relative permeability of Phase 1 k_{r1} describes the resistance of the other phase(s) to Phase 1. Constitutive relations for the relative permeabilities $k_{rw}(S_w)$ and $k_{rn}(S_w)$ describe the factors relating permeability to wetting phase and non-wetting phase saturation, S_w and S_n , respectively.

2.6 Pore-scale properties

In this section, different pore-scale properties are presented.

2.6.1 Idealized geometries and shape factor

The void space geometries of a porous material are usually very complex. Choosing more simple shapes that preserve the relevant geometrical properties is a common

practice to reduce the complexity of pore-scale fluid flow modeling [42]. The governing flow behaviors are conserved as good as possible.

Detailed investigations on different idealized pore and throat geometries are published by Joekar-Niasar and Hassanizadeh [43] and Joekar-Niasar et al. [44]. For a brief overview on their findings, it is referred to Weishaupt [45]. The widely used concept of shape factor proposed by Manson and Morrow [46], which can be seen as a sort of hydraulic diameter, is used to identify similarities in the cross-sectional shapes of the throats. It is defined as the ratio of the area A and the perimeter squared P^2 ,

$$G = \frac{A}{P^2}. \quad (2.17)$$

The shape factor might have a similar or even the same value for different more or less complex structures. A similar shape factor refers to a similar hydraulic diameter and therefore similar flow resistance properties. In Figure 2.5, different complex shapes are analyzed by their shape factor and compared to simple geometric shapes with a similar shape factor. A circle has a shape factor $G = 1/4\pi$ and an almost round but more

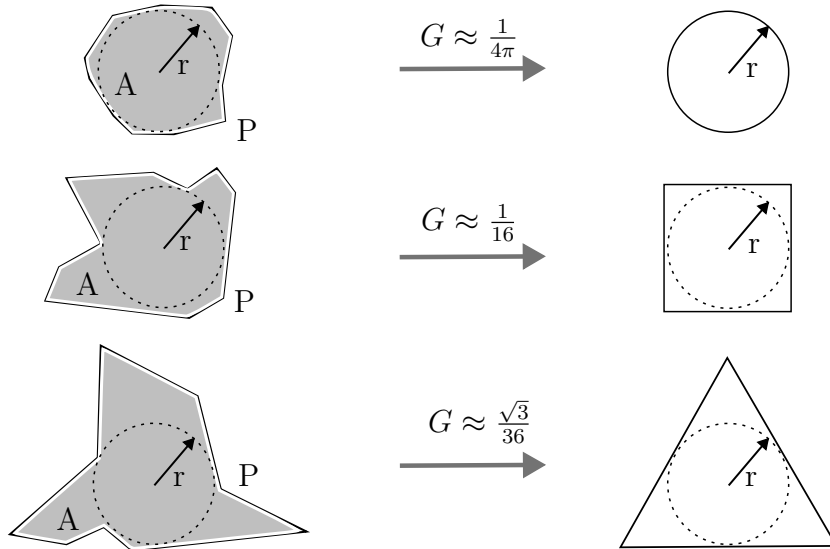


Figure 2.5: Visualization of different pore geometries mapped to simpler, idealized pore shapes using the shape factor G . The idealized geometries have the same or at least a similar shape factor and the same inscribed radius r as the original, more complex form. The perimeter and area might differ between the original and the simplified representation. (cf. [40] and [45])

complex shape has a similar shape factor and can therefore be transferred to the easier to compute round shape for the flow analysis without causing large inaccuracies.

In this work, using a pore-network model approach, we use idealized and geometrical simplified shapes for the pore bodies and throats. The representation of the pore bodies and throats allows an accurate computation of the flow resistances but also the occurrence of corner flow is taken into account in an adequate way. The corner flow in the pores and throats allows the presence of more than one phase in the elements. A wetting phase flux might occur in the corners of the throats and the local capillary pressure-saturation relation in the pore bodies is highly influenced by the wetting fluid in the corner.

2.7 Displacement and transport processes on the pore scale

It is of particular interest in the modeling of fuel cells to improve the material property choices and the flow behavior, and to predict the associated macroscopic properties. Therefore, it is necessary to understand the displacement and transport processes relevant in multi-phase flow systems. This is crucial for the design and the prediction of performance parameters of PEM fuel cells. Different modeling techniques have been developed to simulate flow on the pore scale [47].

2.7.1 Displacement processes in the gas diffusion layer on the pore scale

Lenormand et al. [48] classified the two-phase drainage flow into three regimes:

- stable displacement,
- capillary fingering,
- and viscous fingering.

For the classification, we use the capillary number $Ca = \frac{\mu_n v_n}{\sigma}$ and the viscosity ratio $M = \frac{\mu_n}{\mu_w}$. Here, v_n is the characteristic velocity of the invading fluid. The capillary number is the ratio between viscous forces which act at the pore scale in the injected fluid and capillary forces [48]. The viscosity ratio is the ratio between the dynamic fluid

viscosities μ of the two fluids involved in the displacement process. When the capillary number Ca is small due to slow displacement rate, the non-wetting fluids preferentially invade the larger pores, where the capillary pressure, which is necessary to overcome the narrowing is the lowest in the system. This results in forming long and meandering paths, called capillary fingering. When the viscosity ratio M is small, the non-wetting

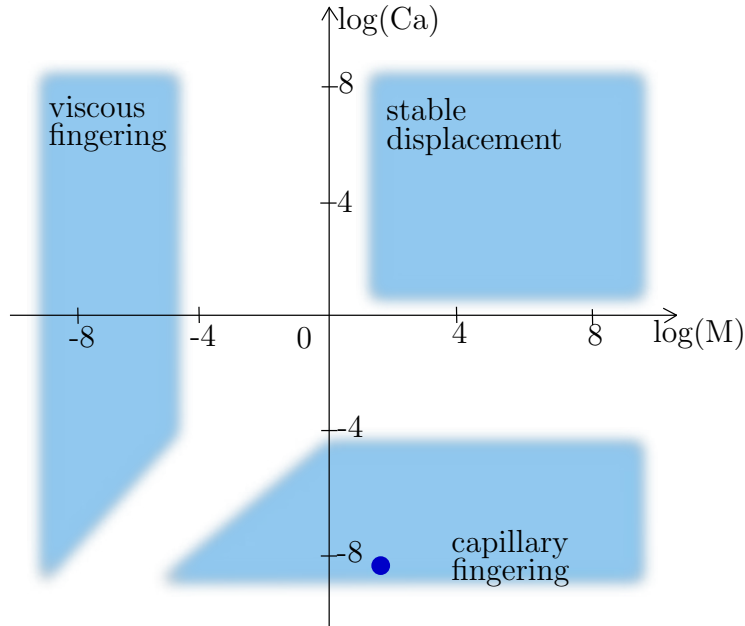


Figure 2.6: Fluid displacement patterns dependent on the capillary number (Ca) and the viscosity ratio (M) following Lenormand et al. [48]. The blue dot marks the conditions occurring in the diffusive layers of PEM fuel cells.

fluids preferentially flow through the pores of lower viscous resistances, resulting in rather straight paths (viscous fingering). When both Ca and M are large, the non-wetting fluids penetrate into porous media forming an approximately flat invasion front, which is called stable displacement. The different flow regimes can be identified by the capillary number and are dependent on the viscosity ratio. Their occurrence is visualized in Figure 2.6. PEM fuel cells are generally operated at current densities below 3 A/cm^2 . Under these operating conditions, the flow rate of liquid water through the hydrophobic MPL-free GDL corresponds to a capillary number Ca of approximately 10^{-8} to 10^{-9} [49]. Taking into account that the ratio of viscosity between water and air is of an order of 10, the two-phase flow in MPL-free GDLs belongs to the capillary fingering regime according to Lenormand et al. [48].

2.8 Modeling techniques for flow on the pore scale

The pore-scale models can be categorized into discretized and network models. In discretized models, multi-phase flow is simulated directly in the pore-space structure.

Discretized models include Lagrangian particle-based methods, which do not require a meshing, such as moving-particle semi-implicit (MPS) [50] and smoothed-particle hydrodynamics (SPH) [51]. Additionally, mesh-based methods, like finite-element [52], finite-volume [53, 54] or Lattice Boltzmann [55, 56, 57, 58], have been developed. These models use a direct representation of the void space, which might be extracted from ct-images. However, studying multi-phase flow with these techniques rises several problems. The mesh-free methods usually allow only small differences in the densities and viscosities of the considered fluids [59]. Therefore, it is difficult to represent the fluid properties of air, vapor, and liquid water in a proper way. For the finite-element and finite-volume methods a dynamic capturing of the local fluid-fluid interfaces is necessary. This can be quite complex and computationally expensive, like the volume of fluid (VoF) approach [42] or phase-field methods [60, 61]. Mesh-based methods in general require a lot of computational effort since the equations have to be solved in every cell and a fine mesh is necessary to represent the flow in the void spaces of the porous medium [62, 42]. Therefore, only a few pores can be considered in each simulation. Also, in general, due to the discretization, VoF simulations require accurate algorithms for advecting the volume fraction function to preserve conservation of mass and avoid interface smearing due to numerical diffusion [24]. Also several assumptions are necessary to perform a discretized model simulation on the PEM fuel cell materials [63].

An alternative for capturing the gap between few-pore direct models and large REV scale models has been introduced in the 1950s by Fatt [64]. Since then, the pore-network modeling has evolved enormously [65, 40]. The pore-network model is well suited for capillary-driven flow regimes (regime of capillary fingering). It is able to capture the relevant ongoing drainage and imbibition displacement processes on the pore scale in the fibrous GDL. Due to the variation of geometric pore shapes, also the effect of corner flow and local capillary pressure-saturation relations can be taken into account. Pore-network models can be divided into quasi-static and dynamic models. The majority of the previously-developed network models are quasi-static in which the pore-scale displacements take place based on their threshold capillary pressure. In this work, a dynamic pore-network model is applied and adapted to capture the dynamic

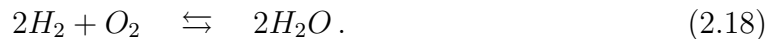
flow processes in the MPL-free GDL. A detailed description of the developed model is given in Section 3.1.

2.9 Polymer electrolyte membrane (PEM) fuel cell functionality

Fuel cells are electro-chemical conversion devices, which convert the chemical energy of a fuel and an oxidizing agent into electrical energy through a pair of redox reactions. Different to batteries, which are electro-chemical storage devices, fuel cells require a continuous source of fuel and oxidizing agent to preserve the reaction and, therefore, the electric energy production.

Inside a fuel-cell unit, various transport processes can be considered to distribute the educts to the reactions in the catalyst layers (CL) and products away from them. These fluid-transport processes are coupled with the chemical reactions. To understand the complex interactions and improve the performance of fuel cells, coupled simulation approaches are used.

In a PEM fuel cell, hydrogen and oxygen react to water producing electric energy and heat:



The name-giving part of this fuel-cell type is the electrolyte which is usually a solid polymer membrane made of a PFSA ionomer produced by Nafion. The cell consists of several different layers. The basic structure is presented in Figure 2.7.

On the anode side, humidified hydrogen (H_2) is injected into the cell and distributes through a channel-land structure as shown in Figure 2.7. A gas-diffusion backend (GDB) and micro-porous layer (MPL) (combined to a GDL) are used to spread the hydrogen gas homogeneously on the catalyst layer (CL), where the anode-side reaction takes place. The hydrogen molecules are split into protons and electrons. The reactive processes are described in more detail in Section 2.9.2. The protons pass through the proton conductive polymer electrolyte membrane (PEM), while the electrons are channeled in the electric circuit to the consumer (e.g. the motor of a car). On the

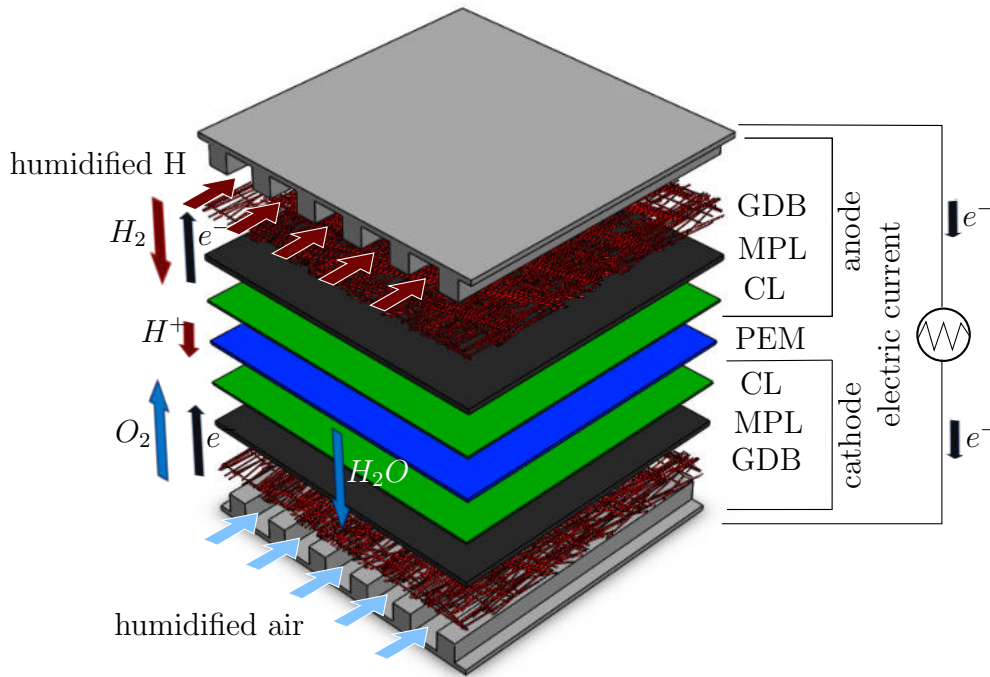


Figure 2.7: Explosion view of a PEM fuel cell presenting the layered structure of the cathode and anode side of the cell

cathode side, humidified air is directed into the cell via the gas distributor. In Figure 2.7, a simple channel-land structure is shown. However, here also other structures and materials can be used to improve the cell performance. This challenge is discussed in Section 2.9.1. The gas distributor is in contact with a GDL to distribute the oxygen molecules (O_2) homogeneously on the cathode catalyst layer. In the catalyst layer, the oxygen reacts with the protons producing water, electric energy, and heat. The exhaust water needs to be removed from the reaction layer mainly through the cathode porous layers. In this thesis, we focus on the processes in GDL and gas distributor. The materials and structural properties of these components are described below.

2.9.1 Materials and structures of GDB (or MPL-free GDL) and gas distributor

The gas-diffusion backend (GDB) is a coated carbon-fiber paper and part of the gas diffusion layer (GDL). The hydrophilic carbon fibers are coated, e.g. by PTFE (Polytetrafluoroethylene) to create a hydrophobic surface with a contact angle between water

and air between 100° and 150° [16]. The fibers have a diameter of 8 to $14\mu\text{m}$ [16]. Combined with a small amount of binder (here 1 to 4% is used), the coated fibers form a paper-like structure as shown in Figure 2.8.

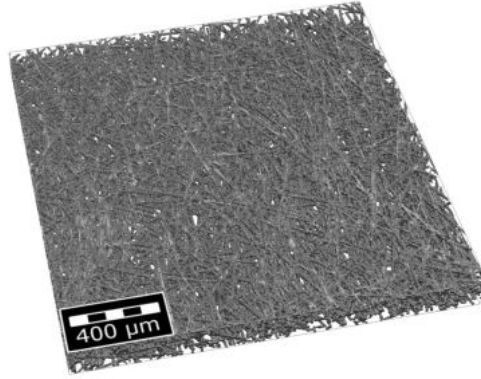


Figure 2.8: Gas diffusion layer (GDL) generated using the software GeoDict® [66] with a porosity of 80% including fibers and coating (dimensions $1000 \times 1000 \times 180[\mu\text{m}]$), fiber material: dark grey, binder material: light grey

For the numerical analysis, a digitally generated representation is used. The structure was generated using the material properties given in [67] using the Math2Market software GeoDict® [66]. The resulting material has a high porosity of approximately 80% with a pore-inscribed radius between 10 and $150\mu\text{m}$.

For the cathode gas distributor, different structures can be found in industrial applications. The classic case, a channel-land structure is shown in Figure 2.7. However, in recent years, open porous gas distributor structures have been investigated to be used for gas distributors in PEM fuel cells [68, 69]. The cells of MIRAI fuel cell vehicle launched in 2014 use an expanded metal gas distributor for the air supply rather than the classic channel structure [70]. An advantage is the expected reduction of pressure fluctuations resulting from water accumulation in the channels or pores. Nevertheless, channel structures offer the advantage of an easy handling during the production and the flow conditions are better understood. In Figure 2.9, a channel structure and an open porous gas distributor are visualized exemplary.

Usually, the gas distributor is fabricated from metal with a hydrophilic surface to remove the liquid water efficiently from the GDL. However, this also supports the accumulation of liquid water in the GDL at land parts of the gas distributor (see Figure 2.10). This accumulation blocks the gas paths for the oxygen supply to the catalyst layer

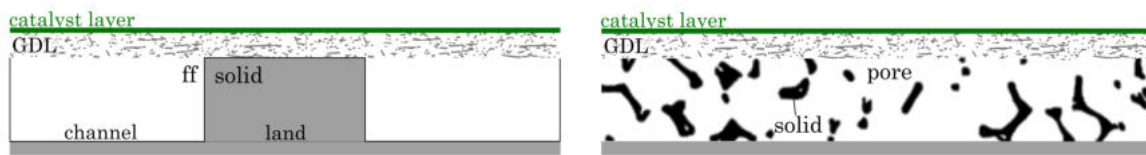


Figure 2.9: Channel structure (left) and open porous structure (right) of gas distributor. Both in contact with the GDL.

reducing the produced energy [71]. Therefore, a hydrophobic coating can be applied on the gas distributor surface at these land parts, while the channels stay hydrophilic. The hydrophilic surface of the gas distributor in the channels supports the liquid water out-take by the mixed-wet interaction with the hydrophobic GDL (right in Figure 2.10).

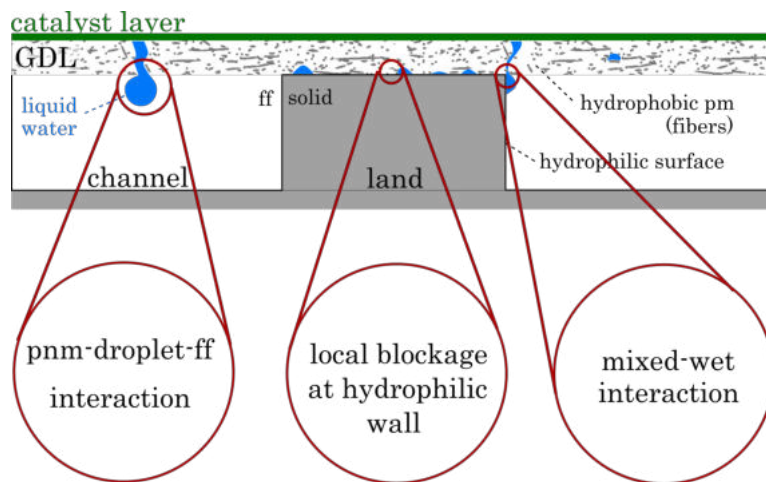
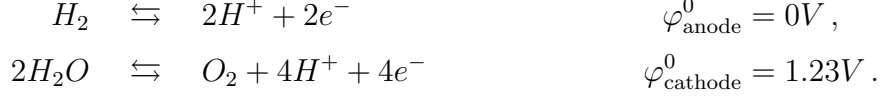


Figure 2.10: Different interface configurations including liquid-water accumulation in the "land" region, where there is a direct contact between the cooling and the GDL, drop formation in the channels and mixed-wet interaction between hydrophobic GDL and hydrophilic gas distributor.

2.9.2 Electro-chemistry in the catalyst layer

At the anode side, hydrogen is split up to protons and electrons in the catalyst layer and on the cathode side, oxygen is reduced by the protons passing through the membrane from the anode side. The reaction equation Eq. (2.18) splits up to the anode and

cathode reaction:



The energy production of a PEM fuel cell is determined by the chemical potential between hydrogen and oxygen as well as the availability of these reactants in the cell. To characterize a fuel cell, the polarization curve is a standard tool. It indicates the voltage as a function of the current density. Since the kinetics of the oxygen reduction reaction at the cathode side are much slower than the hydrogen oxidation at the anode side, the polarization curve behavior is dominated by the cathode reaction conditions [72].

At zero current, the fuel cell electrodes provide the thermodynamic open circuit voltage: $U_{\text{cell}} = U_{OCV}$. Connection of a load induces the current I in the system, and reduces the cell voltage U_{cell} . The value of U_{OCV} is given by the Nernst equation [73]. At open-circuit conditions, the electrochemical reactions are at equilibrium. The equilibrium potential φ^0 (also called normal potential) describes the affinity of the elements to form ions in aqueous solutions at normal conditions ($T = 298.15\text{ K}$ and $p = 1\text{ bar}$) [74]. The cell voltage is the difference of the electric potentials of the cathode and the anode. At equilibrium conditions, this gives the theoretical open-circuit voltage of the unloaded fuel cell:

$$U_{OCV} = \Delta\varphi^0 = \varphi_{\text{cathode}}^0 - \varphi_{\text{anode}}^0 = 1.23V - 0.00V = 1.23V. \quad (2.19)$$

At equilibrium conditions, the electrochemical reaction rates of the forward and back reaction are equal and no net mass transfer results. Closing the external current circuit yields a spontaneous reaction of hydrogen and oxygen producing water, electric energy and heat. The transfer of mass of the reactant gases and the draw of electric current from the system causes a drop in the cell voltage. The over-potential η_i defines the shift from the equilibrium state of the corresponding reaction i

$$\eta_i = \varphi_S - \varphi_E - \varphi_i^0. \quad (2.20)$$

Where φ_S is the potential within the cathode or anode and φ_E is the potential at the electrolyte. The difference between these potentials is known as the Galvani potential

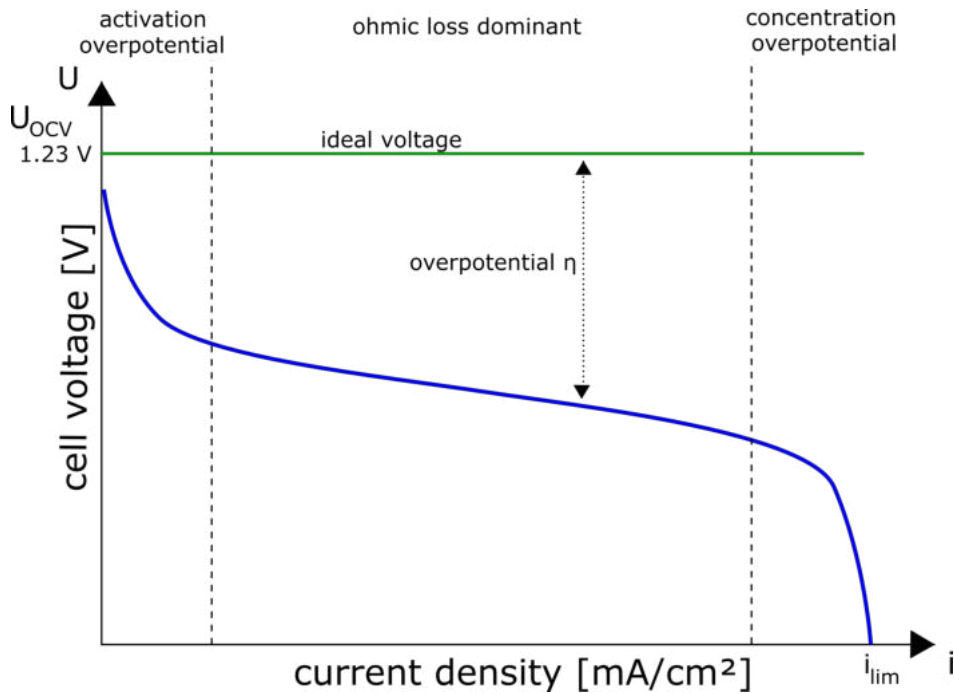


Figure 2.11: Exemplary polarization curve of a PEM fuel cell

($\Delta\varphi_{\text{interface},S} = \varphi_S - \varphi_E$) [74]. By definition, the over-potential η_i becomes positive, when the forward reaction is dominant and the corresponding reactant is oxidized. This process is called anodic reaction, where the electrons and protons are released. If the cathodic back reaction is dominant, the reactant is reduced and protons and electrons are consumed, the over-potential is negative ($\eta_i < 0V$), accordingly. The polarization curve (deviation from equilibrium potential) is shown in Figure 2.11.

The shape of the polarization curve depends on the structure of the fuel cell components and the operating conditions (temperature, pressure, humidification and reactant gas concentration). However, it can be divided into three parts between the open-circuit voltage at $i = 0$ and the maximum cell current i_{lim} , where the cell voltage drops to zero.

The so-called activation over-potential leads to a significant voltage loss at small current densities [74]. The charge transfer between the reactant gases and the electrode or electrolyte occurs at a finite rate. Once the activation over-potential is fully developed and the fuel cell mainly acts as an ohmic resistor, the voltage loss is dominated by the ohmic resistance of the membrane. In this region, the shape of the polarization curve is almost linear. At high current densities, the mass transfer at the catalyst surface becomes fast enough to produce a concentration gradient within the catalyst layer due

to the limited mass transport of the reactant gases. This results in a significant decrease of the reactant gas concentration within the catalyst layer which causes a drop of the cell voltage. Additionally, the removal of the produced water is too slow which blocks the paths for the reactant gases. This phenomenon shall be prevented.

When the catalyst layer is completely starved from the reactant gas, the cell voltage drops to zero. If the maximum current density, i_{lim} , can be increased by preventing starvation of the catalyst layer, the performance of the cell can be improved.

The depletion and production rates depend on the local current density. For low current densities and an overpotential close to the equilibrium state (left part in Figure 2.11), the Butler-Volmer equation describes how the electrical current through the electrode depends on the voltage difference between the electrodes. The electrode current density i is given by

$$i = i_0^{\text{ref}} \left\{ \exp \left[\frac{\alpha_a z F \eta_i}{RT} \right] - \exp \left[-\frac{\alpha_c z F \eta_i}{RT} \right] \right\}. \quad (2.21)$$

where i_0^{ref} represents the exchange current density at a reference state, α_c and α_a are the cathodic and anodic charge transfer factors, respectively, z the number of transferred electrons per molecule of reactant and F is the Faraday constant. For higher overpotentials (center part in Figure 2.11), the Butler-Volmer equation simplifies to the empirically derived Tafel equation. For the cathode, the following expression has been derived by Woehr et al. [75] including the effect of catalyst activation due to platinum loading and water coverage [76]:

$$i = i_0^{\text{ref}} f_v \exp \left[\frac{-\Delta G_0^\ddagger}{R} \left(\frac{1}{T} - \frac{1}{T_{\text{ref}}} \right) \right] (1 - S_w) \frac{p_{O_2}}{p_{\text{ref}}^{O_2}} \exp \left[\frac{-\alpha z F}{RT} \eta_i \right]. \quad (2.22)$$

Where f_v is a surface increasing factor, which describes the relation between the catalytically active and the geometrical surface area of the electrode, ΔG_0^\ddagger is the free activation enthalpy. The factor $(1 - S_w)$ accounts for the covering effect of the catalyst sites by the liquid phase, with the average water saturation at the interface S_w .

The equations above describe the relation between current density and overpotential, which results in the polarization curve in Figure 2.11. Since the current density describes the transfer of electrons, the current density and the reaction rates in the cell are directly related. Therefore, we can calculate the water production dependent on the current density. The molar component flux produced during the reaction in a reference

cell area A_{rc} is then given by

$$\dot{n}_{H_2O}^{\text{react}} = \frac{i \cdot A_{rc}}{z_{H_2}} \cdot \frac{1}{F}. \quad (2.23)$$

This production rate can now be used for fluid transport investigations, which take the effects of electrochemical processes into account.

3 Conceptual and numerical models for the single domains

This chapter explains the mathematical models and the numerical discretization schemes used for the individual domains representing a MPL-free GDL or GDB and a gas distributor channel, respectively. It is followed by a description of the interface conditions required for the coupling of the sub-models. As presented in Figure 3.1, we distinguish between two different model setups. In both models, the MPL-free GDL or GDB is represented by a pore-network model to capture local displacement processes. For the channel domain, either a commonly named free-flow model or a so-called REV-based model is used. For the REV based model, the flow properties and phase presence are averaged over an REV. The free-flow model is directly resolving the flow and component transfer in the channel domain. The single domains for MPL-free GDL or GDB (Ω^{PNM}) and gas-distributor channel (Ω^{REV} or Ω^{FF}) are coupled at the common interface Γ^{REV} or Γ^{FF} , and a distinct boundary condition is applied at the opposite site of the GDB (Γ^{MPL}) to represent the influence of CCL and MPL.

The conceptual models and number of fluid phases considered in each domain are:

- MPL-free GDL or GDB: pore-network model (PNM) with non-isothermal two-phase multi-component flow (2pncni)
- Channel Option 1: (Navier-)Stokes (FF) with non-isothermal multi-component single-phase flow (1pncni)
- Channel Option 2: Darcy (REV) model with non-isothermal two-phase flow (2pni)

Component transport and non-isothermal flow can be considered optionally in the domain formulations. The focus of this research is on the interface processes driven

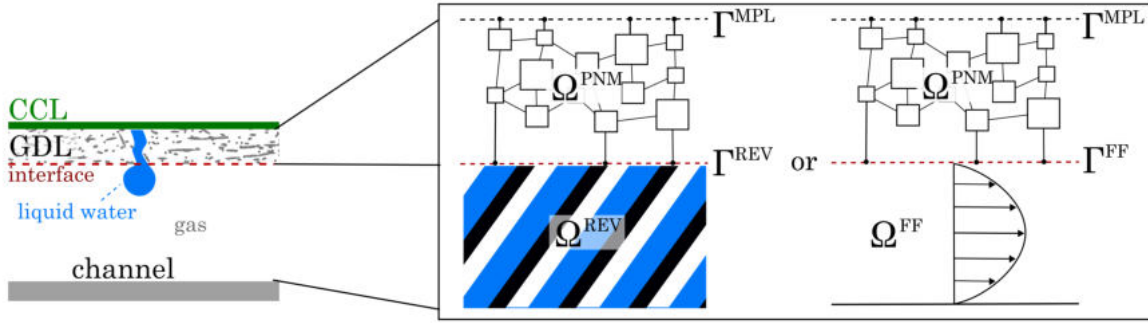


Figure 3.1: Sketch of MPL-free GDL or GDB and gas distributor channel for the coupled models. The considered sub-domains are Ω^{PNM} for the MPL-free GDL or GDB representation and Ω^{REV} and Ω^{FF} for the channel representation dependent on the considered operating conditions, respectively. The domains are coupled at the interface Γ^{REV} and Γ^{FF} , respectively and a special boundary condition is applied at Γ^{MPL} to represent the influence of CCL and MPL.

by wettability changes and droplet formation. Therefore, the non-isothermal model is described but the calculations are performed under isothermal conditions. The models are implemented in such a way that the influence of gravity can be either incorporated or neglected. The dimensions of the pore spaces and the considered droplets are tiny such that the influence of gravity can be neglected, here [77]. Furthermore, we always consider laminar flow regimes in all domains with creeping flow in the GDL model (Ω^{PNM}).

Modeling flow through the GDL The fibrous GDL is a key component concerning the water management in PEM fuel cells. It plays an important role in removing excessive water from the CCL to the gas distributor. Much effort has been invested in gaining insights into pore-scale processes of liquid water transport in the GDL. Many numerical pore-scale studies of the GDL have been performed over the past few years (a.o.) [34, 78, 31, 32, 33, 35, 3, 79, 80, 7, 81, 82]. Nevertheless, water dynamics in the GDL are still not well understood. According to Lee et al. [83], invasion-percolation with capillary fingering is the dominant transport mechanism for transport of two fluid phases in GDLs for common operating conditions of PEM fuel cells. Several distinctive features of liquid-water transport in the GDL make its pore-scale modeling extremely difficult. First, a small flow rate of liquid water, with a capillary number value between 10^{-8} and 10^{-9} [49], results in computationally expensive modeling. Second,

the complexity of the pore structure of the GDL and dynamic displacement processes give rise to the difficulty in developing an efficient and robust pore-scale model. In this work, we develop the model further that has been presented by Weishaupt et al. [45, 84, 85]. The new model captures the MPL-free GDL or GDB-specific properties and represents the two-phase and multi-component transport on the pore scale in this fibrous porous material.

Modeling flow in the gas distributor The gas distributor provides a structure to transport and distribute the reactants and products through the cell. We distinguish between the occurrence of single-phase and two-phase flow dependent on the operating conditions. In the single-phase case, only the gas phase is present in the channel. This means, water is transported out of the cell in vapor form, and we analyze the composition of the gas flux. In this case, not enough water is produced to generate a relevant film flow at the channel walls. If more liquid water is produced or the temperature is lower, a relevant amount of liquid water might be present in the gas distributor. This needs to be represented in the model by taking a liquid film flow into account for the water transport.

In particular, the accumulation of excess water has a detrimental impact on the cell performance. The so-called flooding of the gas distributor, when liquid water blocks a gas flow passage, results in inhomogeneous reactant distributions in the cell and pressure losses along the flow paths. An adequate modeling of liquid-water accumulation and clogging of the gas-distributor structure is difficult due to the highly dynamic flow phenomena and the high sensitivity to cell operating conditions.

Analyzing and modeling two-phase flow in a channel is a challenge. The pressure drop along a channel highly depends on the flow pattern and the liquid-phase presence [86]. Pressure-drop fluctuations result from different flow configurations in the channel. The flow pattern and resulting pressure fluctuations from drops, slugs or film-flow variations are presented and categorized by the group of Kandlikar in the publication of Grimm et al. [86]. Models have been developed to determine the global pressure drop including some fluctuations. An overview is given by Anderson et al. [87] and Lu et al. [88]. However, further investigations are necessary to apply to relevant parts of the gas-distributor channels. The influence of channel-surface wettability, cross-sectional shape, and orientation of the channels (with respect to gravity) is discussed in [88]. Mortazavi et al. [89] published an overview of modeling methods for pressure drop in

a two-phase channel-flow setup.

In this work, two different approaches are investigated. We distinguish between a single-phase multi-component Navier-Stokes formulation for the gas flow and a two-phase REV approach to include the effect of liquid-water film flow on the flow processes in the gas distributor.

3.1 Pore-network model

The applied pore-network model uses the main assumption that the porous medium can be considered as a network of pore spaces (pore bodies) which are connected with each other by constrictions (pore throats). Hereby, it is assumed that the main volume of the pore space is located in the larger pore bodies and the main resistance to the flow in the porous medium is due to the narrowing between the pore spaces. With these assumptions, the pore spaces can be approximated by simple geometric shapes (spheres, cubes, etc.) and combined to a network of pore bodies and pore throats.

The pore-network implemented in the open source project DuMu^x [90] is based on the following principles:

- The whole volume of the void space of the considered porous medium is distributed on the pore bodies.
- For the pore throats, a negligible volume is assumed but only they offer resistance to the flow.
- With this approach, it is not necessary to capture interfaces in the throats.
- The pressure gradients within the pores are neglected, since the resistance of a pore body is much lower than the one of the throats. This gives the possibility to assign only one pressure value per pore body (per phase).

3.1.1 Governing equations for single-phase flow

For pure single-phase flow without component transport, the mass balance equation is given for each pore body i by

$$V_i \frac{\partial}{\partial t} \rho_i + \sum_j (\rho Q)_{ij} = V_i q_i, \quad (3.1)$$

with the pore body volume V_i and the mass flux through throat ij , $(\rho Q)_{ij}$, which is based on the fluid phase density ρ of the upstream pore body i or j (upwinding). A source or sink term can be applied to the pore body which is denoted as q_i .

For compositional single-phase systems, a molar balance equation is formulated for each component κ on each pore body i :

$$V_i \frac{\partial (x^\kappa \rho_{\text{mol}})_i}{\partial t} + \sum_j (x^\kappa \rho_{\text{mol}} Q)_{ij} + \sum_j (J_{\text{diff,mol}}^{\kappa,\text{pnm}} A)_{ij} = V_i q_i^\kappa, \quad (3.2)$$

with the molar density ρ_{mol} and mole fraction x^κ .

The transport term $(x^\kappa \rho_{\text{mol}} Q)_{ij}$ is again evaluated by upwinding using the density in the upstream pore body. The discrete molar diffusive flux through a pore throat ij is given by Fick's law

$$J_{\text{diff,mol}}^{\kappa,\text{pnm}} = \frac{1}{M^\kappa} \frac{\rho_i + \rho_j}{2} \frac{D_i^\kappa + D_j^\kappa}{2} \frac{X_i^\kappa - X_j^\kappa}{l_{ij}}. \quad (3.3)$$

Where D_i^κ is the molecular diffusion coefficient of component κ in the pore body i and X_i^κ is the respective mass fraction. The throat length is l_{ij} .

Common pore-network models use a one-dimensional form of the stationary Stokes equation under the assumption of fully developed stationary, creeping flow ($Re < 1$) to describe the flow through the pore throats. The momentum balance equation for single-phase flow follows as

$$v_{ij} = \frac{1}{A_{ij}} Q_{ij} = \frac{1}{A_{ij}} k_{ij} (p_i - p_j), \quad (3.4)$$

with the cross-sectional area of the pore throat A_{ij} . This means, the average velocity v_{ij} of the fluid through throat ij is proportional to the pressure difference $(p_i - p_j)$ between the connected pores i and j . k_{ij} is a conductance term dependent on the

throat geometry and the fluid viscosity. Considering non-isothermal systems, an energy balance needs to be formulated

$$V_i \frac{\partial (\rho_i u_i)}{\partial t} + \sum_j (\rho h Q)_{ij} + \sum_j \left[A_{ij} \sum_{\kappa} (J_{\text{diff,mol}}^{\kappa, \text{pnm}} h^{\kappa})_{ij} \right] + \sum_j \frac{\lambda_i + \lambda_j}{2} \frac{T_i - T_j}{l_{ij}} A_{ij} = V_i q_i^e, \quad (3.5)$$

with the convective heat transport $(\rho h Q)_{ij}$ evaluated by upwinding of the fluid density ρ , the specific enthalpy h and volume flux Q . T_i and T_j denote the pore-local temperatures, and λ_i and λ_j are the heat conductivities in the pore bodies i and j . A heat sink or source term might be defined on pore body i by q_i^e . The molecular diffusive energy transfer is taken into account by $J_{\text{diff,mol}}^{\kappa, \text{pnm}} h^{\kappa}$. This term is zero for non-compositional systems.

3.1.2 Governing equations for two-phase flow

For two-phase flow, the continuity equation for a pore body i for each phase α is given by

$$V_i \frac{\partial \rho_i^{\alpha} s_i^{\alpha}}{\partial t} + \sum_j (\rho^{\alpha} Q^{\alpha})_{ij} = V_i q_i^{\alpha}, \quad (3.6)$$

with the pore-local saturation s^{α} , the phase densities ρ^{α} and a source term for each phase q^{α} . The volume of the pore body is again denoted by V_i .

For compositional systems, we formulate a molar balance for each component κ in phase α on each pore body i :

$$V_i \frac{\partial \sum_{\alpha} (x^{\kappa} \rho_{\text{mol}}^{\alpha} s^{\alpha})_i}{\partial t} + \sum_{\alpha} \sum_j (x^{\kappa} \rho_{\text{mol}}^{\alpha} Q^{\alpha})_{ij} + \sum_{\alpha} \sum_j (J_{\text{diff,mol}}^{\kappa, \text{pnm}} A)_{ij} = V_i q_i^{\kappa}, \quad (3.7)$$

with the molar density of each phase $\rho_{\text{mol}}^{\alpha}$ and the mole fraction of the component κ , x^{κ} . The discrete molar diffusive fluxes through a pore throat ij are again given by

Fick's law

$$J_{\text{diff,mol},\alpha}^{\kappa,\text{pnm}} = \frac{1}{M^\kappa} \frac{\rho_i^\alpha + \rho_j^\alpha}{2} \frac{D_{\alpha,i}^\kappa + D_{\alpha,j}^\kappa}{2} \frac{X_{\alpha,i}^\kappa - X_{\alpha,j}^\kappa}{l_{ij}}. \quad (3.8)$$

Where $D_{\alpha,i}^\kappa$ is the molecular diffusion coefficient of component κ in phase α in the pore body i and $X_{\alpha,i}^\kappa$ is the respective mass fraction.

The momentum balance for each phase α is then given as

$$v_{ij}^\alpha = \frac{1}{A_{ij}^\alpha} Q_{ij}^\alpha = \frac{1}{A_{ij}^\alpha} k_{ij}^\alpha (p_i^\alpha - p_j^\alpha) \quad (3.9)$$

with the velocity of the phase v^α , the cross-sectional area of phase α within throat ij , A_{ij}^α , the volume flux of each phase through the throat ij , Q_{ij}^α , the conductance term k_{ij}^α for each phase α , and the phase pressures in the connected pore bodies i and j , p_i^α and p_j^α , respectively. The energy balance for multi-phase multi-component systems under the assumption of a local thermal equilibrium is given by

$$\begin{aligned} V_i \frac{\partial \sum_\alpha (\rho_{\text{mol}}^\alpha u^\alpha s^\alpha)_i}{\partial t} + \sum_\alpha \sum_j (\rho_{\text{mol}}^\alpha h^\alpha Q^\alpha)_{ij} \\ + \sum_\alpha \sum_j (J_{\text{diff,mol},\alpha}^{\kappa,\text{pnm}} h^{\kappa,\alpha} A^\alpha)_{ij} \\ + \sum_\alpha \sum_j \frac{\lambda_i^\alpha + \lambda_j^\alpha}{2} \frac{T_i - T_j}{l_{ij}} A_{ij}^\alpha = V_i q_i^e. \end{aligned} \quad (3.10)$$

For compositional systems, the molecular diffusive energy transport is taken into account by $(J_{\text{diff,mol},\alpha}^{\kappa,\text{pnm}} h^{\kappa,\alpha} A^\alpha)_{ij}$. For immiscible fluids, this term is zero. The specific enthalpies of the phases depend on their composition

$$h^\alpha = \sum_\kappa X^{\alpha,\kappa} h^{\alpha,\kappa}, \quad (3.11)$$

with the specific enthalpy of a phase α purely consisting of component κ [1].

The above formulated balance equations allow the description of a dynamic (non-isothermal) multi-phase multi-component system as it is found in the MPL-free GDL or GDB and at the interface to the gas distributor.

The balance equations are implemented in a discrete form in the pore-network model. However, before we proceed with the discretized form of the equations for the imple-

mentation, some constitutive relations are presented to close the system of equations for a pore-network with cubic pore bodies and connecting throats with a circular or polygonal cross-sectional area.

Constitutive relations The capillary pressure p^c links the two phase pressures in each pore body i by a function of saturation s^w (here: wetting phase saturation) [91]

$$p_i^c = p_i^n - p_i^w = f(s^w), \quad (3.12)$$

with the non-wetting phase pressure p^n and the wetting phase pressure p^w . The local capillary pressure-saturation relation can be determined geometrically using simple pore shapes or approximated from experimental data.

For this work, an adaptation of the analytic derivation presented in [91] is used for a cubic pore body. We include a contact angle $\theta > 0$ (measured from the wetting phase) in following the formulation by multiplying the original equation with $\cos \theta$ and get

$$p_i^c(s^w) = \frac{2\sigma \cos \theta}{R_i (1 - \exp(-6.83s^w))}. \quad (3.13)$$

For the analysis in fuel cell applications, the dependence on the wetting angle is of special interest. Therefore, in Figure 3.2, the capillary pressure-saturation relation for cubic pores with an inscribed radius $R_i = 10^{-4}$ m (representing a large pore in GDL) and a surface tension between the phases, of $\sigma = 0.0725$ N/m (gaseous air and liquid water) is shown for different wetting angles.

Discretization of the pore-network model Considering one pore body i , the volume balance is formulated for each phase α

$$V_i \frac{\Delta s_i^\alpha \rho_i}{\Delta t} = - \sum_{j=1}^{N_i} \rho_i Q_{ij}^\alpha, \quad (3.14)$$

with N_i pore throats connected to the considered pore body. The volume flux of each phase through each of those pore throats is denoted by Q_{ij} . The discrete change of saturation of phase α with each time step is given by $\frac{\Delta s_i^\alpha}{\Delta t}$ and V_i is the pore body

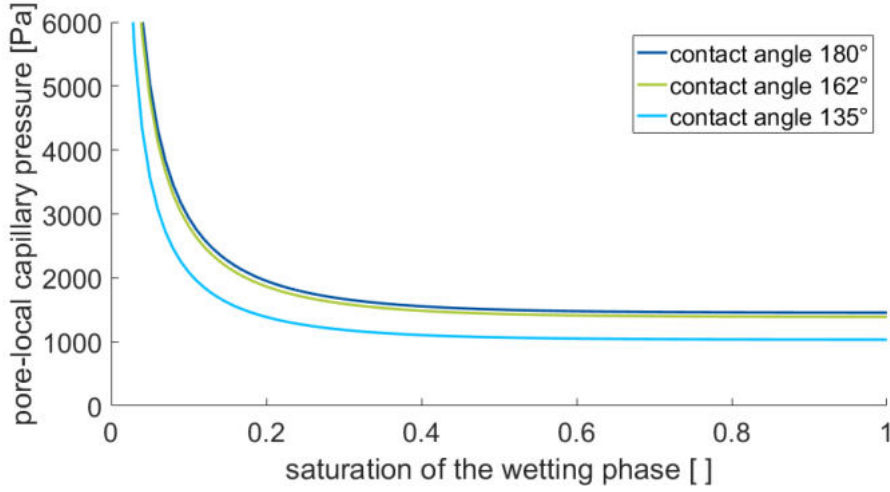


Figure 3.2: Capillary pressure-saturation relation for a pore inscribed radius $R_i = 0.0001$ m, cubic throats and different the wetting angles. The fluids are gaseous air and liquid water with a surface tension $\sigma = 0.0725$ N/m.

volume.

For the flow in the pore throats, a Poiseuille-type flow is assumed [91], which can be described by

$$Q_{ij}^\alpha = -k_{ij}^\alpha \Delta_{ij} p^\alpha, \quad (3.15)$$

with the fluid conductance of the pore throat for each phase k_{ij}^α which depends on the fluid configuration and the throat shape.

When only the wetting phase is present locally in the throat (local single-phase flow), several semi-analytic approaches can be found in the literature to describe the throat conductivity dependent on the shape of its cross-sectional area. An overview on the available approaches is given in [45]. Patzek and Silin [92] extended the work from Oren et al. [93] to a generalized formulation for different cross-sectional shapes. They propose a scaling of the throat transmissibility with the previously discussed shape factor G (see Section 2.6.1)

$$k_{ij}^w = \frac{c A_{ij}^2 G}{\mu_w l_{ij}}, \quad (3.16)$$

$$k_{ij}^n = 0, \quad (3.17)$$

with the dynamic fluid viscosity of the wetting phase μ_w , the length of the throat l_{ij} , and the throat cross-sectional area A_{ij} . Here, c is a proportionality constant dependent on

the cross-sectional area shape. For circles it takes the value 0.5, for squares $c = 0.5623$ and for equilateral triangles $c = 0.6$. The latter value also holds as a close approximation for isosceles triangles. The throat conductivity for the non-wetting phase is zero in the single-phase case. For the case that both phases are present in the throat, the wetting phase is displaced to the corners as shown in Figure 3.3.

However, the wetting phase in the corner vanishes, if the contact angle θ (measured in the wetting phase) or, the corner half angle α do not fulfill the following condition [40]

$$\theta + \alpha < \frac{\pi}{2}. \quad (3.18)$$

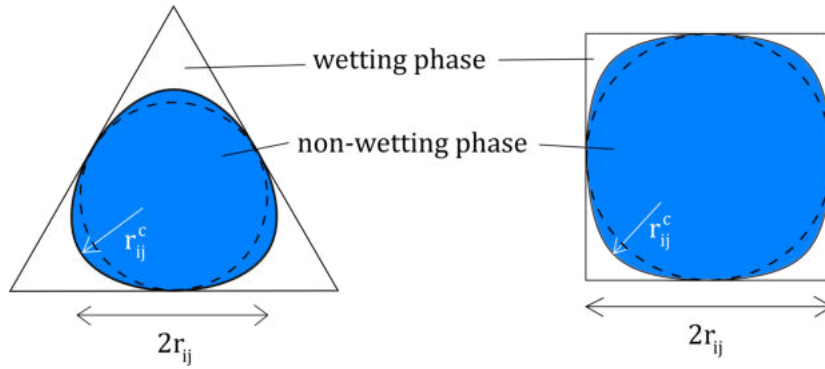


Figure 3.3: Exemplary fluid configuration in a throat with square cross-section if both phases are present. The wetting phase is located in the edges while the non-wetting phase forms the bulk phase.

Once the throat is invaded by the non-wetting phase, in an angular throat two phases are present. The non-wetting phase occupies the central bulk while the wetting phase is reduced to the corners and forms wetting layers. The flow in all fluid domains can be treated individually. There are several approaches to model the flow in the wetting layer which highly depends on the contact angle and geometry of the throat cross section. Usually, the surface roughness is not taken into account explicitly. These approaches are typically geometrically derived or motivated. An expression for the wetting layer conductance is given by Ransohoff and Radke [94],

$$k_{ij}^w = \frac{r_{AM}^2}{\mu_w l_{ij}} \sum_{n=1}^{n_{corner}} \frac{A_{w,n}}{\beta_n}, \quad (3.19)$$

with the dynamic viscosity of the wetting phase μ_w , the throat length l_{ij} , the cross-sectional area of the wetting layer in the corner n $A_{w,n}$ and the dimensionless resistance factor β_n . Where $r_{AM} = \sigma/p_c$ is the radius of curvature of the arc menisci (AM) and n_{corner} the number of corners of the throat shape. The resistance factor β_n can be determined numerically by solving the stationary Stokes equation for a single wetting layer. It depends on the corner geometry and the phase configuration (corner angle and capillary pressure). However, we use an analytic approximation proposed by Zhou et al. [95]

$$\beta_n = \frac{12 \sin^2(\alpha_n) (1 - B)^2}{(1 - \sin(\alpha_n))^2 B^2} \cdot \frac{(\phi_1 - B\phi_2) (\phi_3 + f_2 B\phi_2 - (1 - f_1 B) r_{ij})^2}{(\phi_1 - B\phi_2 - (1 - B) r_{ij}^2)^3}$$

with

$$\begin{aligned} B &= \left(\frac{\pi}{2} - \alpha_n \right) \tan(\alpha_n) \\ \phi_1 &= \cos^2(\alpha_n + \theta) + \cos(\alpha_n + \theta) \sin(\alpha_n + \theta) \tan(\alpha_n) \\ \phi_2 &= 1 - \frac{\theta}{\pi/2 - \alpha_n} \\ \phi_3 &= \frac{\cos(\alpha_n + \theta)}{\cos(\alpha_n)} \end{aligned}$$

where α_n is the half corner angle of corner n and θ is the contact angle in corner n (measured from the wetting phase). The factors f_1 and f_2 correspond to the interface conditions between the phases. Dependent on the fluid viscosity ratio, a no-slip ($f_2 = 1$), a no-stress ($f_2 = 0$), or an intermediate condition ($0 < f_2 < 1$) may be assigned. For a water-air-solid setup, a no-stress condition can be applied while a no-slip condition would be more appropriate in a water-oil-solid setup [40]. For the interface between the solid and the wetting phase, a no-slip condition is assumed and thus $f_1 = 1$ [45].

For the flow of the non-wetting phase also different formulations can be found in the literature. Weishaupt [45] gives again a great overview on the different methods. However, he states that the accuracy of the pore-network model is generally less sensitive to the approximation of the bulk non-wetting phase conductance compared to the one of the wetting layers in the corners.

In this thesis, we use the following expression proposed by Blunt [40]

$$k_{ij}^n = \frac{cA_{n,ij}^2 G}{\mu_n l_{ij}}, \quad (3.20)$$

with the non-wetting phase dynamic viscosity μ_n , the actual cross-sectional area of the non-wetting phase $A_{n,ij}$ and the shape factor G and constant c analogous to Eq. (3.16). If a throat is completely filled with the wetting phase, for the invasion by the non-wetting phase a capillary pressure threshold needs to be overcome. In this work, the approach presented in [93] and [40] is used (converted to radians)

$$p_c^{entry} = \frac{\sigma \cos \theta (1 + 2\sqrt{\pi G})}{r_{ij}} F_d(\theta, G) \quad (3.21)$$

with

$$F_d(\theta, G) = \frac{1 + \sqrt{1 + 4GD / \cos^2 \theta}}{1 + 2\sqrt{\pi G}},$$

$$G = \frac{A_{ij}}{P_{ij}^2},$$

$$D = \pi - 3\theta + 3 \sin \theta \cos \theta - \frac{\cos^2 \theta}{4G}.$$

The wetting angle (again measured in the wetting phase) is denoted as θ , G is the shape factor, A_{ij} is the cross-sectional area and P_{ij} is the perimeter of the throat between pore i and j .

This threshold pressure formulation is derived based on virtual work calculation of the meniscus movement in a pore throat. The work of the displacement must be balanced by the change in free surface energy. The non-wetting phase displaces the wetting phase from the central part of the pore throat such that the wetting phase stays present in each corner (arc menisci) after the invasion. In the absence of gravity, the arc menisci curvature equals the curvature of the main terminal meniscus of the invading non-wetting phase [93].

In Figure 3.4, the function of the capillary entry pressure for a throat with cross-sectional area of the shape of an equilateral triangle, an inscribed radius $A_{ij} = 25 \cdot 10^{-10}$ m and a surface tension between the phases $\sigma = 0.0725$ N/m is shown dependent on the wetting angle.

Considering several components, a continuity equation for each component κ in a pore

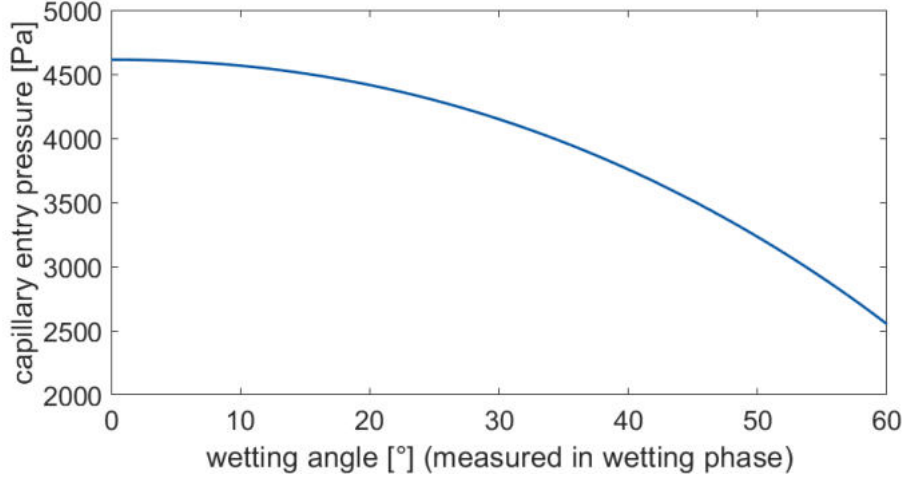


Figure 3.4: Capillary entry pressure for a throat radius $r_{ij} = 25\mu m$ and throats with a cross-section with the shape of an equilateral triangle dependent on the wetting angle

body i is applied

$$V_i \frac{\Delta X^\kappa}{\Delta t} = - \sum_{j=1}^{N_i} \left[X^\kappa Q_{ij} - D^\kappa \frac{\Delta_{ij} X^\kappa}{l_{ij}} a_{ij} \right] + V_i q_i^\kappa = 0, \quad (3.22)$$

with the diffusion coefficient D^κ , the difference of mass fraction between two pore bodies $\Delta_{ij} X^\kappa$, the length and cross-sectional area of the throat l_{ij} and a_{ij} , respectively, and a volume source term for the components q_i^κ .

For now, if there are two phases present, we assume thermodynamic equilibrium such that the respective mole fractions for water vapor in gas and dissolved air are calculated using Henry's and Raoult's law.

For the energy balance, we use Fourier's law

$$q_{ij}^T = \lambda_{ij} \frac{\Delta_{ij} T}{l_{ij}}, \quad (3.23)$$

with the heat flux between two pore bodies q_{ij}^T , the heat conduction coefficient λ_{ij} and the temperature difference between two pores $\Delta_{ij} T$.

3.1.3 Numerical model

Dependent on the presence of multiple phases (liquid and gas) and the consideration of phase changes or component transport, either a single-phase multi-component, a two-phase, or a two-phase multi-component model is applied. The choice of primary variables depends on the desired model. In Table 3.1, the set of primary variables and balance equations for the different kinds of pore-network models considered in this work is summarized. However, if one of the phases vanishes, e.g., due to evaporation, numerical problems arise as the two-phase system degenerates and the pore-local saturation s and mole fraction x of the vanished phase lose their physical meaning. Class et al. [96] propose a solution strategy by switching the local set of primary variables such that they remain physically meaningful. A detailed description of the primary variable switching technique is given in [45]. In Table 3.1, Case A denotes the state, if both phases are present, and Case B, if one phase vanishes.

Table 3.1: Set of primary variables for the different types of pore-network models

model type	primary variables
Single-phase multi-component (1pnc)	$p, x^{k_2}, \dots, x^{k_n}$
Two-phase (2p)	p_n, s_w
Two-phase multi-component (2pnc)	A: $p_n, s_w, x_w^{k_3}, \dots, x_w^{k_n}$ B: $p_n, x_w^{k_2}, \dots, x_w^{k_n}$

The pore-network model is discretized using a box method [1, 97]. The used finite volume scheme is node centered, i.e., a control volume is associated to each grid node on which the balance equations are formulated. Each control volume is divided into sub-control volumes. The fluxes are evaluated over the faces between the sub-control volumes. This makes the scheme locally mass conservative. In the context of pore-network modeling, the grid vertices correspond to the pore bodies while the one-dimensional grid elements represent the pore throats. In Figure 3.5, an example network with six pore bodies and five pore throats is shown. Each pore body corresponds to a control volume which is split into n_{coord} sub-control volumes, with n_{coord} being the coordination number. Pore i is connected to four other pores and therefore features four sub-control volumes. The vertical line at the center of the throat ij is the sub-control volume face over which the flux between pore i and pore j is evaluated. Nevertheless, only one value for the primary variables (e.g. pressure p_i and saturation s_i) is assigned to a pore body.

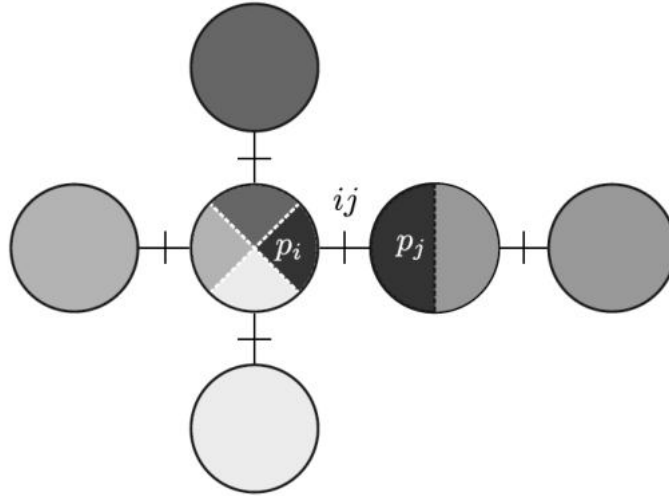


Figure 3.5: Application of the Box scheme for pore-network modeling. The fluid pressures p are located at the centers of the pore bodies. Each pore body corresponds to a control volume, subdivided into n_{coord} sub-control volumes [45].

3.1.4 Pore-network generation

To analyze the representation of real structures used in a PEM fuel cell, the pore-networks can be extracted from μct -scans and digital reconstructions (using the software GeoDict® [98]) of the materials. For the pore-network generation, the open source software PoreSpy [3, 99, 100] is used. It is possible to use an image stack as input and the software creates a representing network of spherical pore bodies and connecting throats. For the application to the MPL-free GDL or GDB structure, the extracted information is transferred and adapted to non-spherical pore shapes. The algorithm developed for PoreSpy first creates an Euclidean distance map from the binary images. A Gaussian filter is used to smooth the images and reduce noisy inaccuracies. Then, the peaks of the distance map are found by applying a maximum filter. Erroneous peaks, like peaks on saddles or plateaus and peaks that are too near to each other, are eliminated. The "true" peaks are then handed as markers to the marker-based watershed algorithm which is the core function of the algorithm. This function generates the segmentation of the pore regions. Based on this information (pore volume, pore coordinates, throat conductivities, throat length, throat diameter, etc.), a pore-network can be generated which represents the considered structure of the pore-scale. This allows a detailed investigation without using a computationally very demanding direct numerical simulation.

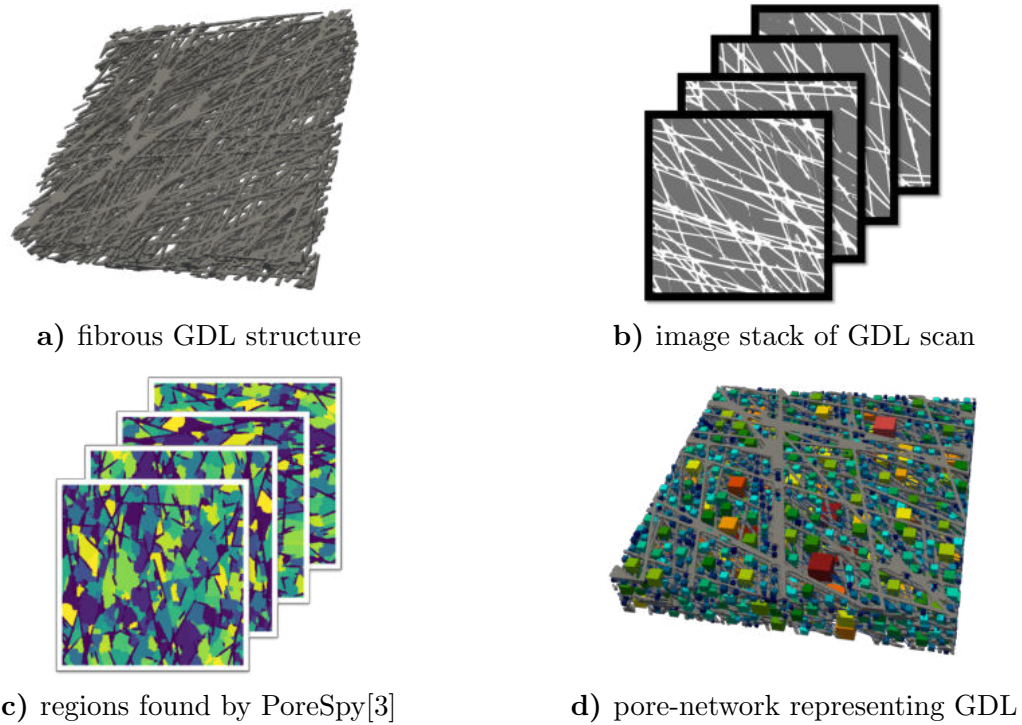


Figure 3.6: Pore-network extraction process using PoreSpy[3]. a) GDL structure that shall be represented by a pore-network; b) image stack (slices) of the structure, e.g. ct-scan images; c) the PoreSpy algorithm identifies large void spaces (regions) as pore bodies and finds connections between them; d) pore-network is generated representing the original GDL structure on the pore scale but in a simplified form.

In Figure 3.6, the process of pore-network generation is visualized in four steps. We start with the original structure, a fibrous GDL, that shall be represented as a pore-network to analyze the flow through the structure (a). The input for the network extraction algorithm is an image stack of the material (e.g., ct-scans)(b). The algorithm extracts the void space of the porous materials and defines regions (which represent the pore bodies) and common interfaces between them (which represent the pore throats)(c). Finally, a pore-network is created that represents the pore-scale properties of the original GDL material. The pore bodies are located in the larger void spaces and connected by throats (d). Here, the pore bodies are scaled and colored according to their size.

3.2 Gas distributor channel model

Dependent on the operating conditions, different amounts of liquid water might be present in the gas distributor. At high gas-flow velocities but low relative humidity in the channel, occurring liquid water (e.g. due to droplet formation) is transported downstream by the gas flow quickly. However, at low relative humidity evaporation processes need to be taken into account. At lower gas-flow velocities and high relative humidity, the liquid water might form films at the hydrophilic gas-distributor walls. Therefore, two-phase flow is observed in the gas distributor channels. We distinguish two modeling approaches: for the first case with low to zero liquid water presence in the gas channels, a free-flow Navier-Stokes model (FF in Figure 3.1) is applied as described in the following section. This model is only valid for single-phase flow, if the liquid-phase flow can be neglected in the channel. If this assumption can not be justified since enough water is present in the channel such that a relevant liquid film might form, we use an REV-type framework with a distinct relative-permeability formulation following Ackermann et al. [101] (REV in Figure 3.1). This model is presented in Section 3.2.2.

3.2.1 Free-flow model

If only the gas phase is present in the channel or if the influence of liquid phase presence on the free flow can be neglected, a single-phase Navier-Stokes formulation can be used to describe the flow in the gas distributor channels.

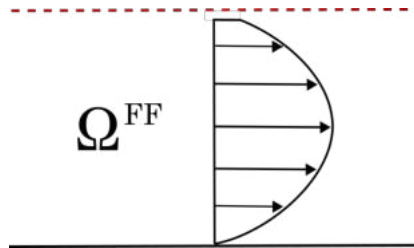


Figure 3.7: Single-phase flow-model concept to describe flow in the gas-distributor channel. This model concept is denoted as the free-flow (FF) model. We use the (Navier-) Stokes equations to describe the gas-flow behavior.

We assume laminar flow ($Re < 2300$) such that turbulent effects can be neglected. For creeping flow ($Re < 1$), we use the Stokes formulation which neglects inertial effects. In this section, the phase subscript is omitted since we only consider the gas phase. In

Figure 3.7, the parabolic flow profile of the gas flow in the channel is visualized for the free-flow (FF) domain.

We assume that the components mix according to binary diffusion which is described by Fick's first law. The gas, which consists of air and water vapor, is assumed to be a compressible ideal gas.

Momentum balance The general transient and compressible form of the momentum balance equation for a single Newtonian fluid phase is given by

$$\frac{\partial(\rho\mathbf{v})}{\partial t} + \nabla \cdot (\rho\mathbf{v}\mathbf{v}^T) = \nabla \cdot \left[\mu (\nabla\mathbf{v} + \nabla\mathbf{v}^T) - \frac{2}{3}\mu (\nabla \cdot \mathbf{v}) \mathbf{I} \right] - \nabla p + \rho\mathbf{g} + \mathbf{f}, \quad (3.24)$$

with the density ρ , the dynamic viscosity μ , the fluid-velocity vector \mathbf{v} and the phase pressure p .

The first two terms result from the total derivative $\frac{D(\rho\mathbf{v})}{Dt}$ and represent the storage term and the convective flux term. The third term represents the viscous term and the last three terms account for the pressure, gravitational and external forces.

In this work, the dilatation term $\frac{2}{3}\mu (\nabla \cdot \mathbf{v}) \mathbf{I}$ is neglected and we do not consider any gravitational effects such that \mathbf{g} is set to zero. If any additional volume force is applied to the flow, this can be applied within the term \mathbf{f} .

For stationary flow and creeping-flow conditions ($Re < 1$), Eq.(3.24) simplifies to the stationary Stokes equation. In this case, the temporal derivative and the convective flux term are neglected:

$$\nabla \cdot [\mu (\nabla\mathbf{v} + \nabla\mathbf{v}^T)] - \nabla p + \rho\mathbf{g} + \mathbf{f} = 0. \quad (3.25)$$

Mass balance Considering the flow of a pure fluid, the conservation of total mass is ensured by the mass balance equation:

$$\frac{\partial\rho}{\partial t} + \nabla \cdot (\rho\mathbf{v}) = q, \quad (3.26)$$

with a storage term $\frac{\partial\rho}{\partial t}$, a flux term $\nabla \cdot (\rho\mathbf{v})$ and a source or sink term q .

For compositional systems, a molar component balance equation can be formulated for

each component κ :

$$\frac{\partial(\rho_{\text{mol}}x^\kappa)}{\partial t} + \nabla \cdot (\rho_{\text{mol}}\mathbf{v}x^\kappa - \mathbf{J}_{\text{diff,mol}}^\kappa\rho\nabla X^\kappa) = q^\kappa. \quad (3.27)$$

Again, we have a storage term and a flux term in the balance equation. The component flux term represents the advective transport with the flow fields and the diffusive molar flux due to the concentration gradient, which is approximated following Fick's first law

$$\mathbf{J}_{\text{diff,mol}}^\kappa = -\frac{1}{M^\kappa}\rho D^\kappa\nabla X^\kappa, \quad (3.28)$$

with the molar fraction x^κ and the mass fraction X^κ .

For a two-component system as it is considered in the gas distributor channel (with air and water vapor), the sum of both component mass balances yields the total mass balance, since $X^{\text{air}} + X^{H_2O} = 1$.

Energy balance Describing a non-isothermal system, an energy-balance equation is required, which accounts for energy storage and flux

$$\frac{\partial(\rho u)}{\partial t} + \nabla \cdot \left(\rho\mathbf{v}h + \sum_{\kappa} \nabla \cdot (\mathbf{J}_{\text{diff,mol}}^\kappa h^\kappa) - \lambda\nabla T \right) = q^e. \quad (3.29)$$

Where q^e denotes an energy source or sink term. The diffusive term ($\mathbf{J}_{\text{diff,mole}}^\kappa h^\kappa$) takes the molar diffusive energy transport into account. The storage term includes the solution-dependent specific internal energy u while the advective term considers the specific phase enthalpy:

$$h = \sum_{\kappa} X^\kappa h^\kappa, \quad (3.30)$$

with the specific enthalpy h^κ of a phase consisting only of component κ . The third term describes the conductive energy flux using Fourier's law, with the phase heat conductivity λ and the phase temperature T .

Numerical model For the spatial discretization of the free-flow model, a staggered-grid finite-volume approach is used, which is also known as MAC scheme [102]. This

scheme inherently provides stable and oscillation-free solutions [103]. In Figure 3.8, the spatial discretization scheme is visualized. Scalar quantities like pressure, density, viscosity, or mole fractions are formulated at the centers of the control volumes of the primal grid (solid lines). The velocity components are located at the faces of the control volumes. Around these faces, dual-grid control volumes are constructed (blue and green). Figure 3.8 shows a section of a two-dimensional grid with two velocity components only.

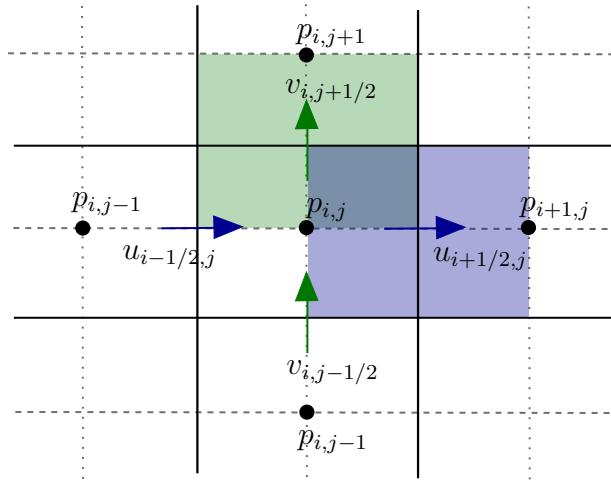


Figure 3.8: Staggered grid for Navier-Stokes discretization

For details on the application of the discretization scheme it is referred to [104]. The primary variables of the Navier-Stokes (FF) model are the pressure p and the velocity vector \mathbf{v} , which are supplemented by the temperature T and the mole fraction x^κ , for compositional non-isothermal systems.

3.2.2 REV model

For operating conditions with lower velocities and high humidification of the cathode gas flow, a two-phase formulation of the gas distributor channels is recommended. The similarities between flow in porous media and the flow in the micro-channel of the gas distributor has been already recognized in prior studies [70]. We are not interested in the detailed flow configurations, but in the saturation-dependent volume fluxes in the channel. Here, we use a two-phase Darcy formulation with a local volume averaging of flow behavior and phase presence as presented by Ackermann et al. [101]. The model



Figure 3.9: Two-phase flow model concept to describe flow in the gas distributor channel. This model concept is denoted as the REV model. We use a Darcy model to describe the flow behavior of both phases, liquid and gas, respectively.

domain is sketched in Figure 3.9.

Describing the channel flow with a Darcy type REV model, analogously to the pore-network model, dependent on the local phase presence, different models with their balance equations and suitable primary variables have to be applied.

Momentum balance Darcy's law yields the REV-scale velocity, a volume flux per area

$$\mathbf{v}_\alpha = -\mathbf{K} \frac{k_{r\alpha}}{\mu_\alpha} (\nabla p_\alpha - \rho_\alpha \mathbf{g}) . \quad (3.31)$$

Where \mathbf{K} is the intrinsic permeability tensor which is a property of the porous material, only. We use a value representing flow through a tube here to approximate the open-channel flow properties. Since the permeability may feature anisotropic (i.e. orientation-dependent) flow resistance, in general, this property is a tensorial quantity. The phase-pressure gradient ∇p_α is the driving force of the Darcy flow. The density ρ_α and dynamic viscosity μ_α are fluid properties. $k_{r\alpha}$ is the relative permeability of each phase α . We use a formulation presented by Ackermann et al. [101] which represents liquid film flow (l) and gas bulk flow (g) in a channel

$$k_{rl}(S_l) = S_l^2 \left(-2S_l + 3 \frac{\mu_l(1 - S_l^2) + \mu_g S_l^2}{\mu_l(1 - S_l) + \mu_g S_l} \right) , \quad (3.32)$$

$$k_{rg}(S_l) = (1 - S_l^2) \left(2(S_l + 2) - 3 \frac{\mu_l(1 - S_l^2) + \mu_g S_l^2}{\mu_l(1 - S_l) + \mu_g S_l} \right) . \quad (3.33)$$

The formulation of the relative permeabilities is derived from an upscaling procedure considering liquid film flow in a gas-flow channel in a one-dimensional domain (flow

between parallel plates). The formulations are based on the following simplifying assumptions: Densities and viscosities are constant, and gravity is neglected. For the non-dimensionalization, we assume the channels to be long and thin, which is the case in the gas distributor of a PEM fuel cell. Nevertheless, the REV-based formulation is an approximation, which does not aim to capture the entire complexity of two-phase flow in the gas distributor channel. It allows an averaged representation including the influence of film flow fed by detached droplets from the GDL surface. The one-dimensional channel representation can be combined with the three-dimensional GDL model to capture the influence of two-phase channel flow on the interface processes between GDL and gas distributor.

Mass balance The mass balance for the domain is given by

$$\sum_{\alpha} \Phi \frac{\partial (\rho_{\alpha} S_{\alpha})}{\partial t} + \nabla \cdot \left(\sum_{\alpha} (\rho_{\alpha} \mathbf{v}_{\alpha}) \right) = \sum_{\alpha} q_{\alpha}, \quad (3.34)$$

with the phase saturation S_{α} and the sink/source term for each phase q_{α} . The porosity Φ is included in the storage term since, in a porous material, only the void volume fraction is available for the fluids. However, to describe the flow in the channels Φ is set to one.

Energy balance Assuming local thermal equilibrium, the energy balance is given by

$$\Phi \frac{\partial (\sum_{\alpha} (\rho_{\alpha} u_{\alpha} S_{\alpha}))}{\partial t} + (1 - \Phi) \frac{\partial (\rho_s c_s T)}{\partial t} + \sum_{\alpha} \nabla \cdot (h_{\alpha} \rho_{\alpha} \mathbf{v}_{\alpha}) - \nabla \cdot (\lambda_{\text{pm}} \nabla T) = q^e, \quad (3.35)$$

with the internal energy u , the solid's density and heat capacity, ρ_s and c_s , respectively, and the temperature T . The second term is presented for the sake of completeness even though it vanishes here since the porosity is set to 1 in the considered channel model. λ_{pm} denotes the effective heat conductivity and h is the phase specific enthalpy. An energy source or sink term might be applied with q^e .

Numerical model Like the pore-network domain, the Darcy domain is spatially discretized using the Box method [97]. In the Box method, the model domain is covered

by a dual mesh where a finite-element grid forms the primary mesh. The approach combines the advantages of the finite-element and finite-volume method. All primary variables are stored and computed at the vertices, which are located at the corners of the elements and represent the surrounding control volume. The two-phase system of partial differential equation for the mass and momentum balance contains the unknowns p_g, p_l, S_g , and S_l . As primary variable for the mass balance the gas-phase pressure p_g is chosen. Additionally, the saturation of the liquid phase S_l (for the two-phase case) and the mole fraction of water in the gas phase $x_g^{H_2O}$ (for compositional models) are chosen. For non-isothermal models additionally, the temperature T is part of the set of primary variable. Analogously to the pore-network model, a variable switch following [96] is applied in case one phase locally vanishes in the two-phase system. The secondary mesh, which describes the finite volumes is obtained by connecting the centers of each element with the associated edge midpoints. Thus, each finite volume is associated with a vertex, as schematically shown in box B_i in Figure 3.10. The finite-element mesh divides the boxes B_i into subcontrol volumes scv_i^k . A control volume is formed consisting of all subcontrol volumes attached to a vertex. A quadrilateral grid is considered, where all primary variables are approximated with piece-wise bilinear functions. For further details on the used Box discretization scheme, it is referred to [4].

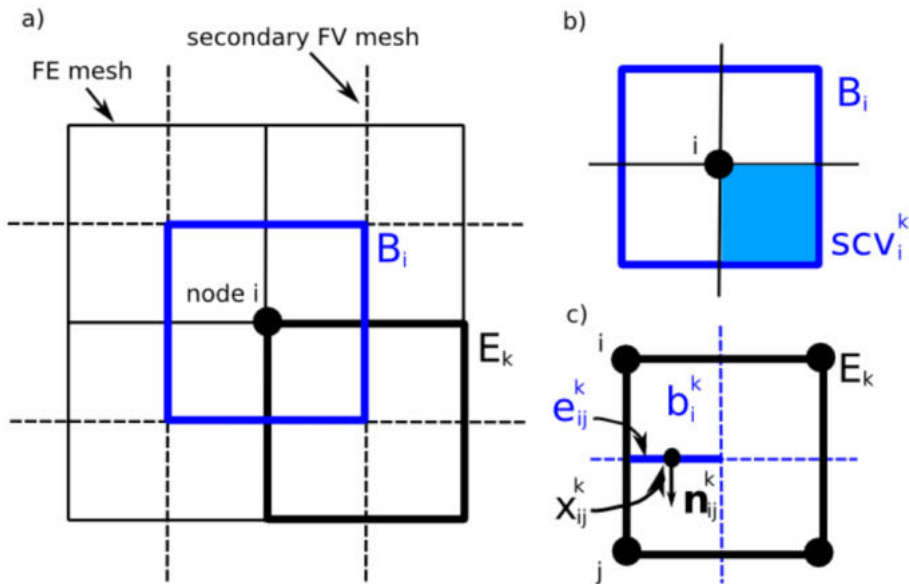


Figure 3.10: Discretization of the box method for the REV domain [4]

4 Boundary and interface configurations

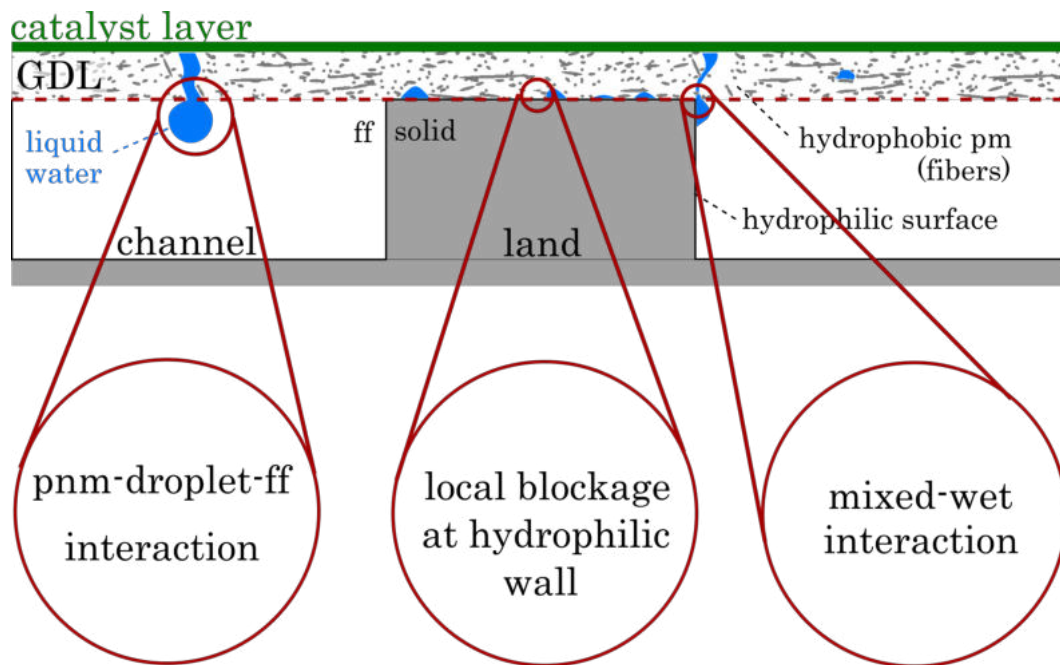


Figure 4.1: Section of the interface between the GDL and a channel-land structured gas distributor presenting the three different zones to distinguish in the interface model

In Figure 4.1, the different interaction regions at the interface between the GDL and the gas distributor are visualized for a classical channel-land structure. In the following sections, the modeling concepts for the three regions at the interface between GDL and gas distributor (red dashed line in Figure 4.1) as well as the interface between GDL and catalyst layer (green in Figure 4.1) are presented.

4.1 Representation of the catalyst layer and influence of the MPL

Based on the operating conditions, including stoichiometry and produced current, the reactions taking place in the cathode catalyst layer (CCL) can be included in the GDL model as a lumped boundary condition. With this condition, the ongoing reactions of protons and oxygen to water in the cathode catalyst layer and the transport through the MPL are implicitly included in the model without implementing all the physical details. Lu et al. [105] investigates the influence of the MPL on GDL flow for different GDL materials and finds that the capillary breakthrough pressure does not increase, as expected from the small pore sizes, but is approximately in the same range as for samples without MPL. The properties of the MPL (hydrophobic material with very small pores ($d_{\text{pore}} < 10\mu\text{m}$)) imply a liquid water flux only through larger cracks in the material. Otherwise, the necessary capillary pressure would need to exceed a physical range ($p_c^{\text{entry}} > 1e4\text{Pa}$). As shown in Figure 4.2, the output of the lumped boundary condition are a (molar) source flux of vapor and liquid water, a (molar) sink flux of oxygen, and an energy source term. These flux terms are calculated analytically in the lumped model.

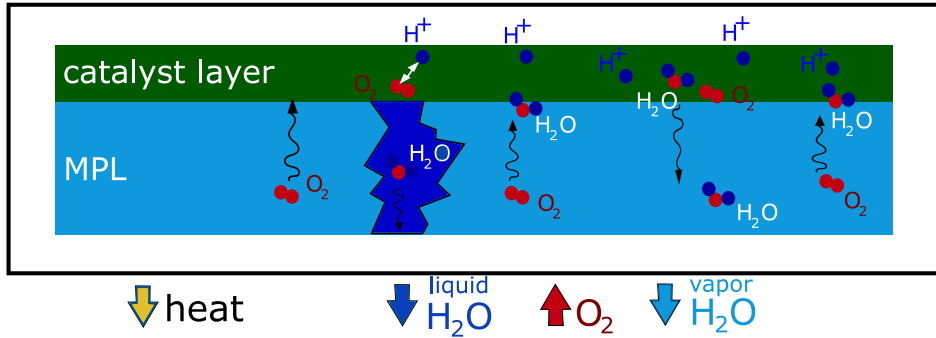


Figure 4.2: Visualization of the lumped boundary concept representing the cathode catalyst layer and the MPL

From the operating conditions, the cell potential can be determined by

$$U_{\text{cell}} = U_{\text{OCV}} - \eta_a - \eta_c - iR_{\text{spec}}, \quad (4.1)$$

where U_{OCV} is the open circuit voltage, η_a and η_c are the anodic and cathodic overpotentials, respectively, and i the cell current density. R_{spec} is the specific ohmic resistance

for the membrane, the electrodes and the contacts between the layers, which is usually determined experimentally by impedance spectroscopy [106]. The overpotentials of anode and cathode side are parameters of the reaction and stoichiometry, and can be determined experimentally using a known reference state of the cell operation [76]. As described in Section 2.9.2, the anodic overpotential can be neglected, due to its insignificant contribution.

With a known current density i , the products of the ongoing reactions can be quantified. The oxygen consumption rate (molar flux) \dot{N}_{O_2} and water production rate \dot{N}_{H_2O} during the electrochemical reactions, respectively, depend on the current density i and the Faraday constant F :

$$\dot{N}_{O_2} = -\frac{i}{4F}, \quad (4.2)$$

$$\dot{N}_{H_2O} = \frac{i}{2F}. \quad (4.3)$$

In the case of zero water flux through the membrane, each oxygen molecule in the cathode channel is replaced with two water molecules. However, depending on the humidity of the gas at the anode side, cross-over of water from the anode to the cathode side can bring additional water molecules to the cathode side [76]. The dynamic of water content is controlled by the electro-osmotic driving force due to the different electrochemical potentials at the anode and cathode, and the diffusion caused by the water concentration gradient at the two electrodes [107].

Therefore, an additional source term for the cross-over flux to the anode side due to osmotic drag is considered by

$$\dot{N}_{H_2O}^{anode} = t_{H_2O} \frac{i}{F}, \quad (4.4)$$

where t_{H_2O} is a transport coefficient, which depends on the conductivity of the membrane and the applied stoichiometry for the operating conditions. This value needs to be determined experimentally by estimation and iterative adaption to match a known experimental contribution.

Following Acosta et al. [76], the heat produced by the reaction, here considered as a

heat source, is calculated based on the cell potential U_{cell}

$$q^T = (U_{th} - U_{\text{cell}}) i, \quad (4.5)$$

with the thermo-neutral voltage U_{th} , which represents the voltage at which the reaction takes place with 100% thermal efficiency (i.e. no waste heat is produced from the reaction). For the considered reaction of hydrogen and oxygen, this is $U_{th} \approx 1.48V$ [76]. It is assumed that a part of the heat generated in the cathode reaction layer flows through the membrane to the anode side, depending on the thermal conductivity of the membrane [76].

Another complex problem, which is not well understood, is the phase state of water at the interface between MPL and gas diffusion backend (GDB). Experimental observations show the occurrence of liquid water results not only from condensation [21]. From the hydrophobicity and the small pore size of the MPL material, it is assumed, that liquid water can only pass through preferential paths, where there are cracks or holes in the material. This results in a number of injection points for the liquid water interacting with the GDL material. It can be surmised that the number of injection points varies depending on the thickness and material properties of the MPL. Carrere et al. [21] induce a parameter for the fraction of injection points of liquid water. However, direct estimates for this parameter are not available in the literature such that this value is used essentially as an calibration and fitting parameter in his work.

Here, this principle is adapted to the lumped boundary concept. A specific probability for the occurrence of liquid water is assumed to capture this effect. In every boundary element that contains liquid water the local relative humidity is set to $rh = 100\%$, meaning that the liquid-vapor equilibrium is reached. Therefore, the molar fraction of water vapor in such an element is $x_v = p_{vs}(T)/p_{\text{ref}}$. Nevertheless, additional investigations are necessary to determine this water-vapor fraction in a more sophisticated way. This procedure, where the reaction and transport in the catalyst layer and the MPL are included using a boundary condition is a simplification since the local concentrations of the components are not included in the reaction rate. This assumption is valid, due to the small computation domain represented by the pore-network of the GDL ($< 10\text{mm}^2$). Here, it can be assumed, that the mixing of the components occurs fast enough to ensure a homogeneous distribution over the complete boundary area.

4.2 Droplets forming in channels of the gas distributor¹

At the interface between GDL and gas distributor different configurations can occur. If the water leaves the GDL at a pore with a large distance to the hydrophilic wall of the gas distributor, a droplet is forming on the hydrophobic surface of the GDL. The influence of the droplet formation, growth and detachment on the flow in the pore-network model representing the flow through the GDL structure is implemented in a boundary formulation for the pore-network model. Investigations on transparent

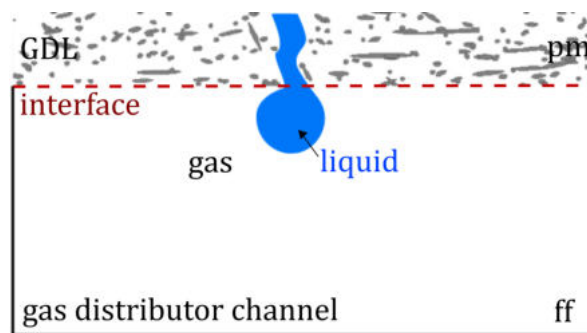


Figure 4.3: Droplet formation on the hydrophobic surface of the GDL structure

testing PEM fuel cells have confirmed that single-droplet formation and detachment from the porous material surface of the GDL is the main water flow mechanism taking place in the cathode channel [108]. Several operation conditions have been recorded by the authors. They concluded that the formation of individual droplets of the surface of the GDL is the dominant mechanism for the water removal from the GDL structure and the water flow within the gas distributor. However, for the considered test fuel cell, a plexiglass has been used as the material of the channel-land structure of the gas distributor and a channel width and depth of $1.46\text{mm} \times 0.28\text{mm}$, respectively. The liquid water might behave differently once in contact with a more hydrophilic wall material and might form film flow. Nevertheless, for the formation and detachment of the droplets, the assumption of single droplet formation is still valid.

In the following, we consider a simplified, well-defined setup as presented in Figure 4.4.

A droplet is forming on a hydrophobic surface in a gas flow channel. The liquid water

¹Portions of this section are part of the publication *Two-phase flow dynamics at the interface between GDL and gas distributor channel using a pore-network model* by Michalkowski et al. that has been submitted to *Transport in Porous Media* by Springer in 2022.

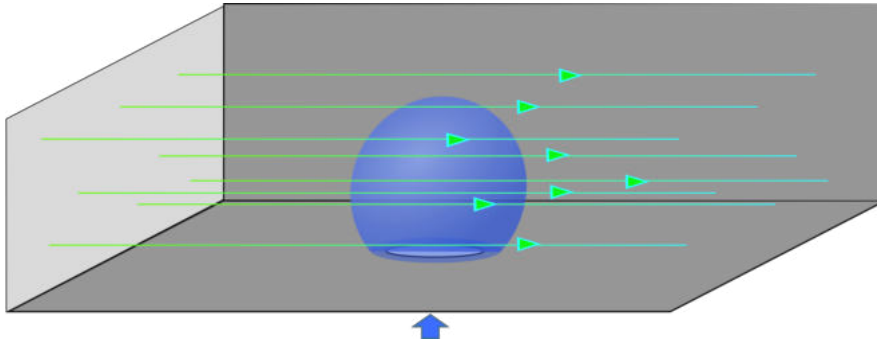


Figure 4.4: Droplet forming on a hydrophobic surface in a gas flow channel

enters the channel domain through a cylindrical pore throat at the bottom of the channel. The throat represents the interface to the porous domain of the GDL, which will be modeled using a pore-network.

For the velocity profile at the channel inlet boundary, a uniform velocity or a parabolic velocity profile can be assumed. A uniform velocity would result from the disturbances due to droplets emerging at different locations in the channel forming obstacles to the flow. Theodorakakos et al. [108] corroborate this assumption by investigations of the influence of the location of the droplet in the channel. It has been found that there is no significant difference in the behavior of a droplet located in the centerline compared to one located closer to a side wall. However, they notice the importance of the flow dynamics rather than the static conditions in the channel to be important for the detachment of droplets [108].

The influence of the droplet growth and detachment on the air flow in the gas distributor needs to be considered separately using a direct numerical simulation of the gas flow. As a simplification, the influence of droplets can be considered with respect to the reduction of the available cross-sectional area for the gas flow. However, in this section, we focus on the description of droplet formation, growth and detachment at the surface of a porous GDL.

4.2.1 Droplet on a porous surface

A droplet forming at the interface between GDL and gas distributor experiences the influence of shear flow, i.e. the gas flow through the gas distributor. The droplet is attached to the surface of the GDL due to adhesion forces between the liquid droplet and the solid surface. The adhesion force depends on the properties of the liquid as well

as the solid, like contact angle, surface tension, and surface roughness of the solid. The shear flow applies a drag force to the droplet dependent on the flow velocity and the viscosity of the gas flow. Additionally, a gravitational force dependent on the orientation of the fuel cell and the size and density of the droplet can be considered. However, for small droplets this is negligible [108], which will be discussed in the following. If the forces acting on the droplet exceed the adhesion force, the droplet is detached from the surface. Once in movement, the droplet can have sliding, rolling, and lifting motion in the presence of a simple shear flow [109].

A droplet forming on the GDL surface is visualized in Figure 4.5. Here, no gas flow is considered at the surface of the GDL.

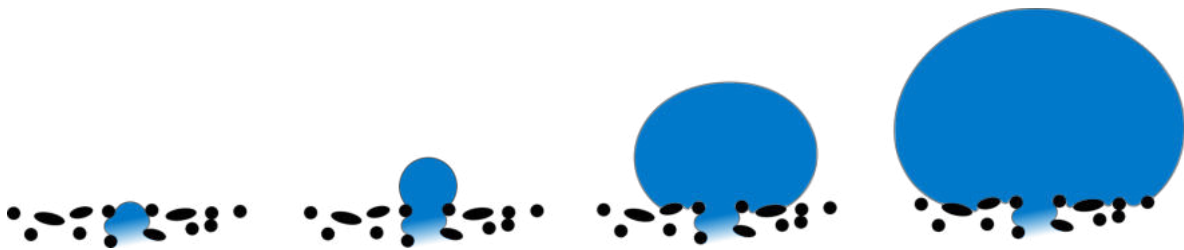


Figure 4.5: A droplet forming and growing on the GDL surface with no surrounding gas flow.

From the preferential flow path of the liquid through the porous GDL, a droplet is forming at the breakthrough location. The droplet is growing based on the liquid flux. Since no gas flow causes a drag force on the droplet, it won't be detached. At a certain size, gravity might cause a deformation otherwise the droplet shape is determined by the surface tension and resulting contact angle. We always assume that the liquid flux is small enough to neglect any deformation due to inertial effects from the liquid flux. In Figure 4.6, the droplet formation on the GDL surface is shown for the case of a drag force acting on the droplet due to a gas flow velocity. Similar to the equilibrium case, a drop is forming and growing based on the flow path through the porous GDL. However, this time, a deformation of the droplet due to the surrounding gas flow is observable. In the last stage, the droplet is detached from the surface. Liquid water is removed from the porous domain. We do not consider the details of liquid water uptake in the free flow domain (light blue sphere with dashed lines). Since the configurations in Figures 4.5 and 4.6 are rather complex and the conditions are not well defined, a simplified configuration is considered to describe and develop the model. The simplified model should include all the relevant effects and phenomena occurring in the complex system at the interface between GDL and gas distributor but is more clear and easier

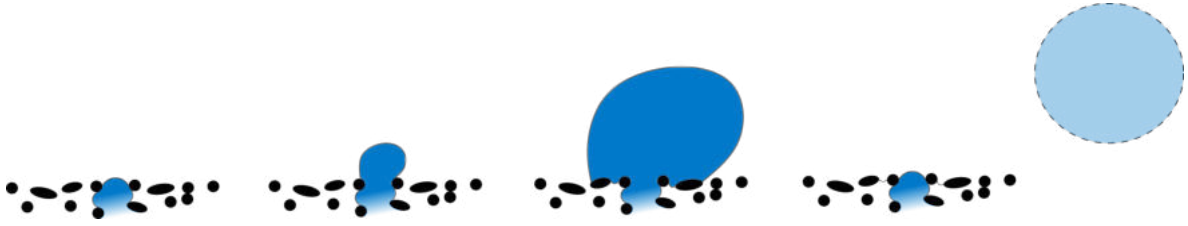


Figure 4.6: A droplet forming and growing on the GDL surface in a gas flow channel.

to understand. First, some assumptions need to be justified.

Including the influence of surface roughness There are two states to classify droplet interaction with a rough surface. The interaction can either be in a Wenzel [110] or Cassie-Baxter state [111]. The Wenzel state describes homogeneous wetting on the surface features. In this case, full water droplet immersion into the surface roughness features is observed, resulting in complete interfacial contact as presented in Figure 4.7b. In the Cassie-Baxter state, the water droplet is resting on gas between the liquid water and the rough surface. This case is shown in Figure 4.7a. For both models, roughness correction factors, based on the material topography, are employed to relate the apparent contact angle to the contact angle on a smooth surface. The corrected contact angles can then be utilized in surface energy balance calculations. Fishman et al. [112], Gostick et al. [113] and Theodorakakos et al. [108] attribute droplet pinning on the GDL to the extent of wetting in the Cassie-Baxter state which is also applied in this work.

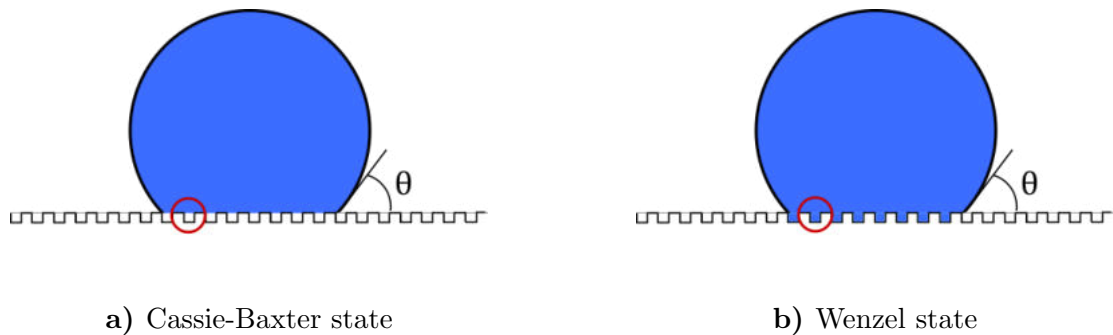


Figure 4.7: Droplet on a rough surface in different states dependent of the wetting properties of liquid and solid

The correction term for the contact angle derived by Cassie and Baxter [111] is based

on the surface roughness to model contact angle on heterogeneous surfaces. For the considered case, where a mixture of water vapor and air is trapped between the solid and the liquid, it holds

$$\cos \theta = f_1 \cos \theta_{\text{smooth}} - f_2. \quad (4.6)$$

Where f_1 is the fractional area for the solid-liquid interface, f_2 is the fractional area for the pores and θ_{smooth} is the contact angle between the liquid and the solid on a smooth surface.

Assuming a nearly homogeneous contact angle distribution on the GDL surface, this correction term includes the surface roughness in the wetting properties and such in the calculation of the adhesion force. Therefore, in the following the corrected contact angle is used as for smooth surfaces.

Neglecting the influence of the pore throat feeding the droplet Theodorakakos et al. [108] state that the influence of the filling tube or pore throat connected to the droplet has only a minor influence on the droplet detachment. They considered different cylindrical pipes with diameters up to 15% of the droplet detachment diameter and various flow velocities through the throat. They concluded that the droplet-filling flow through the pore throat is not strong enough to cause any effects on the detachment behavior and the only influence results from the smaller friction area between the liquid droplet and the wall surface [108]. In our case, no sliding movement of the droplet on the porous surface is considered. Therefore, the reduced friction has no influence, here. The droplet is forming at the end of the pore throat. It grows to a certain size and is detached from the throat and the surface of the porous GDL once the drag force resulting from the surrounding gas flow exceeds the resisting forces. For the detachment, the force balance parallel to the flow direction is considered. Details on the droplet detachment are described in Section 4.2.2. For a throat perpendicular to the surface, the effective adhesion and cohesion forces between the droplet and the fluid in the throat and the solid surface, respectively, do not have an in-flow-direction component and are not considered in the detachment force balance (see Figure 4.13). The influence of a tilted interface throat is neglected, here. Therefore, for the calculations of the force balance and detachment criterion, the influ-

ence of the filling throat is not considered.

Neglecting the influence of gravitational effects The gravitational force acting on the droplet results in a deformation of the droplet (visualized in Figure 4.8).

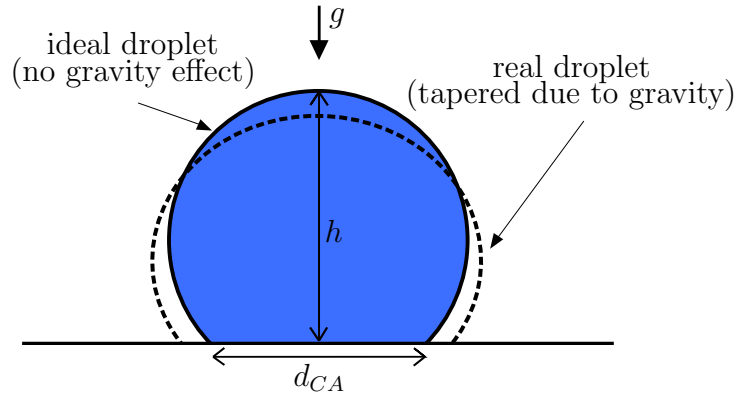


Figure 4.8: Deformation of the droplet due to gravitational force cf. [5]

Due to the gravity g acting perpendicular to the surface, the droplet is tapered. The height h is decreased while the diameter of the contact area d_{CA} is increased.

To express the influence of gravity on the static droplet shape, the dimensionless Bond number Bo can be used

$$Bo = \frac{\rho_{\text{liq}} \cdot g \cdot r_{\text{drop}}^2}{\sigma} \quad (4.7)$$

with the density of the liquid (droplet) ρ_{liq} , the gravitational acceleration g , the droplet radius r_{drop} and the surface tension σ .

The Bond number describes the relation between the gravitational force and the surface tension and is therefore an indicator for the deformation of the droplet due to gravity, meaning its difference from a spherical shape.

For different drop sizes and surface tensions, the Bond number can be calculated. In order to consider any significant effect of gravity, the Bond number should be above 2.5 [108, 114]. In Figure 4.9, the dependence of the Bond number of the droplet radius for water droplets in air is visualized.

Even for droplets with a radius larger than 1mm which is the upper end of typical channel height of gas distributors in PEM fuel cell applications, the Bond number is

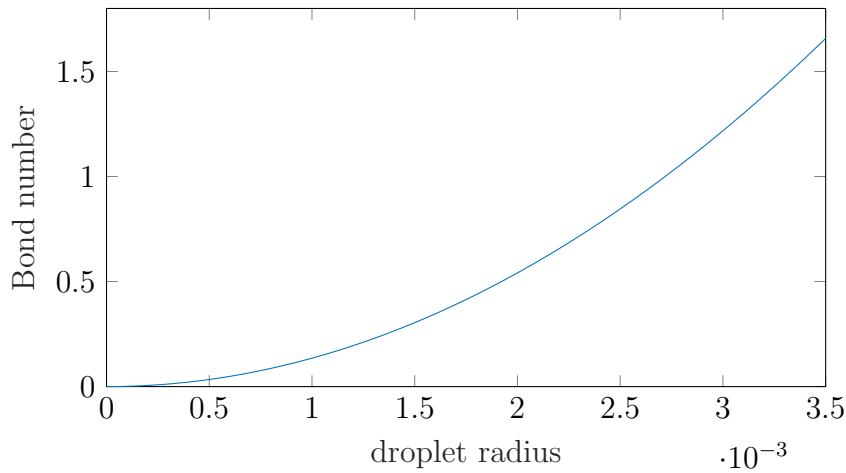


Figure 4.9: Bond number of a water droplet in air environment dependent on the droplet size

far below 2.5, such that the influence of gravity on the droplet deformation is neglected in the following.

Uniform surface curvature of single droplets In Figure 4.10 (left), a droplet deformed due to gas flow is visualized. The deformation results in the formation of an advancing and receding contact angle down- and upstream to the droplet, respectively. However, the influence on the average curvature is small and is negligible for the small droplets occurring at the interface between GDL and gas distributor. We assume, the deformation of the droplet due to external forces from the gas flow is small enough such that the curvature is uniform on the droplet surface. This results in a constant phase pressure difference between the gas and the liquid phase, and therefore, a constant pressure inside the droplet.

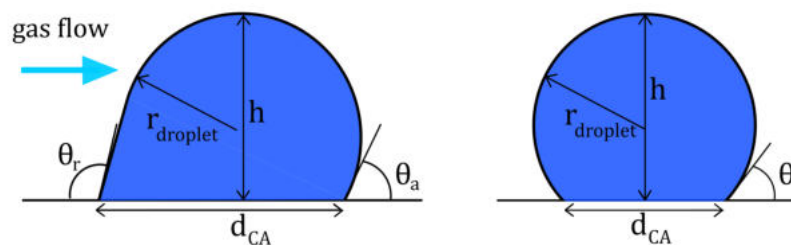


Figure 4.10: Deformed (left) and undeformed (right) droplet on a surface.

Considering surface effects, such as evaporation, or to determine the area perpendicular

to the flow direction that reduces the cross-sectional area of the channel, the simplification on the right side in Figure 4.10 of an undeformed droplet is used. The droplets are assumed to have the shape of a sphere cap. Nevertheless, contact-angle hysteresis is considered in the force balance as described in Section 4.2.2.

4.2.2 Simplified model

With these simplifications and restrictions, the droplet behavior on the GDL surface can be described by the following model (Figure 4.11).

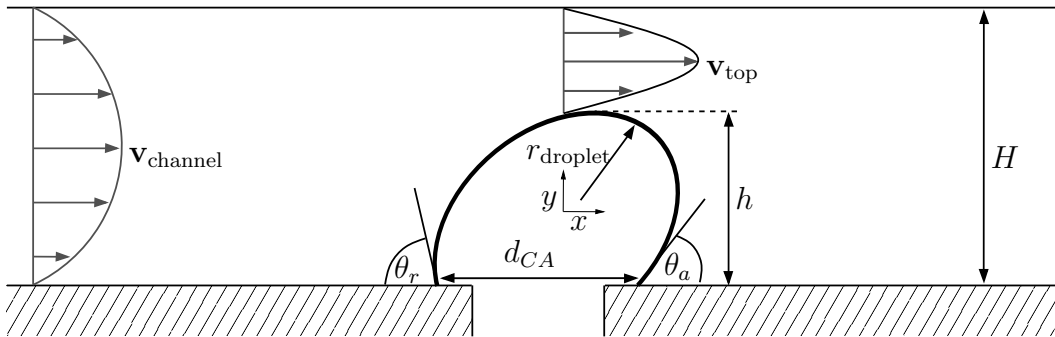


Figure 4.11: Simplified representation of a droplet on the GDL surface.

In Figure 4.11, the median plane through a droplet in a gas flow channel is shown. The droplet deforms due to the drag and pressure force and surface tension acting on the droplet. For the flow in the channel, a fully developed laminar flow profile of a Newtonian fluid is assumed. In the channel, around the droplet, only parallel flow is considered. The velocity profile around the droplet is visualized in Figure 4.12. Since the droplet blocks a part of the channel, the average velocity of the flow at the position of the droplet is increased to fulfill the mass balance and a no-slip condition is applied to the drop surface.

Forces acting on the droplet In Figure 4.13, the different forces acting in and around the droplet are shown. There is a shear force F_{shear} and an inertial force $F_{\rho v^2}$ acting on the droplet surface. However, the inertial force at the surface due to a no-slip condition between the liquid drop and the gas flow is very small compared to the shear force and

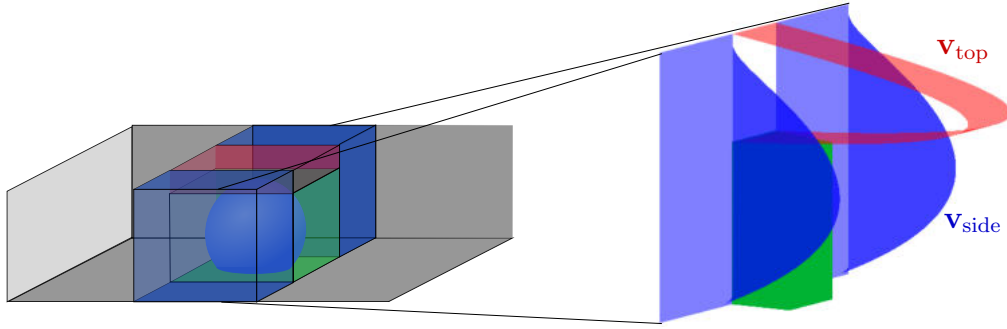


Figure 4.12: Visualization of the parallel flow profile around the droplet. The velocity is increased in the narrowing on top of the droplet (red) and a no-slip condition is applied to the drop surface. The droplet is simplified by a cube. The flow velocity passing by the drop on its sides is colored in blue.

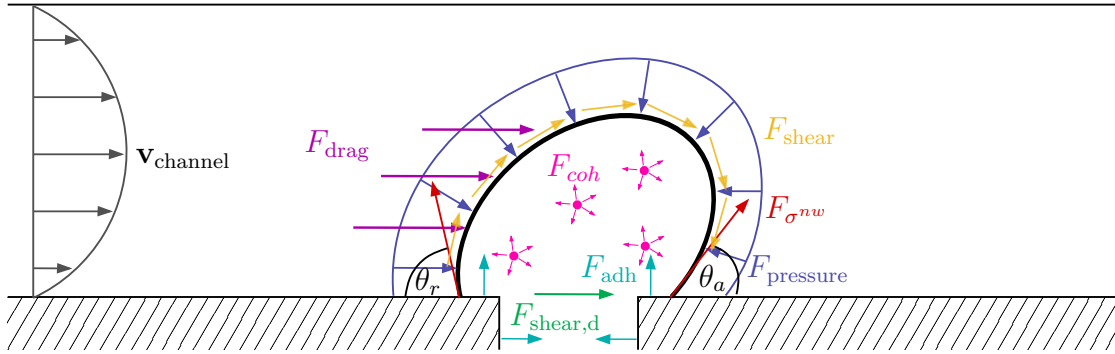


Figure 4.13: Forces acting in and around the deformed droplet

is therefore neglected here. The internal shear force $F_{\text{shear},d}$ in the liquid is given by

$$F_{\text{shear},d} = \tau A_{\text{throat}} = \mu_{\text{liq}} \frac{\partial u}{\partial y} A_{\text{throat}}, \quad (4.8)$$

with the area of the throat, where the drop is formed, A_{throat} , the viscosity of the drop fluid μ_{liq} and the gradient of fluid velocity at the throat $\frac{\partial u}{\partial y}$. Since we assume only small droplet deformations, the velocity gradient is small such that we neglect the internal shear force at the pore throat.

To further simplify the setup, no flow disturbances are considered around the droplet. The pressure force F_{pressure} around the droplet varies along the surface in stream direction due to the gas flow. The surface tension force $F_{\sigma^{nw}}$ acts at the contact line between the liquid droplet and the solid surface. Due to the deformation and the contact-angle hysteresis an effective force results against the gas flow direction. A drag force F_{drag} results from the gas flow acting on the projected area perpendicular to the stream and

represents the overall resistance of the droplet to the flow. In the drag force, all resisting forces of the droplet in the stream are combined (pressure force, shear forces). Internally, cohesion forces F_{coh} between the fluid particles and adhesion forces F_{adh} between the fluid and the solid can be measured. On the whole droplet, a gravitational force is acting dependent on the size of the droplet.

Force balance in tangential direction Some of the forces described above have an effective component in tangential direction. In Figure 4.14, these components are shown in a simplified box around the droplet. The adhesion and cohesion forces are not in-

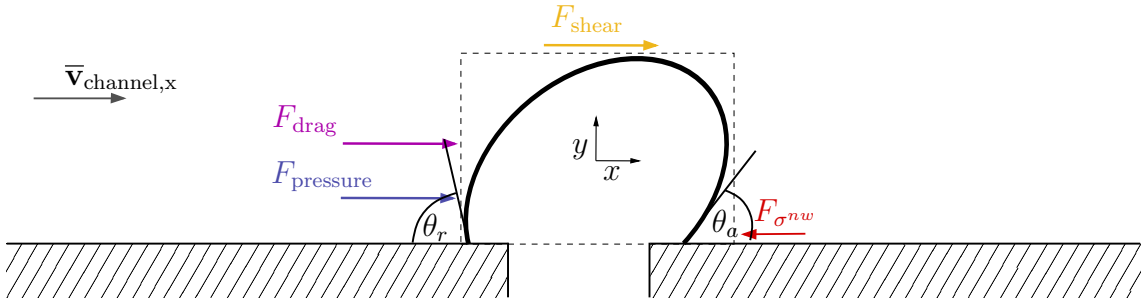


Figure 4.14: Tangential components of the forces acting on the droplet

cluded in this balance, since the effective component in tangential direction is zero. For the pressure force approximation, the pressure loss through the narrowing above the droplet is approximated by the resistance of a rectangular duct. A laminar, fully developed flow profile is applied and no flow disturbances around the droplet are considered. For this case, the pressure force is given following [115]

$$F_{\text{pressure}} = (p_{\text{front}} - p_{\text{back}}) \times A_{\text{channel}} = \frac{24\mu_{\text{gas}}(H/2)^2 v_{\text{channel}}^{\text{mean}} h_{\text{drop}}^2}{(H/2 - h_{\text{drop}}/2)^3 (1 - \cos \theta_a)^2}, \quad (4.9)$$

with the cross-sectional area of the channel A_{channel} , the viscosity of the gas μ_{gas} , the height of the channel H , the height of the droplet h_{drop} , the average gas stream velocity $v_{\text{channel}}^{\text{mean}} = |\bar{v}_{\text{channel},x}|$, and the advancing contact angle θ_a (see Figure 4.11 and Figure 4.14).

The shear force acting around the droplet is divided in the parts above the droplet and on the two sides parallel to the flow. For the top part, a formulation described by

Kumbur et al. [115] can be used and for the sides an integral approach is applied

$$F_{\text{shear}}^{\text{top}} = \tau|_{y'=b/2} A_{\text{top}} = \frac{3\mu_{\text{gas}}H/2v_{\text{channel}}^{\text{mean}}}{(H/2 - h_{\text{drop}}/2)^2} (2r_{\text{drop}})^2, \quad (4.10)$$

$$\begin{aligned} F_{\text{shear}}^{\text{side}} &= \tau_{yz}|_{z=r} A_{\text{side}} = -\mu_{\text{gas}} \int_{y=-H/2}^{y=-H/2+h_{\text{drop}}} \frac{\partial |\mathbf{v}|}{\partial z}(y) dy \cdot 2r_{\text{drop}} \\ &= \frac{12\mu_{\text{gas}}r_{\text{drop}}h_{\text{drop}}v_{\text{side}}^{\text{mean}}}{H} \left(2 - \frac{h_{\text{drop}}}{H}\right), \end{aligned} \quad (4.11)$$

$$F_{\text{shear}} = F_{\text{shear}}^{\text{top}} + 2F_{\text{shear}}^{\text{side}}. \quad (4.12)$$

with the projected areas of the droplet A_{top} and A_{side} , respectively, and the average velocity in the channel and next to the droplet $v_{\text{channel}}^{\text{mean}}$ and $v_{\text{side}}^{\text{mean}}$, respectively.

The effective surface tension force in tangential direction depends on the deformation of the droplet and the resulting contact angles in the front and behind the droplet. As an approximation, a linear relation between the contact angle and the droplet radius is assumed.

$$\theta_a(r_{\text{drop}}) = \theta_0 + \frac{r_{\text{drop}}}{r_{\text{max}}} (\theta_a - \theta_0), \quad (4.13)$$

$$\theta_r(r_{\text{drop}}) = \theta_0 + \frac{r_{\text{drop}}}{r_{\text{max}}} (\theta_r - \theta_0), \quad (4.14)$$

$$\Delta\theta(r_{\text{drop}}) = \theta_a(r_{\text{drop}}) - \theta_r(r_{\text{drop}}) = \frac{r_{\text{drop}}}{r_{\text{max}}} (\theta_a(r_{\text{max}}) - \theta_r(r_{\text{max}})), \quad (4.15)$$

Where the maximum droplet radius before the detachment is denoted by r_{max} . The surface tension force is then given by

$$\begin{aligned} F_{\sigma} &= \sigma \frac{d_{CA}}{2} \pi \left[\frac{\sin\left(\frac{r_{\text{drop}}}{r_{\text{max}}(v)}(\Delta\theta - \theta_a)\right) - \sin\left(\frac{r_{\text{drop}}}{r_{\text{max}}(v)}\theta_a\right)}{\frac{r_{\text{drop}}}{r_{\text{max}}(v)}\Delta\theta - \pi} \right. \\ &\quad \left. + \frac{\sin\left(\frac{r_{\text{drop}}}{r_{\text{max}}(v)}(\Delta\theta - \theta_a)\right) - \sin\left(\frac{r_{\text{drop}}}{r_{\text{max}}(v)}\theta_a\right)}{\frac{r_{\text{drop}}}{r_{\text{max}}(v)}\Delta\theta + \pi} \right], \end{aligned} \quad (4.16)$$

with the maximum droplet radius $r_{\text{max}}(v)$ which denotes the radius of a detaching drop in a channel with a gas stream of average velocity $v = |\bar{\mathbf{v}}_{\text{channel},x}|$.

The maximum surface tension, pinning the droplet to the porous medium, results from the maximum deformation with the advancing and receding contact angle θ_a and θ_r ,

respectively,

$$F_{\sigma^{nw},\max} = \sigma^{nw} \frac{d_{CA}}{2} \pi \left[\frac{\sin(\Delta\theta - \theta_a) - \sin\theta_a}{\Delta\theta - \pi} + \frac{\sin(\Delta\theta - \theta_a) - \sin\theta_a}{\Delta\theta + \pi} \right], \quad (4.17)$$

with the surface tension between liquid water and gaseous air σ and the diameter of the contact area d_{CA} .

The drag force represents the overall resistance of the droplet to the gas stream. It can either be determined using a drag coefficient c_d or by summing up the forces acting on the control volume from the stream

$$F_{\text{drag}} = \frac{1}{2} c_d \rho_{\text{liq}} (v_{\text{channel}}^{\text{mean}})^2 A_{\text{stream}} \quad \text{or} \quad F_{\text{drag}} = F_{\text{pressure}} + F_{\text{shear}}, \quad (4.18)$$

where A_{stream} is the projected area perpendicular to the stream and ρ_{liq} is the density of the droplet fluid. Since the determination of the drag coefficient is difficult and large variations can be found in the literature [77, 116, 117], we use the simplified but analytical formulation in this work. The drag force acting on the droplet calculated from the force balance in tangential direction results in the following formulation:

$$\begin{aligned} F_{\text{drag}} &= F_{\text{pressure}} + F_{\text{shear}} \\ &= F_{\text{pressure}} + F_{\text{shear}}^{\text{top}} + 2f_{\text{channel}} F_{\text{shear}}^{\text{side}} \\ &= \frac{24\mu_{\text{gas}} (H/2)^2 v_{\text{channel}}^{\text{mean}} h_{\text{drop}}^2}{(H/2 - h_{\text{drop}}/2)^3 (1 - \cos\theta_a)^2} + \frac{3\mu_{\text{gas}} H/2 v_{\text{channel}}^{\text{mean}}}{(H/2 - h_{\text{drop}}/2)^2} (2r_{\text{drop}})^2 \\ &\quad + 2f_{\text{channel}} \frac{12\mu_{\text{gas}} r_{\text{drop}} h_{\text{drop}} v_{\text{side}}^{\text{mean}}}{H} \left(2 - \frac{h_{\text{drop}}}{H} \right), \end{aligned} \quad (4.19)$$

with the channel height H and the height of the droplet h_{drop} , the fluid viscosity of the gas phase μ_{gas} , the average gas flow velocity in the whole channel, $v_{\text{channel}}^{\text{mean}}$, and next to the drop, $v_{\text{side}}^{\text{mean}}$, and the advancing contact angle between the liquid and the solid phase, θ_a . This gives a linear relation for the drag force on the average velocity in the channel $v_{\text{channel}}^{\text{mean}}$. For the side shear force, a correction factor f_{channel} is applied to account for the reduction of the cross-sectional area of the channel due to the droplet:

$$f_{\text{channel}} = \left(3/2 \frac{A_{\text{channel}}}{A_{\text{channel sides}}} \right)^2 = \left(3/2 \frac{A_{\text{channel}}}{A_{\text{channel}} - 2r_{\text{drop}}H} \right)^2, \quad (4.20)$$

dependent on the cross-sectional area of the whole channel A_{channel} and the part of the cross-section which is not blocked by the droplet $A_{\text{channel sides}}$.

The multiplier $3/2$ results from the parabolic flow profile. The exponent 2 is used since the channel is limited in height and width. This factor is applied to the shear force on both sides of the droplet.

A comparison of the effect of different detachment criteria is presented in Chapter 8.

4.2.3 Application to the pore-network approach

The drop concept is integrated in the pore-network model defining ghost pores located at the boundary of the porous domain, where the drop can form and grow. The drop formation, growth and detachment are defined by the ghost pore properties as described in the following. The different states during these drop-formation processes in the pore-network are visualized in Figure 4.15.

Let's consider a droplet on a surface in equilibrium, without any external forces, filled by a circular throat placed in a ghost pore (see Figure 4.16).

We start with the drop formation: A drop is formed on the porous surface once it breaks through an open surface pore space of the porous material. Since the liquid water is the non-wetting phase in the GDL, a certain capillary pressure has to be overcome to pass through the surface pore space. In the pore-network model, this pressure is the capillary entry pressure (see Eq. (3.21)). In Figure 4.15b, the drop formation in the pore-network context is shown. The throat connected to the ghost node is invaded, which indicates that the capillary pressure in the pore body exceeds the capillary entry pressure. The capillary entry pressure depends on shape and cross-sectional area of the throat. As described earlier in this section, we assume a circular cross-section. The size of the throat depends on the geometric properties resulting from the network extraction (see Section 3.1.4). This gives us the criterion for the drop formation. A drop is formed once the capillary pressure in the connected pore body exceeds the capillary entry pressure of the connecting throat

$$p_c^{\text{drop form}} = p_c^{\text{entry}} = \frac{\sigma \cos \theta (1 + 2\sqrt{\pi G})}{r_{ij}} F_d(\theta, G), \quad (4.21)$$

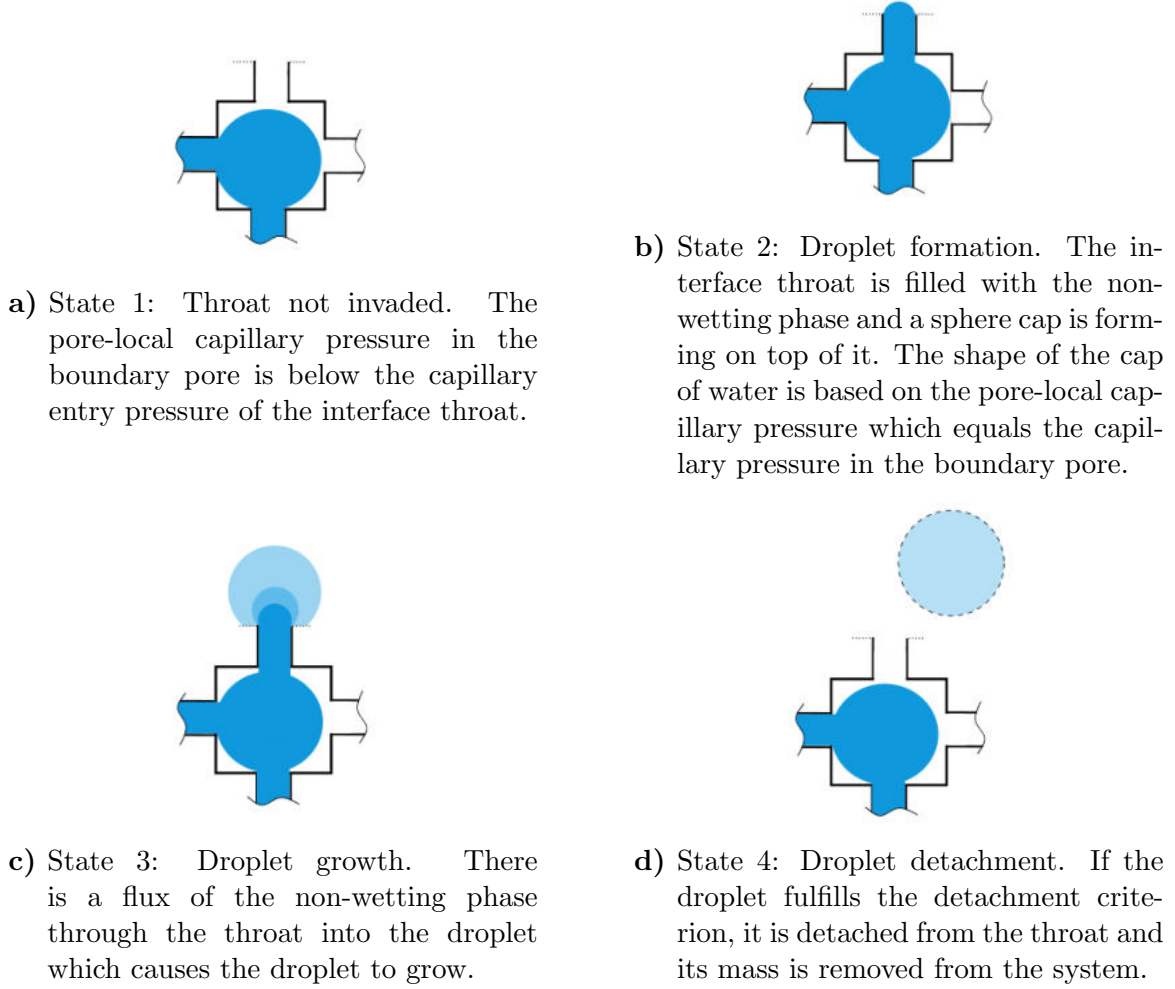


Figure 4.15: Different states of drop formation, growth and detachment in a pore-network model.

with

$$F_d(\theta, G) = \frac{1 + \sqrt{1 + 4GD/\cos^2 \theta}}{1 + 2\sqrt{\pi G}},$$

$$G = \frac{A_{ij}}{P_{ij}^2} = \frac{1}{4\pi},$$

$$D = \pi - 3\theta + 3 \sin \theta \cos \theta - \frac{\cos^2 \theta}{4G}.$$

The drop growth is described using the relation between drop surface curvature and drop radius. Using the fact that the curvature of the interface is inversely proportional

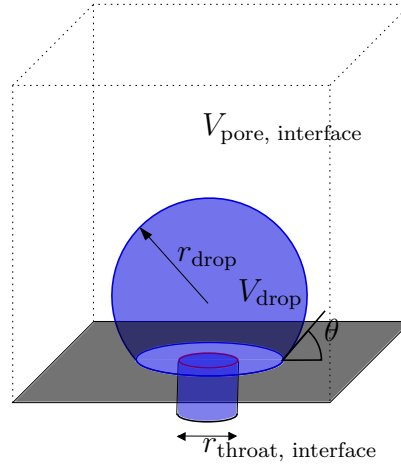


Figure 4.16: Droplet on a surface in equilibrium without any external forces filled by a circular throat. The droplet forms inside an interface pore.

to the pore-local capillary pressure and assuming a spherical cap shape for the droplet, this relation can be expressed as a pore-local capillary pressure-saturation relation. We assume a uniform curvature of the drop surface and therefore a uniform pressure inside the drop. It is assumed that the drop emerges from a throat. Before a droplet with the according contact angle is formed on the hydrophobic surface, a sphere cap is developed with increasing contact angle until the static contact angle of the material is reached. During this state, the contact area of the drop is constant and equals the cross-sectional area of the throat. This first section is visualized in Figure 4.17 (left). Once the final contact angle between drop and surface is reached, it stays constant during the further growing. Instead, the droplet growth causes a change in the contact area of the droplet with the hydrophobic surface. The second stage of droplet growth is visualized in Figure 4.17 (right).

The capillary pressure-saturation formulation for Stage 1 is derived from the volume of a sphere cap and its corresponding radius/curvature

$$V_{drop,1} = \frac{\pi}{3} r_{drop,i}^3 (2 + \cos(\pi/2 - \theta_i)) (1 - \cos(\pi/2 - \theta_i))^2, \quad (4.22)$$

with the curvature radius r_{drop} , and the changing contact angle $\theta_i \in [\pi/2, \pi/2 - \theta_{lim}]$ with $\theta_{lim} = \pi - \theta_a$. The curvature radius is calculated based on the constant contact

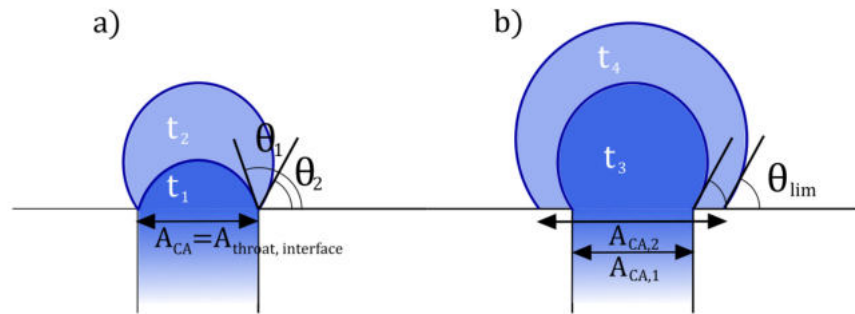


Figure 4.17: Left: First stage of the droplet growth on a pore throat. The contact area of the droplet is constant and equals the throat cross-sectional area, while the contact angle is changing until it reaches the advancing contact angle of the hydrophobic surface. Right: Second stage of droplet growth. The final contact angle between drop and surface is reached and stays constant from now on. The droplet growth causes a change in the contact area of the droplet with the hydrophobic surface.

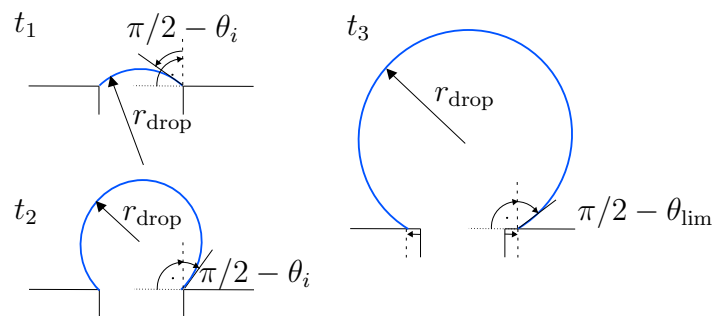


Figure 4.18: Different stages of a growing droplet ($t_1 < t_2 < t_3$).

area $A_{CA} = A_{\text{throat}}$,

$$r_{\text{drop},i} = \frac{r_{\text{throat}}}{\cos(\theta_i)}. \quad (4.23)$$

The resulting capillary pressure formulation for Stage 1 is

$$p_{c,1} = \frac{2\sigma \cos(\theta_i)}{r_{\text{throat}}}. \quad (4.24)$$

If the drop pore is not invaded yet, the capillary pressure is zero.

The saturation in the drop pore is given by the drop volume divided by the pore volume

$$s_{w,1} = 1 - s_n = 1 - \frac{V_{\text{drop},1}}{V_{\text{pore}}}. \quad (4.25)$$

In Stage 2, the contact angle is constant and equals the advancing contact angle of the fluid on the hydrophobic surface ($\theta_i \equiv \theta_{\text{lim}}$). Now, the contact area is changing.

$$V_{\text{drop},2} = \frac{\pi}{3} r_{\text{drop},i}^3 (2 + \cos(\pi/2 - \theta_{\text{lim}})) (1 - \cos(\pi/2 - \theta_{\text{lim}}))^2, \quad (4.26)$$

with the drop radius $r_{\text{drop},i}$. The resulting capillary pressure formulation for Stage 2 is

$$p_{c,2} = \frac{2\sigma \cos(\theta_i)}{r_{\text{drop}}}. \quad (4.27)$$

Again, the saturation in the drop pore is given by the drop volume divided by the pore volume

$$s_{w,2} = 1 - s_n = 1 - \frac{V_{\text{drop},2}}{V_{\text{pore}}}. \quad (4.28)$$

The complete, pore-local capillary pressure-saturation relation for drop pores is visualized in Figure 4.19. The blue part representing Stage a) and the green part representing Stage b). The relation is dependent on the radius of the feeding interface throat $r_{\text{throat, interface}}$. The maximum capillary pressure increases for smaller feeding throats. This results from the smaller sphere cap with a large curvature during the growth in first stage. With larger feeding throats, this peak decreases. The behavior in second stage (Stage b)) is rarely influenced by the throat radius. Only the drop volume at which the critical contact angle θ_{lim} is reached shrinks with shrinking throat radius.

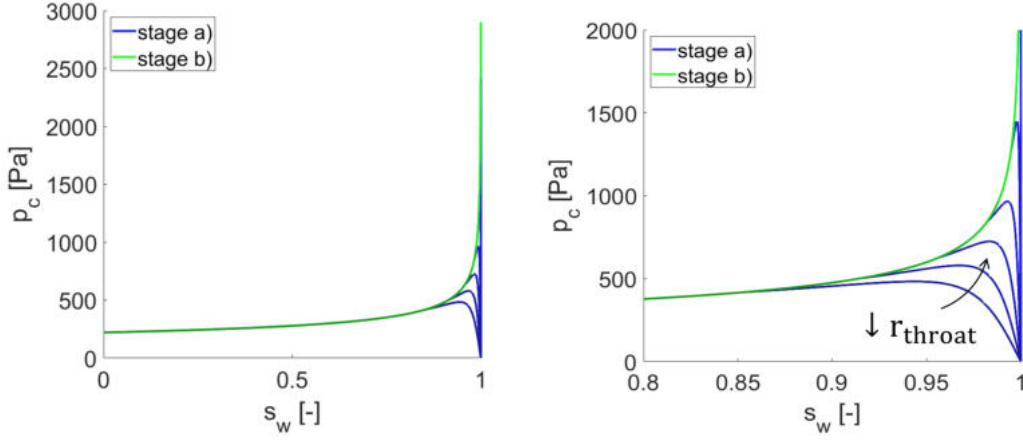


Figure 4.19: Composed local capillary pressure-saturation relation for droplet pores. The $p_c - s_w$ relation is based on geometric analysis describing the drop behavior in interface pores. Left: full wetting phase saturation range, right: zoom in to show the behavior at higher wetting phase saturations (small droplet sizes).

This extends the curve to higher wetting phase saturation. For low wetting phase saturation ($s_w < 0.5$), all curves lie on top of each other. This means, at a certain drop size, the influence of the feeding throat can be neglected.

From the pore-local capillary pressure in the ghost pore, we get the liquid phase pressure in the droplet. With the known capillary pressure in the connected pore, this gives the pressure difference in the liquid phase, which defines the volume flux between the ghost pore (drop) and the connected pore

$$Q_{ij}^{\text{liq}} = k_{ij}^{\text{liq}} \left(p_i^{\text{liq}} - p_{\text{drop}} \right). \quad (4.29)$$

The throat conductivity is described by the throat geometry and can be calculated following Eq. (3.16). Since only one phase can be present in a circular throat the single phase conductivity can be applied. The drop growth is the volume change of the drop volume (assuming liquid water as incompressible fluid):

$$\dot{V}_{\text{drop}} = Q_{ij}^{\text{liq}} \quad (4.30)$$

4.3 Fluidic interaction at the interface between a hydrophobic and a hydrophilic material²

If the water breakthrough does not occur in the center of the channel but near the side walls, the liquid water flow interacts with the hydrophilic surface of the gas distributor as visualized in Figure 4.20. Again, liquid water passes through the fiber structure of the

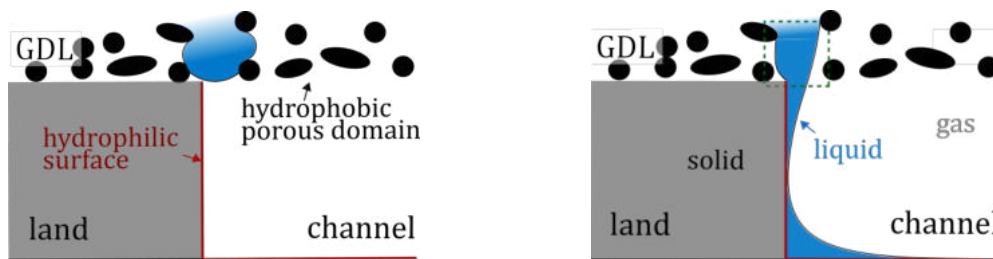


Figure 4.20: Interface configuration between GDL and gas distributor at the edge of a channel of the gas distributor. The red line indicates the hydrophilic surface of the gas distributor while the GDL is a hydrophobic porous domain. The green box shows the location of the interface pore where hydrophobic-hydrophilic interaction takes place.

GDL, but here, the breakthrough location is found at the side wall of a gas distributor channel. Once the liquid water reaches the interface and gets in contact with the hydrophilic surface, the water tends to spread on the surface of the gas distributor and is "sucked" out of the hydrophobic porous material. To describe the influence of this interaction on the flow through the porous GDL, an interface condition has been developed that used the pore-network principles to capture the hydrophobic-hydrophilic interaction on the pore-scale.

As previously, the flow through the hydrophobic porous domain is described using a pore-network model (see Figure 4.22 right circle). At the interface between GDL and gas distributor channel edge, we design the model for the interface pore such that the hydrophilic surface is represented by a hydrophilic throat that is located at the center of one of the pore body faces (see Figure 4.22 left circle). With this geometric simplification, the interface concept can be included in the previously describe pore-network model. We focus on the flow in the porous domain (domain I) which interacts

²Portions of this section are part of the publication *Modeling of two phase flow in a hydrophobic porous medium interacting with a hydrophilic structure* by Michalkowski et al. that is in review by *Transport in Porous Media* (Springer).

with the hydrophilic domain II. The hydrophilic structure (domain II) is not resolved explicitly but its influence on the flow in the porous domain (Domain I) is included in the model by the interface condition.

As before, we assume capillary-driven flow and neglect gravitational effects.

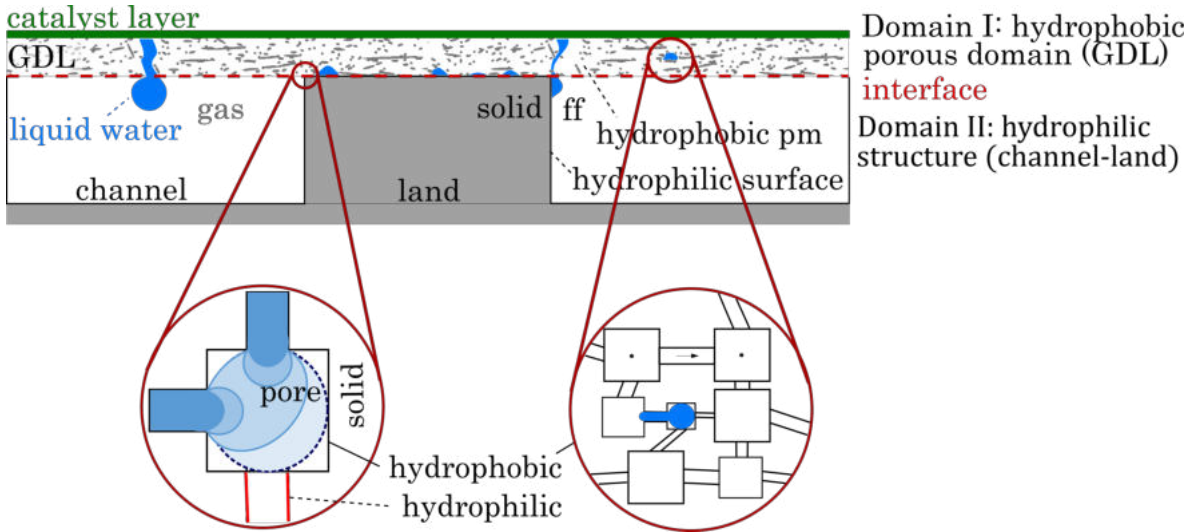


Figure 4.21: Pore-network application on interface configuration between GDL and gas distributor. The red dashed line marks the interface between the GDL and the gas distributor. The hydrophobic porous GDL (Domain I) is represented by a pore-network. At the interface to the hydrophilic gas distributor (Domain II) a special interface condition is applied with a hydrophobic pore connected to a hydrophilic throat.

4.3.1 Application to pore-network approach

Interface model concepts We consider the interaction of fluids in a hydrophobic pore-network interacting with a hydrophilic domain representing a hydrophobic GDL and a hydrophilic gas distributor of a PEM fuel cell, respectively. It is assumed that the flow in the hydrophobic GDL is not influenced by the hydrophilic gas distributor until liquid water gets in touch with hydrophilic surface in the interface pores. For the interface, we assume a cubic pore body with hydrophobic walls. A cutout of the interaction pore of the pore-network is shown in Figure 4.21.

One of the throats connected to that pore is assumed to have hydrophilic walls (red). The liquid water displaces the gas phase in the pore body coming from the connected

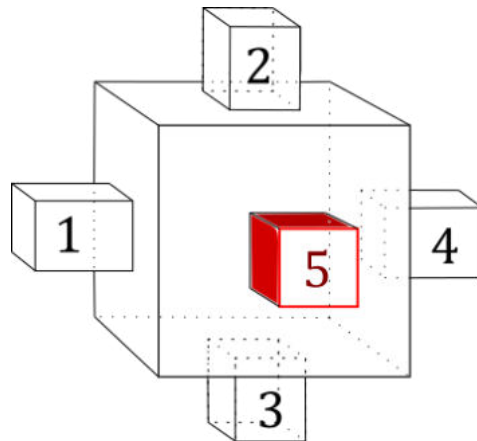


Figure 4.22: Cutout of the network with the interaction pore which has hydrophobic walls (black) and one hydrophilic throat is connected to that pore (red).

hydrophobic throats. The occurring water-gas configurations depend on the geometry and wetting behavior of this pore. In Figure 4.23, the fluid configurations during the invasion process at different time steps in a basic example geometry with a contact angle of 180° in the hydrophobic part are visualized in two dimensions. These states are independent of the contact angle in the hydrophilic throats.

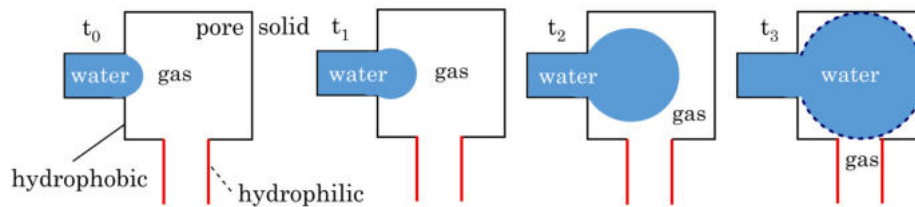


Figure 4.23: Fluid configurations of liquid water invasion in a hydrophobic boundary pore connected to a hydrophilic throat (red) at different time steps $t_0 < t_1 < t_2 < t_3$ during the invasion process. The dashed state at t_3 marks the time, when the liquid water gets in touch with the hydrophilic wall.

The invading liquid water forms a growing sphere inside the cubic pore body. The gas phase is displaced by the liquid water. At a certain time, the liquid water gets in touch with the hydrophilic wall. The moment immediately before the contact is marked with a dashed line in Figure 4.23. Here, we only consider cubic pores connected at their face centers by throats with a square cross sectional area. In Figure 4.24, it is shown that the liquid water configuration immediately before the contact with the hydrophilic throat is independent of the connections and geometric configuration of the cubic pore.

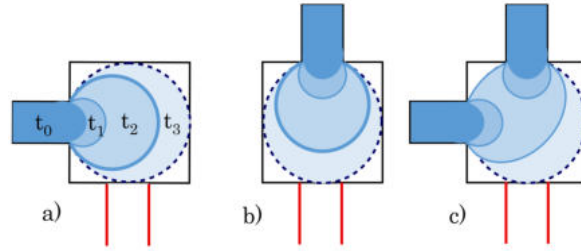


Figure 4.24: Different configurations of liquid water invasion in a hydrophobic boundary pore connected to a hydrophilic throat (red).

The different configurations show the liquid water filling of a hydrophobic pore (solid line) connected to a hydrophilic throat (red line). The dashed state marks the time, immediately before the liquid water gets in touch with a hydrophilic wall and the water behavior is influenced by the hydrophilic domain. The different shades mark the fluid configurations at different time steps ($t_0 < t_1 < t_2 < t_3$). It can be seen that in the Configurations a), b) and c), the non-wetting water touches the hydrophilic throat approximately at the same filling state even though the connections are applied differently. Configuration c) shows that even several connecting (and filling) throats do not influence the liquid water configuration. This results from the assumption that for strongly non-wetting pores, the liquid water forms a sphere in the pore body [44]. The cubic pore needs to be filled by a complete sphere before the liquid water "sees" the hydrophilic throat.

The independence of the filling state from the connectivity configuration allows to take the local water saturation s_{liq} as a threshold criterion at the interface pores (at the interface between the hydrophobic porous domain and the hydrophilic domain).

Since the wetting properties of GDLs in PEM fuel cell are not strongly wetting (180°) but intermediate-wet ($\approx 135^\circ$), the detailed fluid configuration in the pore body varies. However, it is expected to have a negligible influence on the overall flow behavior (as presented in Section 8.2.4). The concept is derived for strongly wetting pore bodies to allow an understandable geometric derivation.

After reaching the hydrophilic throat, the fluid distribution will be influenced by the connected hydrophilic domain. For both domains, a local, pore-scale capillary pressure-saturation relation $p_c(s)$ can be formulated based on the pore sizes, pore shapes and contact angles. In this work, the formulation presented by Joekar-Niasar et al. [44] for cubic pores is used (see Eq. (3.13)). In Figure 4.25, the $p_c(s)$ curves are visualized exemplary for a hydrophobic domain such as the GDL and a hydrophilic domain such

as a gas distributor in PEM fuel cells. Here, the channels of the gas distributors are considered as large pores with a diameter of 1 mm corresponding roughly to the width and height of the channels. This yields similar curvatures of the fluid interface in this pore as in the gas distributor channel and the resulting capillary pressure-saturation relation is comparable.

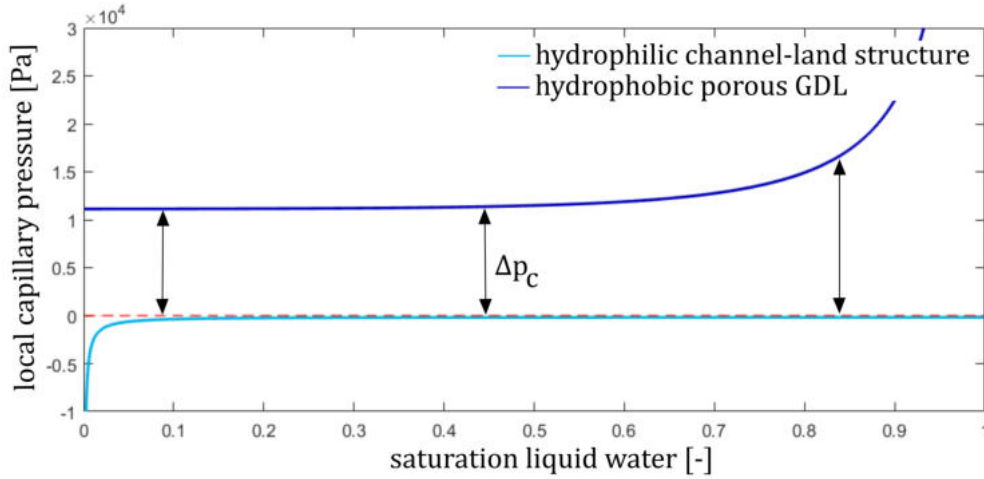


Figure 4.25: Local pore-scale capillary pressure-saturation relation for a hydrophilic (light blue) and a hydrophobic (dark blue) domain. The capillary pressure is defined as the difference between the non-wetting phase pressure (here: liquid) and the wetting phase pressure (here: gas). The water saturation describes the amount of liquid water in the pore with respect to the pore size ($s_{\text{liq}} = \frac{V_{\text{liquid}}}{V_{\text{pore}}}$). In the GDL, the water saturation equals the non-wetting phase saturation s_n , while in the gas distributor channels, the water saturation is the wetting phase saturation s_w .

Note that in Figure 4.25, the local capillary pressure is plotted with respect to the water saturation, which is the wetting phase saturation in the hydrophilic channel-land structure and the non-wetting phase saturation in the GDL. Dependent on the water saturation in the boundary pore, a capillary pressure difference (Δp_c in Figure 4.25) results between the hydrophobic and the hydrophilic domain. To formulate the local capillary pressure-saturation relation in the hydrophilic channel, a cubic pore with the same side length as the channel cross-section is considered (Figure 4.26). The geometry of this representative pore gives a comparable phase interface curvature with the original geometry, and therefore, its capillary pressure-saturation relation is used representing the pressure configuration in the channel. Since the representing pore of the hydrophilic channel is much larger than the hydrophobic pores in the GDL

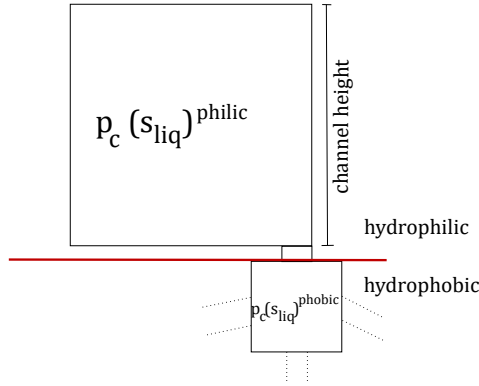


Figure 4.26: Representation of two pores at the interface between the hydrophobic and the hydrophilic domain. The hydrophilic channel is represented by a cubic pore with equal side dimensions to define a local capillary pressure-saturation relation. In each of the pores a different capillary pressure-saturation relation with respect to the water saturation s_{liq} is used.

($R_{channel} = 0.5 \text{ mm}$, $R_{GDL} < 100 \mu\text{m}$), the local capillary pressure curve is steeper and reaches a value very close to zero even for small water saturations s_{liq} . Therefore, as a model assumption, a constant capillary pressure in the hydrophilic domain is applied. This simplification is based on the assumption, that the liquid water is transported to the wall of the channel opposite to the porous GDL (see Figure 4.20) and away from the interface between the domains due to the hydrophilic wall properties in the gas channels. Nevertheless, for a more general formulation, a water saturation dependent capillary pressure $p_c(s_{liq})$ can be implemented for the hydrophilic domain. This might be necessary, if very high water saturations s_{liq} are considered in the channels which might occur during local blocking of the gas channels. However, these situations should be avoided at the operating conditions of the fuel cell such that it is not in the scope of this work.

As previously mentioned, the water saturation s_{liq} in the pore needs to reach a certain value to start an interaction between the hydrophobic and hydrophilic domains.

The capillary pressure difference $\Delta p_c = p_c(s_{liq})^{phobic} - p_c(s_{liq})^{philic}$ (Figure 4.26) between the hydrophobic GDL pores and the hydrophilic gas channel shows the significance of applying a saturation threshold for the interaction. Without the threshold, due to the water-pressure gradient, the total amount of liquid water present in the interface pore would flow into the hydrophilic domain in every time step. This would represent a non-physical behavior.

Once the water saturation (here: non-wetting phase) threshold s_{liq}^{th} is fulfilled (contact

of water with the hydrophilic throat), the liquid water flows out of the pore, the flux is defined by the water-pressure difference (non-wetting phase in GDL) between the considered pore and an assumed water pressure in the connected hydrophilic channel-land structure (wetting phase in gas distributor)).

In addition to the starting threshold, a stop criterion needs to be formulated. Again, different configurations during the emptying process are considered (Figure 4.27).

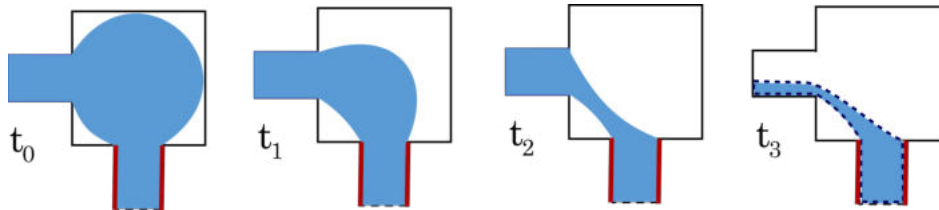


Figure 4.27: Different configurations of liquid water (non-wetting phase in the pore) leaving the hydrophobic pore through the hydrophilic throat (red) at different time steps during the emptying process ($t_0 < t_1 < t_2 < t_3$).

The dashed state marks the time before the phase is separated and no continuous liquid phase exists which connects the hydrophobic network with the hydrophilic gas channels.

In contrast to the filling process (Figure 4.24), the emptying process is not independent of the geometric configuration and connections of the pore as shown in Figure 4.28.

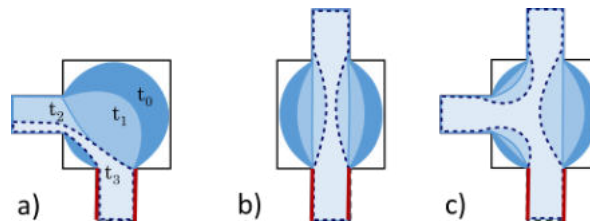


Figure 4.28: Different configurations of liquid water (non-wetting phase in the pore) leaving the hydrophobic pore through the hydrophilic throat (red) for different geometric configurations. The color shades refer to the different time steps (from dark to light).

For the different configurations we see very varying fluid patterns. During the emptying process, the liquid water tries to stay connected. The pore body is "emptied" while the water sticks in the hydrophilic pore throat such that it stays water-filled. The hydrophobic throats connected to the considered pore are also influenced by the outflow through the hydrophilic throat. We assume that the hydrophobic throats are emptied as well and the meniscus moves to its other end connected to the next pore

body, which stays uninfluenced.

Compared to the starting criterion, it is more difficult to formulate a criterion, when a snap-off is happening in the interaction pore such that the liquid water flux is stopped due to a disconnection of the water phase to the hydrophilic domain. For the beginning, we choose a water saturation threshold s_{liq}^{th} (non-wetting phase) analogous to the start criterion. The flux of the liquid water stops once the water saturation s_{liq} (non-wetting phase saturation) in the considered pore is lower than this particular value. In the applications (Section 8.2), we will see that the starting criterion has a dominant influence on the behavior, while the exact value of the stopping criterion is less relevant.

Using the theoretical considerations presented above, we formulate a combined criterion of pressure and water saturation s_{liq} (non-wetting phase in hydrophobic porous domain) configuration at the interface between the hydrophobic porous domain and the hydrophilic domain, which defines the interaction and the influence on the flow behavior:

- The flow is only influenced once the liquid water configuration in the boundary pore "touches" the hydrophilic throat,
- Once the throat is reached, flow is defined by the water-pressure differences between the hydrophobic porous domain and the hydrophilic domain,
- The flow is stopped once the connection between the hydrophilic throat and the "bulk" water is lost (snap-off occurred in the pore body).

Here, the gas phase pressure is nearly constant such that the liquid phase pressure difference equals the capillary pressure difference. Therefore, the flux across the interface between the hydrophobic porous domain and the hydrophilic domain, through the hydrophilic throat, is driven by the capillary pressure difference Δp_c across the interface (Figure 4.25).

Numerical model In the pore-network model, a volume balance equation for each phase $\alpha \in \{n, w\}$ for each pore body i is solved

$$V_i \frac{\partial}{\partial t} \rho_i^\alpha s_i^\alpha + \sum_j^{N_i} (\rho^\alpha Q^\alpha)_{ij}^\alpha = 0. \quad (4.31)$$

N_i is the number of throats connected to pore body i . The volumetric fluxes Q_{ij} through throat ij are calculated by means of the Washburn equation

$$Q_{ij} = k_{ij}^\alpha (p_i^\alpha - p_j^\alpha), \quad (4.32)$$

with the throat conductivities k_{ij}^α and the phase pressure difference between the connected pore bodies $p_i^\alpha - p_j^\alpha$. The balance equations are formulated per pore body, while the fluxes occur within the one-dimensional pore throats [85]. The primary variables of the pore-network model live on the network nodes, i.e. the center of the pore bodies. The pore bodies located at the interface (interface pores) are used to impose the coupling conditions for the pore-network model by connecting ghost nodes representing the hydrophilic domain. A Neumann condition is applied which depends on the fixed pressure in the ghost node p_0 and in the interface pore in the hydrophobic domain p_i

$$Q_{\text{out}} = -k_{\text{int}} (p_i^n - p_0). \quad (4.33)$$

Similar to the general pore-network model (see Section 3.1.2), the hydrophilic throat has a hydraulic resistance based on its geometric properties:

$$k_{\text{int}} = \frac{\pi}{8\mu_{\text{liq}} l_{\text{int}}} (r_{\text{int}}^{\text{eff}})^4 \quad \text{with} \quad r_{\text{int}}^{\text{eff}} = \sqrt{\frac{4}{\pi}} r_{\text{int}}, \quad (4.34)$$

with the inscribed radius and the length of the interaction throat, r_{int} and l_{int} , respectively. Here, μ_{liq} denotes the viscosity of the liquid water phase which is the wetting phase in the interface throat for the considered setup describing the interaction of a hydrophobic GDL with a hydrophilic gas distributor (channel-land structure).

4.4 Trapping in mixed-wet pores below land

In this section, we investigate the behavior of liquid water in the pore bodies located at the interface between GDL and gas distributor land. In Figure 4.29, the part of

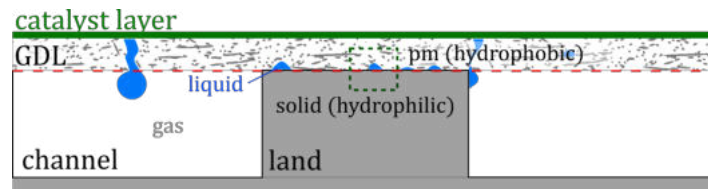


Figure 4.29: Configuration at the interface between GDL and gas distributor. Liquid water is trapped in a mixed-wet pore in the GDL below the land of a channel-land gas distributor structure. The red dashed line marks the interface between GDL and gas distributor.

interest of the interface is marked with a green dashed box. Here, pore bodies with mixed-wet conditions are considered. The wetting properties of the interface pores depend on the GDL wettability (hydrophobic conditions) as well as on the wettability of the gas distributor. Here, a gas distributor with hydrophilic surface conditions is considered. In this section, the situation is observed, where liquid water is trapped in partly hydrophilic pores in the GDL at the land parts of a channel-land gas distributor structure. A sketch of the configuration is shown in Figure 4.30.

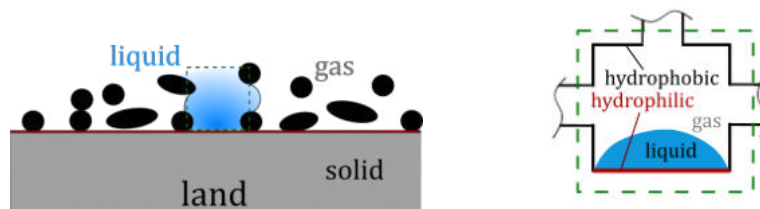


Figure 4.30: Liquid water in hydrophobic GDL which is in contact with the hydrophilic surface of the gas distributor at the land parts. This configuration is transferred to a pore body with one hydrophilic side wall. The red part is hydrophilic while the black sides are hydrophobic

Here, we consider only cubic pore bodies with the throat connected to the center of the pore body faces and gravitational effects are neglected. We assume capillary driven flow and neglect any influence of inertial effects on the fluid configurations in the pore bodies.

4.4.1 Application to pore-network approach

Interface concept The fluid behavior in the mixed-wet pore can be classified in five different states. In the following, the processes in the mixed-wet pore body are described for liquid water as the non-wetting phase in the hydrophobic porous medium (pm), which is in contact with a hydrophilic solid material (e.g., land part of PEM fuel cell gas distributor). The principles also hold for reverse wetting properties but we focus on the configuration occurring in a PEM fuel-cell cathode. The terms *filling* and *emptying* of a pore body again refer to the liquid-phase (water) behavior. We consider cubic pore bodies as they are chosen to represent the cavities in GDL structures (see Section 3.1.4). Only one face of the pore body is hydrophilic (red in Figure 4.29 right). This results from the assumption of a smooth surface of the hydrophilic solid.

First displacement by the liquid phase (water) We describe the occurring fluid displacement processes in the mixed-wet pore body and start with initially dry conditions, i.e. the pore body is completely filled with gas. Now the liquid is pushed into the pore. In Figure 4.31, the first time steps ($t_1 < t_2 < t_3 < t_4$) of the displacement of the gas phase by the liquid phase (water) are visualized. Before the liquid gets in contact with the hydrophilic face (red side of the pore body), the filling process equals the behavior in a completely hydrophobic pore. The dashed line marks the configuration, when the

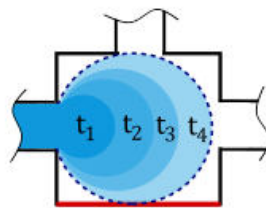


Figure 4.31: Primary drainage of a mixed-wet pore. As long as the non-wetting phase (water) is not in contact with the hydrophilic wall, there is no difference to drainage in a completely hydrophobic pore.

interaction with the hydrophilic side starts. For the contact configuration, a saturation threshold criterion can be formulated in analogy to the previously described hydrophilic throat concept (see Section 8.2). The contact occurs once a complete sphere is formed in the pore body. Again, we formulate a saturation threshold criterion for the liquid

phase to separate the different states. For cubic pore bodies, the saturation threshold to identify the contact of liquid water with the hydrophilic side is:

$$s_{\text{liq}}^{\text{th1}} = \frac{V_{\text{sphere}}}{V_{\text{pore}}} = \frac{\frac{4}{3}\pi r_{\text{pore}}^3}{8r_{\text{pore}}^3} \approx 0.52. \quad (4.35)$$

Contact with the hydrophilic pore body side As soon as the liquid water gets in contact with the hydrophilic pore side, the fluid distribution in the pore changes and the water is suddenly attached to the hydrophilic side as visualized in Figure 4.32 on the left side (t_5).



Figure 4.32: Reconfiguration of the water in the pore body after contact with the hydrophilic wall and further filling of the mixed-wet pore body.

For this redistribution, it can either be assumed that the saturation in the pore body stays constant during the spontaneous event or the phase pressures stay constant. Since the throat holds a resistance to the liquid phase (water) and the liquid viscosity is high compared to the gas viscosity, for the considered case, it is assumed that the mobility of the liquid is not high enough to support an immediate change in saturation in the pore body. An immediate change of the phase pressures is more likely to occur, and is therefore chosen to describe the interaction behavior. After the sudden redistribution, the pore body filling might continue dependent on the conditions in the neighboring pores (t_6). In Figure 4.32, the resulting liquid-gas distributions in the pore body are shown ($t_5 < t_6$).

Displacement by the gas phase and snap-off of the liquid phase (water) in the pore body If the pore body is not filled with liquid but the surrounding conditions of the pore body result in an emptying, the liquid-phase saturation decreases in the pore

body. During the emptying process, the liquid-gas distribution in the pore body equals the ones during the filling process (see Figure 4.32). However, if the liquid saturation is further reduced, the surface tension cannot keep an affiliated phase configuration and snap-off occurs inside the pore body.

During the emptying process, the fluid configuration changes as presented in Figure 4.33. The fluid configurations in the pore at time steps before and at snap-off are visualized ($t_6 < t_7 < t_8 < t_9 < t_{10}$). After snap-off, we have a trapped configuration.



Figure 4.33: Emptying of the pore body, where water got in contact with the hydrophilic wall, results in snap-off inside the pore body

Trapped residual liquid-phase saturation Once the pore body has been invaded by liquid water, after the emptying process including snap-off, a residual liquid phase saturation stays trapped in the pore body and cannot be removed by pressure driven flow. The resulting fluid distribution in the pore body is shown in Figure 4.34

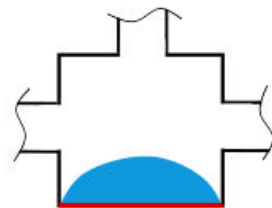


Figure 4.34: Residual water saturation being trapped in the pore body

The amount of liquid trapped in the pore depends on the shape and size of the pore and the hydrophilic side. For a cubic pore body with an inscribed radius R_i the volume

of the trapped water is calculated based on the shape of a spherical cap

$$V_{\text{trapped}} = \frac{\pi}{6} \left(\frac{r_{\text{trapped}}}{1 - \cos \theta} \left(3R_i^2 + \left(\frac{r_{\text{trapped}}}{1 - \cos \theta} \right)^2 \right) \right). \quad (4.36)$$

with $r_{\text{trapped}} = \frac{R_i}{\sin \theta}$. As a formulation of liquid phase (water) saturation, this holds

$$s_{\text{liq}}^{\text{res}} = \frac{\frac{\pi}{3} \left(\frac{r_{\text{pore}}}{\sin \theta} \right)^3 (1 \pm \cos \theta)^2 (2 \mp \cos \theta)}{V_{\text{pore}}}. \quad (4.37)$$

Second invasion by the liquid phase If the pore body is invaded again by liquid water, while the residual (trapped) saturation of the liquid phase (water) is still located in the pore, the configuration of the fluids is influenced by the trapped fluid. The behavior before the newly invading liquid gets in contact with the trapped liquid is presented in Figure 4.35. The behavior changes at the moment the newly invading

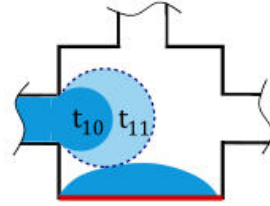


Figure 4.35: Residual water saturation being trapped in the pore body

liquid touches the trapped liquid (dashed). Again, we define a saturation threshold to distinguish the different process states:

$$V_{\text{liq, inv}}^{\text{th2}} = \frac{4}{3} \pi (R_i - h_{\text{trapped}})^3 \quad \text{with} \quad h_{\text{trapped}} = r_{\text{trapped}} (1 - \cos \theta), \quad (4.38)$$

$$s_{\text{liq}}^{\text{th2}} = \frac{V_{\text{liq, inv}}^{\text{th2}} + V_{\text{trapped}}}{V_{\text{pore}}} \quad \text{with} \quad V_{\text{pore}} = (2R_i)^3. \quad (4.39)$$

After the contact, the phase merges and a filling process similar to Figure 4.32 starts.

Numerical model From the fluid configurations in the pore body described above, a numerical concept is developed that uses the principles of pore-network modeling. We formulate pore-local capillary pressure-saturation relations for the different filling

and emptying processes. Since the interface concept is applied to the pore-network model representing the hydrophobic GDL, the pore-local capillary pressure-saturation relations ($p_c - s_w$) are formulated for the gas phase as the wetting phase.

Relations for first displacement by the liquid phase For State 1, the first displacement of the gas phase by the liquid phase, before first contact of liquid water with the hydrophilic face (see Figure 4.31), we apply the same pore-local capillary pressure-saturation relation as for completely hydrophobic pore bodies:

$$p_c^{\text{state 1}}(s_w) = \frac{2\sigma \cos \theta}{R_i (1 - \exp(-6.83(s_w)))}. \quad (4.40)$$

This relation is applied for $s_{\text{gas}} < 1 - \pi/6$.

After the contact of liquid water with the hydrophilic pore face (see Figure 4.32), the following geometric derived formulation is used:

$$p_c^{\text{state 2}}(s_w) = \left(\frac{\sqrt{\frac{27a^2 s_w - 4b^3}{s_w}}}{2 \cdot 3^{3/2} s_w} + \frac{a}{2s_w} \right)^{1/3} + \frac{b}{3s_w \left(\frac{\sqrt{\frac{27a^2 s_w - 4b^3}{s_w}}}{2 \cdot 3^{3/2} s_w} + \frac{a}{2s_w} \right)^{1/3}}. \quad (4.41)$$

with

$$a = \frac{(\sigma \cos(\theta))^3 (24 - 16/3\pi + 2\pi)}{V_{\text{pore}}} \quad (4.42)$$

$$b = \frac{(\sigma \cos(\theta))^2 (8R_i - 2\pi R_i)}{V_{\text{pore}}}. \quad (4.43)$$

This relation is applied for $1 - \pi/6 \leq s_w \leq 1$. The formulation is derived from geometric approximations of the fluid configurations similar to the approach described by Joekar-Niasar et al. [91], but here, there is no wetting phase (gas) in the corners and edges at the hydrophilic face.

In Figure 4.36, the resulting pore-local capillary pressure-saturation relations for the first two states (first displacement of the gas phase by liquid water before and after contact with the hydrophilic face) are visualized and compared to the pore-local capillary pressure-saturation relation for completely hydrophobic pore bodies.

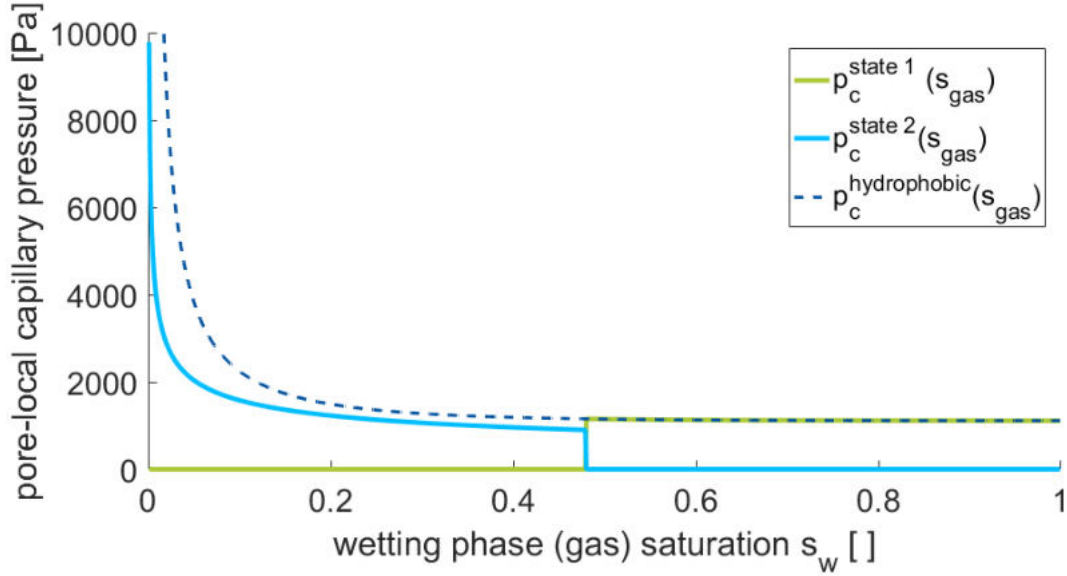


Figure 4.36: Capillary pressure-saturation relation for the configurations during primary drainage in a cubic shaped pore

Relations for second invasion by the liquid phase After the first filling of the pore body with liquid and subsequent emptying, a residual amount of liquid is trapped in the pore body. The trapped saturation is determined by the pore shape and the contact angle (see Figure 4.34)

$$s_{\text{liq}}^{\text{trapped}} = \frac{V_{\text{trapped}}}{V_{\text{pore}}} . \quad (4.44)$$

The capillary pressure at the interface between the trapped liquid and gas is defined by the curvature of the trapped fluid

$$p_c^{\text{trapped}} = \frac{2\sigma \cos \theta}{r_{\text{trapped}}} \quad (4.45)$$

If the pore body is newly invaded by the liquid phase (water), in the beginning, two interfaces between the gas and the liquid phase exist in the pore body (see Figure 4.35). The capillary pressure at the interface between the invading liquid and the gas in the pore equals the primary drainage formulation before contact, Eq. (4.40). However, for the calculation of the fluid interface curvature, the amount of trapped liquid needs to be subtracted from the gas-phase saturation since it is not part of the invading amount

of fluid.

$$p_c^{state3} = \frac{2\sigma \cos \theta}{R_i \left(1 - \exp \left(-6.83 \left(1 - \left(s_n - \frac{V_{trapped}}{V_{pore}} \right) \right) \right) \right)}. \quad (4.46)$$

Once the saturation threshold for the merging of the liquid phase is overcome, the capillary pressure-saturation relation behaves as in the first invasion case. As before, we see a strong increase in the capillary pressure for low gas-phase saturations since the gas phase is repressed in the edges and corners of the pore body $1 - \left(\frac{V_{trapped}}{V_{pore}} \right) \leq s_w < 1$:

$$p_c^{state4}(s_w) = \left(\frac{\sqrt{\frac{27a^2 s_w - 4b^3}{s_w}}}{2 \cdot 3^{3/2} s_w} + \frac{a}{2s_w} \right)^{1/3} + \frac{b}{3s_w \left(\frac{\sqrt{\frac{27a^2 s_w - 4b^3}{s_w}}}{2 \cdot 3^{3/2} s_w} + \frac{a}{2s_w} \right)^{1/3}}. \quad (4.47)$$

with

$$a = \frac{(\sigma \cos \theta)^3 (24 - 16/3\pi + 2\pi)}{V_{pore}}, \quad (4.48)$$

$$b = \frac{(\sigma \cos \theta)^2 (8R_{pore} - 2\pi R_{pore})}{V_{pore}}. \quad (4.49)$$

Relations for displacement by the gas phase If no hysteresis of the contact angle during drainage and imbibition is considered, the capillary pressure-saturation relation for displacement by the gas phase equals the one for second displacement by the liquid phase.

4.5 Effects of wettability, surface roughness and fiber structure

Contact angle variations and wettability of the GDL Since the flow in the GDL is capillary driven, it is crucial to include the wettability of the materials and structures

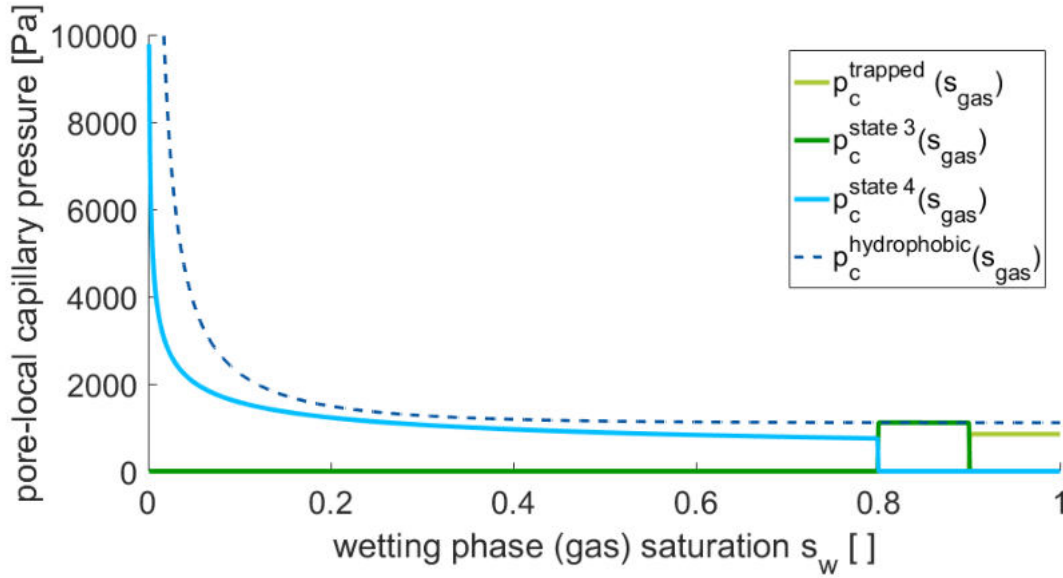


Figure 4.37: Capillary pressure-saturation relation for the configurations during secondary drainage in a cubic shaped pore

at the interface in the model to capture the ongoing flow processes. The coating of the GDL results in hydrophobic surfaces. However, due to the fabrication, where the coating is applied by putting the fiber structure in a solute bath, the PTFE content, and, therefore, the resulting contact angle might not be homogeneous. There might be pores that have not been reached during the bath. In experimental investigations [118], it was found that external forces are necessary to remove water from GDL structures. This indicates that the structure is still partially hydrophilic after the PTFE coating. Overall, the effective contact angle can be approximated from the global capillary pressure-saturation relation. Pore-network models in the literature show that a contact angle of around 130° is suitable to fit experimental data [119]. The influence of these variations in the contact angle are analyzed in Section 7.1.3. Nevertheless, a stronger influence is expected from the wettability change at the interface between GDL and gas distributor. Dependent on the location, different configurations presented above can occur.

Effect of surface roughness The effect of the rough surface of the GDL structure, rather than the single fiber roughness, on droplet is discussed in Section 4.2.

The fibers of a GDL consist of carbon which is a relatively smooth material compared to other natural porous materials. However, the PTFE coating and fabrication issues

might cause local roughness that influences the fluid flow. The effect of fiber surface roughness on the flow through the GDL could be included using variations in the contact angle (see Section 4.2). However, due to the lack of information on the exact conditions quantitative investigations are difficult. The influence of the binder material in a GDL is discussed in the following section.

Structural properties of the GDL and the influence of binder The binder applied to the GDL samples is taken into account for the model by the network extraction algorithm. Therefore, the influence on the pore geometry and connectivity of the pores is directly captured. Since the PTFE coating is applied to the bound structure, a difference in the contact-angle is not expected. However, micro-porous properties are not included. It is expected that the micro-porous structure has a minor influence on water transport since the capillary entry pressure to invade these pores is unlikely to be reached and a connected gas phase by corner flow is assumed for the pore-network. Therefore, the gas flow through the micro-pores of the binder material does not need to be considered separately.

Effects of fibrous structure and intermediate-wet conditions The weak hydrophobic conditions and the cylindrical fiber structure of the GDB material result in a so-called intermediate-wet behavior at the interface to a free flow.

Intermediate-wet means a porous material is neither completely wetting nor completely non-wetting to a fluid. One reason for the behavior are pore-local contact angle and wettability variations. This means, some pores are stronger wetting than others to the fluid of interest. Another reason for intermediate-wet behavior of flow in porous media are structural properties and weak wetting conditions. In GDLs, a contact angle around 130° is considered. With the circular fibers and some variations in the local contact angles, this is sufficient to show intermediate-wet conditions. The behavior is described exemplary in Figure 4.38.

In Figure 4.38, the orientation of the net surface tension force is shown for different interface configurations in a fibrous structure with a contact angle of 90° . Due to the round fibers, the curvature of the meniscus changes dependent on the position and direction of the flow. Therefore, the behavior of water varies dependent on the conditions: On one hand, the liquid water does not enter the material spontaneously but a pressure has to be applied to overcome the capillary entry pressure. On the other hand,

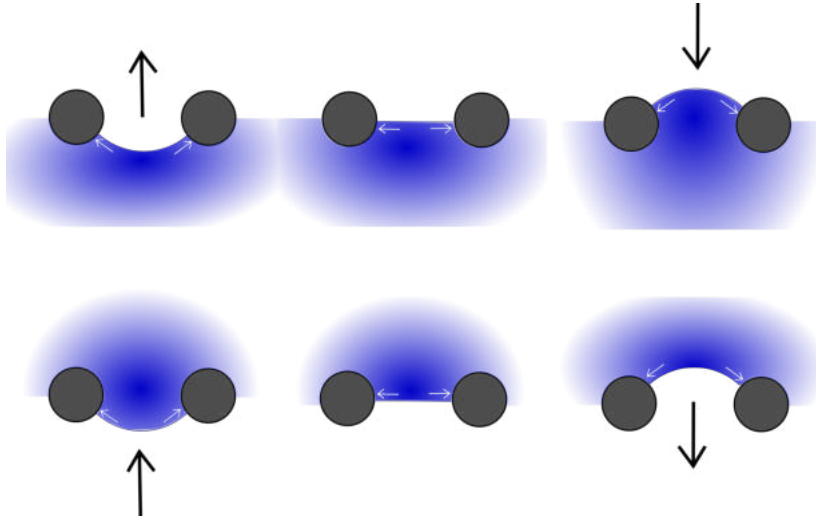


Figure 4.38: Intermediate wet conditions at surface of fibrous material. Surface tension force orientation in an intermediate wet structure due to the fibrous structure

the curvature of the meniscus does not let the water leave the structure spontaneously. However, considering the fuel cell cathode side, during operating conditions, only water invasion of the GDL is relevant and it is not necessary to take the strong hysteresis of the global capillary pressure into account. No external forces are expected in the operating fuel cell that could *pull* the water out of the GDL. The GDL dries due to evaporation rather than forced imbibition.

In this work, the maximum capillary pressure is used to define the capillary entry pressure of the throats. We take the fact into account, that the maximum curvature does not occur at the narrowest location of the throat such that the local (material based) contact angle differs from the pore-network effective contact angle. This allows to apply the Washburn formulation for the invasion of water in the GDL pore-network.

Harkness et al. [120] present a concept that takes the non-constant cross-section of a throat between cylindrical fibers into account rather than applying a strong contact-angle hysteresis [120]. Tranter et al. [121] performed detailed investigations on neutrally-wet fibrous materials with pore-network models. They found, the effect of fiber-structure-induced hysteresis gets stronger with smaller throat radius to fiber radius ratios $r_{\text{throat}}/R_{\text{fiber}}$. For the primary invasion of the GDL and the main water breakthrough paths mainly the largest throats have to be taken into account, which are invaded at the lowest water pressures. One has to keep in mind, considering almost fully saturated GDB pore-networks, that errors might occur due to the stronger influence of intermediate wettability and fiber-structure-induced hysteresis. However, this is

beyond the scope of this work. The intermediate-wet effects are not relevant where the GDL material is in contact with hydrophilic surface of the gas distributor. Here, the wettability change dominates the flow configuration. For the interface between GDL and free flow regions, the droplet concept captures the change of the curvature during the droplet formation. Imbibition of liquid water from the gas distributor into the GDL is not considered in this project and the intermediate-wet behavior of the material is not investigated for this situation.

5 Coupling approach pore-network with free-flow domain

In this section, the balance equations for the implementation of the interface concept, coupling the pore-network with the free-flow domain, as visualized in Figure 5.1, are considered. We distinguish between the single-phase interface, where only the gas phase

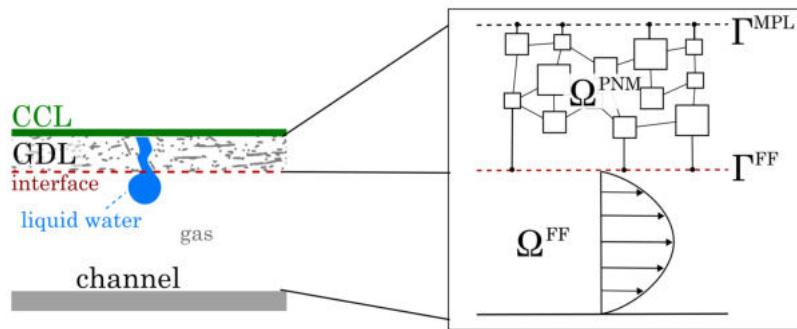


Figure 5.1: Sketch of GDL and gas distributor channel for the coupled pore-network and free flow models. The considered sub-domains are Ω^{PNM} for the GDL representation and Ω^{FF} for the channel representation. The domains are coupled at the interface Γ^{FF} .

is interacting between the domains and the droplet interface. The discretization of the two domains as well as the normal and tangential directions at the coupling interfaces are shown in Figure 5.2.

On the left side and in the center, two droplets of different size are forming at the interface. The droplets are fed from the pore-network. On the right side, an empty interaction pore is shown. Here, the interface is locally not invaded by the liquid phase and gas phase interaction occurs.

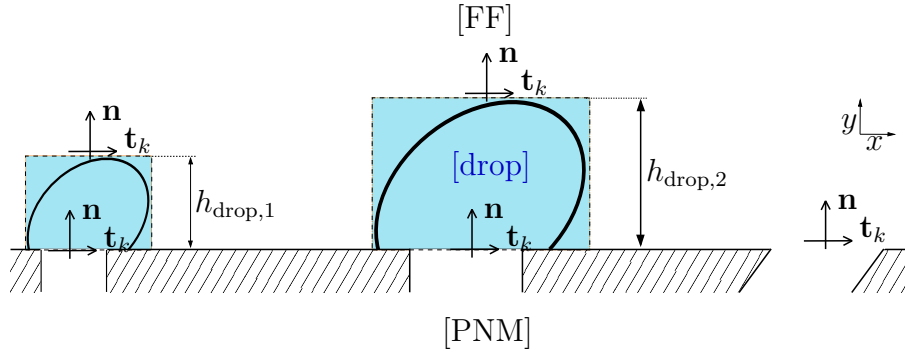


Figure 5.2: Interface configurations with different droplet sizes (left) and single phase interaction only (right). We consider two different domains [PNM] and [FF] as well as a droplet domain [drop] in between in the case if a droplet is formed at the interface.

5.1 Assumptions and simplifications to capture the relevant processes at the interface

The droplet formation on a porous medium and the detachment in a channel flow is a complex phenomenon. To implement such a phenomenon in an interface condition several simplifications and assumptions are necessary. Their justification is discussed in the previous sections. The following assumptions are made to formulate the presented interface concept:

- Gravitational effects can be neglected (see Figure 4.8).
- Interface throats are oriented perpendicular to the channel flow direction. Therefore, parallel flow can be assumed in the channel (no normal velocity component).
- Surface roughness of the porous material is captured by the contact angles.
- Interface pore throats interacting with the droplet have a spherical shape such that no corner flow is considered here.
- For the droplet detachment, only the tangential forces are considered without any lift.
- For the surface-tension force, a linear distribution of the contact angle along the contact line is assumed.

- For the detachment criterion, a separation line is used based on the 3D control volume concept (see Section 4.2.2).

5.2 Total mass balance

The total mass balance is fulfilled via the continuity of normal fluxes between the pore-network model (PNM) and the free-flow domain (FF).

Single-phase interface concept If there is no droplet formed at the interface, we can follow the approach presented by Weishaupt [45]. For the mass balance, the two domains are coupled with a source/sink term from the pore-network feeding the free flow and vice versa

$$[(V_{\text{pore}}q_{\text{pore}})_i]^{\text{PNM}} = \sum_{\sigma \in \Gamma_i} [(\rho_g \mathbf{v} \cdot \mathbf{n})_\sigma |\sigma|]^{\text{FF}} \quad (5.1)$$

with the volume of pore i , V_{pore} , and the volume specific mass flux q_{pore} leaving the pore, which form a source/sink term representing the pore-network (PNM). In the free-flow domain, this source/sink term is distributed to the adjacent free flow grid cells σ at the interface bounding pore i , Γ_i , based on the cell size $|\sigma|$ (length of cell at the interface). The gas density is denoted by ρ_g , \mathbf{v} is the velocity vector and \mathbf{n} is the unit vector normal to the interface.

Droplet interface concept for boundary pores invaded by the liquid phase For the drop concept, an interface region between the pore-network and the free flow is implemented. For the gas phase, the one-phase concept described above is used. For the liquid phase a balance between the interface pore and the formed droplet is applied

$$[V_{\text{pore}}q_{\text{pore}}]^{\text{PNM}} = \left[\frac{d}{dt} V_{\text{drop}} \right]^{\text{drop}}, \quad (5.2)$$

with the volume specific mass flux q_{pore} , the volume of the pore V_{pore} and the drop volume V_{drop} .

The volume of the droplet can be related to the droplet radius using a volume formulation of a sphere cap [77]

$$V_{\text{drop}} = \frac{\pi h_{\text{drop}}^2}{3} (3r_{\text{drop}} - h_{\text{drop}}) \quad \text{with} \quad r_{\text{drop}} = \frac{h_{\text{drop}}}{1 - \cos(\pi - \theta)}, \quad (5.3)$$

with the radius and the height of the droplet r_{drop} and h_{drop} , respectively, and the contact angle between drop and porous surface θ . The droplet detachment is not included in the mass balance, since for the free flow only the gas phase is considered. For the detachment, a discontinuity in the mass balance is accepted. The droplet is transported by the gas stream out of the computation domain but does not interact with it. This means, the droplet detachment is a sink for the liquid phase. This approach has also been used in [77].

The drop growth and detachment is handled in the interface region. For the droplet detachment criterion, a separation line is implemented which gives the critical size of a droplet corresponding to the average flow velocity in the channel (see Section 4.2.2).

5.3 Momentum balance

For the momentum balance, a mechanical equilibrium is considered between the pore-network, the drop (if formed) and the free-flow domain in the channel.

Gas-phase interface concept for non-invaded boundary pores In his thesis [45], Weishaupt presents a formulation for the mechanical equilibrium at a single phase interacting interface. He introduces a slip velocity similar to the Beavers Joseph condition to capture tangential interactions for all throat orientations at the interface

$$\begin{aligned} [p_g]^{\text{PNM}} &= [p]^{\text{FF}} \quad \text{on} \quad \Gamma_i, \\ v_{\text{slip},k} &= [\mathbf{v} \cdot \mathbf{t}_k]^{\text{FF}}, \\ v_{\text{slip},k} &= \frac{1}{\beta_{\text{throat}}} [\mathbf{t}_k \cdot (-\nabla \mathbf{v} + \nabla \mathbf{v}^T) \cdot \mathbf{n}]^{\text{FF}} + [\mathbf{v}_g \cdot \mathbf{t}_k]^{\text{PNM}}. \end{aligned} \quad (5.4)$$

Where p_g denotes the gas pressure in the pore-network, where a second phase (liquid) might be present without a mechanical interaction with the free flow. At the interface Γ_i , the free flow pressure p equals the pressure in the pore-network. The tangential

component of the free flow velocity \mathbf{v} equals the slip velocity $v_{\text{slip},k}$, which is derived from a shear force balance. For detailed information it is referred to [45].

Droplet interface concept for boundary pores invaded by the liquid phase If a droplet is formed, we introduce an interface domain "drop". The mechanical equilibrium holds between the pore-network and the drop as well as the drop and the free flow

$$[p_{\text{liq}}]^{\text{PNM}} = [p_{\text{liq}}]^{\text{drop}} , \quad (5.5)$$

$$\left[p_{\text{liq}} - \frac{2\sigma}{r_{\text{drop}}} \right]^{\text{drop}} = [p]^{\text{FF}} , \quad (5.6)$$

$$\underbrace{\left[(1 - \cos(\pi - \theta)) \frac{d}{dt} r_{\text{drop}} \right]^{\text{drop}}}_{\approx 0} = [\mathbf{v} \cdot \mathbf{n}]^{\text{FF}} . \quad (5.7)$$

Similar to the single phase approach, the liquid phase pressure p_{liq} in the pore-network interface pore equals the droplet pressure. The pressure in the droplet p_{drop} is linked to the size of the droplet by the curvature and representing capillary pressure. The normal velocity at the interface equals the growth of the droplet normal to the interface. Nevertheless, this velocity is assumed to be negligible.

For the continuity of the tangential shear stresses in the liquid phase, the tangential forces acting on the droplet are taken into account. The interaction of the drop with the free flow is modeled, balancing the tangential component of the inertial force, the pressure force and the viscous force around the droplet, which are derived above (see Section 4.2.2):

$$[F_{\text{drag}}]^{\text{drop}} = [\mathbf{t}_k \cdot \mathbf{F}_{\text{ff}}]^{\text{FF}} , \quad (5.8)$$

$$[F_{\text{pressure}} + F_{\text{shear}}]^{\text{drop}} = [\mathbf{t}_k \cdot ((\rho_g \mathbf{v} \mathbf{v}^T - \mu_{\text{gas}} (\nabla \mathbf{v} + \nabla \mathbf{v}^T)) \cdot \mathbf{n})]^{\text{FF}} . \quad (5.9)$$

5.4 Chemical equilibrium and molar flux conservation

For compositional flow, the conservation of the individual component fluxes across the interface for each component is required. Therefore, the chemical equilibrium evaporation and condensation in the pore and at the droplet surface is considered.

Gas phase interface concept for non-invaded boundary pores In the free flow, only the gas phase is present. Therefore only diffusion in the gas phase g from the pore-network to the free flow and vice versa is considered.

$$\left[(x^\kappa \rho_{\text{mol}} \mathbf{v} + \mathbf{J}_{\text{diff,mol}}^\kappa)_g \cdot \mathbf{n} \right]^{\text{PNM}} = - \left[(x^\kappa \rho_{\text{mol}} \mathbf{v} + \mathbf{J}_{\text{diff,mol}}^\kappa) \cdot \mathbf{n} \right]^{\text{FF}}, \quad (5.10)$$

with the mass fraction of component κ , x^κ , molar density ρ_{mol} , the molar diffusion coefficient $\mathbf{J}_{\text{diff,mol}}^\kappa$.

In Figure 5.3, the interface between pore-network and free-flow domain is visualized. The gas phase is interacting across the interface between the domains dependent on the local velocity in the free-flow domain and the concentration in the pore-network and the free flow.

The interaction of the pore-network and the free flow is implemented using a source/sink term in pore body i for each component κ

$$[(Vq)_i]^{\text{PNM}} = \sum_{\sigma \in \Gamma_i} \left[((x^\kappa \rho_{\text{mol}} \mathbf{v} + \mathbf{J}_{\text{diff,mol}}^\kappa) \cdot \mathbf{n})_\sigma |\sigma| \right]^{\text{FF}}. \quad (5.11)$$

The diffusion of the components across the interface depends on the concentration gradients

$$[\mathbf{J}_{\text{diff,mol}}^\kappa \cdot \mathbf{n}]^{\text{FF}} = - \frac{1}{M^\kappa} [D^\kappa \rho]^{\text{FF}+1} \frac{[X^\kappa]^{\text{FF}} - [X^\kappa]^{\text{FF}+1}}{0.5 [\Delta h]^{\text{FF}+1}}, \quad (5.12)$$

with the molar mass of the component κ , M^κ , the molecular diffusion coefficient D^κ and the mass density ρ .

We assume local chemical equilibrium [122] within a pore body and at the interface [45],

$$[X_{\text{gas}}^\kappa]^{\text{PNM}} = [X^\kappa]^{\text{FF}}, \quad (5.13)$$

with the mass fraction of component κ , X^κ .

In the pore body, the molar fraction of the component can be determined assuming an ideal gas mixture

$$[x_g^\kappa]^{\text{PNM}} = \frac{[p_g^\kappa]^{\text{PNM}}}{[p_g]^{\text{PNM}}}, \quad (5.14)$$

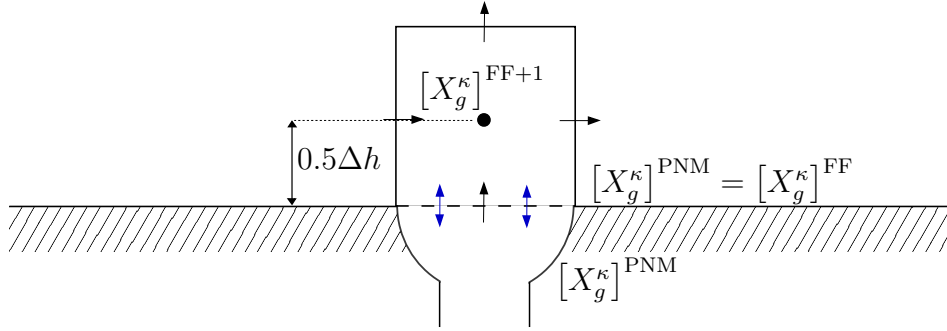


Figure 5.3: Implementation of the diffusive flux calculation for the coupling of free flow and the pore-network model if no droplet is formed (cf.[45])

with the total gas pressure p_g and the partial pressure of the component p_g^κ . To get the mass fraction X^κ from the molar fraction x^κ , the molar masses M^κ need to be taken into account by

$$X^\kappa = x^\kappa \frac{M^\kappa}{\sum_i x^i M^i}, \quad (5.15)$$

with the average molar mass of the mixture $\sum_i x^i M^i$.

Droplet interface concept for boundary pores invaded by the liquid phase In the approach described in [45], the presence of multiple phases within the pore body at the interface is captured by assuming that all phase-transfer processes occur within the pore body in local thermodynamic equilibrium. If a droplet is formed on the pore, the evaporation and condensation occurring at the surface of the droplet needs to be considered. Again, for the implementation a source/sink term is derived and coupled with the free-flow domain. However, in this case, there is no advective flux of the gas phase across the interface.

$$[(Vq)_i]^{\text{PNM}} = [(V_{\text{drop}}q_{\text{drop}})_i]^{\text{drop}} + [(\mathbf{J}_{\text{diff,mol}}^\kappa \cdot \mathbf{n}_{\text{drop}}) S_{\text{drop}}]^{\text{FF}}, \quad (5.16)$$

with the drop volume V_{drop} , the unit vector normal to the drop surface \mathbf{n}_{drop} and the drop surface are S_{drop} .

Since the drop is not computed directly, the normal vector on the drop surface cannot be resolved. Therefore, analogously to the no-drop approach, the first free flow grid cell adjacent to the interface with the pore-network is used with the normal vector

perpendicular to this interface. However, the surface area of the droplet is included to take the droplet size into account.

The diffusive molecular flux $\mathbf{J}_{\text{diff,mol}}^\kappa$ is derived using a Fickian ansatz based on the mass fraction gradient within the free-flow domain directly at the interface between the pore-network and the free flow or the droplet surface and the free flow, respectively,

$$[\mathbf{J}_{\text{diff,mol}}^\kappa \cdot \mathbf{n}]^{\text{FF}} = -\frac{1}{M^\kappa} [D^\kappa \rho]^{\text{FF}+1} \frac{[X^\kappa]^{\text{FF}} - [X^\kappa]^{\text{FF}+1}}{0.5 [\Delta h]^{\text{FF}+1} - h_{\text{drop}}}, \quad (5.17)$$

with the molar mass of the component κ , M^κ , the molecular diffusion coefficient D^κ and the mass density ρ .

Assuming a chemical equilibrium within the phases at the PNM-FF interface Γ^{FF} , the molar fraction of the components can be determined using Raoult's law

$$[x^\kappa]^{\text{FF}} = \frac{p_g^\kappa}{[p_g]_{\text{FF}}^\kappa} = \frac{p_{\text{sat}}^\kappa}{[p_g]_{\text{FF}}^\kappa}. \quad (5.18)$$

The mass fractions can be calculated using Eq. (5.15).

Assuming local thermodynamic equilibrium, the partial pressures of water vapor p_g^κ can be assumed to equal their saturation vapor pressure p_{sat}^κ presuming that the corresponding liquid phase is present, which is the case at the droplet surface. The total gas pressure above the droplet, in the free-flow domain, is denoted by $[p_g]_{\text{FF}}^\kappa$.

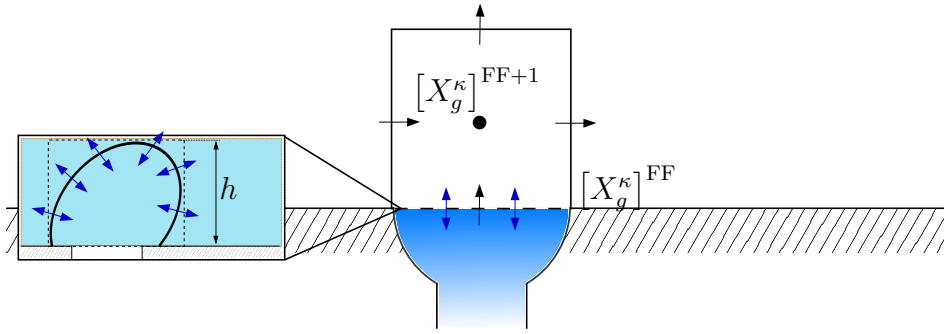


Figure 5.4: Implementation of the diffusive flux calculation for the coupling of free flow and the pore-network model if a droplet is formed at the interface between pore-network and free flow such that no phase transfer occurs in the pore body.

5.5 Energy balance and thermal flux conservation

Gas phase interface concept for non-invaded boundary pores For non-isothermal flow, the conservation of thermal fluxes across the interface in the gas phase is balanced by

$$\begin{aligned} & \left[\left((h\rho\mathbf{v})_g + \sum_{\kappa} (\mathbf{J}_{\text{diff,mol}}^{\kappa} h^{\kappa})_g - \lambda_g^{\text{eff}} \nabla T \right) \cdot \mathbf{n} \right]^{\text{PNM}} \\ & = - \left[\left(h\rho\mathbf{v} + \sum_{\kappa} (\mathbf{J}_{\text{diff,mol}}^{\kappa} h^{\kappa}) - \lambda_g \nabla T \right) \cdot \mathbf{n} \right]^{\text{FF}}, \end{aligned} \quad (5.19)$$

with the sum of the occurring phases α and components κ .

If no droplet is formed at the interface, the energy exchange including the diffusive, conductive and convective energy transfer does only occur through the gas phase. A local thermal equilibrium holds directly at the coupling interface with

$$[T]^{\text{PNM}} = [T]^{\text{FF}} \quad \text{on} \quad \Gamma_i^{\text{FF}}. \quad (5.20)$$

Droplet interface concept for boundary pores invaded by the liquid phase If a droplet is formed at the interface, the heat conduction from the liquid droplet to the gas phase in the free flow needs to be taken into account

$$\begin{aligned} & \left[\left(\sum_{\kappa} (\mathbf{J}_{\text{diff,mol}}^{\kappa} h^{\kappa})_g \right) \cdot \mathbf{n} - q_{\text{drop}}^T \right]^{\text{PNM}} \\ & = - \left[\left(h\rho\mathbf{v} + \sum_{\kappa} (\mathbf{J}_{\text{diff,mol}}^{\kappa} h^{\kappa}) - \lambda_g \nabla T \right) \cdot \mathbf{n} \right]^{\text{FF}}, \end{aligned} \quad (5.21)$$

with the conductive heat transfer between the droplet and the surrounding gas following Fourier's law

$$q_{\text{drop}}^T = f_e Nu(Re, Pr) \lambda_{nw}^{\text{eff}} S_{\text{drop}} \frac{[T]^{\text{drop}} - [T]^{\text{FF}+1}}{0.5 [\Delta h]^{\text{FF}+1} - h_{\text{drop}}} \quad (5.22)$$

with $[T]^{\text{drop}} = [T]^{\text{PNM}}$,

with the temperature at the cell center FF+1 in the free flow, $[T]^{\text{FF}+1}$, the temperature of the liquid phase in the drop, T_{drop} , the distance between the interface and the cell center, $0.5\Delta h$, a factor for kinetic energy transfer f_e and the Nusselt number Nu . The effective heat conduction coefficient $\lambda_{nw}^{\text{eff}}$ can be determined by algebraic averaging. For the Nusselt number, no relation for multi-phase flow is available. As in Nuske et al. [123], the relation given by Wakao and Kaguei [124] is used, which was defined for single-phase flow

$$Nu(Re, Pr) = 2 + 1.1Pr^{1/3}/Re^{0.6}. \quad (5.23)$$

To account for possible differences between the single-phase Nusselt number and a multi-phase Nusselt relation, the dimensionless energy-transfer factor f_e is introduced. Assuming a local thermodynamic equilibrium, there is no temperature gradient across the drop interface with the gas flow such that the heat conduction can be reduced to the gas phase (Eq.(5.19)).

Like the mass fluxes described above, the energy flux between the two sub-models is implemented in terms of an equivalent sink/source term for pore body i at the local interface Γ_i^{FF}

$$[(Vq^e)_i]^{\text{PNM}} = \sum_{\sigma \in \Gamma_i^{\text{ff}}} \left[\left(\left(h\rho\mathbf{v} + \sum_{\kappa} (\mathbf{J}_{\text{diff,mol}}^{\kappa} h^{\kappa}) - \lambda_g \nabla T \right) \cdot \mathbf{n} \right)_{\sigma} |\sigma| \right]^{\text{FF}}. \quad (5.24)$$

6 Coupling approach pore-network (GDL) with REV domain (gas channel)

In Figure 6.1, the representation of GDL and gas distributor channel domain with a pore-network and an REV-domain, respectively, is shown. In this section, we focus on the interface between pore-network and REV-domain (Γ^{REV}). Additionally, the balance equations for the implementation of the interface concept coupling the pore-network with the REV domain are considered.

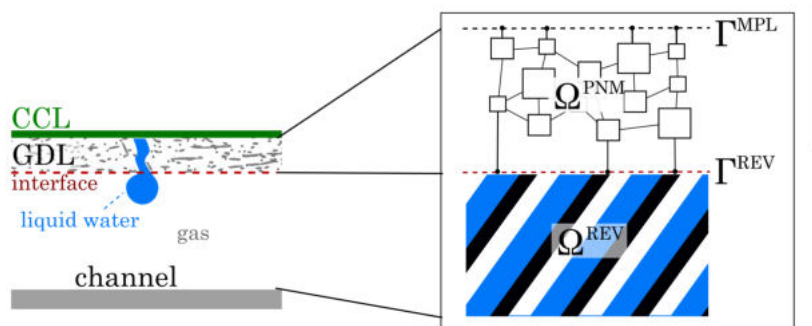


Figure 6.1: Representation of GDL and gas distributor channel using a pore-network and an REV approach, respectively. The models for the single domain are coupled at the common interface Γ^{REV} . A boundary condition representing the reactions in the CCL and the transport of the produced liquid water through the MPL is applied at the interface Γ^{MPL} .

We analyze the interaction of gas flow between the domains and the occurrence, growth and detachment of droplets forming at the breakthrough locations of liquid water transport through the GDL.

In contrast to REV-scale coupled models (e.g. [122]), pore-scale coupling models consider discrete coupling locations. Coupling models for free flow and porous media on the pore scale locally distinguish between the void space (pores) and solid at the interface. In this work, using pore-network models, we couple flow at the locations associated with the pore throats using ghost nodes located in the channel domain. The details of this approach are presented in the following. The conditions presented here are referring to the application of a Box scheme [97].

6.1 Assumptions and simplifications of the interface concept

As presented in Figure 6.2, we use ghost nodes at the interface to capture droplet formation.

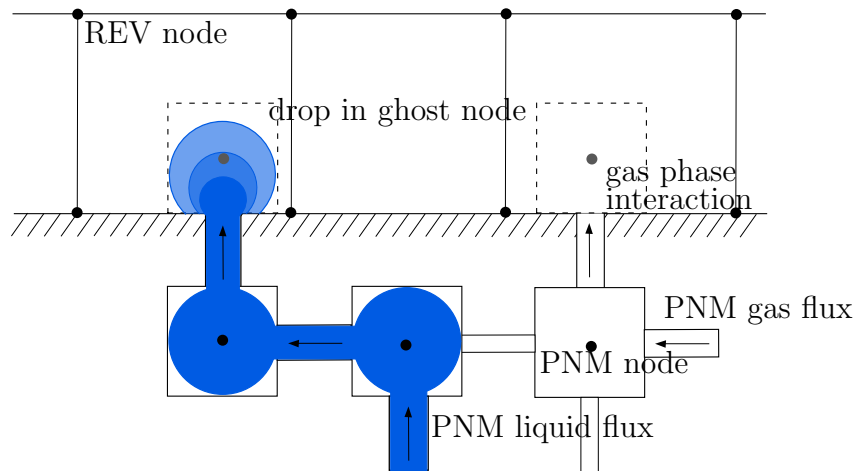


Figure 6.2: Interface configuration coupling the pore-network with the REV domain. Ghost nodes are applied at the interface which are located inside the REV domain.

On the left side, a droplet is forming in a ghost node. The droplet is fed by a preferential flow path of the liquid phase through the pore-network. On the right side, an empty interaction pore is shown. Here, the interface is locally not invaded by the liquid phase and gas phase interaction occurs between the pore-network node in the pore body and

the REV cell. In the following, the mass and momentum coupling conditions applied to the pore-network and the REV domain are presented.

6.2 Mass balance gas phase

The continuity of the total gas mass flux of the gas phase across the interface is required for non-compositional systems [45]:

$$\int_{\Gamma_{\text{box},k}} [\rho^\alpha \mathbf{v}^\alpha \cdot \mathbf{n}]^{\text{REV}} d\Gamma = - \sum_{i \in \Gamma_{\text{box},k}} \left[V_i \frac{\partial \rho_i^\alpha}{\partial t} + \sum_i (\rho Q)_{ij}^\alpha \right]^{\text{PNM}}, \quad (6.1)$$

with the phase density ρ^α , the velocity vector in the REV domain \mathbf{v}^α , the pore body volume of the interface pore V_i and the volume flux of phase α , Q_{ij}^α . As shown in Figure 6.3, $\Gamma_{\text{box},k}$ denotes the sub-control volume face (scvf) k of the box sub-control volume (scv) of the REV domain, where the coupling occurs.

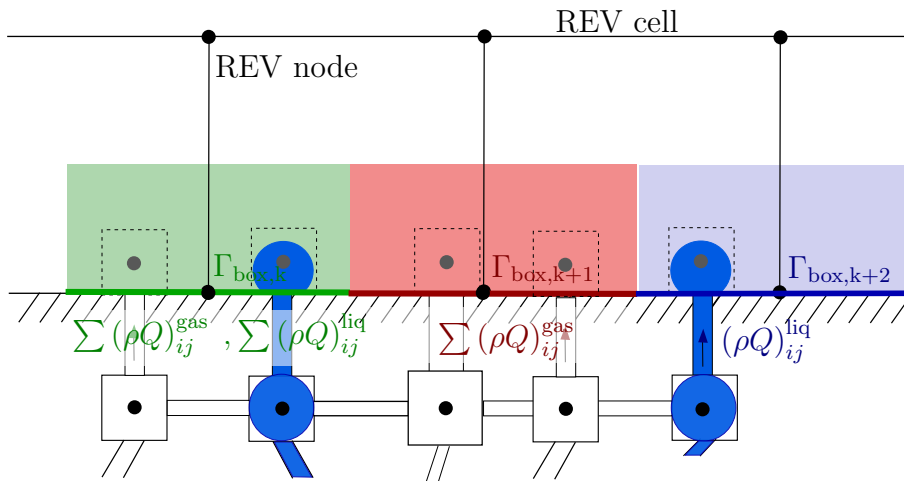


Figure 6.3: Interface configuration coupling the pore-network with the REV domain. Implementation of the coupling fluxes between the pore-network model and the REV-scale model.

6.3 Momentum balance gas phase

We assume the continuity of gas phase pressure at the coupling interface. This is a simplification since we ignore the conceptual discrepancy regarding the usage of averaged pressure on the REV-scale and pore-scale pressure in the pore-network.

$$[p_g]^{\text{PNM}} = [p_g]^{\text{REV}} \quad (6.2)$$

This issue is discussed by [125, 126, 127]. However, this simplification can be found repeatedly in the literature (e.g., Weishaupt [45], Balhoff et al. [128, 129], Mehmani and Balhoff [130], and Zenyuk et al. [80]).

In detail, the local gas phase pressure of the REV domain at the interface pore is calculated from the neighboring REV nodes using linear basis functions $w_k(x)$ (see Figure 6.4).

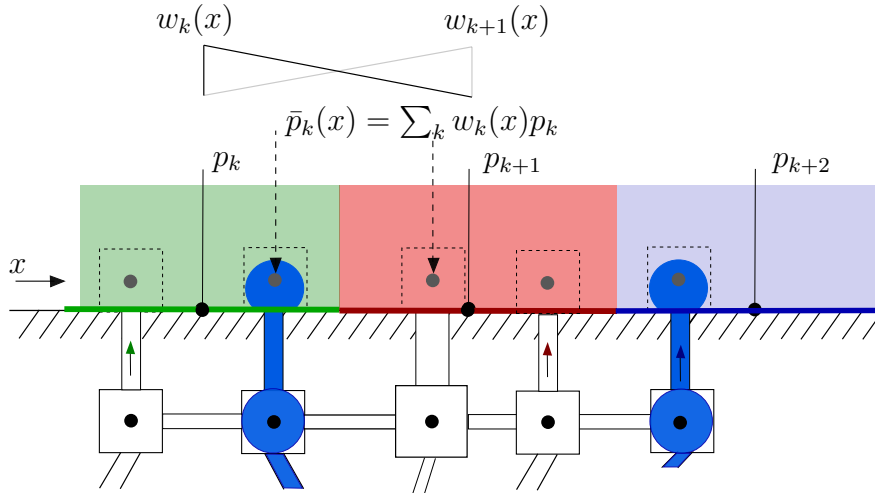


Figure 6.4: Interface configuration coupling the pore-network with the REV domain. Implementation of the coupling pressures between the pore-network model and the REV-scale model.

6.4 Mass balance liquid phase

The transfer of mass of the liquid phase from the pore-network to the REV domain is taken into account using a drop based concept.

The drops formed in the interface pores of the pore-network are detached once the detachment criterion is fulfilled. This results in a reduction of the liquid phase saturation of the drop mass implemented using a sink term in the pore-network

$$[q_{\text{drop}}]^{\text{PNM}} = \frac{\partial}{\partial t} \left(\frac{\rho_{\text{liq}} V_{\text{drop}}}{V_{\text{pore}}} \right), \quad (6.3)$$

on the residual formulation of the liquid phase

$$\underbrace{V_i \frac{\partial (\rho_{\text{liq}} S_{\text{liq}})_i}{\partial t} + \sum_j (\rho_{\text{liq}} Q_{\text{liq}})_{ij} - (V q_{\text{liq}})_i - V_i q_{\text{drop}}}_{=: \mathbf{r}_{\text{PNM}}(\mathbf{u})} = 0. \quad (6.4)$$

And a source term in the REV domain:

$$[\mathbf{q}_{\text{drop}}]^{\text{REV}} = \begin{pmatrix} 0 \\ -q_{\text{liq}} \end{pmatrix} = \begin{pmatrix} 0 \\ -\frac{\partial (\rho_{\text{liq}} V_{\text{drop}})}{\partial t} \end{pmatrix}. \quad (6.5)$$

The source term is applied to the residuum of the REV domain as volume sources:

$$\underbrace{\Phi \frac{\partial \rho_\alpha S_\alpha}{\partial t} - \nabla \cdot \left(\rho_\alpha \frac{k_{r\alpha}}{\mu_\alpha} \mathbf{K} (\nabla p_\alpha - \rho_\alpha \mathbf{g}) \right)}_{=: \mathbf{r}_{\text{REV}}(\mathbf{u})} - \mathbf{q}_\alpha - \mathbf{q}_{\text{drop}} = 0. \quad (6.6)$$

In Figure 6.5, the detached droplet mass is added as a source term to the nearest REV node at the interface (left). The gas phase pressure in the now uninvasion interface pore (ghost pore) stays according to the interpolation of the neighboring REV node gas phase pressures (right).

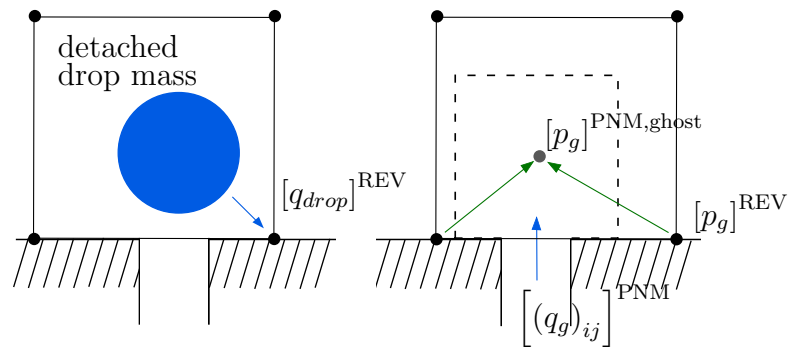


Figure 6.5: Interface configuration coupling the pore-network with the REV domain. Ghost nodes are applied at the interface which are located inside the REV domain. The detached drop volume is applied as a source term to the REV nodes at the interface.

7 Simulation results of pore-scale flow and transport through MPL-free GDLs

In this chapter, first the structural and flow characteristics of a GDB or MPL-free GDL are investigated. We analyze the sizes and shapes of void spaces in the fibrous material. Additionally, different influences on the global capillary pressure-saturation relation of GDB or MPL-free GDL materials are presented. In the second part of this chapter, single phase investigations of a GDL-gas distributor setup are shown. We present the influence of the gas distributor channel width and pressure differences between channels on the distribution of oxygen and water-vapor concentrations in GDBs or MPL-free GDLs.

7.1 Structural and flow characteristics of MPL-free GDL representation

7.1.1 Pore shape characterization

The generation of a representative pore-network of the GDB or MPL-free GDL structure requires an analysis of the shapes of pore bodies and throats of the fibrous porous material. We investigate these structural characteristics based on cubic samples with side length $200\ \mu\text{m}$. Four different realizations have been generated using the Math2Market software GeoDict®[98]. The four samples are visualized in Figure 7.1. All samples have a fiber diameter of $10\ \mu\text{m}$ and a porosity of 82%. The fibers are always straight, as it is

typical for GDBs from SGL, but oriented differently. The used option in GeoDict®[98] is *short circular fiber* as grain object type. The length of the fibers is chosen with 1 mm in this case to ensure the fibers to cross the entire domain. The different realizations have been generated by using different fiber-orientation parameters of the software GeoDict®[98] and different resolutions (voxel sizes of $0.1\ \mu\text{m}$, $0.5\ \mu\text{m}$ and $1\ \mu\text{m}$). The first realization in Figure 7.1 has a voxel size of $0.1\ \mu\text{m}$ and for the fiber orientation an "anisotropic orientation" specification is used with anisotropy parameter 3 for both directions. The second sample has a voxel size of $0.5\ \mu\text{m}$ and for the fiber orientation an "anisotropic direction" specification with anisotropy parameter 3 for both directions is set. The third sample is specified with the same orientation parameters as sample 2 but a voxel size of $1\ \mu\text{m}$. The last samples is again generated based on the fiber "anisotropic orientation" specification as sample 1 and a voxel size of $1\ \mu\text{m}$. The "anisotropic orientation" and "anisotropic direction" are parameter settings from GeoDict to specify the distribution of fiber orientation with respect to each other and the distribution of fiber direction in the three-dimensional space.

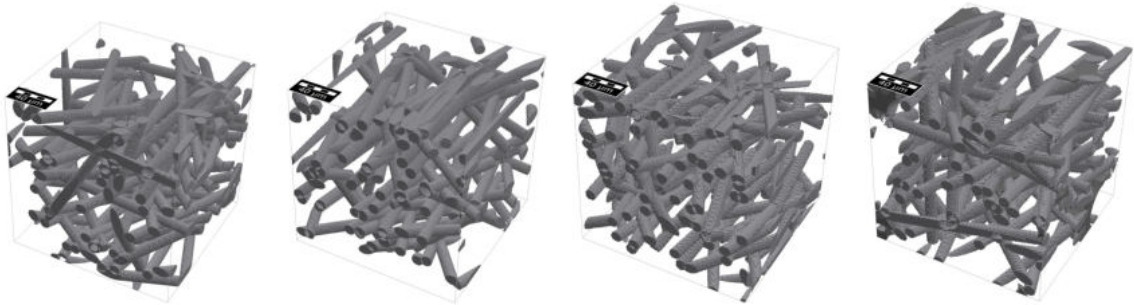


Figure 7.1: $200\ \mu\text{m}$ cube samples of fibrous MPL-free GDL structures or GDB structures generated using GeoDict®[98] with varying parameters to analyze the shapes of the void spaces (pores) in the material

From these four realizations, pore-networks have been extracted using PoreSpy [99] with the extraction parameters $\sigma = 0.4$ and $r_{\text{max}} = 0.4\ \mu\text{m}$. For the pore bodies, the most important parameter is the volume of the pores which defines the storage properties. Since the PoreSpy algorithm counts the volume of the cavities by voxels only, the resolution of the sample has a small influence here. In Figure 7.2, a histogram of the pore sizes of a $4\ \text{mm} \times 4\ \text{mm}$ sample is shown.

It can be seen, that many pores are of a rather small size. Most pore bodies have an inscribed radius between 10 and $20\ \mu\text{m}$. However, they only have a small influence on the displacement processes in the porous GDL since the connected pore throat inscribed

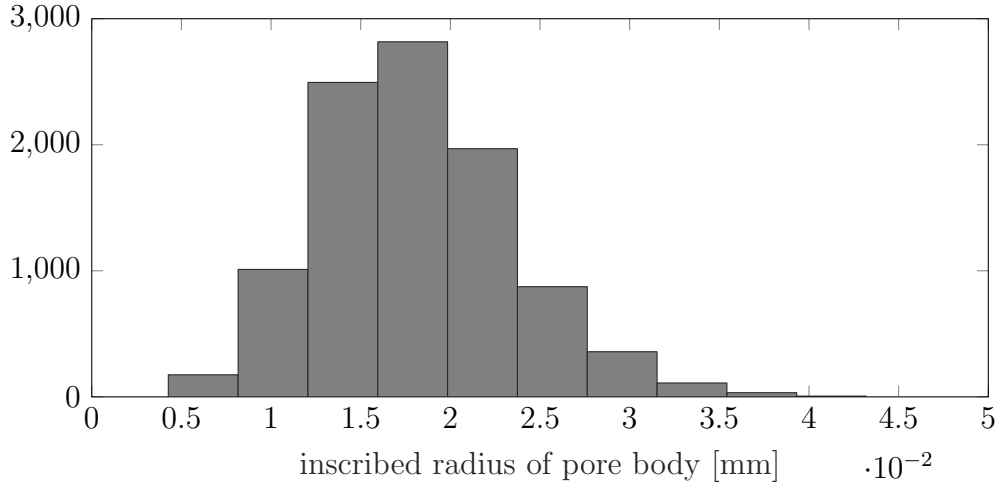


Figure 7.2: Histogram of the inscribed radius of the pore bodies of a 4 mm×4 mm sample representing a GDL structure.

radii are even smaller (see Section 3.1) and can only be invaded at very high capillary entry pressures which do not occur during PEM fuel cell operating conditions. However, the many small pores have a major contribution to the overall void space volume such that the global saturation of the GDL stays low during water drainage.

For the fluxes and resistances of the network, the pore throats are relevant. Pore-Spy [99] defines the throats as the narrowest cross-section between two cavities (pore bodies). This two-dimensional plane is well defined by its area and shape. These two properties define the conductivity of the throats. The area is directly represented in the pore-network by the throat sizes but for the throat shape, we are restricted to simple geometric shapes. Nevertheless, as described in Section 2.6.1, complex shapes can be transferred to a regular geometric shape using the shape factor G . In Figure 7.3, the occurring shape factors of the throats in the realizations described above are shown. The bars represent the mean value of all four realizations and the error bars the minimum and maximum value of all samples.

The shape factor of an equilateral triangle is $G = \sqrt{3}l^2/36l^2 = \sqrt{3}/36 \approx 0.048$, and from a square, we get a shape factor of $G = 4l^2/64l^2 = 1/16 = 0.0625$ [40]. Most pore throats of the samples have a shape factor between 0.04 and 0.08. As described in Section 3.1, the pore-network model has a contact angle restriction dependent on the half-corner angle of the pore throats. Since the triangular shape allows to use a contact angle $\theta < \pi/2 - \pi/6$ (measured in the wetting phase) while the square shape allows only $\theta < \pi/2 - \pi/4$ (see Eq. (3.18)), we use equilateral triangles to represent the pore

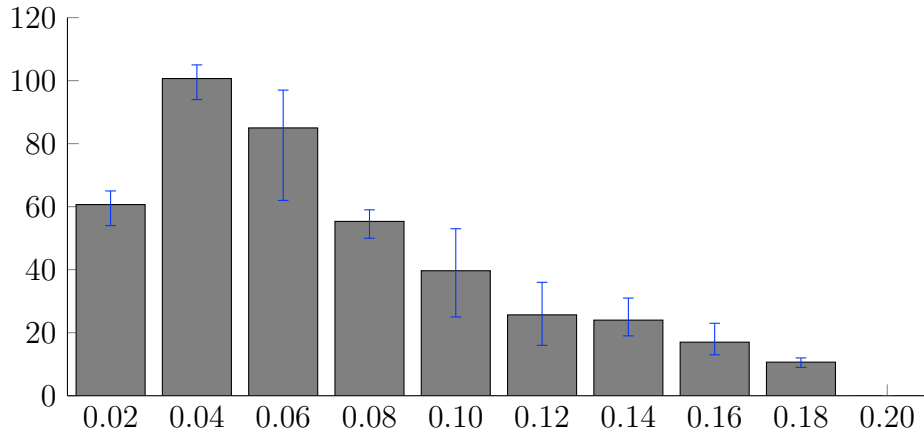


Figure 7.3: Histogram of the shape factor of the pore throats in the MPL-free GDL or GDB sample materials with the deviations between the samples as error bars

throats in the GDL representation pore-network.

The realizations in Figure 7.1 do not include any binder. Usually, the fibers of a GDL are clued together with a binder to increase the strength of the structure. From optical analysis, we estimate a porosity reduction of 3% by adding the binder material. In Figure 7.4, two $200\ \mu\text{m}$ cubic samples with a voxel size of $0.5\ \mu\text{m}$ are visualized. The fiber properties and orientations are the same but in the right sample 3% binder is added with a contact angle of 20° between binder and fiber.

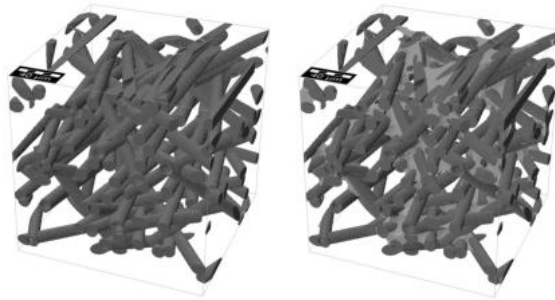


Figure 7.4: $200\ \mu\text{m}$ cube samples of fibrous MPL-free GDL or GDB structures generated using GeoDict®[98] with and without binder material

The influence of the added binder on the pore throat shapes is shown in Figure 7.5. The considered sample without binder resulted in many pores with small shape factors. Small shape factors occur for example in slit-like pore throats. Adding the binder reduced the number of pores with very small shape factors but resulted in more pore throats with a shape factor between 0.04 and 0.08. The slit-like pore throats might

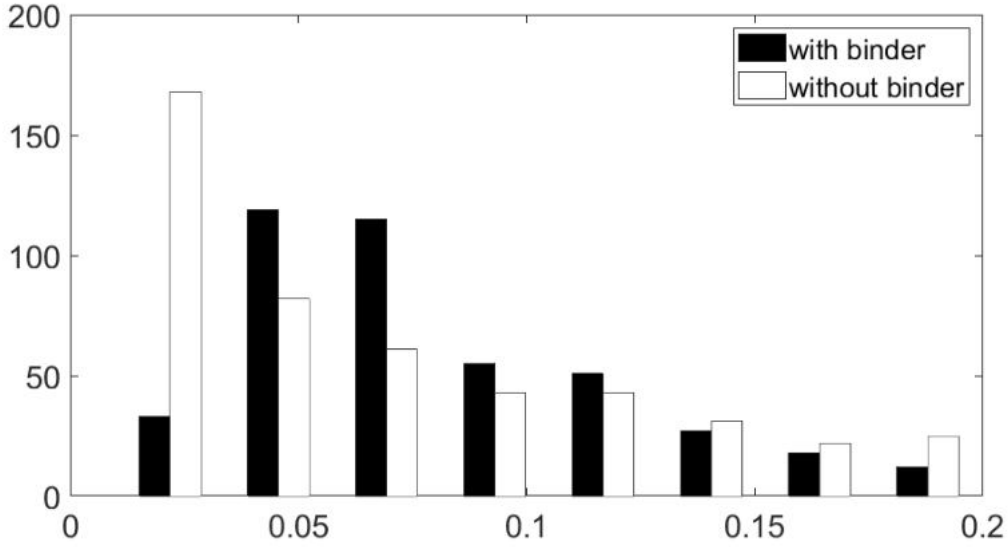


Figure 7.5: Histogram of the shape factor of the pore throats in a GDL sample with and without binder

have been blocked by the added binder or reduced and segmented.

The results show that the added binder has an influence on the pore throat shapes and on the pore bodies by the volume reduction of the void space.

7.1.2 Global capillary pressure-saturation curves

In this section, we consider a sample of $1\text{mm} \times 1\text{mm}$ and a thickness of $180\mu\text{m}$ which is representative for commercial GDLs [131]. Again, the sample is generated using GeoDict®[98] with a voxel size of $0.5\mu\text{m}$. We specify the fiber orientation by an anisotropic direction specification with anisotropy parameter 3 for both directions and add 3% binder with a contact angle of 20° between binder and fiber. The considered sample is visualized in Figure 7.6.

On this sample, we analyze the macroscopic behavior of the porous GDL based on the pore-scale network properties. In Figure 7.7, the stationary global capillary pressure-saturation relation is shown. S_w denotes the global wetting-phase saturation, which is the sum of the air volume in all pore bodies divided by the volume of the total void space of the porous GDL. The global capillary pressure is the difference between the non-wetting phase pressure (water) at bottom side of the GDL and the wetting phase

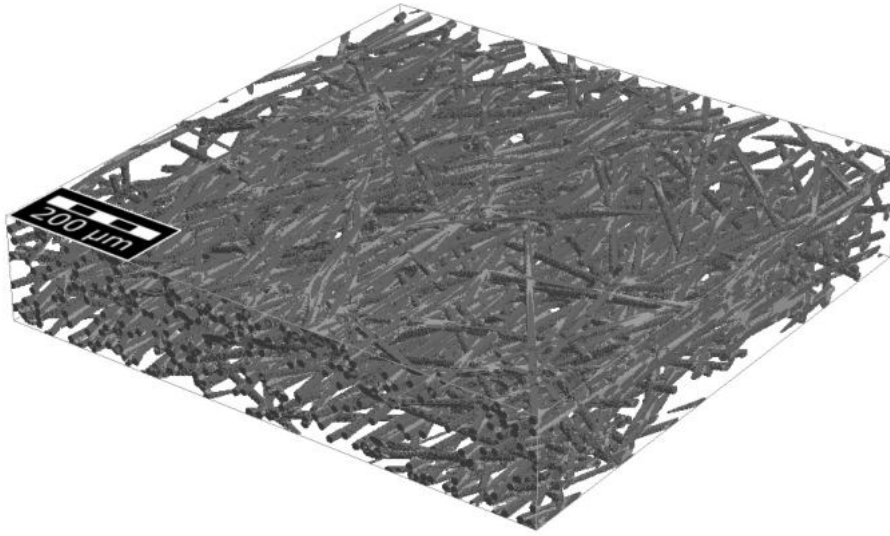


Figure 7.6: 1mm×1mm sample of a MPL-free GDL or GDB structure generated using GeoDict®[98]

pressure (air) at the top side of the GDL. The stationary $P_c - S_w$ curve results from step-wise simulation applying different global capillary pressures and calculating the global saturation at equilibrium. It can be seen, to get a low wetting phase saturation, which means a high water content in the GDL, very high global capillary pressures need to be applied. During operating conditions of a PEM fuel cell, such high pressures do not occur. This shows that the GDL cannot be flooded based on external fluid pressures during fuel cell operation. Figure 7.7 also presents a zoom into the relevant pressure range to show the behavior of the $P_c - S_w$ curve for lower water content.

In Figure 7.8, the water pattern at equilibrium corresponding to a global capillary pressure between bottom and top side of $P_c = 5050$ Pa. At this moderate global capillary pressure only the large pores are filled with water while the smaller ones are filled with air. In the largest pores the highest water content is present.

Nevertheless, the local saturation does not only depend on the pore sizes but also if the pores can be reached by the water through the throats. Therefore, the capillary entry pressure needs to be overcome to invade a throat. In Figure 7.9, the invasion state of the throats is shown. It can be seen that many throats cannot be passed by the water such that the connected pores won't be reached at this global capillary pressure. Once a throat is invaded, the connected pores are filled with water. This rises the local capillary pressure in a pore body and determines whether additional throats can be

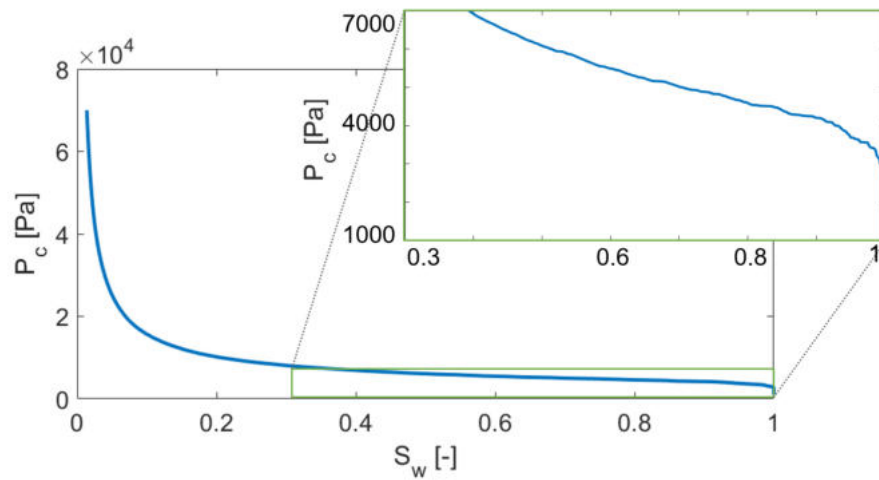


Figure 7.7: Global static capillary pressure-saturation relation of a network which represents a MPL-free GDL or GDB structure. Right: zoom in the relevant range for PEM fuel cell operating conditions.

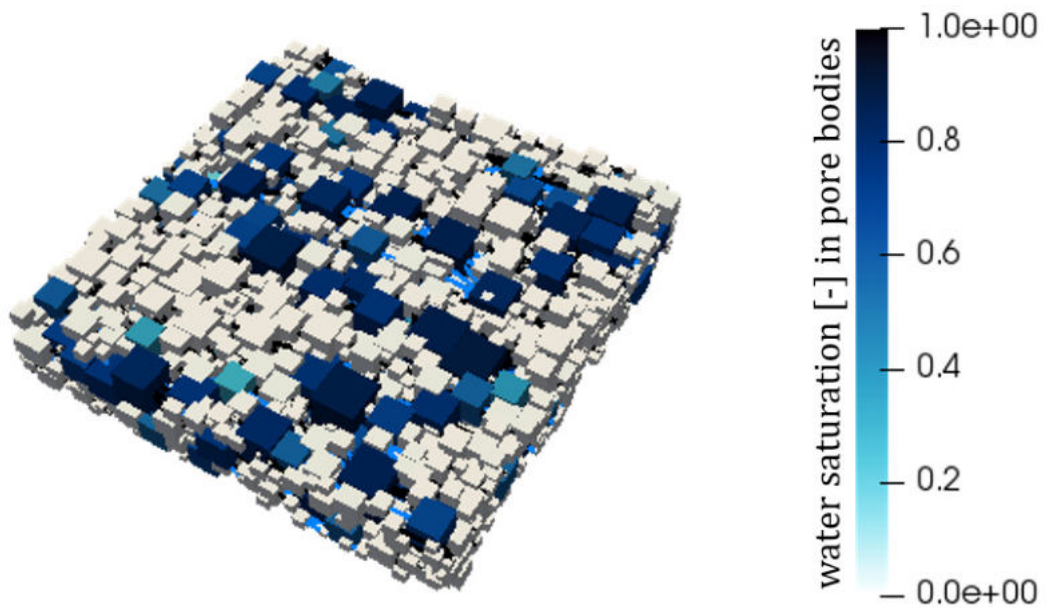


Figure 7.8: Saturation of the liquid (non-wetting) phase resulting from a stationary simulation with a global capillary pressure $P_c = 5050$ Pa.

invaded. Therefore, the capillary entry pressure of the connected throats is compared to the local capillary pressure in the pore body. This procedure is repeated until an equilibrium state is reached. The equilibrium invasion state corresponding to a global capillary pressure of $P_c = 5000$ Pa is shown in Figure 7.9.

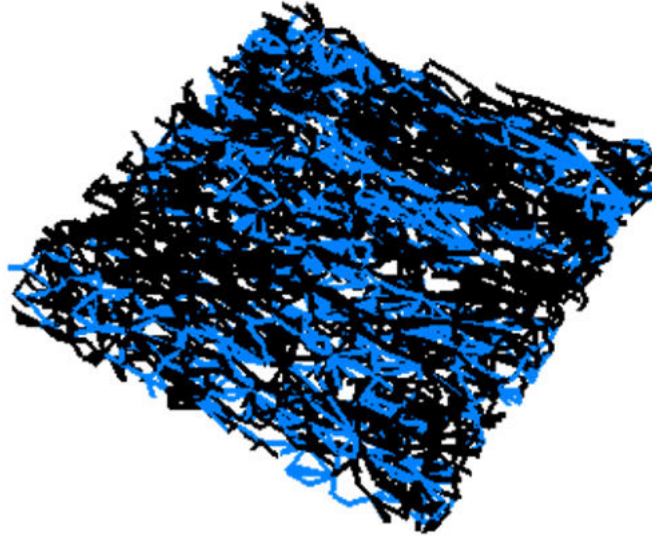


Figure 7.9: Pore throats invaded by the non-wetting phase resulting from a stationary simulation with a global capillary pressure $P_c = 5050$ Pa.

As discussed in the previous section, the throat shape has an influence on the flow through the pore-network. The throat shape and the contact angle are local material properties that influence the capillary entry pressure (see Eq. (3.21)) and the conductivity (see Eq. (3.16)) of the pore throats. In Figure 7.10, global $P_c - S_w$ curves for pore-networks representing the GDL structure in Figure 7.6 are shown. For the different curves either a square cross-sectional shape for the throats is applied or an equilateral triangle. Additionally the contact angle is varied between 180° and 142° (both measured from the liquid phase).

In pore-network models, often a contact angle of 180° is applied assuming perfectly wetting behavior of the gas phase [44, 132]. The results in Figure 7.10 show the relevance of applying an accurate contact angle. For GDLs a contact angle between 110° and 150° [133, 134] has been measured dependent on the manufacturer and GDL types. Using square throat shapes, the minimal possible contact angle for the pore-network is 145° . For equilateral triangles, contact angles down to 120° can be applied. The $P_c - S_w$ curves in Figure 7.10 show that the contact angle has a stronger influence than the throat shape. Therefore, it is suggested to adapt the throat shape away from the optimum if necessary to apply a better fitting contact angle.

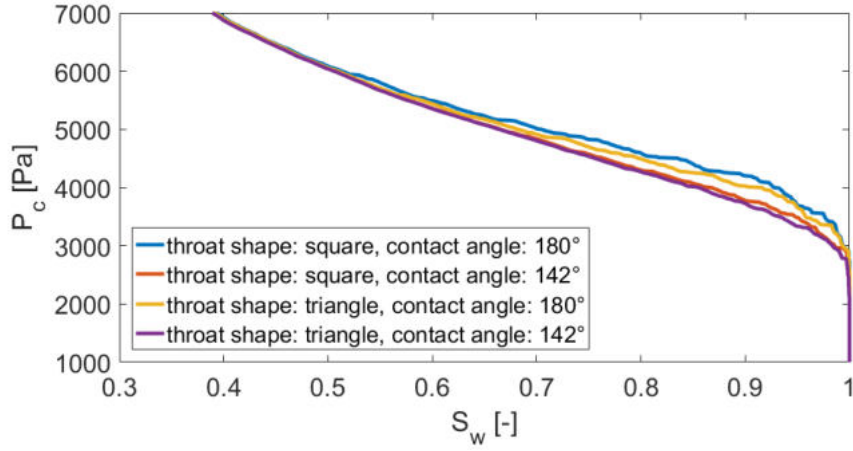


Figure 7.10: Dependence of the static capillary pressure-saturation relation on the throat shape and the contact angle

7.1.3 Influence of local contact-angle variations

In this section, we analyze the influence of the contact angle on the water distribution in a GDL sample. Therefore, a GDL sample of $2\text{ mm} \times 2\text{ mm}$ is generated using GeoDict®[98] and a pore-network is extracted using PoreSpy [99].

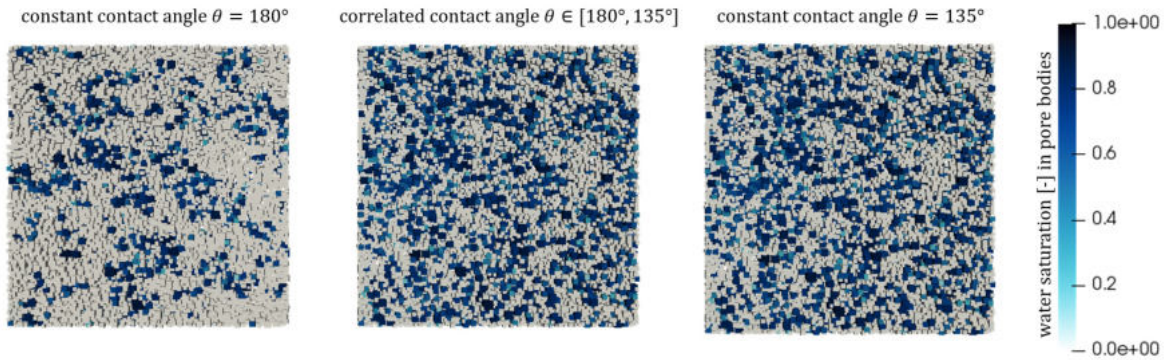


Figure 7.11: Pore-network representation of MPL-free GDL or GDB structures. Left: with a constant contact angle in all throats ($\theta = 180^\circ$), center: contact angles in the throats dependent on the throat inscribed radius ($\theta \in [180^\circ, 135^\circ]$). The larger the throat cross-section, the more hydrophobic it is chosen. Right: with a constant contact angle in all throats ($\theta = 135^\circ$).

A cubic pore shape is chosen for the pore bodies. For the pore throats, we use equilateral triangles for the cross-sectional area. In Figure 7.11, the water distribution resulting from a global capillary pressure of $P_c = 4060\text{ Pa}$ is visualized. On the left side, we see a

perfectly wetting pore-network with homogeneous contact angle $\theta = 180^\circ$. On the right side, a homogeneous contact angle $\theta = 135^\circ$ is applied. The water distribution is again visualized for $P_c = 4060$ Pa. The lower contact angle results in lower capillary entry pressures for the pore throats. Therefore, more pore bodies can be invaded at lower global capillary pressures which results in a higher global saturation in Figure 7.11. In the center, a contact angle distribution is applied to the pore-network. The local contact angles in the pore throats are between 135° and 180° and are correlated to the pore throat inscribed radii. As discussed earlier, a GDL material is coated with PTFE using a chemical dip tank. It is likely that the coating fluid does not reach the smallest pore throats which results in locally lower contact angles. Therefore, we correlate the contact angle with the pore throat inscribed radius with a linear distribution. The lowest contact angles are applied to the largest pore throats and vice versa. The resulting water distribution looks similar to the one of a homogeneous contact angle of 135° (right in Figure 7.11). The similarities indicate that the larger throats define the water distribution for the static investigation due to the lower capillary entry pressures.

In Figure 7.12, the global capillary pressure-saturation curves are visualized for the three presented cases.

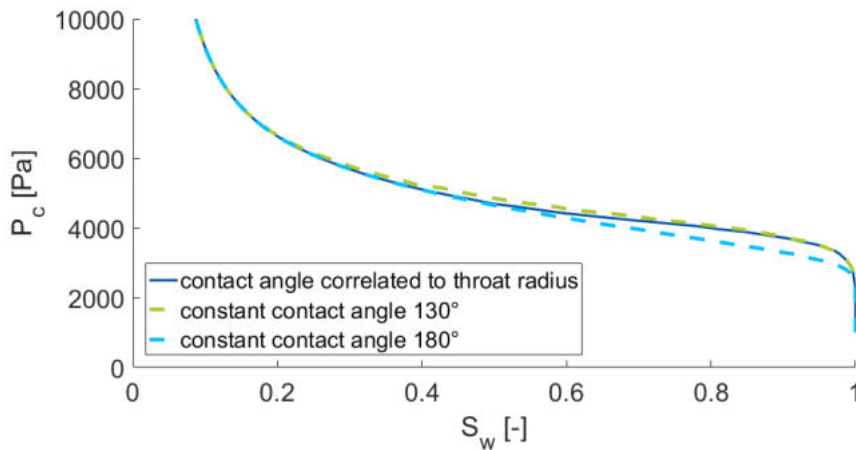


Figure 7.12: Comparison of the stationary capillary pressure-saturation curves for a GDL representation with a constant contact angle in all throats ($\theta = 135^\circ$ and $\theta = 180^\circ$) and correlated contact angles in the throats dependent on the throat inscribed radius ($\theta \in [180^\circ, 135^\circ]$) (the larger the throat cross-section, the more hydrophobic).

The curve of the pore-network with distributed contact angle is located between the

curves with constant contact angle. The curves differ in particular at high wetting-phase (gas) saturations. Here, the distributed contact angle case almost matches with the curve of lower contact angle ($\theta = 135^\circ$). This again shows that the largest pore throats with lowest capillary entry pressure define the behavior at high wetting phase (gas) saturations. The properties of these largest pore throats equal the ones in the homogeneous network with $\theta = 135^\circ$.

7.1.4 Discussion

For the analysis of the pore body and pore throat properties in fibrous MPL-free GDLs or GDBs, small samples of $200\ \mu\text{m} \times 200\ \mu\text{m} \times 200\ \mu\text{m}$ are used. The small sample size allows an analysis of the influence of image resolution and fiber orientation for the pore-network generation (see Section 3.1.4) but gives limited insights into representative properties. Therefore, for the analysis of pore-body size a larger sample of $4\ \text{mm} \times 4\ \text{mm}$ is chosen. For the investigation of the global capillary pressure-saturation relation a sample of $1\ \text{mm} \times 1\ \text{mm}$ is considered and for the contact angle variations a sample of $2\ \text{mm} \times 2\ \text{mm}$. Nevertheless, the small samples help to get an overview on the general material properties and influencing parameters.

In this thesis, the considered fiber structures are generated artificially using the software GeoDict®[98]. The artificial GDBs show a more homogeneous structure than the real counterpart. Nevertheless, the method is not restricted to these structures but can also be applied to μct -scans of real GDLs or GDBs.

The focus of this thesis is the investigation of interface processes between the GDL and gas distributor of a PEM fuel cell. It is important to understand the transport processes in both domains. The fibrous GDB structure has special properties which influence the interface processes between GDL and gas distributor. The basic properties and structural influences have been investigated in this section.

7.2 Single phase investigations of a GDL-gas distributor setup

In this section, not only the behavior of flow through a GDL-representing pore-network but also the influence of different gas distributor configurations is investigated. We use a single-phase multi-component setup, here. The model considers dry fuel cell operating conditions when no liquid water is present. We investigate the component transport of water vapor H_2O , oxygen O_2 and nitrogen N_2 through a GDL sample. Water vapor is induced on one side and oxygen is reduced corresponding to the reaction taking place in a PEM fuel cell corresponding to a current density of 1 A/cm^2 ($q_{H_2O} = 4.1457 \cdot 10^{-7} \text{ mol/s}$ and $q_{O_2} = 2.07286 \cdot 10^{-7} \text{ mol/s}$). The oxygen sink and water vapor source are applied to the whole area and distributed to the boundary pores based on the pore-body sizes. We use a container boundary condition as visualized in Figure 7.13 to properly distribute the flux.

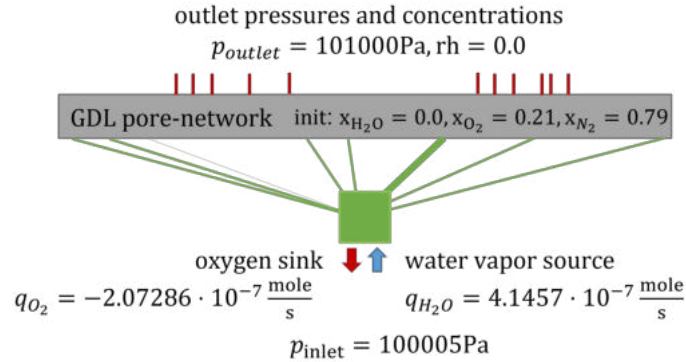


Figure 7.13: Container boundary condition which is used to distribute source and sink fluxes over the complete inlet surface area according to the pore-body sizes of the boundary pores.

On the other side, the GDL sample ($4 \text{ mm} \times 2 \text{ mm}$) shares an interface with the gas distributor which is modeled as a boundary condition. We apply zero relative humidity $rh = 0$ in the channels. The condition is implemented as a Dirichlet condition using the following relations:

$$x_{H_2O} = \frac{rh \cdot p_{sat}^{H_2O}}{p_{outlet}}, \quad (7.1)$$

$$x_{O_2} = 0.21 \cdot \left(1 - \frac{rh \cdot p_{sat}^{H_2O}}{p_{outlet}} \right). \quad (7.2)$$

Initially, no water vapor is present in the GDL pore-network and the gas configuration consists of 21% oxygen and 79% nitrogen. Between inlet and outlet, a pressure difference of 995 Pa is applied ($p_{\text{inlet}} = 101000$ Pa and $p_{\text{outlet}} = 100005$ Pa).

In Figure 7.14, the model setup is presented. We consider two channels and three ribs and distinguish between two different channel widths $W_1 > W_2$.

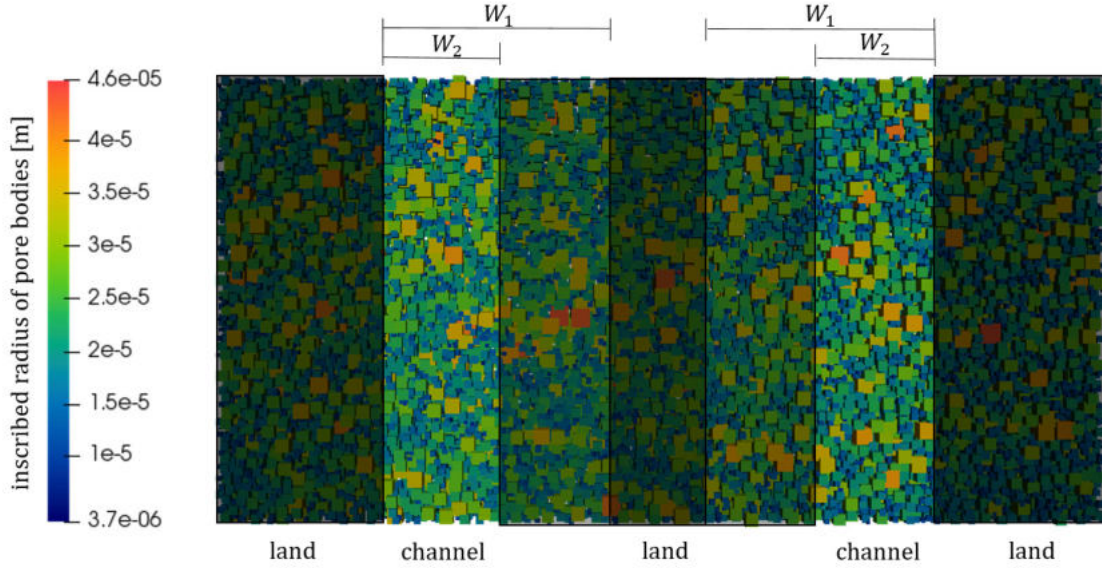


Figure 7.14: Pore sizes and gas distributor channel configurations for the single phase multi-component investigation. Three different configurations are considered: Same pressure in both channels of with $W_1 = 1$ mm, same pressure in both channels of with $W_2 = 0.5$ mm, pressure difference of 100 Pa between channels of with $W_1 = 1$ mm.

The colors of the cubic shaped pore bodies in Figure 7.14 indicate the pore sizes.

In the following three different flow simulations are performed: We consider a setup where the same pressure is set in both channels of with $W_1 = 1$ mm, one where the same pressure is applied in both channels of with $W_2 = 0.5$ mm, and a setup with a pressure difference of 100 Pa between the two channels of with $W_1 = 1$ mm.

7.2.1 Influence of the channel width on component transport

First, we consider a setup with two channels of the same width $W_1 = 1$ mm. In Figure 7.15, the water vapor distribution at the interface between GDL and gas distributor after equilibration is shown.

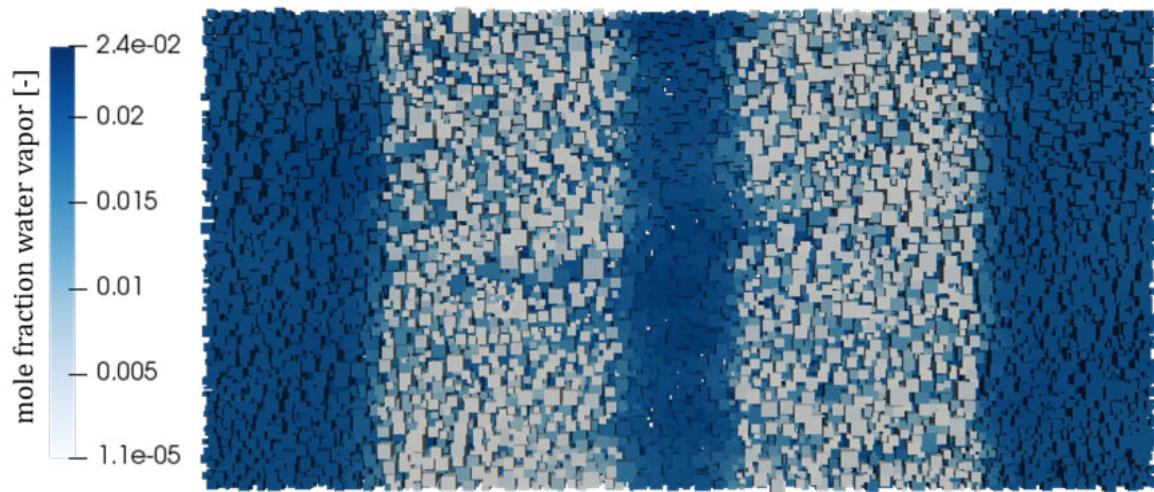


Figure 7.15: Mole fraction of water vapor at the interface between GDL and gas distributor with a gas distributor channel width of 1 mm.

We see water accumulation at the land parts where the water cannot exit the porous GDL. In the channels, the water-vapor content is lower. Also, we see no different water-vapor content at the interface to the two channels.

In Figure 7.16, the oxygen concentration at the interface to the MPL and cathode catalyst layer (CCL) is presented.

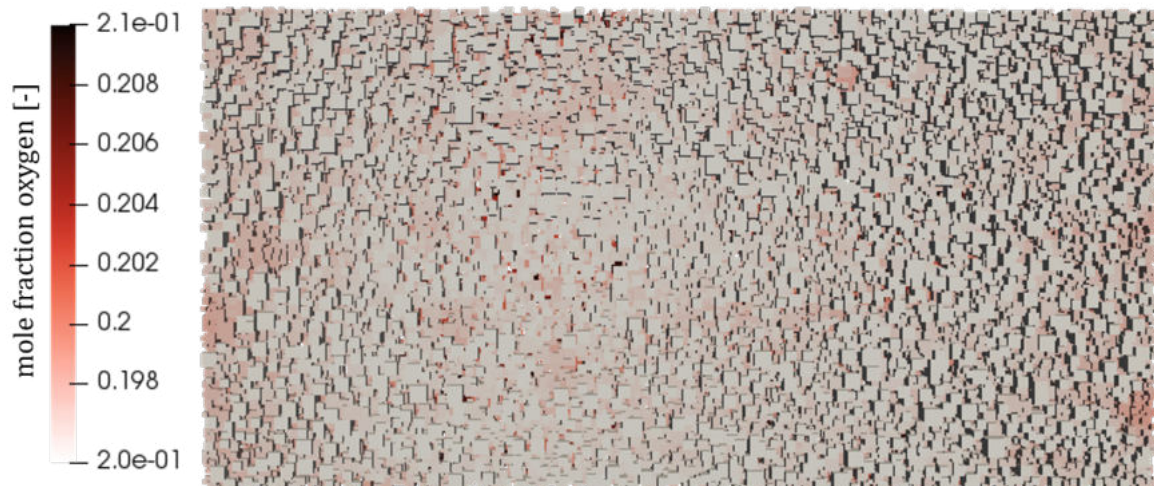


Figure 7.16: Mole fraction of oxygen at the interface between GDL and MPL/catalyst layer and a gas distributor channel width of 1 mm.

The visualization shows a homogeneous mole fraction of oxygen at the interface between MPL and GDL. The mole fraction is low compared to the rest of the pore-network due

to the oxygen sink boundary condition which represents the reactions in the catalyst layer.

Next, we investigate the influence of channel width and investigate a setup with smaller channels but of the same width $W_2 = 0.5$ mm. The applied initial and boundary conditions equal the previously presented setup with wider channels.

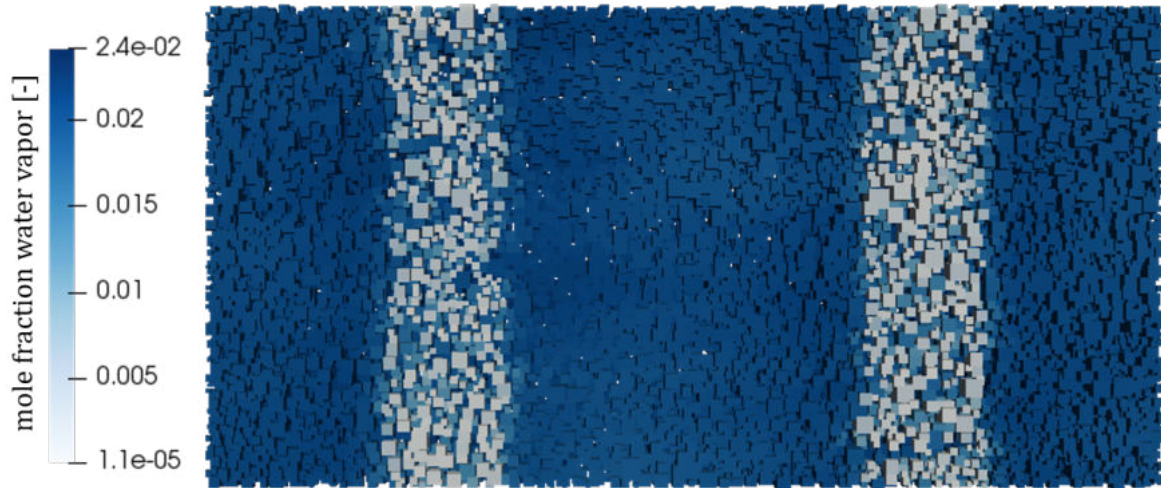


Figure 7.17: Mole fraction of water vapor at the interface between GDL and gas distributor with a gas distributor channel width of 0.5 mm.

In Figure 7.17, the water-vapor content is again presented at the interface between GDL and gas distributor. Again, the water vapor is accumulated at the land parts while the open channels show a relatively low water content at the interface pores.

In Figure 7.18, the interface to the MPL and catalyst layer corresponding to the setup with narrow channels is presented.

No differences can be observed between the two setups considering the oxygen concentration at the interface between GDL and MPL. Again the concentration is low due to the applied outflow condition for oxygen.

7.2.2 Influence of pressure difference between two gas distributor channels on component transport

In this section, the influence of different pressures in neighboring gas distributor channels on the transport through the GDL is investigated. We apply a pressure difference

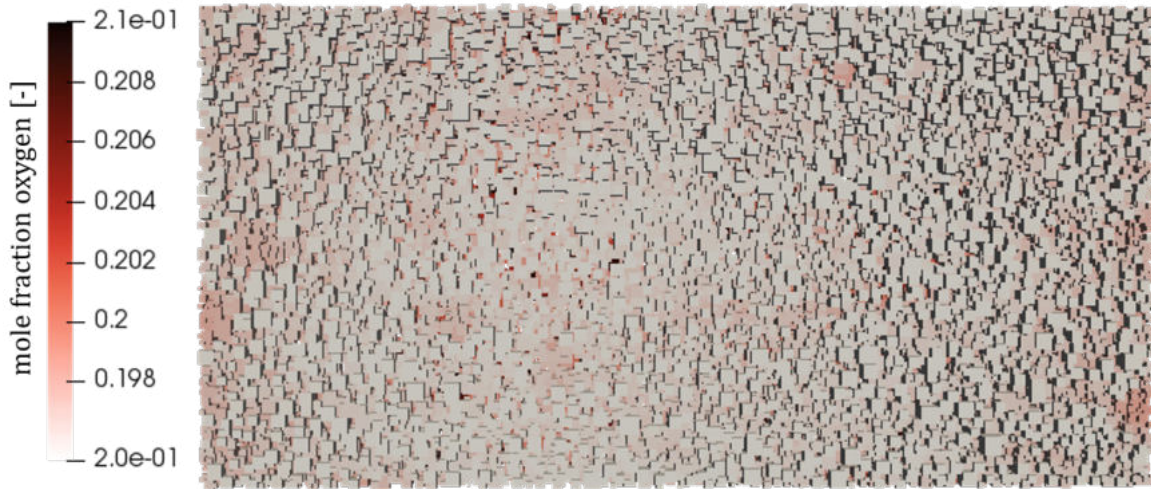


Figure 7.18: Mole fraction of oxygen at the interface between GDL and MPL/catalyst layer and a gas distributor channel width of 0.5 mm.

of 100 Pa between the channels of width $W_1 = 1$ mm and use the same initial conditions as for the previously described setups. The pressure boundary condition in the channel is modified to create the pressure difference ($p_{\text{channel},1} = 100055$ Pa and $p_{\text{channel},2} = 99955$ Pa). The inlet pressure is again $p_{\text{inlet}} = 101000$ Pa. And the source and sink terms for oxygen and water correspond again to a current density of 1 A/cm^2 . Different pressures in the gas distributor channels of a PEM fuel cell might result from fabrication differences or local blockage of one of the channels.

In Figure 7.19, the water vapor concentration at the interface between GDL and gas distributor is visualized after equilibration.

We see a clear difference in the water-vapor content between the two channels. In both channels, the pore bodies directly connected to the outlet condition pores in both channels have a low mole fraction of water vapor. But in the left channel, where a higher pressure is applied also the neighboring pores near the channel interface show a low water-vapor content. Here, we see a clear influence of the pressure difference between the channels of a gas distributor on the transport in the GDL.

In Figure 7.20, the oxygen concentration at the interface to the MPL and CCL is shown. An inhomogeneous distribution of oxygen is visible. On the right side, a higher oxygen concentration is available. The reactions taking place in the CCL can only produce electric current if enough reactants are available. An inhomogeneous distribution of the reactants results in inhomogeneous production rates and an inefficient productivity of

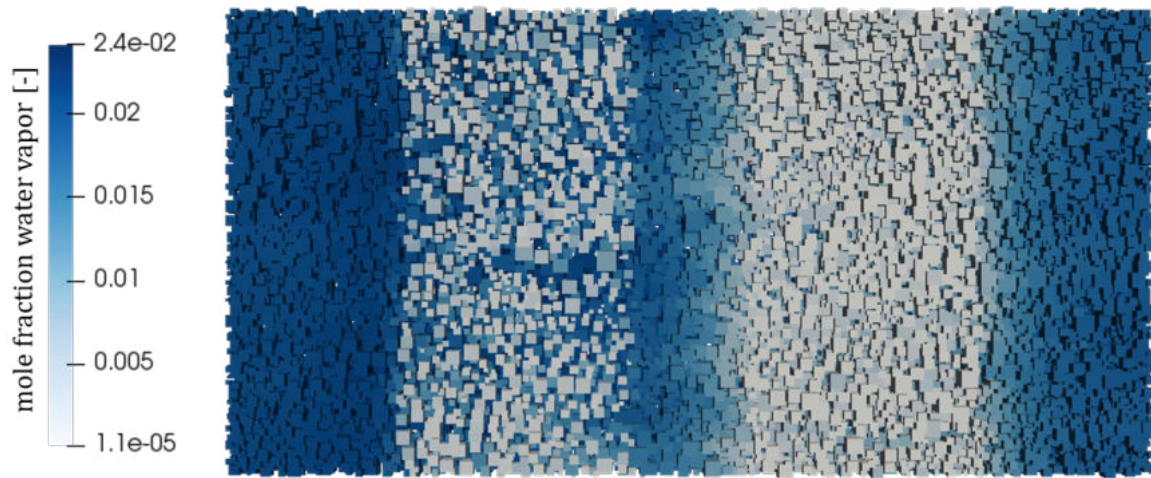


Figure 7.19: Mole fraction of water vapor at the interface between GDL and gas distributor with a gas distributor channel width of 1 mm with a pressure difference of 100 Pa.



Figure 7.20: Mole fraction of oxygen at the interface between GDL and MPL/catalyst layer and a gas distributor channel width of 1 mm with a pressure difference of 100 Pa.

the PEM fuel cell. Therefore, it is important to reduce pressure differences between the single gas distributor channels over time. Short fluctuations cannot be prevented but with a detailed fabrication and well controlled operating conditions, long-term pressure differences can be prevented to ensure a homogeneous distributions of the reactants at the interface to the MPL and cathode catalyst layer.

7.2.3 Discussion

The single-phase investigations represent transport through an MPL-free GDL or GDB influenced by reactions in the CCL and the structural and flow properties of the gas distributor. The range of representable operating conditions is limited for the single-phase model but gives insights into the behavior at low current densities.

The results show that the channel width has only a minor influence at low current densities and dry operating conditions, when single-phase transport is expected. It is important to keep as much open area as possible at the interface between GDL and gas distributor to prevent water accumulation and a good exchange of reactant and produced gases between GDL and gas distributor.

Two-phase models capable to capture the interface processes are necessary to represent a wider range of operating conditions in a PEM fuel cell cathode. These two-phase investigations including different interface configurations are presented in the following section.

8 Simulation results of the uncoupled interface configurations occurring at the interface between GDL and gas distributor

In this chapter, we consider two-phase flow in pore-network models, where the previously developed interface conditions are applied as boundary conditions. Here, the pore-network models are not coupled with a free flow or REV model yet but the influence of a second domain (e.g. gas distributor of PEM fuel cell) on the flow in a porous domain (e.g. MPL-free GDL or GDB in PEM fuel cell) is captured in a simplified way.

8.1 Pore-network model including droplets at the porous surface¹

We start with the application of the developed drop concept on exemplary pore-network models.

¹Portions of this section are part of the publication *Two-phase flow dynamics at the interface between GDL and gas distributor channel using a pore-network model* by Michalkowski et al. that has been submitted to *Transport in Porous Media* by Springer in 2022.

8.1.1 Formation, growth and detachment of a single droplet

First the formation, growth and detachment of a single droplet is analyzed and compared to available data in the literature.

Drop growth without surrounding gas flow

In this section, we compare the drop growth behavior of the developed model to experimental data and a comparable drop model previously presented in the literature. Both data sets are presented by Ackermann et al. in [101]. We analyze the droplet behavior without any surrounding gas flow. Similar to the REV scale model presented in [101], a very simple setup is used to analyze the growth of a single droplet (see Figure 8.1).

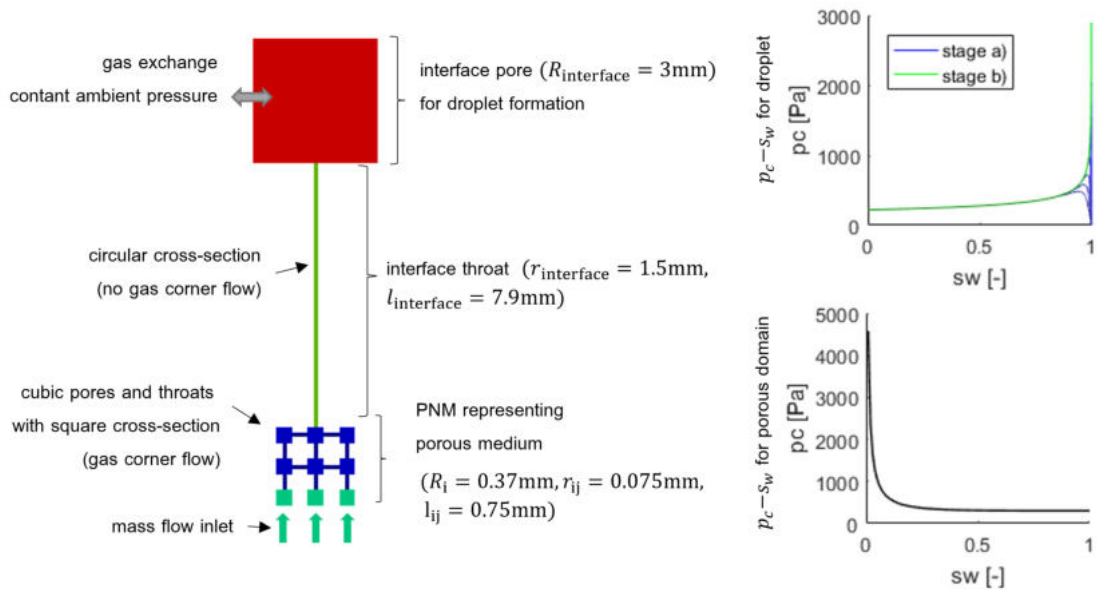


Figure 8.1: Setup to analyze a single droplet forming in the interface pore of the pore-network model. green pores: inlet pores ($R_i = 3.7 \cdot 10^{-4} \text{ m}$), red pore: interface pore ($R_{\text{interface}} = 3 \cdot 10^{-3} \text{ m}$), green throat: drop-feeding throat ($r_{\text{interface}} = 1.5 \cdot 10^{-3} \text{ m}$), dark blue throats: network throats ($r_{ij} = 7.5 \cdot 10^{-5} \text{ m}$). On the right side, the local capillary pressure-saturation relations are visualized. Top: interface pore with two stages of drop growth, bottom: regular network pore in hydrophobic porous medium.

On the right side in Figure 8.1, the local capillary pressure-saturation relations of the

pores in the network are visualized. The curve on the top shows the relation corresponding to the interface pore (red) with the two stages of drop growth. The shape depends on the radius of the interface throat (green). The relation shown at the bottom of the figure represents the local capillary pressure-saturation relation of a regular network pore in hydrophobic porous medium. This relation is applied to the network at the bottom of the single tube setup (blue and green pores).

The model setup is designed as a mixture of the REV framework in [101] (the authors denote the framework as Darcy framework) and the experimental setup described in [101]. The feeding throat for the interface pore equals the tube used in the experiment and a pore-network is applied to represent the porous domain of the Darcy model, where the inlet condition is applied. For the pore-network, a completely homogeneous two-dimensional network is chosen with pore body inscribed radii of $R_i = 3.7 \cdot 10^{-4}$ m, pore throat inscribed radii $r_{ij} = 7.5 \cdot 10^{-5}$ m and pore throat length $l_{ij} = 7.5 \cdot 10^{-4}$ m. The feeding tube in the experiment has a length of 7.9 mm and a radius of 1.5 mm. Therefore, the feeding throat in the pore-network model is chosen accordingly ($l_{\text{interface}} = 7.9 \cdot 10^{-3}$ m, $r_{\text{interface}} = 1.5 \cdot 10^{-3}$ m). The interface pore is large enough to capture a droplet up to 2.5 mm as it is expected from the experiment and Darcy model ($R_{\text{interface}} = 3 \cdot 10^{-3}$ m).

The comparison of the droplet growth considering the drop radius in time shows very good agreement between the pore-network model (solid lines in Figure 8.2) and the experimental data (black dots in Figure 8.2). A change in the initial saturation of the pore-network result in a time shifting of the curve. With a lower initial saturation ($s_{n,\text{init}} = 0.95$), the drop formation starts a little later. This results from the capillary entry pressure which has to be overcome to invade the droplet feeding interface throat. Therefore, the pore-network is filled first before the droplet starts forming. A perfect match of the numerical data (in Figure 8.2: Darcy model blue dots, pore-network model solid lines) is achieved, using an initial water saturation $s_{n,\text{init}} = 1.0$ (fully saturated).

Drop detachment from a single tube by drag force from surrounding gas flow

In this section, we compare the developed drop detachment criterion with available concepts from the literature and with a CFD volume of fluid (VoF) simulation of a droplet emerging from a single tube in a channel. A flow velocity is applied to the upstream end of the channel such that a drag force from a parabolic gas flow profile acts

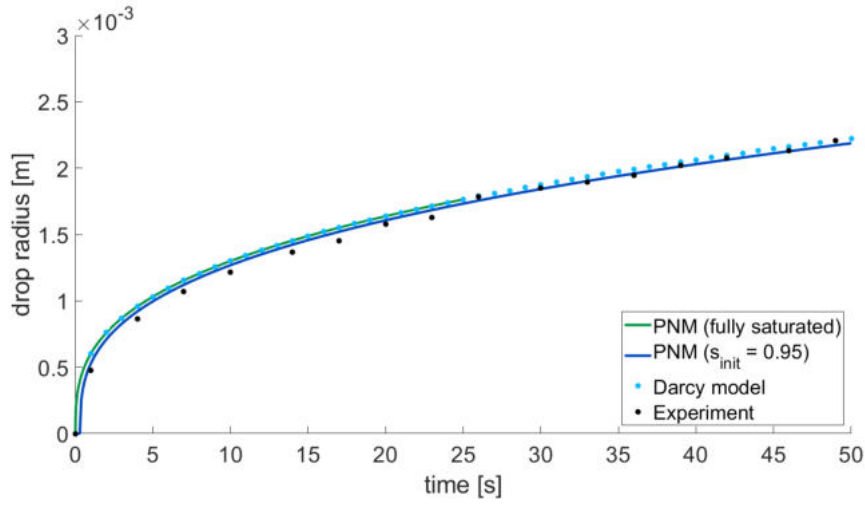


Figure 8.2: Drop radii from PNM simulations with different initial saturations (fully saturated: $s_{\text{init,water}} = 1.0$, $s_{\text{init,water}} = 0.95$) and Darcy simulation calculated by Ackermann et al. [101]

on the droplet causing its deformation and finally detachment. We use the commercial software ANSYS Fluent for the investigations. The VoF model setup is presented in Figure 8.3.

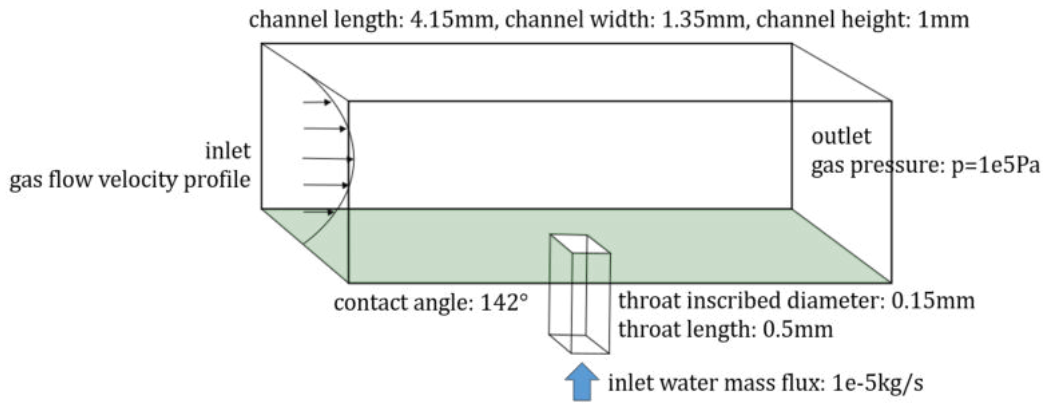


Figure 8.3: Setup of the CFD simulation performed using Ansys Fluent R2019. Gas channel with parabolic gas flow velocity inlet and pressure outlet. In the center, water is injected through a throat with a mass flux boundary conditions. The drops form inside the channel and are deformed and detached by the surrounding gas flow.

A channel of length $L = 4.15\text{mm}$, width $W = 1.35\text{mm}$ and height $H = 1\text{mm}$ has been analyzed with a two-phase VoF model without phase change (immiscible phases) as implemented in ANSYS Fluent version R2019. A filling throat with square cross-sectional area is connected to the channel as shown in Fig.8.3. The square cross-sectional shape

of the filling throat is chosen to simplify the meshing of the domain. Since a mass flux boundary condition is applied to the complete inlet face of the throat (volume fraction of water equals 1), no wetting phase flow (corner flow) can form in this throat and the square shape has only a minor influence on the drop formation. The equilibrium contact angle of water with the solid surface is 142° at the bottom of the channel (green in Fig.8.3) and the filling throat which represents GDL properties. Hydrophilic surfaces are applied to the other channel walls such that the liquid water is attached to the wall in case of contact. This has no influence on the drop formation, growth and detachment in the considered cases. No contact-angle hysteresis is implemented. The droplet deformation results from local forces at the drop surfaces. At the channel inlet, air is injected into the channel with a fully developed laminar flow with a parabolic velocity profile [135]:

$$v(y, z) = \max(v_{gas})^{inlet} \cdot \left(1 - \left(\frac{|y-a|}{a}\right)^2\right) \cdot \left(1 - \left(\frac{|z|}{b}\right)^{2.3}\right)$$

where, a and b are half of the width and height of the channel, respectively. Atmospheric conditions (pressure boundary condition) are applied at the channel outlet and water back-flow of the liquid phase is permitted in the ANSYS Fluent model.

Water is injected into the throat at a constant mass flow rate of $\dot{m} = 10^{-5} kg/s$. Droplets form and grow in the channel filled by the throat. Finally, the droplets detach due to the forces resulting from the gas flow in the channel.

We investigate the droplet radius based on the volume of the detached droplet. Therefore, we consider the drop as a sphere segment. The radius and volume based on the contact area CA and the contact angle θ are given by:

$$r_{drop} = \frac{h_{drop}}{1 - \cos \theta} = \frac{d_{CA}}{2 \sin \theta} \quad (8.1)$$

$$V_{drop} = \frac{\pi}{3} h_{drop}^2 (3r_{drop} - h_{drop}) = \frac{\pi}{3} \left(\frac{d_{CA}}{2}\right)^3 \frac{(1 - \cos(\theta))^2 (2 + \cos(\theta))}{(\sin(\theta))^3} \quad (8.2)$$

r_{drop} is the radius of the drop curvature, h_{drop} is the drop height, V_{drop} is the volume corresponding to the sphere cap shaped (undeformed) droplet and d_{CA} is the diameter of the contact area between liquid and solid. From the VoF Simulation, we measure the drop volume and calculate the corresponding drop radius for the comparison.

Since, we are interested in an appropriate detachment criterion, we analyze the *separa-*

tion line which gives the critical mean velocity at which a droplet with a certain radius will be detached. In Figure 8.4, six different approaches to determine the critical velocity for drop detachment are visualized. Kumbur et al. [115] expound a two-dimensional

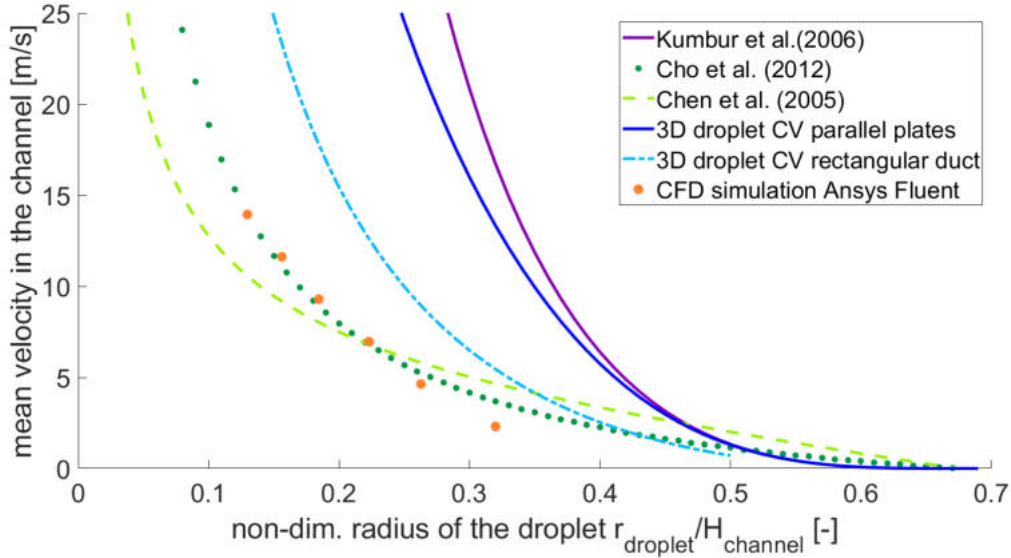


Figure 8.4: Detachment lines from different derivation approaches. Minimal average velocity for detachment with respect to non-dimensionalized drop radius (non-dimensionalized with respect to the channel height H_{channel}). Solid lines: completely analytical derivation, stars: numerical calculation, dashed/dotted lines: empirical and mixed approaches.

(2D) description of the force balance around a droplet on a solid surface which is influenced by surrounding gas flow. In the retention force, the authors include the contact angle hysteresis, and in the drag force, the pressure and shear forces at the top of the droplet are taken into account. The resulting detachment or separation line is based on the balance of these two forces. The droplet is detached once the drag force exceeds the retention force. The 2D approximation represents an infinitely wide channel (parallel plates) but also an infinitely wide droplet (deformed cylindrical shape) such that shear forces at the sides of the droplet are not included. The model presented by Kumbur et al. [115] is derived completely analytical. In contrast, Chen et al. [116] developed a semi-analytical approach by using an experimental fitting for the drag coefficient c_D . The used experiment for the fitting represents an ex-situ PEMFC cathode setup. For the retention force, they use a similar approach than Kumbur et al. [115]. Cho et al. [117] extended the concept presented in [116] by further developing the contact angle formulation along the contact line. For the drag force Cho et al. [117] use the same

drag coefficient formulation as Chen et al. [116]. These empirical approaches are plotted with dotted and dashed lines in Figure 8.4 while completely analytical approaches are visualized with solid lines. We have derived an extension of the analytic model of Kumbur et al. [115] which considers a spherical droplet in an infinite wide channel rather than a cylindrical shape. In this case, the shear force at the sides of the spherical droplet are included. For the derivation of the separation line, a control volume (CV) is placed around the droplet in the channel. At the top surface of the CV the top shear force is calculated similar to the approach presented by Kumbur et al. [115]. Additionally, the shear forces at the sides of the droplets are taken into account which allows the consideration of a spherical drop in the wide channel. The resulting separation line of this extension is shown by the dark blue line (3D droplet CV parallel plates). In the concept resulting in the dashed, light blue line (3D droplet CV rectangular ducts), we additionally considered the reduction of the cross-sectional area due to the droplet. Therefore, we developed the reduction factor in Eq. (4.20) that allows arbitrary aspect ratios of the channel. The detailed derivations of the CV approaches are presented in Section 4.2.2.

The orange dots show the detachment evaluations of six different VoF simulations with the corresponding mean gas flow velocity resulting from an inlet condition with parabolic flow profile. The lowest mean velocity analyzed is $\bar{v} = 2.32\text{m/s}$ (corresponding $v_{\text{max}} = 5\text{m/s}$). At lower gas flow velocity, no detachment due to the gas flow drag force occurred but the droplet touched the channel walls which are chosen hydrophilic. Higher gas flow velocities than $v_{\text{mean}} = 13.94\text{m/s}$ (corresponding $v_{\text{max}} = 30\text{m/s}$) have not been analyzed since their occurrence in the cathode PEMFC channels is unlikely. Especially for low gas flow velocities the VoF simulation results differ from the other data resulting in smaller drop sizes at detachment.

Overall, the data lines in Figure 8.4 spread widely. For the analytic derivations inaccuracies result from the chosen simplifications while for the empirical approaches the uncertainty of the data is more difficult to determine. The differences to the VoF simulation might result from the different detachment criteria. In the used ANSYS Fluent model no contact angle hysteresis is implemented. In the presented pore-network model, the droplet detachment occurs once the drag force exceeds the retention force based on the contact angle hysteresis. This means, the droplet is detached once the three-phase contact line starts to move. In the ANSYS Fluent model, the three-phase contact line can move freely on the smooth surface but the droplet stays attached to the interface throat. A surface tension force holds the liquid phase together while maintaining the

minimum possible surface area of the droplet. Here, the droplet detaches once drag force overcomes this surface tension force and the droplet is teared off from the liquid water in the interface throat.

Further investigations are necessary to determine the "correct" separation line and reduce the uncertainties.

For the pore-network drop model, we choose the analytic CV approach derived for three-dimensional rectangular channels (3D droplet CV rectangular duct). The approach is based on a force balance (see Section 4.2.2) and clear assumptions and simplifications which can be adapted if further knowledge on the system is available.

8.1.2 Formation, growth and detachment of multiple droplets in a system

In this section, the ability of the developed model to simulate the formation, growth and detachment of several droplets at the interface between a porous domain and a free-flow domain is shown and compared to experimental findings from the literature.

Comparison with experimental data

Quesnel et al. present experimental investigations of multi-drop interactions in their publication [6]. They explain the growth behavior of several droplets forming at an interface from feeding throats of different size. Due to the capillary pressure changes in the droplet during the growth, the initially faster growing droplets are favored and are fed by the surrounding smaller droplets which decrease as a result. This is caused by the non-monotonic capillary pressure curve.

They also present the so called *bulging menisci model* which is similar to a common *bundle-of-tubes model*, but the volume of fluid in the tubes themselves only considers the inflating and deflating of menisci with time [6]. In Figure 8.5, the interactive behavior of the forming droplets is visualized. For details on the model, it is referred to the developers [6].

The bulging menisci model explains the behavior of the drops forming on a GDL surface by simplifying the geometrical setup to straight tubes rather than the complex fiber structure.

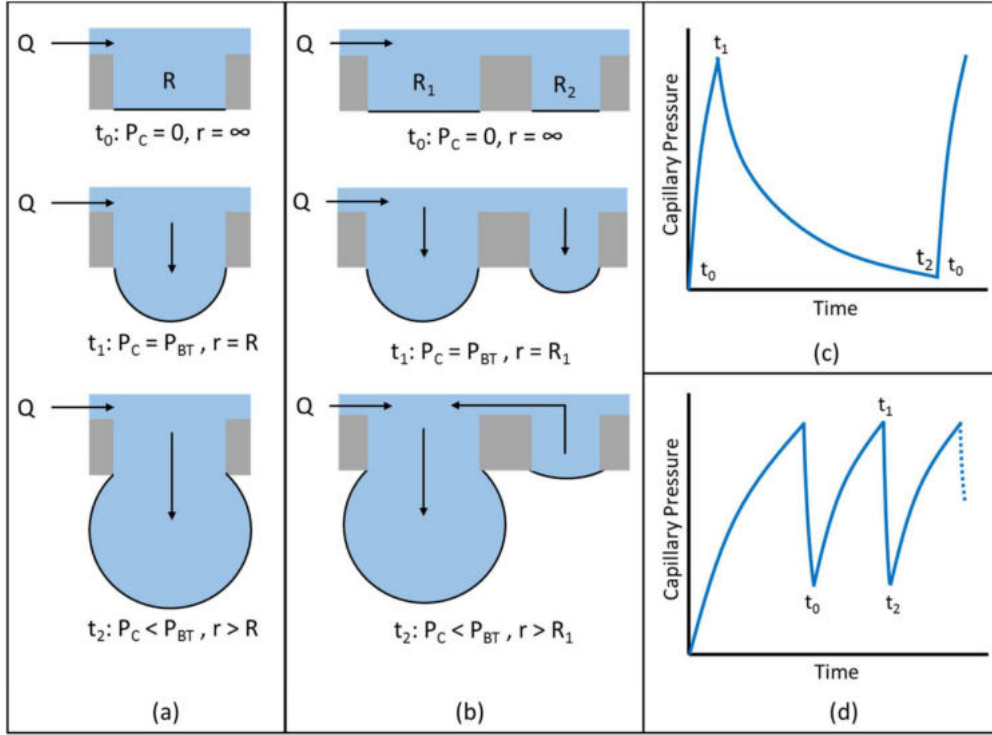


Figure 8.5: Bulging menisci model: Schematic of pressure profiles observed during droplet grow-detachment cycle. (a) Single tube, (b) Multiple tubes with a single breakthrough site, (c) Pressure profile for the single tube, (d) Pressure profile for the multi-tube system [6].

In this section, we show that the interactive behavior of multiple droplets in the system is automatically included in the developed model. Therefore, we use a simplified geometry and consider a setup with 2, 16 and 101 tubes (see Figure 8.6).

For the two-drop interaction, we consider two interface pores which are connected by an interface throat to the network. The two interface throats have a different size such that one of them will be favored during the drop growth caused by the flow resistance in the throat ($r_{\text{interface},1} = 2 \cdot 10^{-5} \text{ m}$ and $r_{\text{interface},2} = 1.8 \cdot 10^{-5} \text{ m}$). The network pores are much smaller than the interface pores ($R_{\text{network}} = 5 \cdot 10^{-5} \text{ m}$ and $R_{\text{interface}} = 5 \cdot 10^{-4} \text{ m}$) to prevent water storage in the network. The network pores are connected with wide, short throats ($r_{ij,\text{horizontal}} = 3 \cdot 10^{-5} \text{ m}$, $l_{ij,\text{horizontal}} = 1 \cdot 10^{-5} \text{ m}$) to ensure a fast exchange (large flux) between the forming droplets. As inlet condition a water mass flux is applied to the inlet pore. The gas-phase pressure in the interface pores is kept constant by a Dirichlet boundary condition.

For the setup with 16 interface pores, not only two but 16 interface pores are places

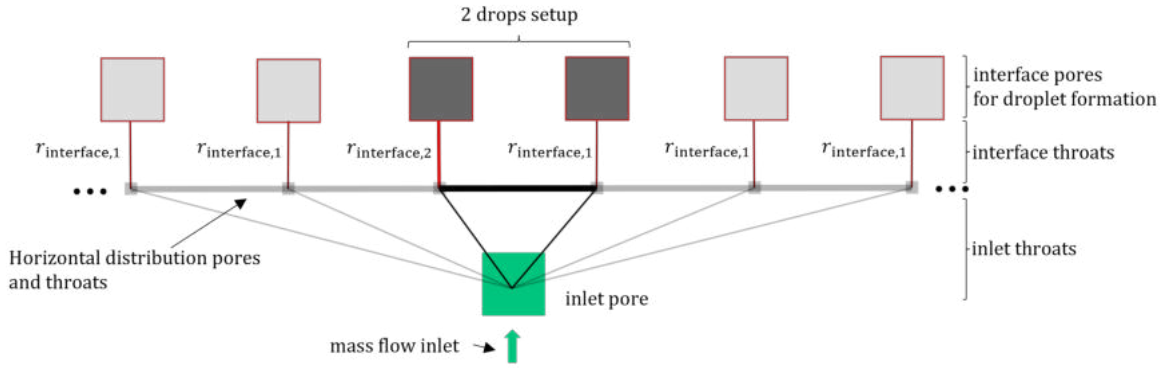


Figure 8.6: Geometric pore-network configurations to analyze the interactive behavior of several drops in a multi-tube system. Different configurations have been analyzed: 2 pores, 16 pores, 101 pores.

next to each other. Again, one interface throat is larger than the other ones to be favored during the drop growth. For the setup with 101 interface pores, ten interface throats are chosen to be larger than the rest. Since inertial forces are negligible for the creeping flow in the network, the position of the interface pores is not important.

In Figure 8.7, the drop radius and corresponding local capillary pressure in the interface pores are shown for the two-interface-pores investigation. It can be seen how both droplets start growing but then one of them is favored while the other drop volume is decreasing. The favored droplet growing rate increases with the shrinkage of the other one since the volume of drop 1 is transferred to drop 2. The local capillary pressure curves in Figure 8.7 explain why drop two is favored. The larger drop volume results in a smaller curvature and therefore a lower pressure in the droplet. The gas phase pressure is kept constant such that the shape of the curves equals the one of the water pressure in the droplet. In Figure 8.8, the water pressure in the inlet pore of the two-interface-pores setup is shown. The shape is similar to the capillary pressure in the interface pores. The fluctuations at the lower level, when the drop volume of the favored drop increases while the other one stays constant, result from numerical instabilities in the small dynamic network.

With a constant gas phase pressure in the drop pores, the shape of the curve equals the global capillary pressure ($P_{c,global} = p_{liq, inlet} - p_{gas, drop}$).

Therefore, the interaction of only two droplets in the simple network is not sufficient to explain the change in the global capillary pressure behavior in Figure 8.5. In the experiments in [6], a GDL structure is used where more than two droplet occurred and interacted. In the next step, a network with 16 parallel interface pores is analyzed.

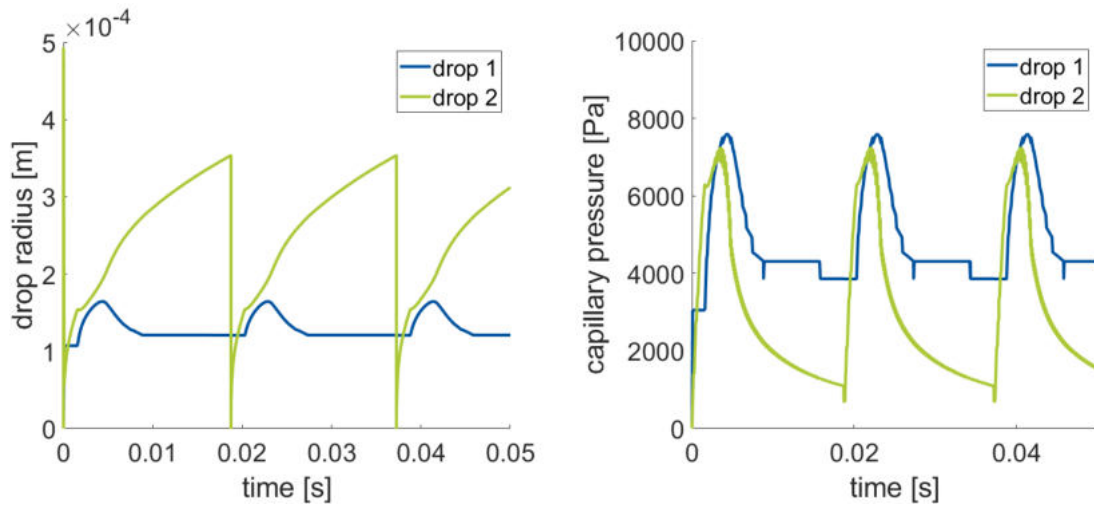


Figure 8.7: Two-drop interaction. Left: drop radius evolution with time of the droplets forming at the two different interface throats. Right: Corresponding capillary pressure of the droplets (capillary pressure is defined by the interface curvature of the drop surface).

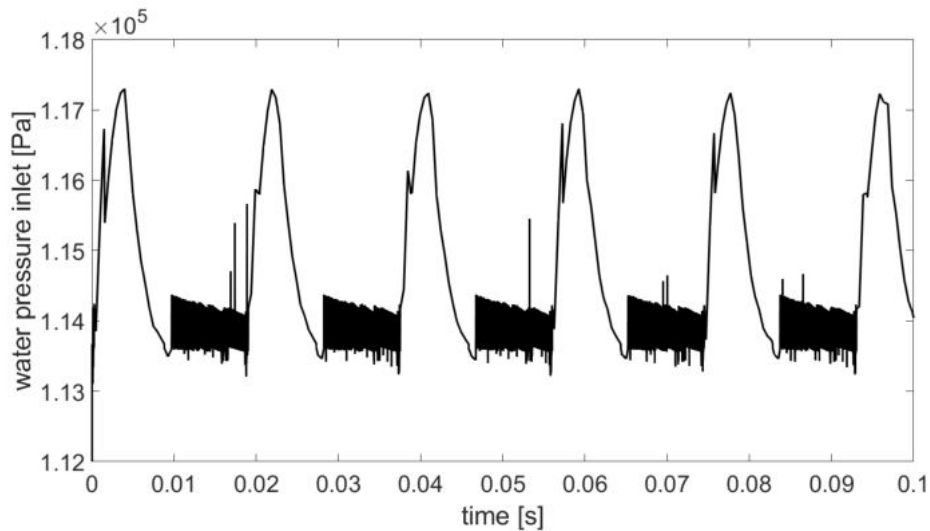


Figure 8.8: Water pressure in the inlet pore of a multi-tube setup with two interface throats to fill droplets and two connected interface pores for droplets to grow in.

Again, one interface pore is chosen to be favored by connecting it with a larger interface throat. In Figure 8.9, two droplets in the network with 16 interface pores are compared. The drop radius shows a similar behavior than in the two-interface-pores setup. However, the growing rate before and after the shrinkage of the other droplets differs more than before. This results from the larger number of droplets which are formed and where the water mass flux is distributed to and the resulting larger num-

ber of shrinking droplets and, therefore, the larger volume which is transferred to the favored droplet afterwards. The local capillary pressures in the interface pores look similar than before but with a few numerical fluctuations.

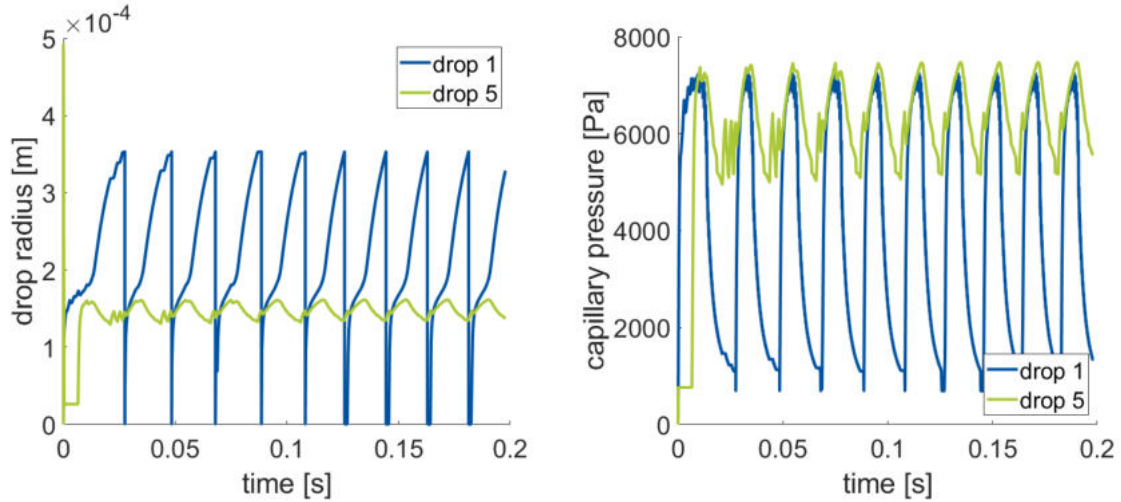


Figure 8.9: Two-drop interaction. Left: drop radius evolution with time of the droplets forming at the two different interface throats. Right: Corresponding capillary pressure of the droplets (capillary pressure is defined by the interface curvature of the drop surface).

In Figure 8.10, the corresponding water phase pressure in the inlet pore for the setup with 16 interface pores is shown. Here, a clear difference can be seen in comparison to the behavior of the water pressure in Figure 8.8. The fast increase of the pressure is hindered such that it almost equals the rate of pressure decrease. Again, we see some numerical fluctuations in the pressure during the growth of the favored droplet and while the size of the other droplets stays nearly constant (except small numerical fluctuations). The overall behavior now gets closer to the pressure behavior which has been predicted by the bulging menisci model.

To further analyze the behavior of the water pressure in the inlet pore and therefore the global capillary pressure during the multi-drop interaction, a setup with 101 interface pores is analyzed. In this case, ten interface throats are slightly larger than the rest such that droplet formation will be favored. The resulting water pressure behavior in the inlet pore is presented in Figure 8.11.

In this simulation, the average rate of pressure growing is smaller than the one of pressure decreasing. The behavior is not as strong as expected from the bulging menisci model but a trend can be seen from the analyzed simple test cases with 2, 16 and

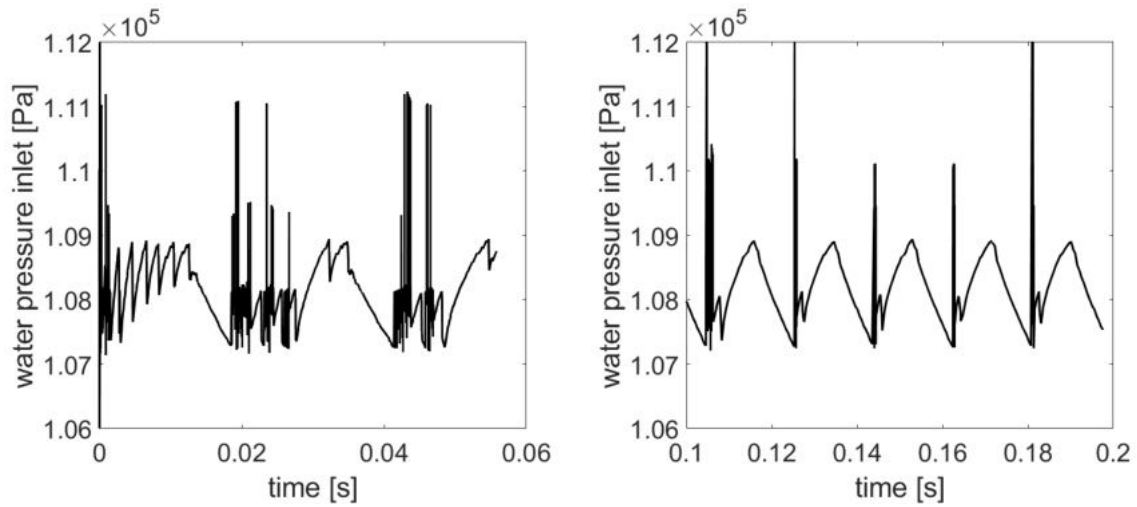


Figure 8.10: Liquid phase pressure in the inlet pore of the 16 interface pores setup. Left: first three drop formation cycles. Some numerical fluctuations occur. But the system stabilizes and less fluctuations occur at later time (right). Here, a repeating behavior of the pressure curve establishes for drop formation, growth and detachment.

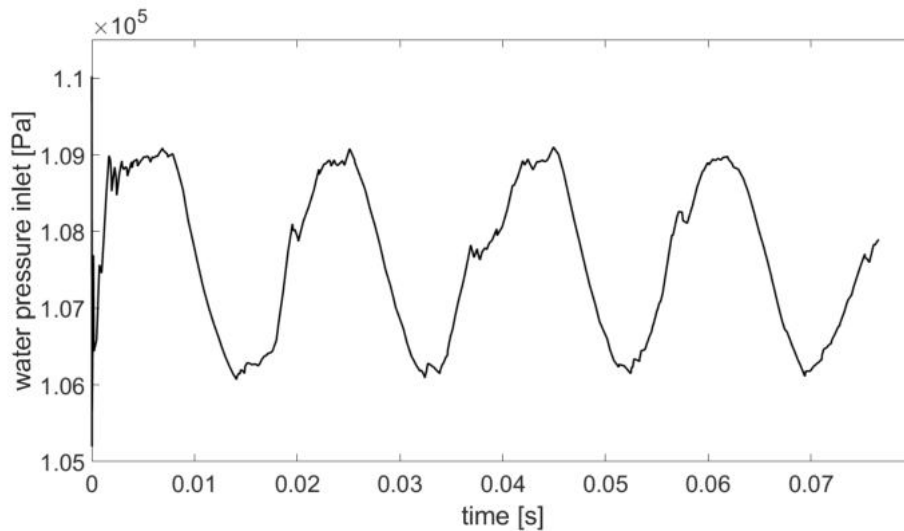


Figure 8.11: Liquid phase pressure in the inlet pore of the 101 interface pores setup.

101 interface pores. The trend shows, the more droplets strongly interact with each other the closer the water pressure behavior is to the predicted curve. For a large GDL sample, where many droplets occur and interact, a long pressure increase followed by an almost sudden decrease might occur

8.1.3 Formation, growth and detachment of droplets at the surface of a GDL

In this section, the pore-network model including the interface concept to model drop occurrence, growth and detachment is applied to a network representing a small GDL unit cell. In Figure 8.12, the pore-network representing a GDL structure is visualized. The network resulting from the fiber structure shows wide pore-size and throat-size ranges. We apply a mass flow boundary condition to the bottom side. Therefore, an inlet pore is added which is connected to each pore at the bottom side of the network, which represents the water production rate corresponding to a current density of 1 A/cm^2 . The connecting throats equal the size of the network pores such that the mass flux is distributed to all inlet pores based on their pore size due to the capillary entry pressure of the connecting throats.

The considered GDL sample is small enough such that only one breakthrough location occurs where a droplet forms, grows and finally detaches. The drop radius and the corresponding local capillary pressure are shown in Figure 8.13. The step wise behavior results from the low water inlet flux and small time step sizes. Locally in the network, the capillary entry is overcome in a pore but the flux through the freshly invaded throat results in a decrease of the local saturation and therefore a decrease of the local pressures. These anomalies based on the pore-network model nature result in step wise fluxes in the network.

Influence of the drop formation at the interface between GDL and gas distributor on the flow in the GDL

Not only the droplets forming at the interface between GDL and gas distributor are influenced by the water displacement and fluxes in the pore-network but also the pore-network itself is influenced by the formation, growth and detachment of the droplets. The developed model is capable to capture these influences pore-locally. In the following section, the developed model is again applied to the previously described unit cell and the flow behavior inside the GDL is analyzed during the drop formation, growth and detachment. The behavior during drop formation and growth is compared to CFD investigations presented by Niblett et al. [7].

Niblett et al. [7] present a CFD model (VoF) that allows analysis of two-phase flow

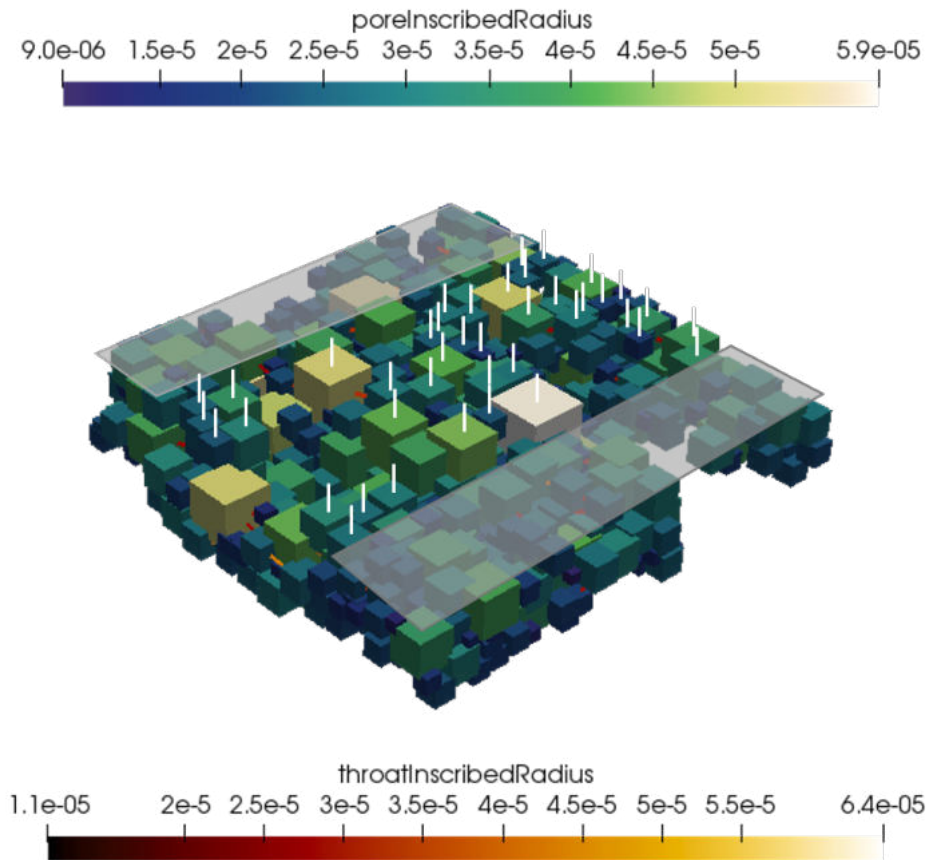


Figure 8.12: Pore-network representing a MPL-free GDL or GDB structure. The white lines mark the locations of open pores in the channel, where droplets can form. The gray shaded areas are part of the ribs. Here, the network pores are blocked and have no access to the channel.

in a GDL structure. The results show a highly dynamic flow behavior. Especially during breakthrough (and the formation of droplets), when menisci recede from certain pores (see Figure 8.14). In Figure 8.14, a VoF simulation of two-phase flow through the two-dimensional cross-section of a GDL is shown. The visualization focuses on a single breakthrough path of water in the void space (black) between fibers (white). The breakthrough path feeds a droplet at the GDL surface (at the top of the figures). The growing droplet is not shown in the figure. In the water phase, the flow velocity is visualized. Light colored areas indicate a higher velocity than the darker ones. The four presented time steps in Figure 8.14 present the behavior of a certain meniscus, which is receding during the formation of a droplet fed by this breakthrough path. In Figure 8.14, white arrows point on the receding meniscus. A larger droplet has a lower

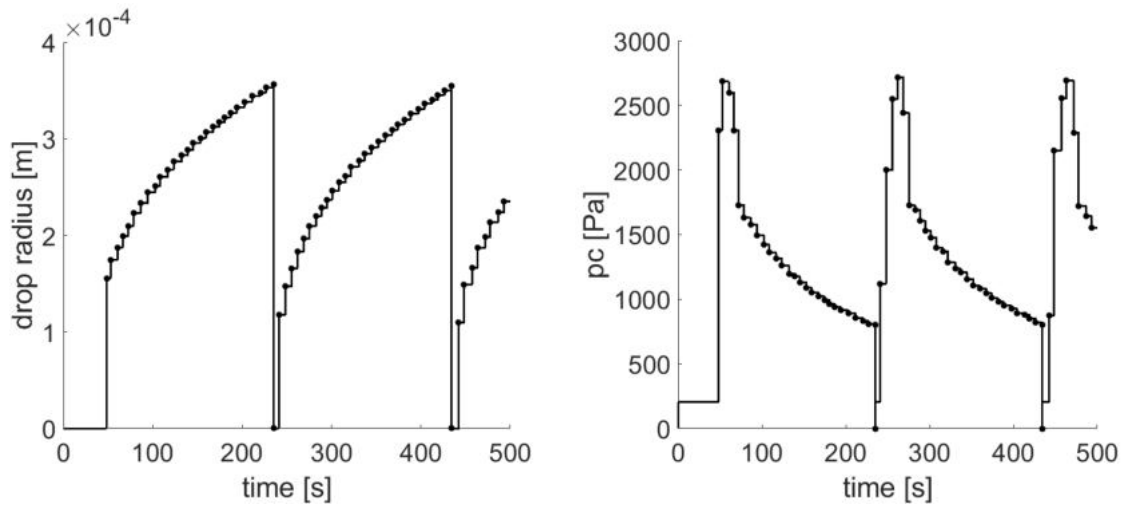


Figure 8.13: Left: droplet radius, right: corresponding capillary pressure in the interface pore (capillary pressure at droplet surface)

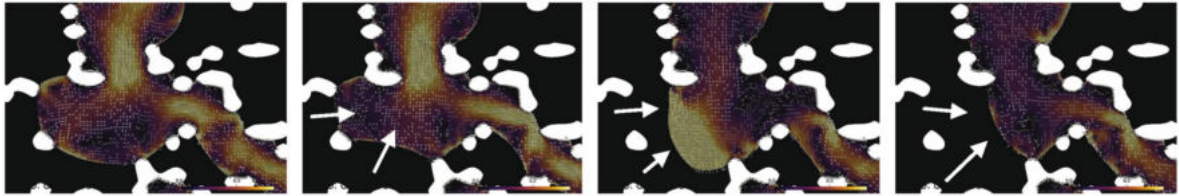


Figure 8.14: Close up of dynamic receding of pore contents in the analyzed GDL structure resulting from the growth of droplet on the surface of the GDL in the GC (gas channel). Velocity magnitude; vectors represent direction of flow [7].

water phase pressure such that the water tends to fill the droplet rather than pores in the porous medium. This results in receding menisci in certain pores.

This behavior is also captured by the pore-network model. In Figure 8.15, the local saturation at three different time steps are presented. At $t_1 \approx 48$ s, the water reaches the pores at the top side of the GDL but breakthrough did not occur yet. Several pores are visibly invaded and filled with water. At $t_2 \approx 49$ s, breakthrough occurred at one of the pores located in the channel region of domain II (marked with the red arrow). A flux goes through the interface throat filling a droplet in the interface pore (not visible in Figure 8.15). At the same time, the saturation in several pores, connected by invaded throats, decreased. This behavior equals the receding menisci observed in the CFD analysis by Niblett et al. [7] (Figure 8.14). Since the developed pore-network model allows the simulation of dynamic droplet formation and detachment. The behavior of the network during several growth and detachment periods can be analyzed. It shows,

for the small GDL unit cell with only one breakthrough, a stable breakthrough path establishes ($t_3 \approx 500$ s in Figure 8.15), which does not change significantly during the simulation.

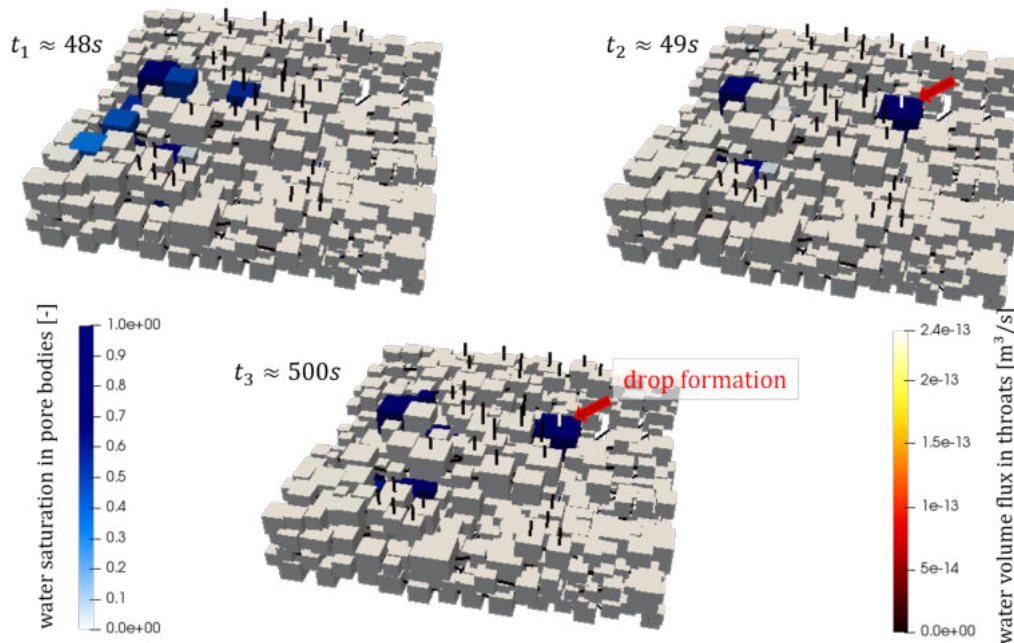


Figure 8.15: Top left: local water saturation pattern in the pore bodies and water volume flux in the throats before break through and drop formation ($t_1 \approx 48$ s), top right: local water saturation pattern in the pore bodies and water volume flux in the throats after break through ($t_2 \approx 49$ s), the water flux through the interface throat forms a droplet in the interface pore. Bottom: established local water saturation pattern in the pore bodies and water volume flux in the throats after multiple drop formations ($t_3 \approx 500$ s). The final pattern shows the stabilized break through path.

8.1.4 Discussion

The developed model is able to simulate the pore-scale behavior of single and multiple droplets forming on simplified and complex but realistic porous materials. The comparisons to available experimental and numerical data show very good agreement for the drop growth behavior. Since in the literature a wide variation of the presented separation lines has been found, further investigations are recommended to determine the detachment criterion. The criterion developed for this work is a (semi-)analytic

approach which can be adapted if further information on the force balance composition is available.

The presented model is capable of modeling multi-drop interactions and confirms the bulging menisci model. Also the flow behavior inside the GDL of receding menisci during the drop occurrence has been successfully captured. Modeling GDL structures is difficult due to the high heterogeneity and complex network structure. To evaluate a representative volume of a GDL structure, the efficiency and numerical stability of the model has to be improved. Nevertheless, a small sample of a fibrous GDL structure could be represented and the pore-local flow behavior has been analyzed. Even though the detailed local behavior has to be handled with care due to pressure fluctuations and numerical inaccuracies in such a complex network, the developed model is capable to represent the general behavior during droplet formation, growth and detachment and presents reasonable and validated results.

8.2 Pore-network model including fluidic interaction at the interface between a hydrophobic and a hydrophilic material²

8.2.1 Fundamental behavior of the interacting pores

To investigate the fundamental behavior of the system described in Section 8.2, a basic, homogeneous, two-dimensional, hydrophobic network with cubic pore bodies and throats with square cross-sectional area (Domain I) is considered (Figure 8.16 (left)). Imagine a thin porous medium between two hydrophobic coated plates. In one of the plates, a hole is drilled. The inner surface of the drilling hole is now uncoated and therefore hydrophilic (here: contact angle of 0°). The position of the drilling hole denotes the position of the interaction pore (Figure 8.16 (right)). The outer surface of the plate is hydrophilic (Domain II). In the representing pore network (Domain I), the pore bodies and throats are of uniform size (pore size ($R_i = 10^{-4}\text{m}$), throat size ($r_{ij} = 0.5 \cdot 10^{-4}\text{m}$) and length ($l_{ij} = 3.3 \cdot 10^{-3}\text{m}$)). In the hydrophobic network, a contact angle of 180° is applied. The domain is initially filled with the gas phase ($S_{gas} = 1.0$) and a primary drainage process of the water phase displacing the gas phase in the entire domain is considered in the hydrophobic Domain I. The blue pores denote the inlet pores, where a water saturation $s_n = s_{liq} = s_{inlet}$ is fixed as a Dirichlet boundary condition. The orange pores are the outlet pores, where the gas saturation is fixed to one $s_{gas} = s_w = 1.0$. No pressure difference is applied for the gas (wetting phase) pressure ($\Delta p^w = p^{gas} = 0$). The red pore is connected to the hydrophilic Domain II. Here, an outflux is applied and suppressed dependent on the fulfilled water saturation thresholds. The applied time step size is $\Delta t = 10^{-5}\text{s}$.

In Figure 8.17, the water saturation (non-wetting phase) in the pore (in Domain I) interacting with the hydrophilic Domain II (interaction pore) (blue line) and the global saturation of the network (red line) during the invasion process are shown. The interface pore (in Domain I) is filled and emptied with water due to the interaction with the hydrophilic Domain II based on the applied water (non-wetting phase) saturation thresholds ($s_{n,liq}^{start} = 0.52$ and $s_{n,liq}^{stop} = 0.01$). The total water saturation S_{liq} increases

²Portions of this section are part of the publication *Modeling of two phase flow in a hydrophobic porous medium interacting with a hydrophilic structure* by Michalkowski et al. that is in review by Transport in Porous Media (Springer).

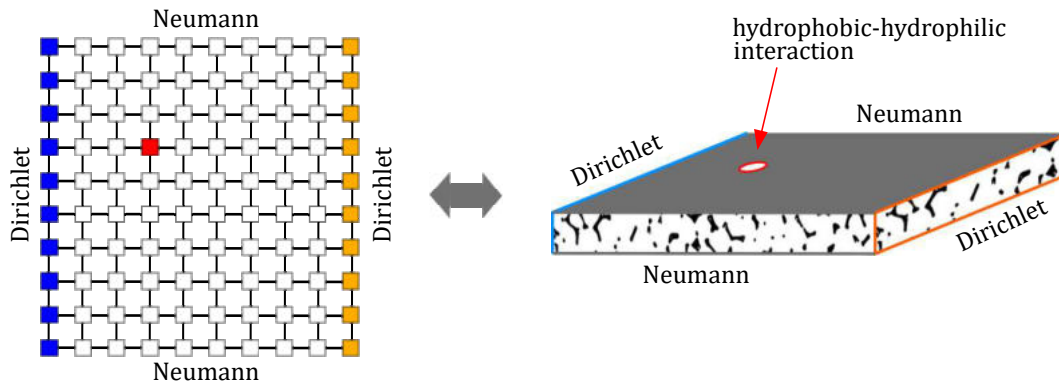


Figure 8.16: Visualization of the investigated hydrophobic network (left) which is an exemplary representation of the porous medium setup on the right (Domain I). The basic setup is built to show the fundamental behavior of the interacting pores. The hydrophobic porous medium (right) is placed between hydrophobic coated plates (the material of the plates itself is hydrophilic) with a hole at the position of the interaction pore. The inner surface of the hole is hydrophilic (red). The outer surface of the plate is hydrophilic too (Domain II). The water flow goes from left (blue inlet) to right (orange outlet) (right).

monotonously, while the saturation in the interaction pore shows a varying, oscillating behavior. The volume flux leaving the hydrophobic Domain I is very small compared to the overall water flux through the system. Therefore, the outflux through the interaction pore has only a small influence on the overall (global) saturation of the network. In the following, the four marked states in Figure 8.17 are described and explained in detail to understand the behavior of the water (non-wetting phase) saturation curve corresponding to the interaction pore (in Domain I).

Figures 8.18-8.21 show the volume flux of the water through the connecting throats in the hydrophobic network (Domain I).

At State 1 (Figure 8.18), the water saturation (non-wetting phase) threshold ($s_{n/liq} = 0.52$) in the pore (in Domain I) connected to the hydrophilic Domain II is reached and the interaction between the hydrophobic network (Domain I) and the hydrophilic domain (Domain II) starts through this pore such that the pore-local water phase saturation s_{liq} decreases.

At State 2, the water saturation (non-wetting phase) in the pore (in Domain I) connected to the hydrophilic Domain II falls below the threshold of the stop criterion ($s_{n/liq} = 0.01$) and the flux between the hydrophobic pore network (Domain I) and the

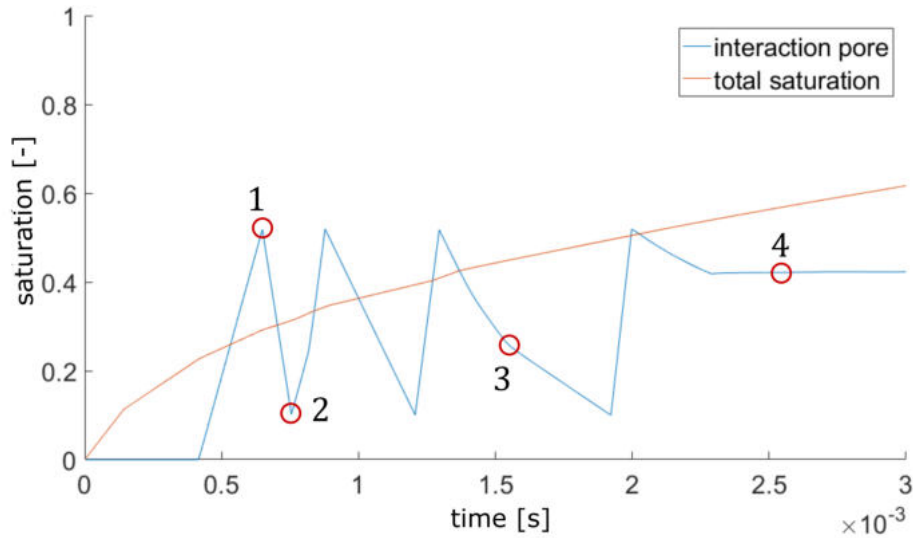


Figure 8.17: Saturation s_{liq} in the interface pore (blue) and total water saturation S_{liq} of the network (red) over time during the interaction with the hydrophilic Domain II. The four states marked red are investigated in detail in the following.

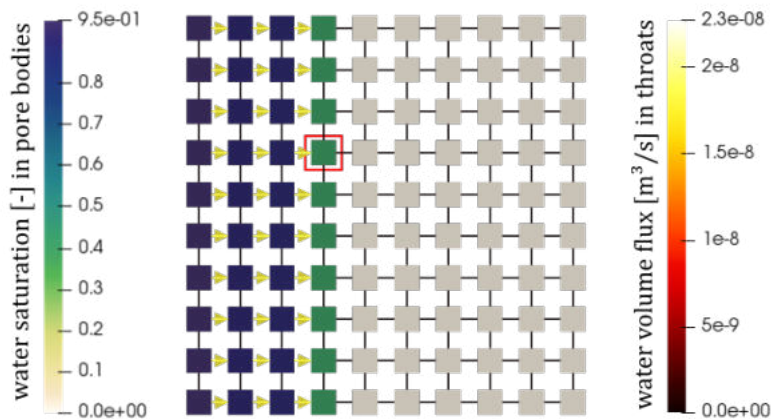


Figure 8.18: State 1: Water flux in throats and water saturation in pore bodies at $t = 0.0006$ s. The interaction pore is marked with a red square.

hydrophilic domain (Domain II) stops (State 2, Figure 8.19).

This small saturation leads to a fast refilling of the interaction pore. This occurs again before State 3. At State 3, the decrease of the water saturation (non-wetting phase) in the pore (in Domain I) connected to the hydrophilic Domain II is halted due to the flux from the invaded neighboring pores (denoted by arrows in Figure 8.20), where

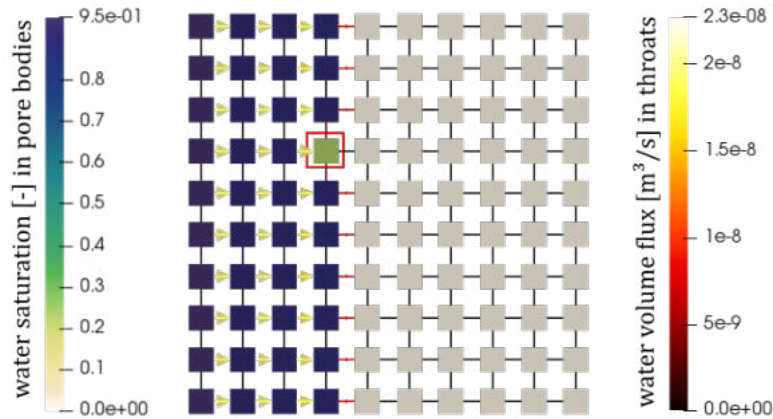


Figure 8.19: State 2: Water flux in throats and water saturation in pore bodies at $t = 0.000815$ s. The interaction pore is marked with a red square.

the capillary entry pressure, which is necessary to overcome, to invade the connecting throat is met (State 3, Figure 8.20).

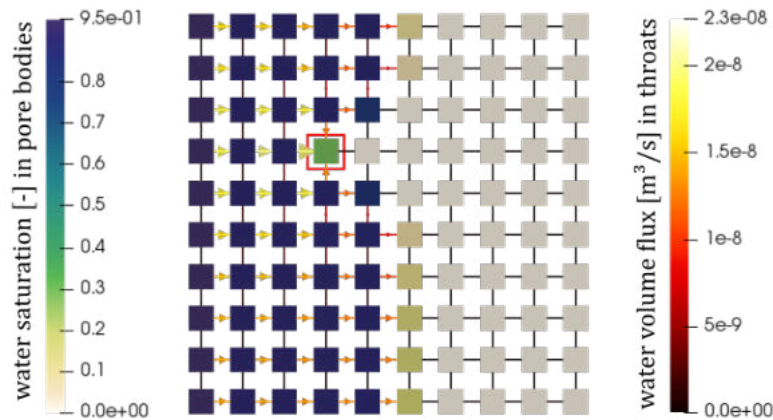


Figure 8.20: State 3: Water flux in throats and water saturation in pore bodies at $t = 0.0015$ s. The interaction pore is marked with a red square.

Once the downstream neighboring throat (Throat 4 in Figure 4.22) is invaded, water flows through this throat as well into the interaction pore following the local water pressure gradient. This results in a filling from all four hydrophobic throats connected to the interaction pore. In the considered test case, this results in an equilibration of the fluxes in and out of the interaction pore and the saturation stays constant (State 4, Figure 8.21).

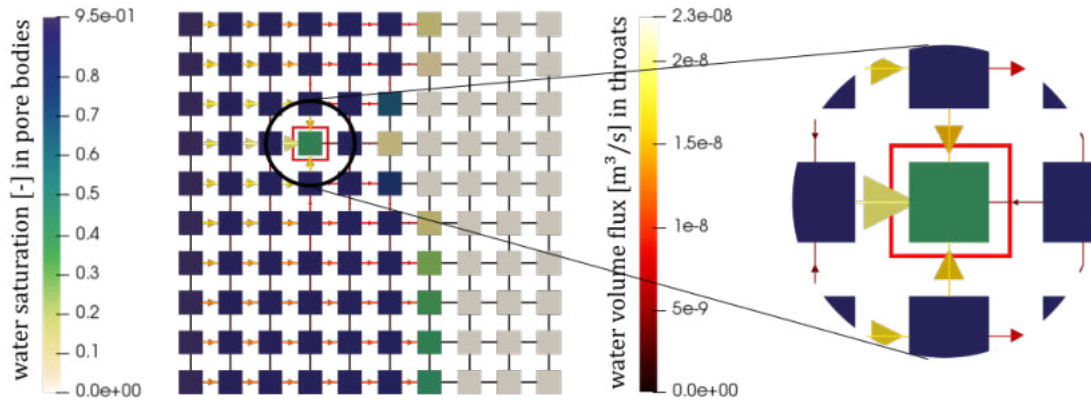


Figure 8.21: State 4: Water flux in throats and water saturation in pore bodies at $t = 0.0025$ s. The interaction pore is marked with a red square.

8.2.2 Investigation of the network response to interaction of several interface pores

The presented model does not only capture the interaction of one single pore (in Domain I) with hydrophilic Domain II but allows an arbitrary combination of interface pores. In the presented example, the complete pore row at the top of the network (Domain I) is in contact with hydrophilic Domain II.

The interface pores are located at the top of Domain I and are in contact with a gas-filled (no water present) hydrophilic Domain II. The interface pores are marked red and numbered consecutively in Figure 8.22.

It is assumed that the water distributes fast in the hydrophilic Domain II and is transported away from the interface between the hydrophobic porous Domain I and the hydrophilic Domain II such that there is no influence on the outflow behavior between the different interface pores.

As in the previous example, water is used as the non-wetting fluid and pushed through the domain from left to right (Figure 8.16). The hydrophobic Domain I is initially filled with air (gas). In Figure 8.23, the oscillating water saturations in the interface pores are shown. For transparency reasons, only the first two oscillations are plotted.

The water saturation in the first interface pore in the top row (interface pore 0) does

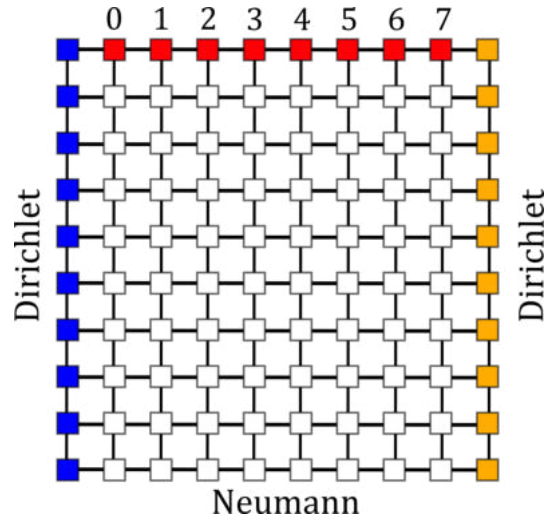


Figure 8.22: Visualization of the investigated hydrophobic network with several interface pores interacting with the hydrophilic Domain II. The interface pores are marked red and numbered consecutively

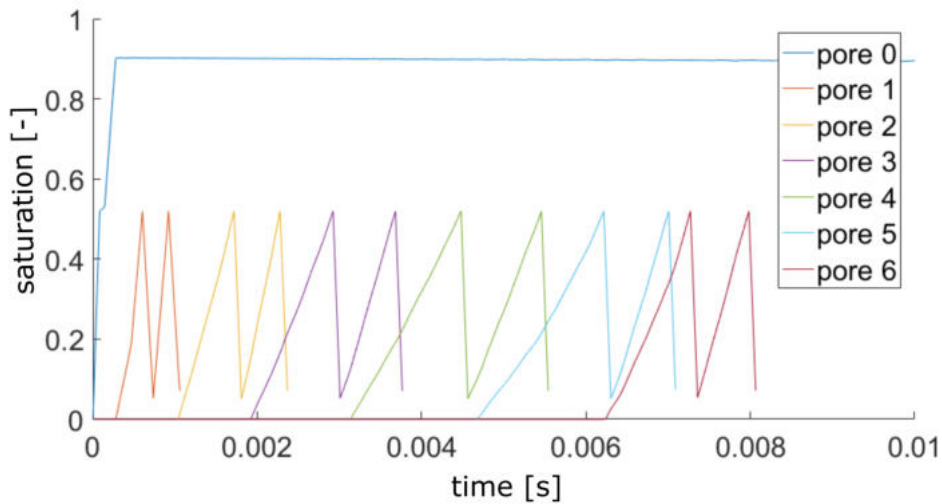


Figure 8.23: Water saturation in the interface pores at the top face during the interaction with the hydrophilic Domain II.

not show an oscillation. We see a kink in the curve at a water saturation of $s_{\text{liq}} = 0.52$, which is the threshold for the interaction with the hydrophilic Domain II. At this time, an outflux through this pore from the hydrophobic Domain I to the hydrophilic Domain II starts. The fluid configuration in the network (Domain I) during this time step is shown in Figure 8.24. However, the fluxes into the interface pore from the neighboring pores in the hydrophobic network (Domain I) is still higher than the outflux, such that

the water saturation keeps increasing. This is a boundary effect which results from the position of the interface near the inlet pores. Pore 0 gets virtually unlimited fresh water from the left edge and an equilibrated water saturation is reached based on the equilibrium of in- and outflux of the interface pore. With increasing water saturation in the pore, the local capillary pressure and water phase pressure rise. This might cause a steeper gradient between the interface pore and the surrounding pores in the hydrophobic network (Domain I) but also a larger pressure difference between the hydrophobic Domain I and the hydrophilic Domain II influencing the fluxes through the hydrophobic and hydrophilic throats. These fluxes equilibrate for interface pore 0 at a constant water saturation.

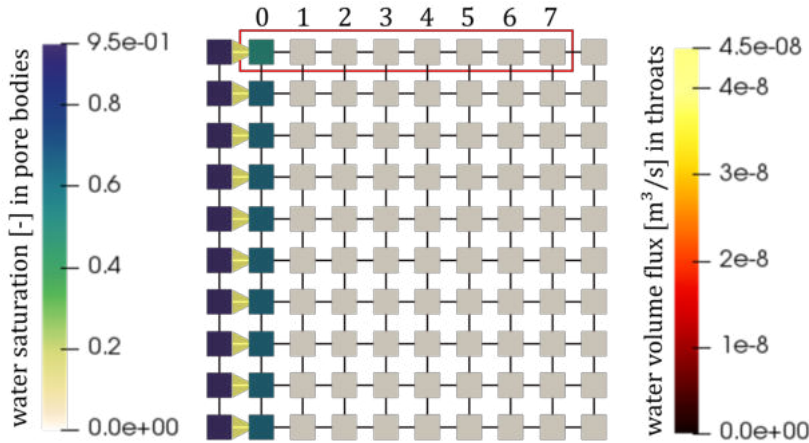


Figure 8.24: Water volume flux in $[m^3/s]$ in throats and water saturation $[-]$ in pore bodies at $t = 0.0001s$

The replacement process continues due to the water (non-wetting phase) pressure gradient between the left and right side of the network (Domain I) such that the next column of pores is invaded by the non-wetting phase (water). The second interface pore (interface pore 1) shows an oscillating behavior of the water saturation (see Figure 8.23). In this case, no equilibrium is reached between the in- and outfluxes. The outflow starts with the start threshold at $s_{liq} = 0.52$ and causes an emptying of the pore body. Once the stop threshold is reached, the interaction with the hydrophilic Domain II stops and the water saturation increases due to the fluxes through the connecting throats of the hydrophobic network (Domain I). The oscillating behavior shows that the outflux from the hydrophobic pore into the hydrophilic Domain II is larger than the "refilling" fluxes coming from the surrounding hydrophobic pores (Domain I). In Figure 8.25, the time step is captured when interface pore 1 is filled with the non-wetting water for the first

time.

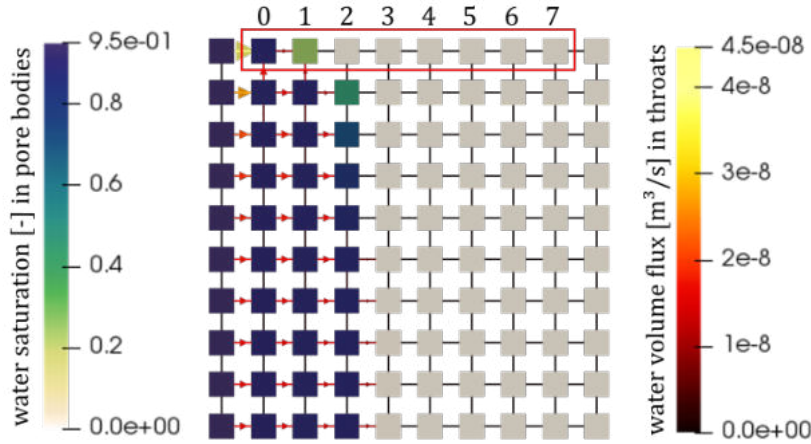


Figure 8.25: Water volume flux in $[\text{m}^3/\text{s}]$ in throats and water saturation $[-]$ in pore bodies at $t = 0.00082 \text{ s}$

The water fluxes in the hydrophobic throats (in Domain I) show that the water does not invade the network straight from left to right as it would be the case in a network without interface pores. We see a clear upward-oriented flux perpendicular to the applied pressure gradient due to the outflux from the interface pores. The resulting decrease of the water saturation causes a gradient of the local capillary pressure such that the interface pores are refilled from the hydrophobic adjacent pores (in Domain I).

In Figure 8.27, we see how the second interface pore (Pore 1) is emptied compared to the previous state (Figure 8.25). At the same time, the third interface pore (Pore 2) is invaded. From the water saturations in the top row pores (interface pores), we see that the water saturations are not synchronic oscillating. The time dependent evolution of the water saturations (Figure 8.26) shows that the frequency of the oscillations depend on the position of the interface pore in the network (Domain I). Early invaded pores (pores further left), where the pressure gradient is higher during primary drainage, oscillate with a higher frequency. In Pore 5, we see the influence of the small size of the network (Figure 8.26). Once the overall network reaches the maximum water saturation, the flux into the interaction pores is increased. The water does not need to be distributed elsewhere.

The row of interface pores does not only influence the adjacent pores but the fluid pattern in the complete Domain I. In Figure 8.28, we see the deformation of the invasion front resulting from the outflux in the interface pores.

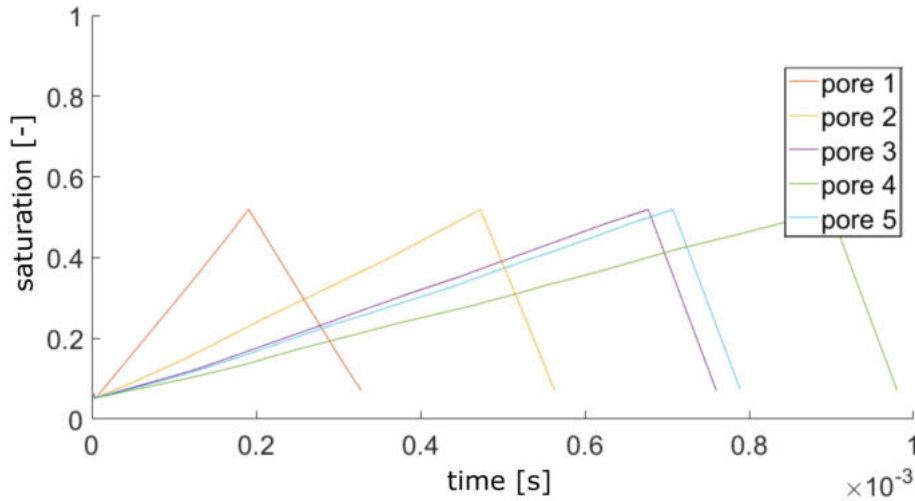


Figure 8.26: The time dependent liquid water saturation s_{liq} evolution shows the different filling velocity of the interaction pores. For the first five pores the second oscillation is shown to compare the frequency of the water saturation oscillations in the pores. Here, only the first water filling of each pore is plotted. Pore 0 is missing since the water saturation does not oscillate but reaches an equilibrium (see Figure 8.23)

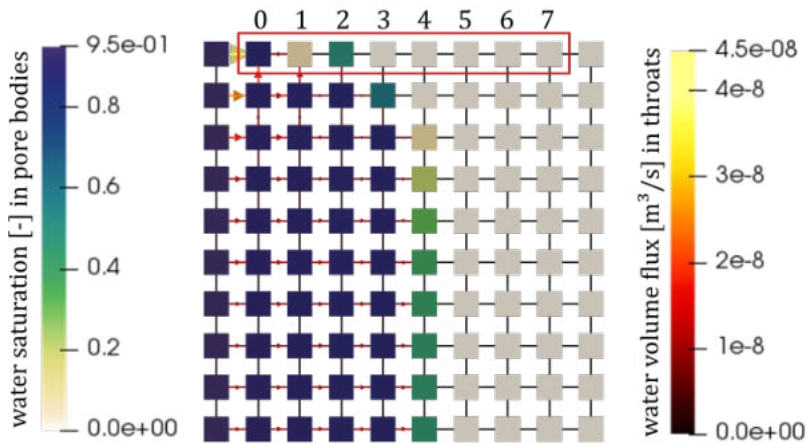


Figure 8.27: Water volume flux in $[m^3/s]$ in throats and water saturation $[-]$ in pore bodies at $t = 0.0017s$)

However, it has to be noticed that this is just a basic example with a small network. We aim to show the complex interplay of the hydrophobic network (Domain I) interacting with a non-resolved hydrophilic domain (Domain II). The example shows that, with this quite simple approach, the complex interactions can be captured on the pore-scale.

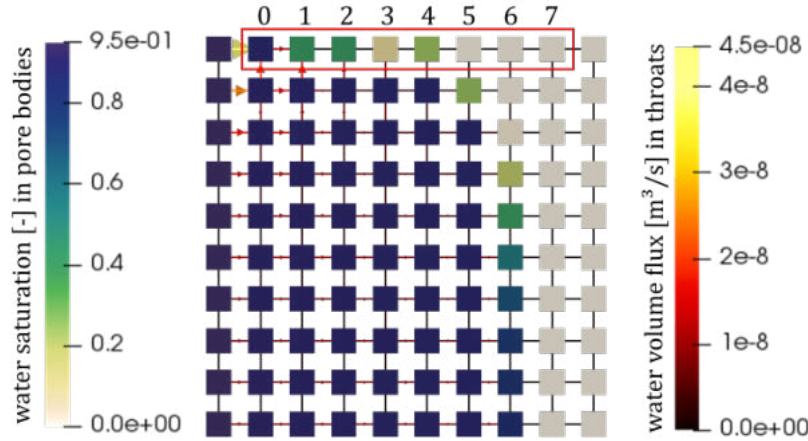


Figure 8.28: Water volume flux in $[\text{m}^3/\text{s}]$ in throats and water saturation $[-]$ in pore bodies at $t = 0.0038 \text{ s}$

8.2.3 Application to the interface between GDL and gas distributor

With the developed concept, we want to capture parts of the interaction between the fluid displacements in the GDL (Domain I) and the gas distributor flow (Domain II). Since the GDL consists of a hydrophobic material and is partly in contact with the hydrophilic gas distributor, local effects of this interaction need to be captured by the model to simulate the flow through the GDL structure (Domain I). As an example application, here, the primary displacement of air by water through a pore network extracted from a fibrous GDL representation structure is shown. For the representation of the GDL on the pore-scale, a network of cubic pores is used. The size and connectivity of the pores is based on the void space of the fiber structure. For the network extraction the python-based open-source tool PoreSpy [99] is used. In Figure 8.29, a part of the resulting network embedded in the base structure is shown.

In this hydrophobic pore network a contact angle of 135° is applied. However, as presented in Section 8.2, for the hydrophobic-hydrophilic interaction between Domain I and II, a contact angle of 180° is set in the interaction pore body and 30° in the hydrophilic throat. The network (Domain I) is initially filled with gas. We are interested in the interaction of the flow in the hydrophobic GDL (Domain I) with the hydrophilic wall of the gas distributor channel (Domain II) (see Figure 8.29). Therefore, a piece of the GDL is considered, which is partly covered by the land (shaded area in Figure 8.29), an area open for gas and water flow out of the GDL and a line of interface pores (red area in Figure 8.29), where the channel is opening. For simplicity reasons, the land surface

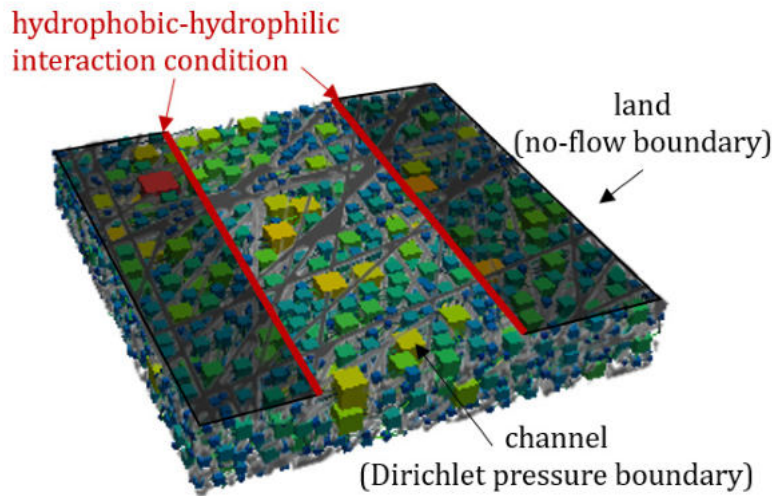


Figure 8.29: Part of a pore network with cubic pore bodies embedded in the GDL structure, from which the network has been extracted using PoreSpy [99]. The grey area represents the part where a no-flow boundary condition is applied representing the land part. The red part is the line, where the interaction condition between the hydrophobic GDL (Domain I) and the hydrophilic channel-land structure (Domain II) is applied. The open area represents the channel. Here, a Dirichlet pressure boundary condition is applied to allow outflow of the phases.

is assumed to be hydrophobic but the surface in the channels is hydrophilic. Similar to previous numerical and experimental investigations in the literature [136, 137, 32], the water passes through the GDL network (Domain I) following preferential paths and leaves the GDL at a few breakthrough locations. As inlet boundary condition a mass flux corresponding to the water production at a current density of approx. 2 A/cm^2 ($\dot{m}_{\text{liq}} = 9.32 \cdot 10^{-10} \text{ kg/s}$) is chosen. At the outlet a constant pressure with atmospheric conditions is set. Since the considered GDL sample is very small, only one breakthrough location is formed. The water saturation (non-wetting phase) in the network (Domain I) before the breakthrough is shown in Figure 8.30.

The setup is designed such that this breakthrough location lays on the line of interacting pores (red line in Figure 8.29), where the hydrophobic network pores (Domain I) are in contact with the hydrophilic gas distributor surface (Domain II). The resulting saturation fluctuations in that pore are presented in Figure 8.31.

The fluctuating behavior is similar to the one observed in the basic test scenarios. However, at the refilling of the pore, the water saturation curve shows a convex behavior which results from the highly heterogeneous network structure. While in the

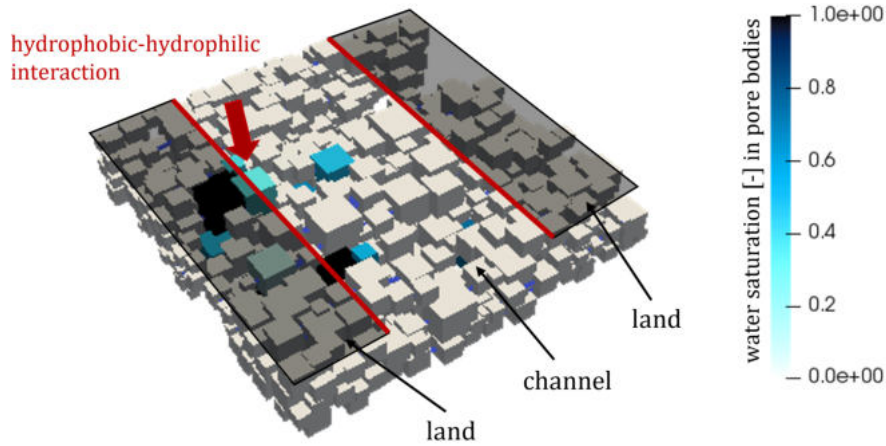


Figure 8.30: Water saturation (non-wetting phase) in the pores before the breakthrough (saturation threshold not fulfilled).

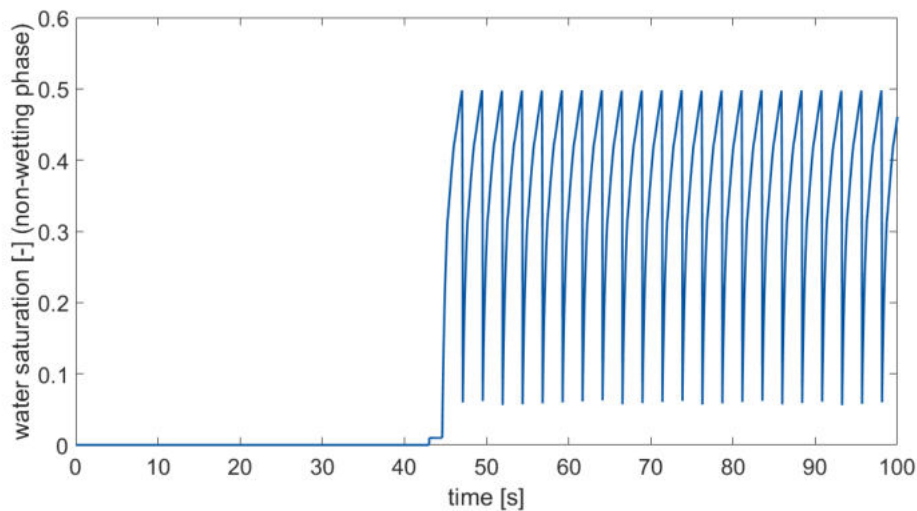


Figure 8.31: Water saturation in the pore interacting with the hydrophilic domain.

basic setup (Figure 8.23), the interface pore is refilled by a few neighboring pores of the same size, the refilling neighboring pores in the GDL network vary in size. Also, as it can be seen in Figure 8.30, there are a lot more pores connected to each other (coordination number between 1 and 50 compared to coordination number between 2 and 4 in the basic test scenarios) than in the basic, structured network. The water pressure (non-wetting phase) difference to an empty interface pore is high, resulting in high fluxes through the connecting throats. Meanwhile, the smaller pores connected to the interface pore, which have a higher local capillary pressure, are emptied (or the

water saturation is reduced significantly, such that the local capillary pressure drops) and the flux in the interface pore is reduced since the neighboring pores need to be refilled from the surrounding network (Domain I) as well. Because the water can be distributed on the hydrophilic channel walls (Domain II), the pressure does not build up during the emptying process. Therefore, the water saturation drops quickly after the threshold $s_{liq} = 0.52$ is reached.

The high frequency of the oscillations results from the small pore sizes and high inlet flux of water for the small sample.

The considered GDL sample does not represent a representative volume of the GDL, it only shows the specific behavior at a certain breakthrough location. For representative studies, much larger GDL samples need to be considered. This is not the scope of this work, where we focus on the presentation of a concept to model the interaction of a hydrophobic porous medium (Domain I) with a hydrophilic domain (Domain II). However, the presented concept can be used for these kind of investigations and is the basis for further analysis of the hydrophobic-hydrophilic interactions between GDL and gas distributor structures.

8.2.4 Comparison of the pore-network behavior to CFD investigations using ANSYS Fluent

In this section, we investigate the hydrophobic-hydrophilic interaction on the pore-scale using a direct numerical solver model, where the porous domain is discretized on the sub-pore-scale (multiple grid cells per pore body). Analogously to Section 8.1.1, we use a volume of fluid (VoF) method implemented in the commercial software package ANSYS Fluent R19. We simulate a small setup of two pores which are connected via a pore throat. The setup is visualized in Figure 8.32. Both pores have a side length of $800 \mu\text{m}$, all throats have diameter of $500 \mu\text{m}$ and a length of $800 \mu\text{m}$. The black part of the computation domain has hydrophobic surface properties and the red part has hydrophilic ones. We are interested in the interaction between the hydrophobic pore body with the hydrophilic throat. The VoF simulation reproduces the processes which have been implemented in the pore-network model and are described in the previous section on the sub-pore-scale. This allows a detailed investigation of the filling and emptying process as described in Section 8.2 and a more detailed determination of the saturation thresholds which are implemented in the pore-network model to control the

interaction. To discretize the two pores and connecting throats 546051 cells are used and a time step size of $\Delta t = 10^{-5}$ s is applied.

The hydrophobic outlet at the top in Figure 8.32 allows gas to leave the domain and keeps the gas pressure at atmospheric conditions. Otherwise the gas would be trapped in the hydrophobic pore once the hydrophilic throat is invaded. In the hydrophilic throat, we don't have gas corner flow due to the wettability of the side walls and in the inlet throat the inflow condition fills the complete throat with liquid and is also blocking the path for gas. Therefore, the additional outlet at the hydrophobic pore is the only way for the gas to escape the hydrophobic pore after invasion of the hydrophilic part. In the hydrophilic part, both, gas and liquid, can leave the domain at the outlet. Liquid phase backflow is prevented and the gas phase pressure is fixed to atmospheric conditions. In Figure 8.32, a plane in the center of the pores is added which is used to visualize the results.

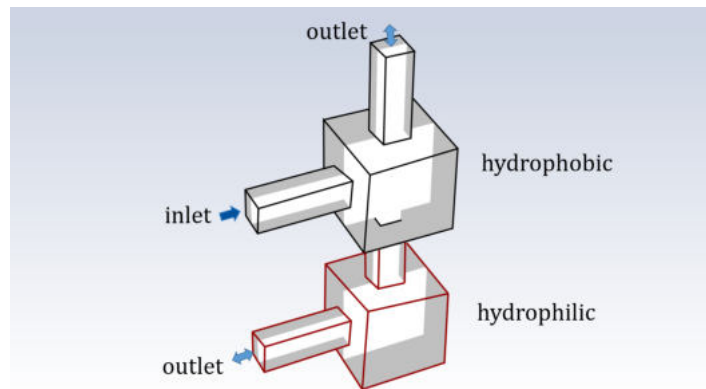


Figure 8.32: Setup for CFD simulation of hydrophobic pore interacting with hydrophilic throat and pore using ANSYS Fluent.

The domain is initially filled with air (gas) and liquid water is pushed in the domain at the inlet throat with a mass flux of $5 \cdot 10^{-6}$ kg/s. First, we investigate the pore-local fluid displacement processes in a setup with a contact angle of $\theta_1 = 180^\circ$ in the hydrophobic pore body and pore throats and a contact angle of $\theta_2 = 0^\circ$ in the hydrophilic pore body and pore throats. In Figure 8.33, the fluid distributions in the hydrophobic pore are presented and the interaction with the hydrophilic throat (red) is shown.

We see, how a sphere is formed by the liquid before contact with the hydrophilic surface of the red throat (t_1). Once the liquid gets in touch with the hydrophilic throat, the liquid flows out of the pore with a higher volume flux than the influx from the inlet throat. Therefore, the saturation of liquid water in the hydrophobic pore decreases (t_2

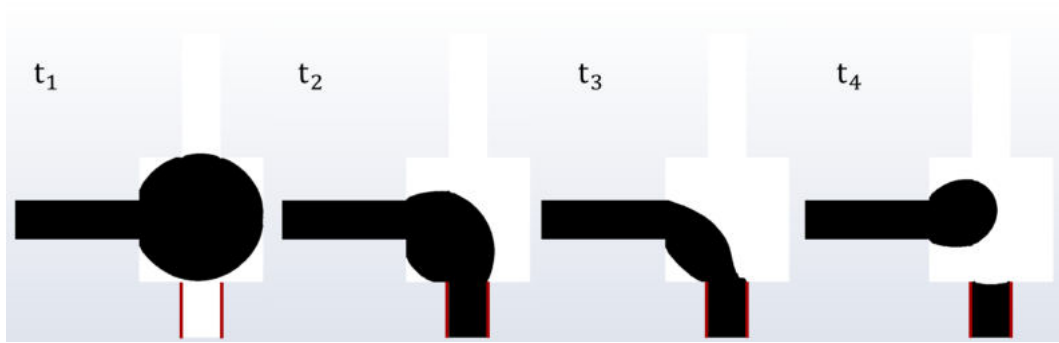


Figure 8.33: Water distribution in hydrophobic pore with contact angle $\theta_1 = 180^\circ$ in contact with hydrophilic throat (red) with contact angle $\theta_2 = 0^\circ$. Time dependent behavior showing the four stages during interaction.

and t_3). At a certain time, the liquid saturation in the pore body is too low to hold a continuous phase and snap-off occurs in the pore body (t_4). Now the liquid phase is not influenced by the hydrophilic throat any more and the pore body is refilled with liquid from the inlet throat. This behavior is repeating as long as the liquid water can be transported out of the computation domain from the hydrophilic pore body.

In Figure 8.34, the behavior of liquid water in the hydrophobic pore body is investigated in a setup with contact angle $\theta_1 = 120^\circ$ in the hydrophobic part and $\theta_2 = 30^\circ$ in the hydrophilic part.

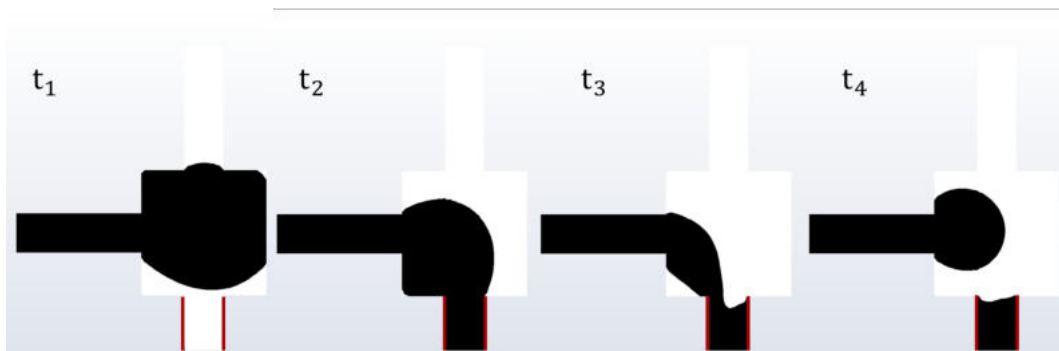


Figure 8.34: Water distribution in hydrophobic pore with contact angle $\theta_1 = 120^\circ$ in contact with hydrophilic throat (red) with contact angle $\theta_2 = 30^\circ$. Time dependent behavior showing the four stages during interaction.

We observe a slightly different filling behavior since the surface of the pore body is not as repellant for the liquid water as in the previous case with contact angle $\theta_1 = 180^\circ$ (t_1 in Figure 8.34 vs. t_1 in Figure 8.33). However, the behavior after contact with the hydrophilic throat (red) is similar to the previous scenario. After the contact, liquid

water leaves the hydrophobic pore body through the hydrophilic throat and the outflux is higher than the influx of liquid. Again snap-off occurs once the saturation is low enough and a repeating behavior is observed.

These VoF model results gain insight into the displacement processes and fluid configuration inside the hydrophobic pore body. The presented results support the previously made assumptions and concepts for filling and emptying of the pore body and the interaction between hydrophobic pore body with hydrophilic throat. We take these VoF results to verify the chosen saturation thresholds and investigate the influence of the different contact angles in the computation domain parts (θ_1 and θ_2).

In Figure 8.35, the saturation of liquid water in the hydrophobic pore body is plotted over time during the interaction with the hydrophilic throat.

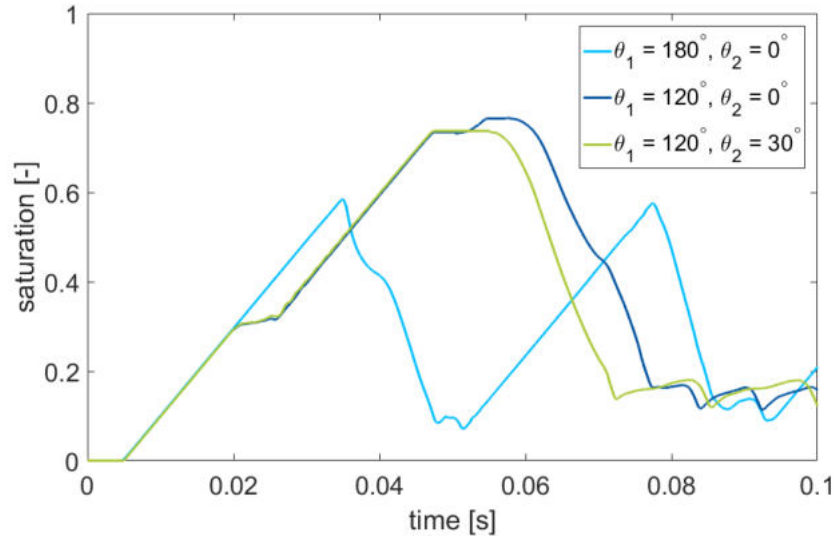


Figure 8.35: Saturation of liquid water in the hydrophobic pore with different contact angles in the hydrophobic and the hydrophilic pores.

It shows how the maximum liquid saturation (threshold for start of interaction) varies with the contact angle in the hydrophobic pore body (θ_1). A lower contact angle results in higher saturation which results from the different fluid configurations in the hydrophobic pore body (compare t_1 in Figure 8.34 and t_1 in Figure 8.33). The influence of the hydrophilic domain contact angle on the first threshold is very small and might result from numerical inaccuracies. Here, the saturation threshold for a contact angle $\theta_1 = 180^\circ$ is $s^{th1} \approx 0.58$ which is a little higher than the estimation ($s_{estimate}^{th1} \approx 0.52$) which is derived from a liquid water configuration forming a sphere in a cube. Considering the configuration in t_1 of Figure 8.33, we see the reason for the higher saturation.

The liquid water in the pore body shares the area of the throat cross-section with the liquid water in the throat such that not a sphere but a spherical cap is formed which radius and volume are a little larger. At the snap-off, we see some fluctuations in the saturation. The configuration is very unstable at this time and the newly built fluid interfaces oscillate in the simulation. We approximate the second saturation threshold with $s^{th2} \approx 0.09$. The second threshold seems to be less influenced by the contact angles in both domains. This can be explained by the configuration at t_3 in both presented setups. Before snap-off occurs in the hydrophobic pore body the liquid phase connects between both throats (hydrophobic inlet throat and hydrophilic throat). There is not enough contact area between the liquid and the walls of the hydrophobic pore body such that the contact angle has only a minor influence here. Also, the hydrophilic throat is just filled by the liquid water and the contact angle is not visible at the three-phase contact line. Nevertheless, the strongly wetting throat in Figure 8.33 might create a numerically more stable interface. Overall, we see a more stable behavior for the strongly wetting and non-wetting configuration ($\theta_1 = 180^\circ$ and $\theta_2 = 0^\circ$).

8.2.5 Discussion

Especially for modeling the processes at the interface between GDL and gas distributor in a PEM fuel cell, we need to capture the effects of the different wetting behaviors of the materials. The fluids (water and air) passing through the hydrophobic GDL (Domain I) interact with the hydrophilic surface of the gas distributor channels (Domain II) (see Figure 8.29). The presented concept considers the interaction at the contact line between GDL and channel wall and we focus on the water outtake from the hydrophobic GDL.

To develop a model that allows two phase flow in a hydrophobic porous medium (Domain I) interacting with a hydrophilic structure (Domain II), the following assumptions are used:

- the GDL can be represented by a pore-network model,
- in the gas channel, the water is removed efficiently from the interface between the hydrophobic porous domain (GDL) (Domain I) and the hydrophilic channel-land structure (Domain II) such that the water saturation remains close to zero and

the resulting local capillary pressure equals the non-wetting (gas) phase pressure at the interface,

- local saturation thresholds can be defined to identify the time frame of water interaction across the interface between the hydrophobic porous domain (GDL) (Domain I) and the hydrophilic channel-land structure (Domain II),
- these saturation thresholds are sufficiently independent of the connectivity of the boundary pore. From the description of the pore and throat structure, analytic threshold formulations can be derived.

With these assumptions, a model is built that captures the main processes at the mixed-wet interface on the pore-scale. It allows to include the interface effects in a rather simple representation of the porous material (Domain I) and helps to understand the ongoing processes and their interactive behavior. The developed model captures the effects of the mixed-wet interface not only on the bounding pores but also on the neighbors and the whole hydrophobic network flow (Domain I). Therefore, the implementation is able to capture the dominating water flow behavior at the interface between a hydrophobic porous structure (Domain I) and a hydrophilic open flow (Domain II) as it occurs at the interface between the cathode GDL and the gas distributor in a PEM fuel cell as shown in Figure 8.29.

The results of the VoF model generated with ANSYS Fluent support the approximated fluid configurations and chosen thresholds.

8.3 Pore-network model including trapping in mixed-wet pores below land

8.3.1 Proof of concept on simple, regular pore-network

The functionality of the developed concept to describe the influence of mixed-wet pores below the land parts of a gas distributor is shown with a exemplary, regular pore-network of 10×10 pores shown in Figure 8.36. The water flow goes from left to right driven by Dirichlet boundary conditions at the inlet and outlet pores. The pore bodies are colored and scaled based on their inscribed radius.

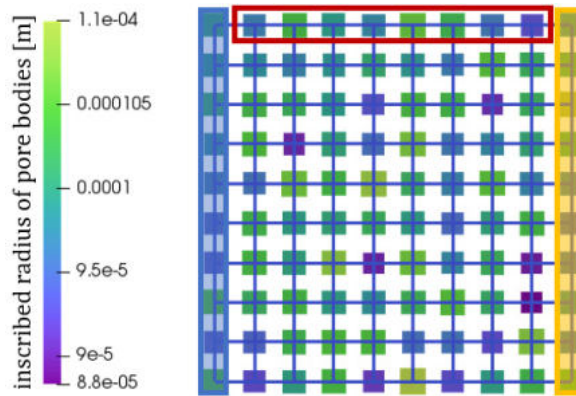


Figure 8.36: Exemplary, regular pore-network to present the functionality of the developed concept to describe the influence of mixed-wet pores below the land parts of a gas distributor. At the pores in the top (marked red), the interface condition is applied. The water flow goes from left to right driven by Dirichlet boundary conditions at the inlet and outlet pores.

All throats have the same size (throat inscribed radius: 0.025 mm and throat length: 0.33 mm) with a square cross-sectional area. The pore bodies are of random size with mean inscribed radius of 0.1 mm and a standard deviation of 0.005 mm. The mixed-wet boundary condition is applied to the pores in the top row which are marked red. At the inlet (left, marked blue) a Dirichlet boundary condition is applied with fixed inlet saturation ($s_n = 0.96$) and gas phase pressure ($p_w = 10^5$ Pa). No pressure difference is applied between in- and outlet and in the outlet pores (right, marked orange) the water saturation is fixed to $s_n = 0.0$ with a Dirichlet condition for saturation and pressure. The network is initialized with a gas phase pressure $p_w = 10^5$ Pa and zero water saturation everywhere except the inlet pores, where the Dirichlet boundary condition

is applied.

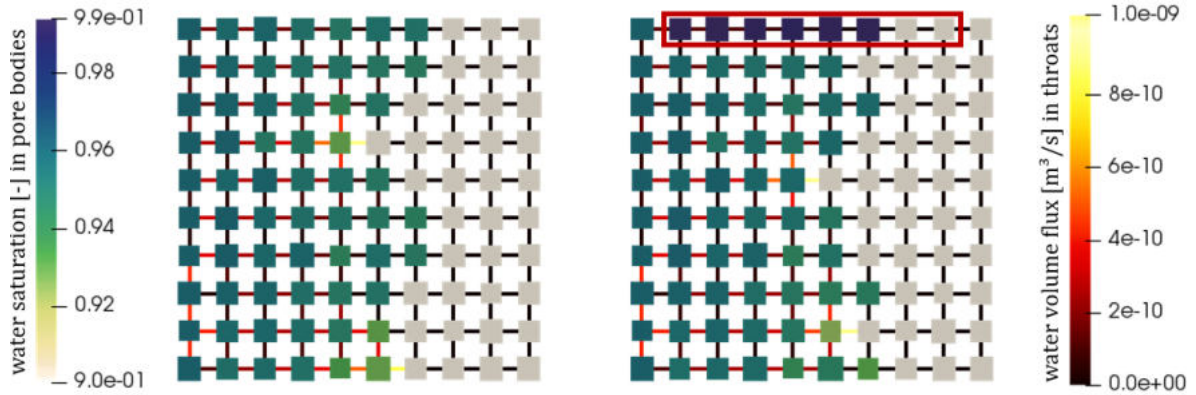


Figure 8.37: Water saturation in the network with (right) and without (left) mixed-wet boundary condition. For the saturation a range from 0.9 to 0.99 is shown but the beige pores are not invaded at the current time step ($t = 0.1s$).

The simulation results show that the mixed-wet boundary condition has a minor influence on the displacement in the overall network but a higher water saturation is stored in the mixed-wet pores. The higher storage capability results from the water configuration in the single pores as shown in Figure 4.32.

8.3.2 Application on GDL representing pore-network

The concept described above is now applied to a pore-network representing a GDL structure. We use a sample of $4\text{mm} \times 4\text{mm}$ and analyze the stationary behavior of the liquid phase distribution in the network dependent on the applied global capillary pressure. Therefore, a global phase pressure difference is applied between the inlet and the outlet ($P_c = p_n^{\text{inlet}} - p_w^{\text{outlet}}$). The liquid water saturation distribution in the pore-network representing a GDL sample at a global capillary pressure $P_c = 4060\text{ Pa}$ is presented in Figure 8.38. The inlet pores are located at the side of the GDL which represents the interface to the MPL and catalyst layer (not visible in Figure 8.38). The outlet pores lay on the side of the GDL which represents the interface to the gas distributor. Here we have a channel land structure and the outlet boundary condition is applied only to the pores located in the channel areas (green area in Figure 8.38). At the land parts, the mixed-wet boundary condition described in Section 4.4 is applied (left in Figure 8.38) or regular hydrophobic pores are defined such as in the rest of the

pore-network (right in Figure 8.38). For the whole hydrophobic pore-network a contact angle of 135° is set.

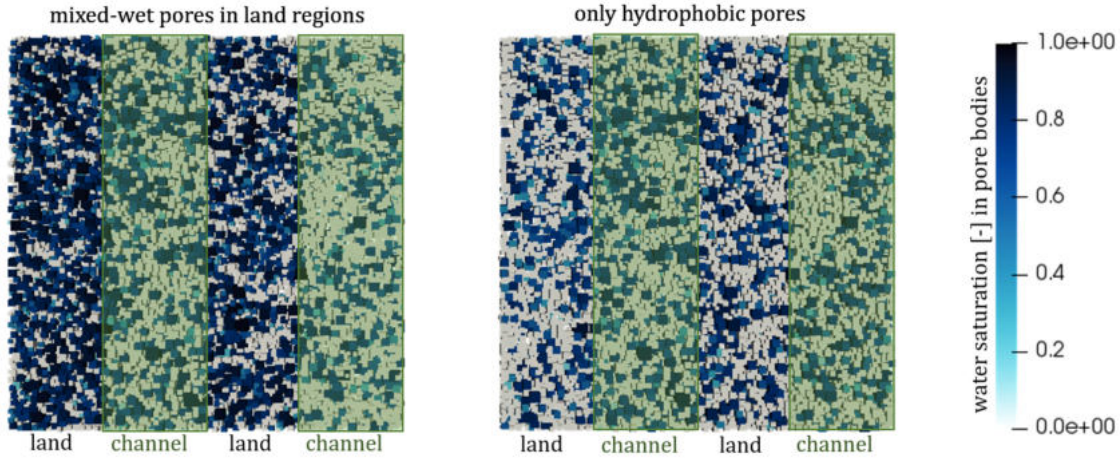


Figure 8.38: Pore-network representing a MPL-free GDL or GDB sample of $4\text{ mm} \times 4\text{ mm}$. View on the shared interface between GDL and gas distributor with the interface parts covered by channels or lands. Left: at the land parts mixed-wet pore concept is applied, the rest of the network is hydrophilic with a contact angle of 135° , right: the whole network consists of regular hydrophobic pores with a contact angle of 135° . The network is colored based on the local water saturation in the pore bodies corresponding to a static simulation with global capillary pressure of 4060 Pa.

We see a higher liquid saturation in the land regions where the mixed-wet boundary condition is applied. This setup represents the case, where a completely hydrophilic gas distributor is used in a PEM fuel cell. Here, at the land parts, the hydrophobic GDL is in contact with the hydrophilic gas distributor which results in mixed-wet pores at the interface as described in Section 4.4. On the right side in Figure 8.38, the liquid water saturation in the land part is lower than in the sample on the left side. Here, we see no difference between the liquid water saturation at the interface between GDL and channels and GDL and land parts. This sample represents a setup, where the parts of the gas distributor which are in direct contact with the GDL (land parts) are coated hydrophobic. This technique might prevent water accumulation in the GDL at the land parts of the gas distributor. Our results show that indeed the liquid water accumulation is lower in the land parts for the hydrophobic coated land parts (right in Figure 8.38) resulting from a global capillary pressure of $P_c = 4060\text{ Pa}$. In Figure 8.39, the global capillary pressure-saturation relation of a GDL with mixed-wet pores at the interface to the land parts and the one of a completely hydrophobic GDL without contact to hy-

drophilic surfaces are compared. The calculations of the capillary pressure-saturation curves are based on stationary simulations.

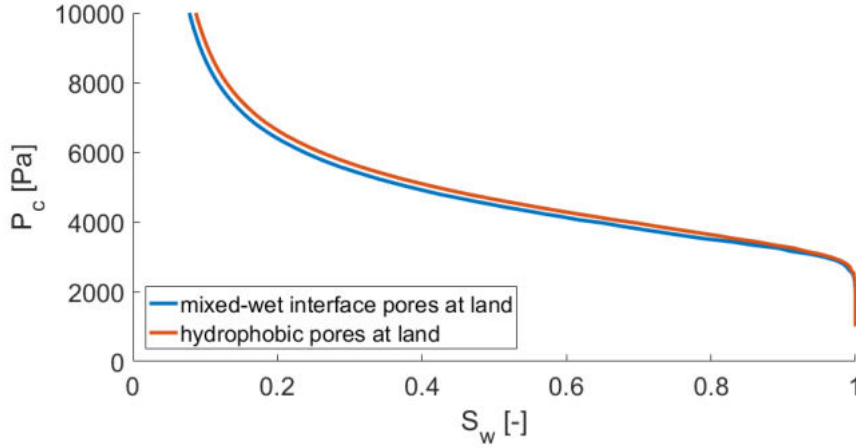


Figure 8.39: Comparison of the stationary global capillary pressure (P_c) vs. global wetting phase (gas) saturation (S_w) curves for a GDL representation including the mixed-wet pores at the land interface and the network with only hydrophobic pores. For both networks, a contact angle of 135° is applied in the hydrophobic parts.

We see a slight difference in the global saturation at different global capillary pressures but not in the capillary entry pressure for the primary invasion (first rise of P_c at S_w close to 1). This results from the different pore-local capillary pressure relations for the interface pores. Once the pore-local saturation is higher than the chosen threshold (here: $s_{\text{liq}}^{\text{th}} = 0.52$) the mixed-wet pores result in higher water contents in the interface pores at the land regions for the same capillary pressure than the completely hydrophobic pore-network.

8.3.3 Discussion

The presented interface condition allows to include mixed-wet pore bodies into the pore-network model. The results show a visible influence of these varied wetting properties of the pore bodies on the global liquid water distribution. However, the influence on dynamic flow properties is low since the water is trapped in the mixed-wet pores. This results from the derivation of the interface condition, where only the pore bodies are chosen to be mixed-wet. This assumption is justified for fibrous GDL structures

where liquid water interacts with the hydrophobic GDB and the hydrophilic gas distributor structure. Due to the compression of PEM fuel cells, the mixed-wet interaction only occurs in pore-bodies while the completely hydrophobic fibers of the GDB form the pore throats (see Section 4.4 Figure 4.30). For more general materials this interface formulation would need to be revised.

8.4 Uncoupled pore-network representing GDL with three interface configurations representing gas distributor

In the last part of this chapter, we combine the developed interface concepts in one application to a $1\text{ mm} \times 1\text{ mm}$ unit cell including a channel of width $W = 0.5\text{ mm}$ and height $H = 0.5\text{ mm}$ in the center of the unit cell and two half-ribs (rib half-width is 0.25 mm) next to it. The unit cell is visualized in Figure 8.40.

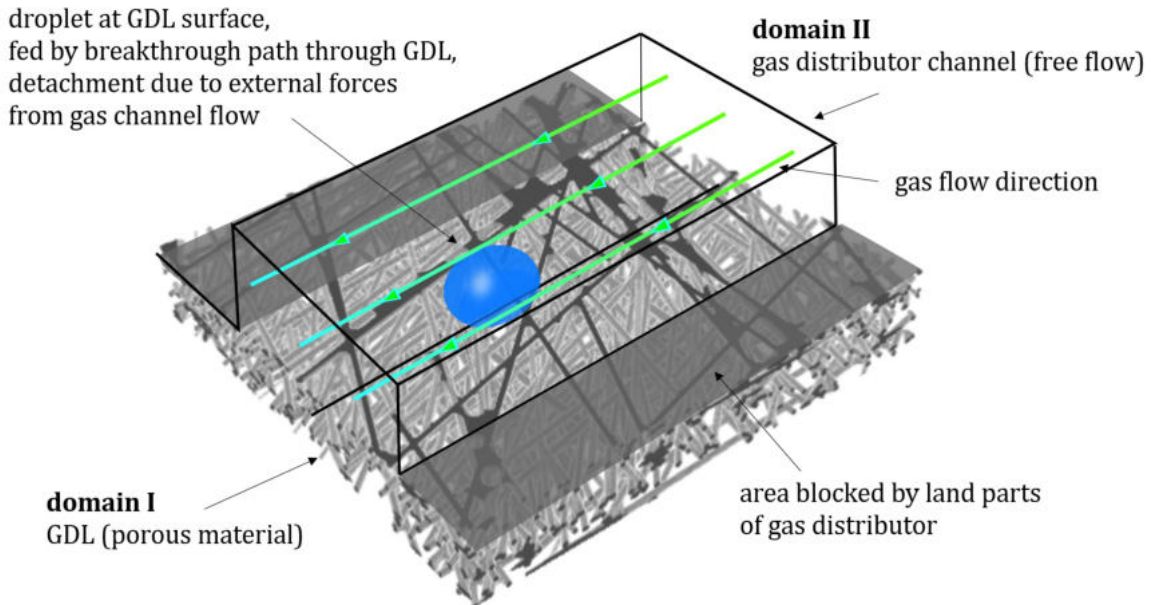


Figure 8.40: MPL-free GDL unit cell: $1\text{ mm} \times 1\text{ mm}$ MPL-free GDL or GDB sample with straight fibers $d = 9\text{ }\mu\text{m}$ and porosity 80% in combination with central channel and two half ribs. In the channel, gas flow interactions and droplet formation is considered.

The GDL structure is generated using GeoDict [98] with straight fibers of thickness $9\text{ }\mu\text{m}$ and a porosity of 80%. The thickness of the GDL is $\delta_{GDL} = 180\text{ }\mu\text{m}$ and we consider a channel height of $H = 0.5\text{ mm}$. To reduce the computation time, a sample of $1\text{ mm} \times 1\text{ mm}$ is chosen for the investigation. Note that this is not an representative elementary volume but it allows fast calculations and is sufficient to show the working concept of the presented interface drop model applied to a realistic GDL geometry.

The GDL is directly represented by a pore-network which is extracted using the open

source algorithm PoreSpy [99]. This allows pore-scale investigations corresponding to the real fiber structure of the GDL without specifying pore body and pore throat size distributions. The pore bodies are represented by cubes and the pore throats have a cross-sectional area of the shape of an equilateral triangle to account for corner flow of the wetting phase (gas) and allow contact angles up to 120° [40]. We apply a homogeneous contact angle of 135° in the whole pore-network. In Figure 8.41, the resulting pore-network with cubic pores bodies is presented. The colors indicate the size of the pore throats and pore bodies.

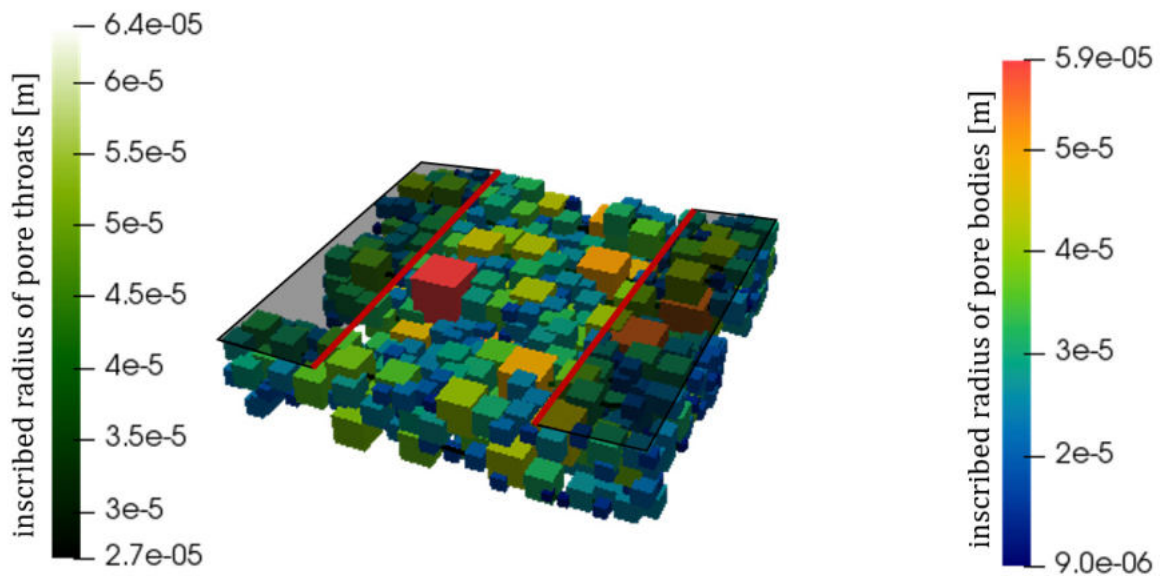


Figure 8.41: Pore sizes (inscribed radii of pore bodies and pore throats) of a pore-network representing a $1\text{ mm} \times 1\text{ mm}$ GDL sample with different boundary condition applied. Visible of the top surface, in the center a gas distributor channel is located and a boundary condition allowing the formation, growth and detachment of droplets is applied. At the red lines a condition representing the interaction of fluid with hydrophobic and hydrophilic surfaces is applied and in the grey shaded area mixed-wet pores are placed to represent the influence of hydrophilic land parts of the gas distributor.

We apply a massflux boundary condition representing the production of liquid water during the reaction. We don't take the production of water vapor into account here. All water enters the pore-network in liquid form. We use a similar boundary condition as for the single phase investigation (see Figure 7.13). The container boundary condition is used to distribute the inflow to the pore bodies at the interface between GDL and

catalyst layer. In the two-phase case, not all boundary pores are invaded by liquid water but only the largest ones where the capillary entry pressure of the throat connecting it to the inlet/container pore is low and will be overcome first. On the other side of the GDL, at the interface between GDL and gas distributor, three different domains for the occurring configurations are considered. The black shaded areas mark the land parts of the gas distributor. Here, the mixed-wet boundary pores (Section 8.3) are applied and the liquid water is trapped and cannot leave the GDL domain. The red lines mark the domain, where the hydrophobic-hydrophilic interaction (Section 8.2) is applied. All pore bodies which are crossed by the red line are connected to a hydrophilic throat with an inscribed radius $r_{ij}^{\text{interaction}}$ of the half pore body inscribed radius R_i ($r_{ij}^{\text{interaction}} = 0.5R_i$). In the center (uncovered area), the open channel boundary condition is applied where droplets can form, grow and detach (Section 8.1).

In Figure 8.42, the pore-local saturation in the pore-network is presented in the pore bodies and the volume flux of liquid water is shown in the pore throats.

As before, we see a few preferential flow paths through the small sample. Two of them are located in the center of the channel, where drops are forming (white and red throat) and one path can be found at the edge of the channel, where a hydrophobic-hydrophilic interaction condition is applied. In Figure 8.43, on the left side, the drop radii of the two droplets, which are formed in the open channel area, are plotted over time.

We see that one of the droplets is favored and is fed with a larger flux, while the other one is growing much slower. On the right side in Figure 8.43, the liquid water saturation in a pore body is presented that is interaction with the hydrophilic surface of the gas distributor edge. All interface conditions influence each other. The flux to the hydrophobic-hydrophilic interaction pore decreases with time such that the pore body is finally not filled anymore. The capillary pressure in the drop interface pores changes with growing droplet size and the fluxes in the pore-network are redistributed during the simulated time.

8.4.1 Discussion

The model which combines all developed interface configurations is able to represent a PEM fuel cell unit cell consisting of an MPL-free GDL of $1\text{ mm} \times 1\text{ mm}$, a gas distributor channel and two half channel ribs (lands) with hydrophilic surfaces. Droplets can form in the open channel part. Near by the channel side walls, the liquid water interacts with

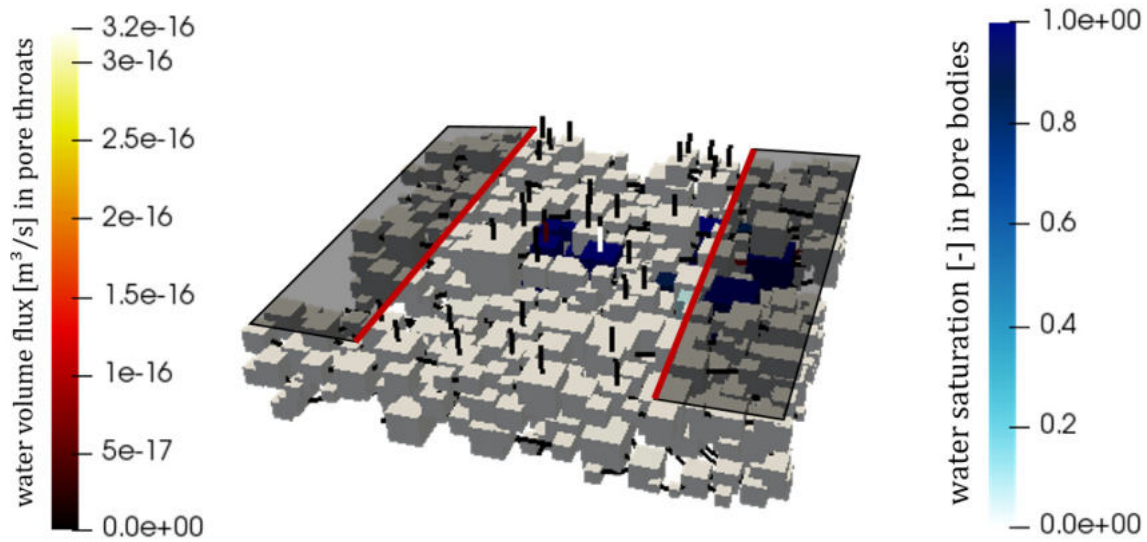


Figure 8.42: Liquid water saturation in the pore bodies and water flux in the pore throats of a pore-network representing a $1 \times 1 \text{ mm}^2$ MPL-free GDL sample with different boundary condition applied. As inlet condition a mass flux condition representing a current density of 2 A/cm^2 ($\dot{m} = 9.32 \cdot 10^{-10} \text{ kg}/(\text{m}^2\text{s})$) is chosen. In the center a gas distributor channel is located and a boundary condition allowing the formation, growth and detachment of droplets is applied. At the red lines a condition representing the interaction of fluid with hydrophobic and hydrophilic surfaces is applied and in the grey shaded area mixed-wet pores are places to represent the influence of hydrophilic land parts of the gas distributor. The visualization shows the state at $t = 1000 \text{ s}$.

hydrophobic and hydrophilic surfaces and below the land, liquid water gets trapped once in contact with the hydrophilic surface and an adapted capillary pressure-saturation relation is applied. In this small unit cell, only the basic functionality can be shown. Nevertheless, the principles can be applied to a larger sample if more computation time can be investigated.

The presented results in this section do not include direct coupling with the channel domain. The results of two different coupling methods which describe the interaction of pore-network with a channel flow are presented in the following.

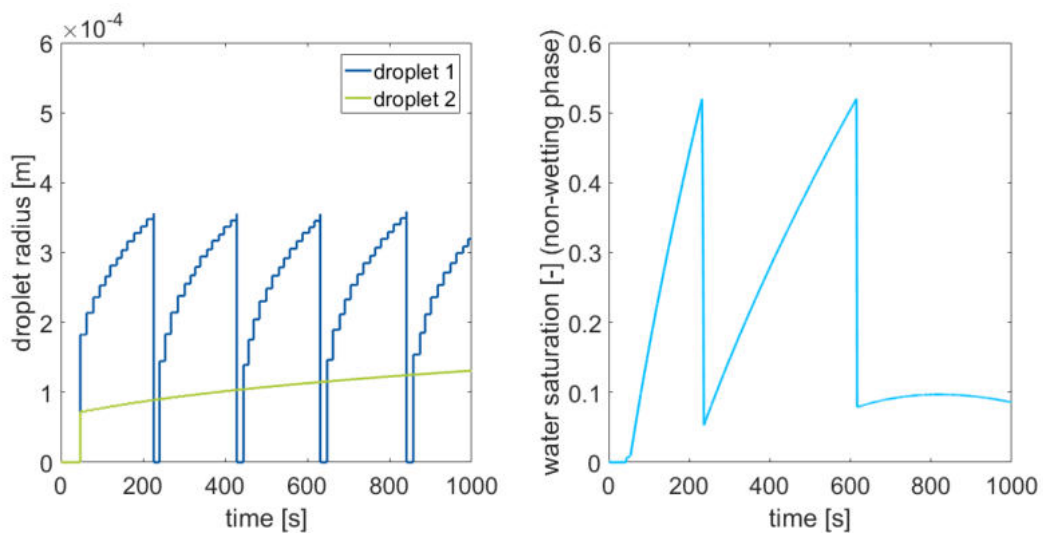


Figure 8.43: Left: drop radii of two droplets forming and growing in the channel area. The droplets are fed with different flow rates dependent on their location in the channel and the flux through the filling flow path. The faster growing droplet is detached several times during the simulation. Right: Fluctuating saturation in the pore body of pore below the red line (hydrophobic-hydrophilic interaction pore) that is invaded during the simulation.

9 Simulation results of coupled domains models

9.1 Coupling pore-network with free flow domain including drop interaction

In this section, we investigate the interaction between a pore-network Ω^{PNM} and a free flow domain Ω^{FF} . We analyze the formation, growth and detachment of droplets at the interface between the two domains. In the free flow domain, we solve the Navier-Stokes equation on a staggered-grid discretization in a two-dimensional domain. We investigate a two-phase two-components system (2p2c) in the pore-network, namely gas and liquid for the phases and water and air for the components, and single-phase two-components system (1p2c) in the free flow domain with only a gas phase consisting of water vapor and air. The free flow model is described in Section 3.2.1 and the pore-network model in Section 3.1.

In the following, different pore-networks all with a contact angle of $\theta = 145.6^\circ$ are analyzed. The surface properties for the drop interaction are defined with an advancing contact angle of $\theta_a = 120.5^\circ$ and a receding contact angle $\theta_r = 154.7^\circ$ which influence the retention force acting on the droplet (see Section 4.2.2). These dynamic contact angles are representative for common GDL surfaces [138].

The water content in the gas phase is specified by the relative humidity of the gas phase. Note that the relative humidity is defined as

$$rh = x_g^{H_2O} \frac{p_g}{p_{\text{sat}}^{H_2O}(T)}, \quad (9.1)$$

with the mole fraction of water vapor in the gas phase $x_g^{H_2O}$, the gas phase pressure p_g and the temperature-dependent saturation pressure $p_{\text{sat}}^{H_2O}(T)$.

For the multi-component investigations of a pore-network coupled to a free flow domain, all setups are chosen two-dimensional to reduce the computational costs. Since we are mainly interested in the drop formation and interaction rather than in the detailed gas flow behavior, we always couple one free flow cell to one interface pore throat of the pore-network domain.

We consider isothermal conditions with different temperatures which are specified for the single investigations described in the following.

9.1.1 Pore-network coupled with free flow including single droplet interaction

First, we evaluate the general behavior of a single droplet interacting with a two-dimensional free flow domain Ω^{FF} . The setup is presented in Figure 9.1.

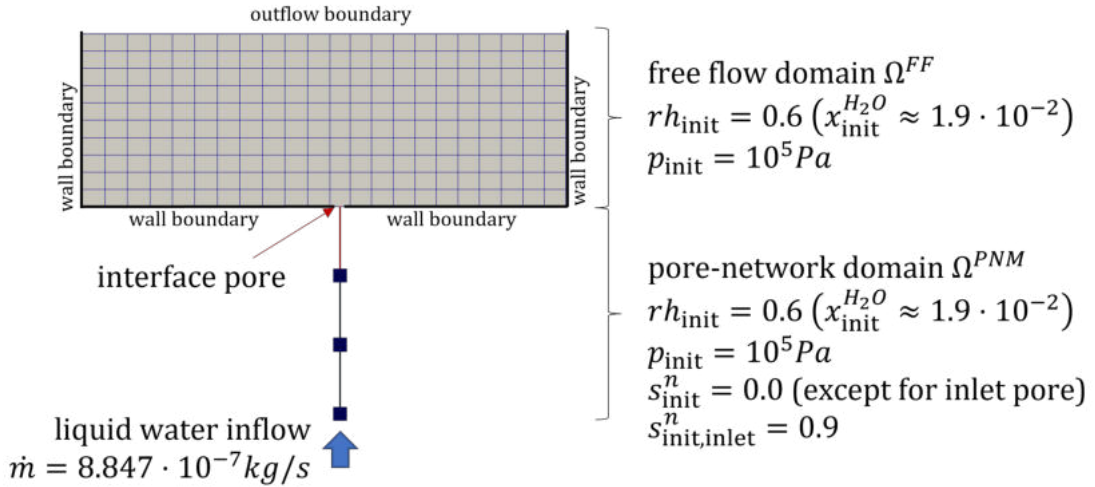


Figure 9.1: Simulation setup to investigate the behavior of a single droplet forming and growing at the interface in interaction with the free flow domain Ω^{FF} .

A small network consisting of three network pores and one interface pore is chosen for this two-phase two components (2p2c) investigation. All pore bodies have a cubic shape and the throats have a circular cross-section. The network pores have all the same size ($R_i = 1.1 \cdot 10^{-3} \text{ m}$) as well as the throat radii ($r_{ij} = 1 \cdot 10^{-3} \text{ m}$) but for the interface throat a slightly larger throat radius is chosen ($r_{\text{interface}} = 1.459 \cdot 10^{-3} \text{ m}$). The

interface pore is chosen with a larger pore body inscribed radius to allow a droplet to form and grow in ($R_{\text{interface}} = 3 \cdot 10^{-3}$ m). For this first setup, we do not apply any flow in the free flow domain Ω^{FF} . At the bottom and the sides of the domain, a wall boundary condition with no-flow/no-slip conditions is applied. The top is kept open to allow the gas to escape the simulation domain.

Initially, the pore-network is filled with gas (air and water vapor) except for the inlet pore, where an initial water saturation of $s_{\text{init,inlet}}^n = 0.9$ is applied to speed up the simulation time. However, the initial pore-local capillary pressure in the inlet pore is lower than the capillary entry pressure of the connected throat. In the gas phase a relative humidity of $rh_{\text{init}} = 0.6$ is applied as initial condition in the pore-network and the free flow domain. This represents a molar fraction of $1.9 \cdot 10^{-2}$ for water in the gas phase. The pressure of the gas phase is initialized with 10^5 Pa.

We apply a constant molar flux of liquid water of $4.9109 \cdot 10^{-5}$ mol/s into the inlet pore which represents a mass flux of $8.847 \cdot 10^{-7}$ kg/s. The liquid interacts with the gas flow by evaporation and condensation processes based on the isothermal conditions. Here, a temperature of 25°C is applied. In the considered case, the inflow flux is high enough to result in a displacement of the gas phase by the liquid phase in the pore-network. Once the liquid water reaches the interface pore, a droplet forms.

In the following, the mole fraction of water vapor in the gas phase is visualized in the free flow domain Ω^{FF} for different time steps and the liquid water saturation in the pore bodies of the pore-network. We are interested in the interface interaction and droplet formation and start the analysis at $t_1 = 3$ s (see Figure 9.2). At this time, all network pores have been invaded by the liquid water but the interface pore is still only gas filled.

At $t_1 = 3$ s, as presented in Figure 9.2, the mole fraction of water vapor in the gas phase has increased in the cell directly connected to the interface pore. This results from evaporation from the liquid surface inside the network and the resulting component transport to and across the interface to the free flow domain. Compared to the initial conditions, we see a small increase of the mole fraction of vapor water in the gas phase in the cell in contact with the interface pore of (increase of mole fraction $\Delta x_g^{H_2O} \approx 3 \cdot 10^{-6}$) and diffusive component transport through the free flow domain. The water vapor then diffuses to the neighboring cells in the free flow domain. At $t_2 = 29$ s, the interface pore is invaded by the liquid and a droplet has already formed. Now, a larger amount of water has been transferred to the gas phase in the free flow domain. This state is visualized in Figure 9.3. The mole fraction of water in the free flow cell connected to

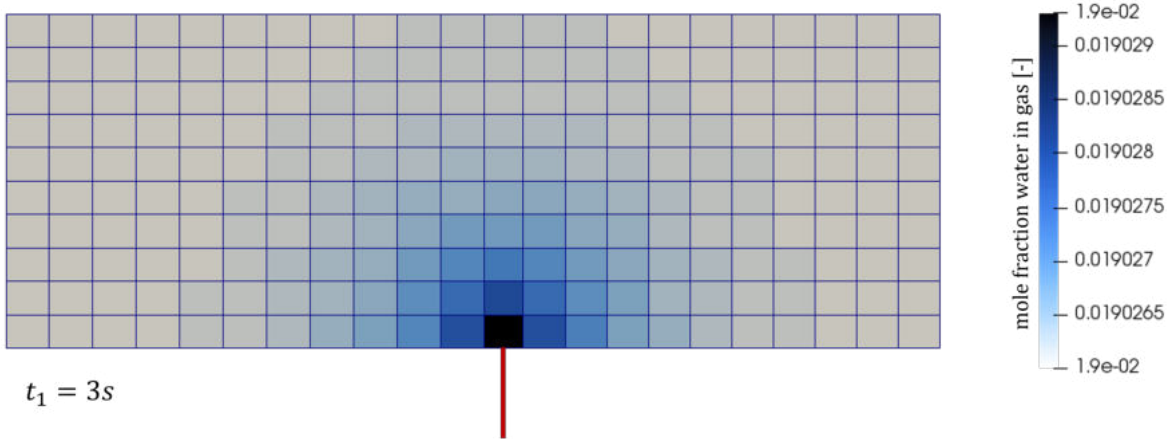


Figure 9.2: Water vapor fraction in the gas phase in the channel domain and water volume flux in the pore-network throats. For the pore bodies, the pore-local water saturation is visualized. The presented stat is at $t_1 = 3s$.

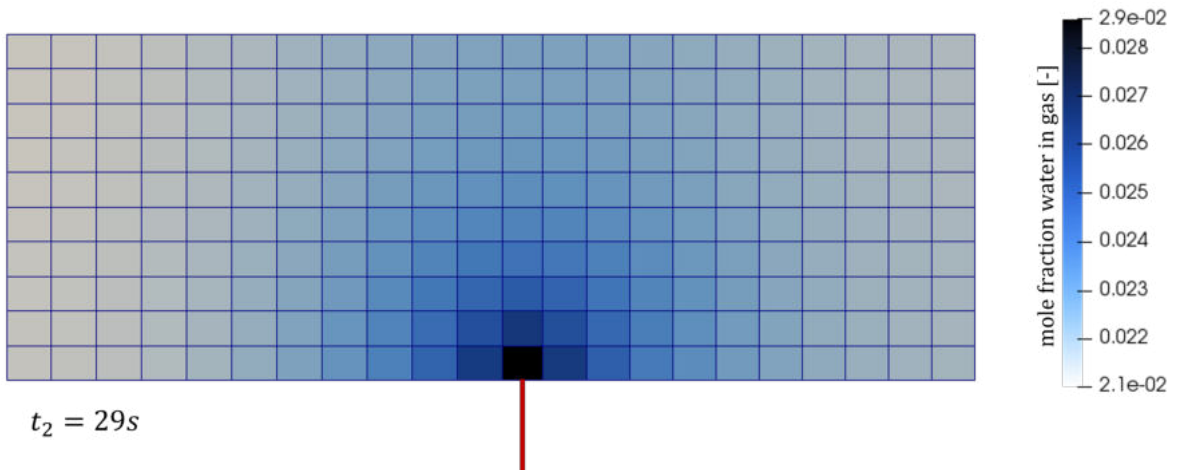


Figure 9.3: Water vapor fraction in the gas phase in the channel domain and water volume flux in the pore-network throats. For the pore bodies, the pore-local water saturation is visualized. The presented stat is at $t_2 = 29.0s$.

the interface pore increases further to $x_g^{H_2O}(t_2) \approx 2.86 \cdot 10^{-2}$. Now, the water vapor mole fraction everywhere in the free flow domain is increased.

In the next time step $t_3 = 54s$ (see Figure 9.4), we see a further increase of water mole fraction in the free flow domain due to evaporation from the drop surface. Due to the larger drop surface a larger amount of water can be evaporated but since we only have diffusive transport processes in the free flow domain in the considered setup, the water concentration in the free flow cell connected to the interface pore is higher

which results in a lower evaporation rate. The highest water concentration does not change significantly between t_2 and t_3 but the lowest water mole fraction in the domain increases to $2.35 \cdot 10^{-2}$.

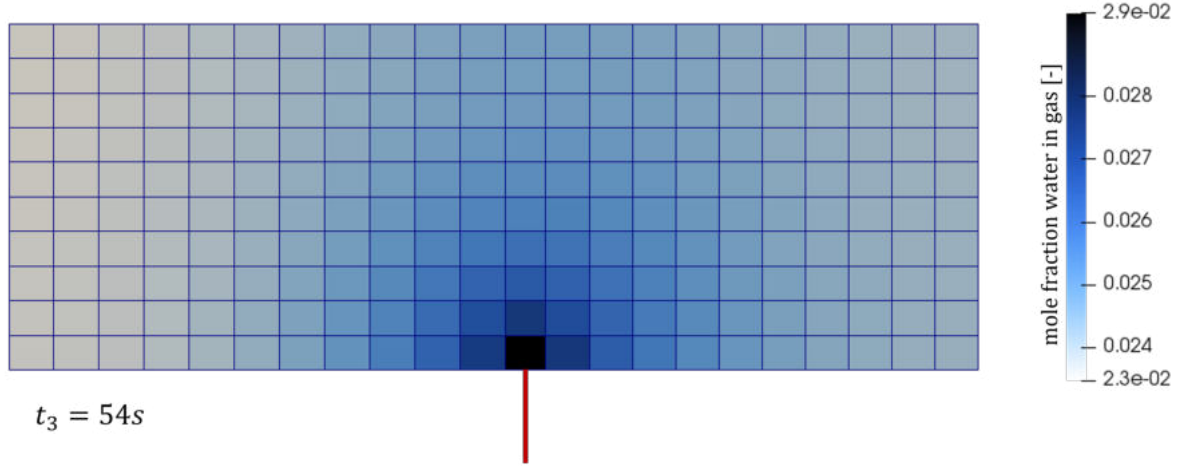


Figure 9.4: Water vapor fraction in the gas phase in the channel domain and water volume flux in the pore-network throats. For the pore bodies, the pore-local water saturation is visualized. The presented state is at $t_3 = 54$ s.

In Figure 9.5, the drop radius of the droplet forming in the interface pore is presented (2p2c PNM and 1p2c FF ($rh=0.6$)) and compared to the two-phase simulation result with no phase change nor component transport (2p PNM). The results from the two-phase simulation are shifted by 4 seconds to simplify the comparison of the curves. Additionally, the resulting drop growth of a setup with $rh = 1.0$ is plotted (2p2c PNM and 1p2c FF ($rh=1.0$)).

We see a similar behavior at the beginning of drop formation. However, the drop in the coupled system with $rh = 0.6$ (solid blue line), which includes phase change and component transport in the pore-network and the free flow domain as well as across the interface, grows slower than the droplet simulated in the uncoupled two-phase system (solid green line). This is expected since we have seen evaporation from the liquid surface to the gas phase which reduces the volume of liquid in the network and the interface pore, and therefore reduces the resulting drop radius. The results of the coupled system with $rh = 1.0$ (dashed blue line) match well with the two-phase simulation (2p PNM) (green line). Here, due to the high water vapor concentration in the gas surrounding the droplet, the drop volume is not reduced due to phase change processes. In Figure 9.5 additionally the considered time steps of the visualizations are marked.

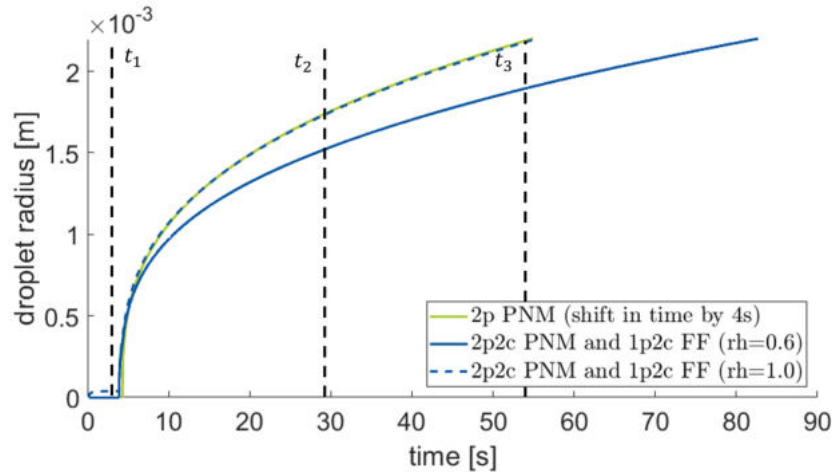


Figure 9.5: Comparison between uncoupled 2p pore-network investigation and coupled two-phase two-component (2p2c) pore-network model and single-phase two-component (1p2c) free flow model at atmospheric conditions with $T = 25^\circ\text{C}$ and $rh = 0.6$.

In Figure 9.6, the influence of temperature T and initial relative humidity rh on the drop formation and growth is shown. Different relative humidities between 0.01 and 1.0 are initially applied to both domains, respectively. For each case, simulations at 25°C and 60°C are performed. The temperature has an influence on the relative humidity

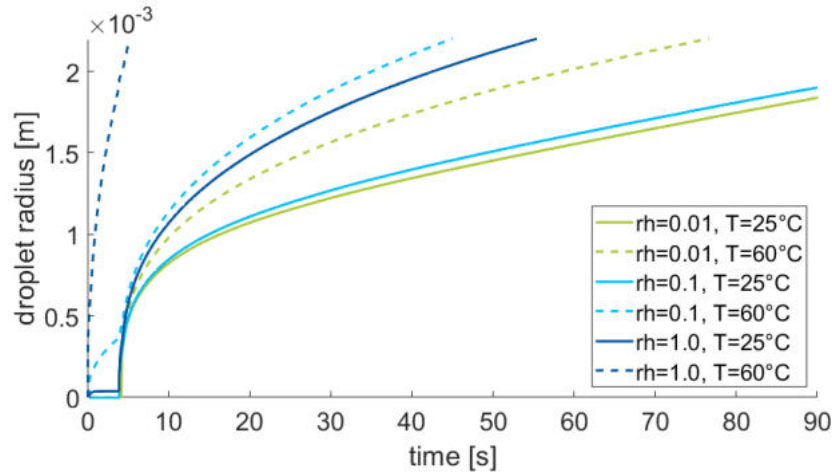


Figure 9.6: Dependence of the drop radius evolution on temperature in $^\circ\text{C}$ and relative humidity in the free flow domain.

since it depends on the saturation pressure p^{sat} . Especially for low relative humidities, we see a higher influence of temperature on the time dependent drop size than of relative humidity. The curves of $rh = 0.01$, $T = 25^\circ\text{C}$ and $rh = 0.1$, $T = 25^\circ\text{C}$ are close by each other, while we have a larger difference between $rh = 0.01$, $T = 25^\circ\text{C}$

and $rh = 0.01$, $T = 60^\circ\text{C}$. For high relative humidities at high temperature, i.e. if a lot of water vapor is present in the gas phase, we see an earlier drop formation. In this case, we see condensation processes occurring in the pore-network and also in the interface pore. The curve for the case $rh = 0.1$, $T = 65^\circ\text{C}$ shows two stages: First the drop grows due to condensation in the pore body and, starting at approximately 5 s, the inlet water flux feeds the droplet.

9.1.2 Pore-network coupled with free flow including two-droplets interaction

In this section, we extend the previously presented model by a second interface pore where a droplet can form. Additionally, we consider gas flow in the free flow domain. Wall boundary conditions are now applied at the top and the bottom of the free flow domain to form a channel. At the left side an inflow condition is applied with a constant velocity of 0.1 m/s. The simulation setup is shown in Figure 9.7. Again, we consider cubic pores with an inscribed radius of $R_i = 1.1 \cdot 10^{-3}$ m and circular throats with a radius of $r_{ij} = 10^{-3}$ m. For the interface throats, we choose different throat radii: $r_{i1} = 0.8$ mm and $r_{i2} = 0.9$ mm. Both interface pores have the same size ($R_{\text{interface}} = 3$ mm).

We increase the influx compared to the previous setup by a factor of two to a molar flux of $1 \cdot 10^{-4}$ mol/s which represents a mass flux of $1.8 \cdot 10^{-6}$ kg/s. This achieves a comparable growth rate for both droplets in the new setup as the single droplet in the previous setup. The relative humidity is initially 0.6 and we apply a temperature of 25°C . As in the previous setup, the pore-network is initially filled with gas but we use an initial water saturation of $s_{\text{init,inlet}}^n = 0.9$ in the inlet pore.

In the following, the water content in the free flow domain is presented for two different times. Figure 9.8 shows the water mole fraction in the free flow domain before drop formation at $t_1 = 5$ s.

We clearly see the influence of the gas flow. The water vapor is transported away from the interface pores to the outlet side of the channel. Nevertheless, before droplet formation (invasion of the interface pores by liquid water), the amount of water vapor transferred to the free flow domain is low. We observe a difference of $\Delta x_g^{H_2O} \approx 3 \cdot 10^{-7}$ to the initial conditions.

Some time steps later, at $t_2 = 50$ s, drops are forming in both interface pores (see

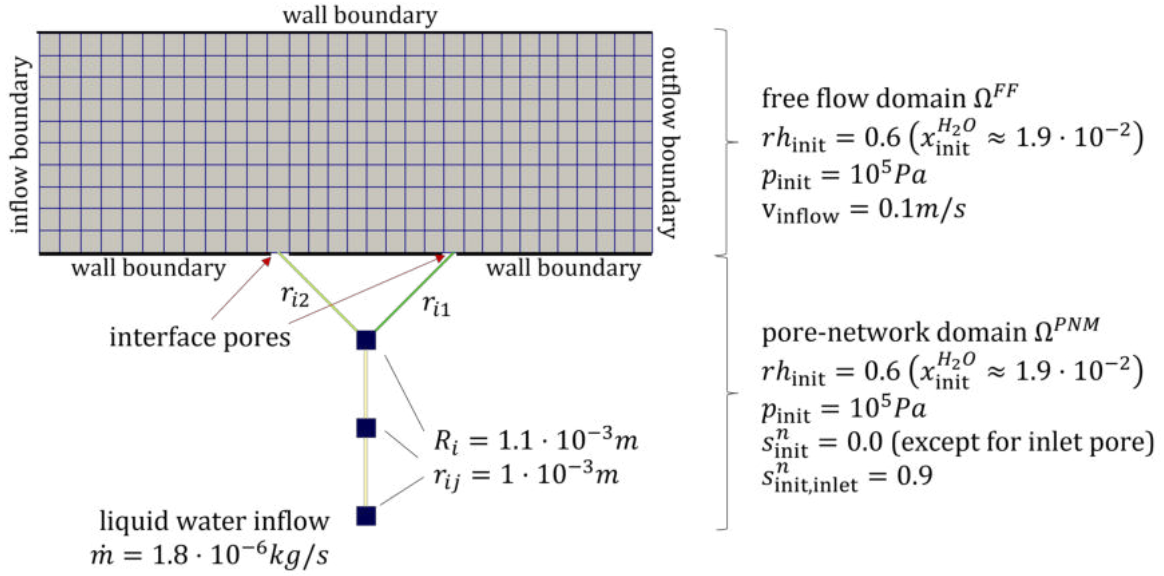


Figure 9.7: Simulation setup to investigate the behavior of two interface pores where droplets can form and grow at the interface between pore-network and free flow and interact with the free flow domain Ω^{FF} .

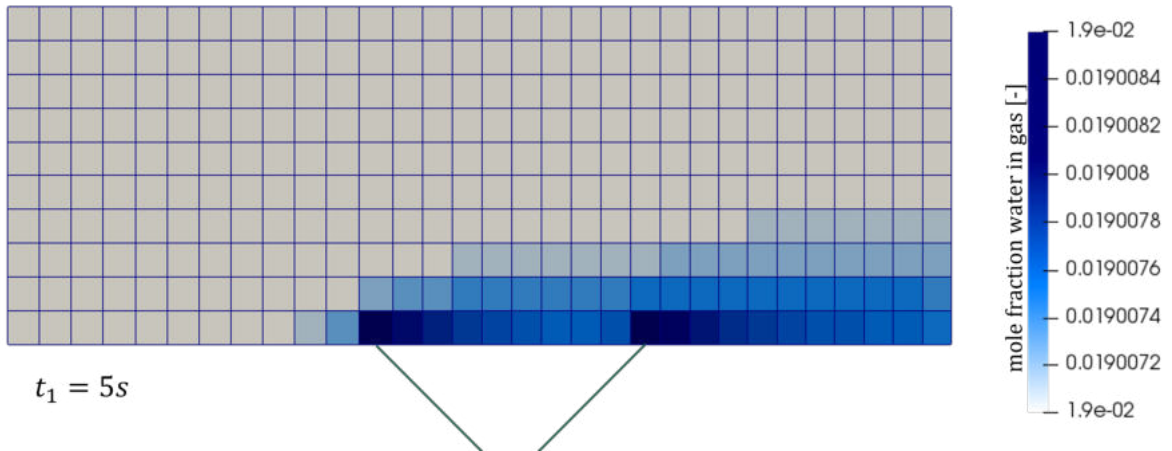


Figure 9.8: Water vapor fraction in the gas phase in the channel domain at 5 s.

Figure 9.9). The flux filling the drops differs between the two interface pores. The left drop experiences a higher liquid water mass flux $\dot{m}_1^{H_2O} = 9.11 \cdot 10^{-7} \text{ kg/s}$ than the right one $\dot{m}_1^{H_2O} = 8.54 \cdot 10^{-7} \text{ kg/s}$.

As shown in Figure 9.10, the droplets have a slightly different size at this state. Due to the gas flow from left to right, in the surrounding of the left droplet a stronger concentration gradient is established which results in stronger diffusive fluxes and more evaporation from the drop surface. The evaporated water is then transported to the

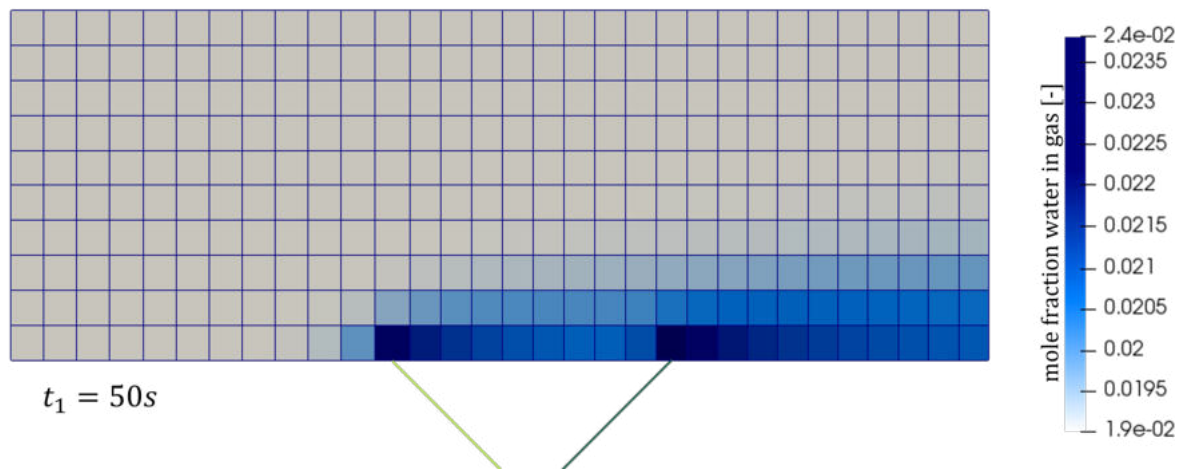


Figure 9.9: Water vapor fraction in the gas phase in the channel domain at 50 s.

right droplet which experiences a higher water concentration at the interface between pore-network and free flow domain. Therefore, we have less evaporation.

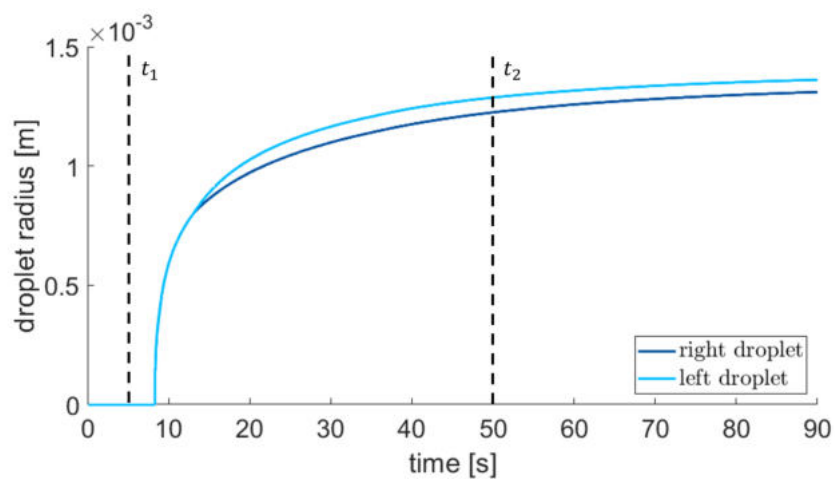


Figure 9.10: Droplet radii of both evolving droplets at the interface between pore-network and free flow domain.

In Figure 9.10 again the considered time steps are marked.

9.1.3 Regular lattice network coupled with free flow including multiple-droplets interaction

After the testing scenarios and analysis of influencing parameters, we now apply the developed model to a more complex setup. A regular structured pore-network with random pore sizes between $\min(R_i) = 7.9 \cdot 10^{-5} \text{ m}$ and $\max(R_i) = 9.1 \cdot 10^{-4} \text{ m}$ is considered. For the interface pores, we choose $R_{\text{interface}} = 2 \cdot 10^{-3} \text{ m}$. The throat radius is chosen according to neighbored pores and is between $\min(r_{ij}) = 3 \cdot 10^{-5} \text{ m}$ and $\max(r_{ij}) = 6.6 \cdot 10^{-5} \text{ m}$. We consider a channel flow from left to right with a constant gas velocity of 10 m/s at the inlet side and wall boundary conditions applied to the bottom and top setup. A finer grid resolution in flow-direction is applied to the inlet. The channel has a height of $2.5 \cdot 10^{-3} \text{ m}$. Liquid water is added to the inlet pores located at the bottom of the pore-network (blue box) by a molar flux of $4.8 \cdot 10^{-3} \text{ mol/s}$ which corresponds to a mass flux of $8.64 \cdot 10^{-5} \text{ kg/s}$. The initial relative humidity is $rh = 0.01$. The setup is shown in Figure 9.11 with numbered interface pores. With this setup not only the formation and growth but also the detachment of droplets is considered in the coupled system of pore-network and free flow domain.

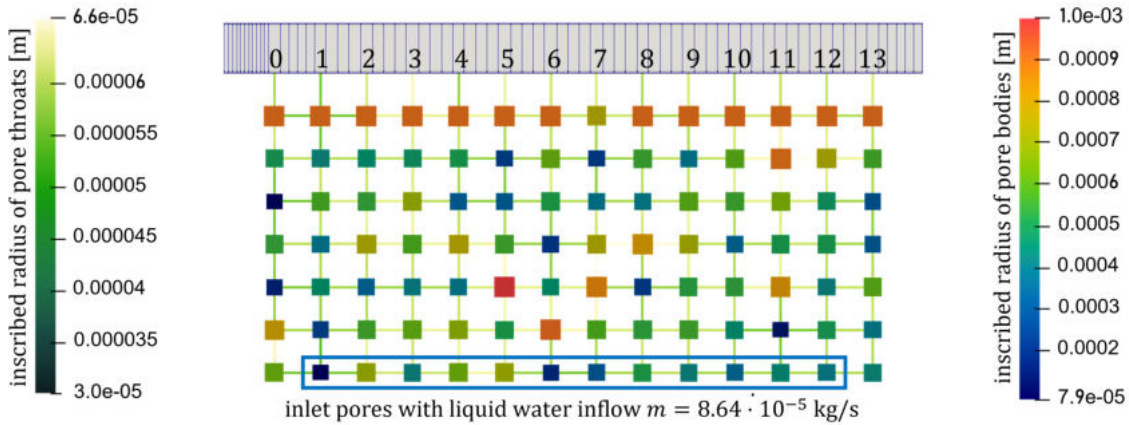


Figure 9.11: Setup to investigate the behavior of a pore-network coupled with an free flow domain including droplet formation, growth and detachment.

We apply a relative humidity of 0.01, which is a low value and results in high evaporation rates at the fluid surfaces. In Figure 9.12, the mole fraction of water vapor in the gas phase is visualized in the pore bodies and the free flow domain, while the pore throats are colored according to the gas volume flux. The figure shows the state at

0.01 s.

We see how the water concentration in the gas phase is increasing due to evaporation from the liquid phase which is injected from the bottom. We see a low concentration pore on the right side of the pore-network which probably results from numerical inaccuracies. Note that these results correspond to isothermal conditions.

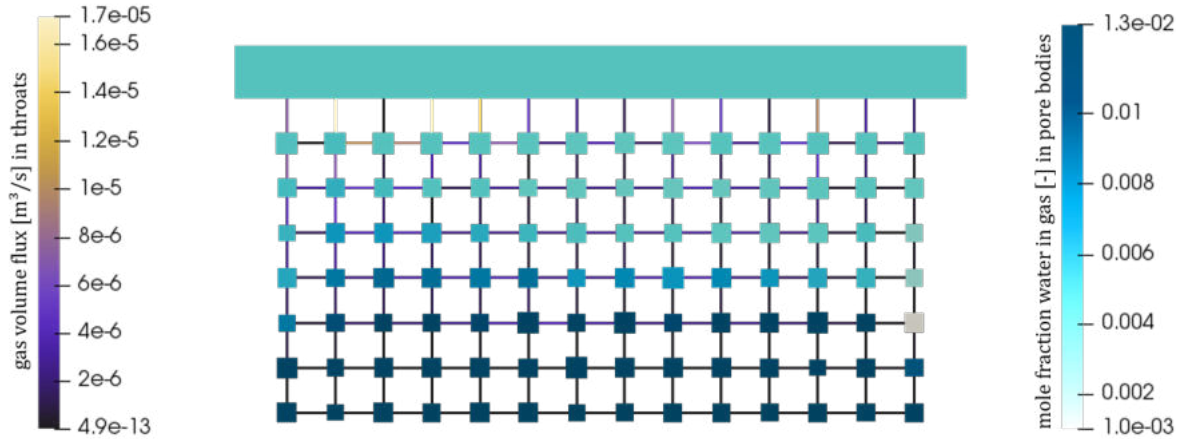


Figure 9.12: Mole fraction of water vapor in the gas phase in the pore bodies, gas volume flux through the pore throats of the pore-network. In the free flow domain again the mole fraction of water vapor in the gas phase is presented. The visualization shows the state at 0.01 s.

In Figure 9.13, the corresponding liquid water saturation in the pore bodies is presented. Here, the pore throats show the liquid phase volume flux. In the single-phase free flow domain again the mole fraction of water vapor in the gas phase is visualized. At this time step, the water vapor concentration in the free flow domain is still low, which results from the high flow velocity which transports the component out of the domain and replaces them by the low relative humidity inflow. The liquid water inflow at the bottom results in an invasion of the first pore rows dependent on the throat sizes. This results in an irregular invasion front.

The pore-network is further filled with liquid water in the following time steps as shown in Figure 9.14 for 0.02 s.

Here, the free flow still remains with low water vapor concentration.

In Figure 9.15, the configuration at 0.038 s is shown. At this time step, some of the top row network pores are invaded by the liquid water but none of the interface pores yet. We see a slight increase in the water concentration in the free flow domain ($\Delta x_g^{H_2O} =$

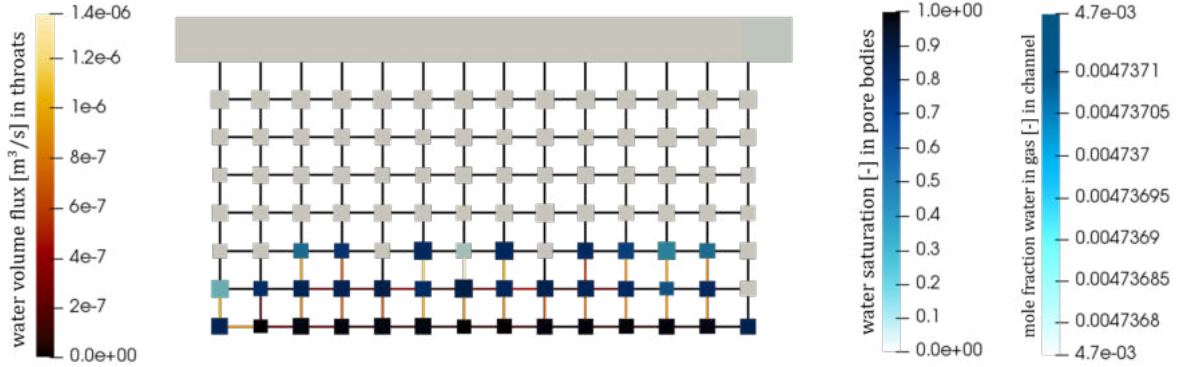


Figure 9.13: Saturation in the pore bodies, water volume flux through the pore throats of the pore-network. In the free flow domain the mole fraction of water vapor in the gas phase is presented. The visualization shows the state at $t_1 = 0.01$ s.

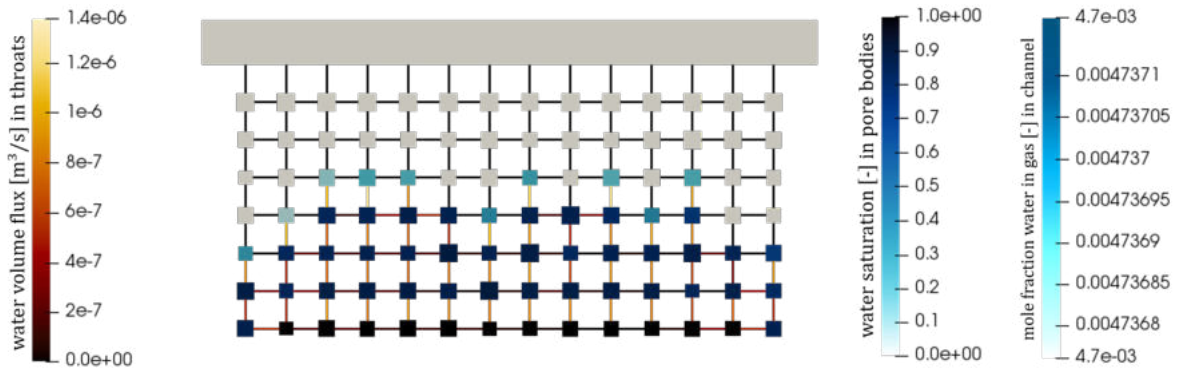


Figure 9.14: Saturation in the pore bodies, water volume flux through the pore throats of the pore-network. In the free flow domain the mole fraction of water vapor in the gas phase is presented. The visualization shows the state at $t_2 = 0.02$ s.

$3 \cdot 10^{-10}$). Once the interface pores are invaded and droplets are forming at the interface between pore-network and free flow domain, the water vapor concentration in the free flow domain increases noticeable as shown in Figure 9.16. The visualization shows the state at $t_4 = 0.043$ s. In Figure 9.18, the radii of the droplets forming at the interface between pore-network and free flow domain are visualized. For a better overview only the first drop forming in every second interface pore are plotted. Additionally, the investigated time steps are marked in the plot. At $t_4 = 0.043$ s, we see that only the interface pores at the left side (upstream direction of free flow) are invaded. This matches well with the increased water vapor concentration in this upstream part as presented in Figure 9.16.

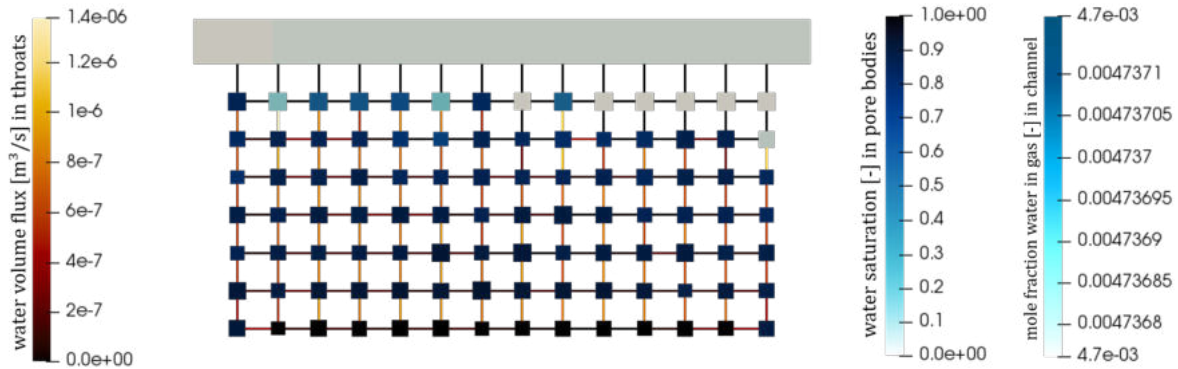


Figure 9.15: Saturation in the pore bodies, water volume flux through the pore throats of the pore-network. In the free flow domain the mole fraction of water vapor in the gas phase is presented. The visualization shows the state at $t_3 = 0.038$ s.

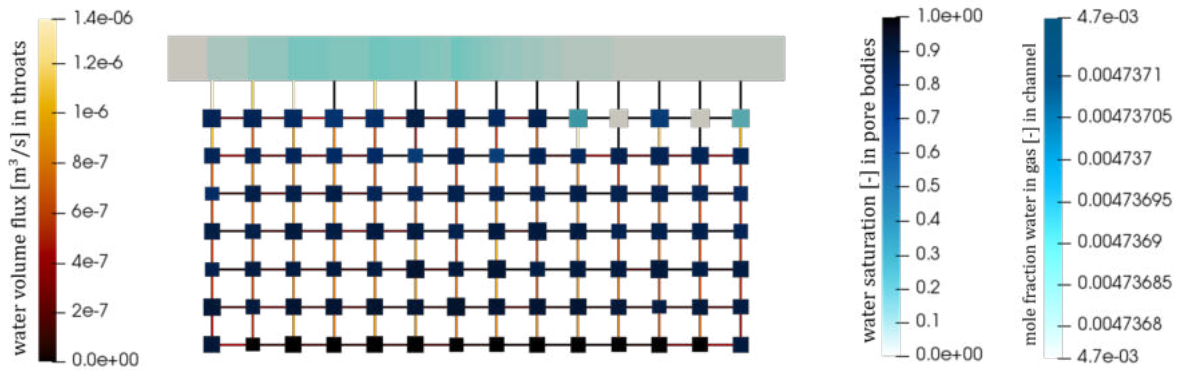


Figure 9.16: Saturation in the pore bodies, water volume flux through the pore throats of the pore-network. In the free flow domain the mole fraction of water vapor in the gas phase is presented. The visualization shows the state at $t_4 = 0.043$ s.

In Figure 9.17, the configuration at $t_5 = 0.05$ s is presented. Now, even more interface pores are invaded and more droplet contribute to evaporation into the free flow domain. The water vapor concentration accumulates downstream from several droplets resulting in the increasing mole fraction of water vapor in the gas phase downstream. However, the gradient of the concentration changes at pore 9. This results from the not-yet-invaded interface pores at the right end of the network as shown in Figure 9.18.

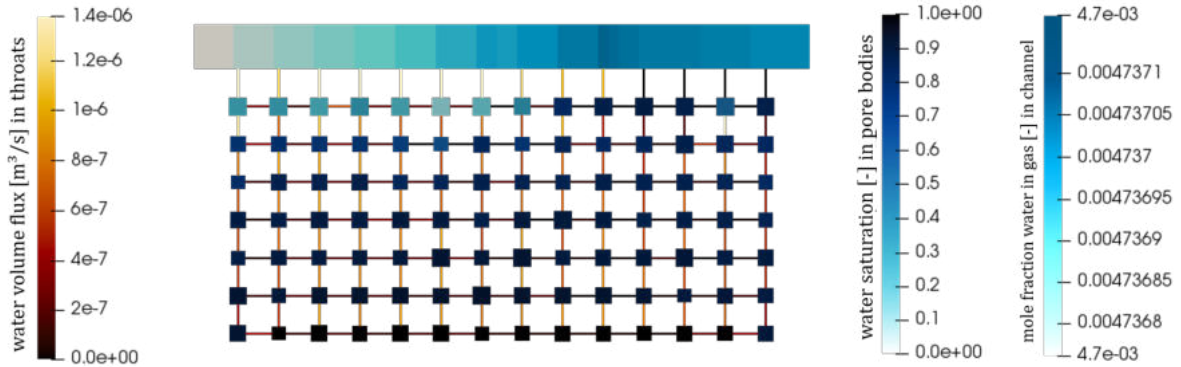


Figure 9.17: Saturation in the pore bodies, water volume flux through the pore throats of the pore-network. In the free flow domain the mole fraction of water vapor in the gas phase is presented. The visualization shows the state at $t_5 = 0.05$ s.

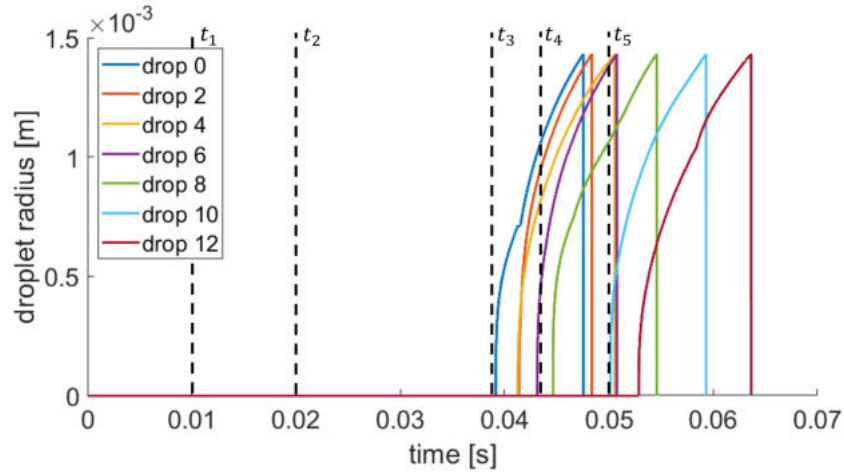


Figure 9.18: Drop radius of first droplets in the interface pores. Visualization of every second pore.

9.1.4 Discussion

The presented coupled PNM-FF model is able to capture interface processes between the pore-network domain Ω^{PNM} and the free flow domain Ω^{FF} including advective and diffusive gas transfer in interface pores that are not invaded by liquid and the formation, growth and detachment of droplets at the interface between the two domains. The single-droplet example presents how evaporation from the pore-network and especially the droplet surface is captured. Phase change takes place based on the chemical equilibrium between both phases. We observe a diffusive mixing in the domains and at the

interface between gas and liquid based on the local concentrations and diffusion coefficients. The phase diffusion coefficients depend on the phase's composition, temperature and pressure. At the interface Henry's law is fulfilled with the temperature dependent Henry coefficient H . As shown in Figure 9.6, the model is able to capture the influence of ambient temperature and relative humidity on the drop growth behavior.

The second example (Section 9.1.2) shows that also the influence of gas flow in the channel and the interaction of multiple droplets can be investigated with the presented model. The evaporation from the upstream droplet's surface influences the behavior of the downstream drop due to its location in the water vapor plume.

In the last example (Section 9.1.3), the pore sizes (pore bodies and throats) have a similar size as the largest pores we observe in the considered MPL-free GDL representing pore-networks but a less heterogeneous pore size distribution is chosen. Heterogeneous pore and throat sizes cause numerical issues that result in tiny time step sizes or divergence of the solvers. An explanation for this behavior might be the occurrence of Haines instabilities which are sudden jumps of the fluid interface once the capillary entry pressure is overcome and are accompanied by fluid redistribution and a transient pressure response. The Haines jumps result locally in high fluxes through the pore throats and short but large pressure fluctuations. These transient pressure fluctuations influence the local chemical equilibrium which has to be adapted quickly. In a heterogeneous pore-network, Haines jumps occur at multiple time steps in different locations while in a homogeneous network, the pore body rows are invaded simultaneously.

A low water vapor concentration is applied initially to encourage evaporation rather than condensation in the pore-network. Therefore, high liquid water influxes are applied to the inlet pore bodies. Liquid water breakthrough occurs at several locations at the interface Γ^{FF} between pore-network Ω^{PNM} and free flow domain Ω^{FF} . Here, droplets are forming, growing and are finally detached by the drag force resulting from the gas flow in the free flow domain Ω^{FF} .

Difficulties arise when the model is applied to a realistic GDL pore-network. From experience it is known that droplets, which form from the produced excess water in the PEM fuel cell, only occur in the downstream parts of the gas distributor channels. Here, the water vapor concentration in the gas flow is too high to take up the water in vapor form. This means, we expect droplets to form on the PEM fuel cell cathode only at high water vapor concentrations in the gas phase or for very high water production rates which are above the representative range for PEM fuel cell operating conditions. High water vapor concentrations in the gas phase result in condensation in the pore-

network pores with unconnected liquid phase. Condensation is favored in the smallest pores where the pore-local capillary pressure is highest. Here, the saturation pressure is lowered following the Kelvin equation [139]

$$p_{\text{sat,Kelvin}}^{\kappa} = p_{\text{sat}}^{\kappa} \exp\left(-\frac{p_c M^{\kappa}}{\rho_{\text{liq}} R_{H_2O} T}\right),$$

with the saturation pressure of the component κ , p_{sat}^{κ} , the pore-local capillary pressure p_c , the molar mass of the component M^{κ} , the liquid phase density ρ_{liq} , the gas constant for water vapor $R_{H_2O} = 461.6 \text{ J}/(\text{kg K})$ and the temperature T . Nevertheless, in the smallest pore, small non-wetting phase (liquid) saturation already result in relatively high pore-local capillary pressures. If this small pore is connected to another pore by a throat with relatively large cross-sectional area, this throat might be invaded by the liquid phase due to the condensation process. This results in percolation paths of small pores which have a high resistance and high snap-off tendency. The high resistance to the liquid phase flow makes these paths not favored for droplet formation at the interface but increases the risk of numerical instabilities. Therefore, to investigate the formation of droplets in a coupled system of pore-network representation of MPL-free GDL and gas distributor channel, a two-phase simulation is favored neglecting the influence of multi-component transport and phase change. The results of this investigation are presented in the following section.

9.2 Coupling pore-network with REV-model domain including drop interaction

In this section, we investigate the interaction of a pore-network with an REV domain. In contrast to the previous section, here, a two-phase model is used in the channel representing REV domain but we do not consider component transport nor phase change, i.e. coupling of 2p pore-network with 2p REV domain.

Again, we are interested mainly in the interface processes between the pore-network and the channel representation which is an REV domain, here. For the droplet interaction again the following contact angles are applied: $\theta = 145.6^\circ$, $\theta_a = 120.5^\circ$ and $\theta_r = 154.7^\circ$ [138].

The porosity Φ is always set to 1.0 to represent an open channel. For the intrinsic permeability, we use an approximation based on the Poiseuille equation for a cylindrical tube

$$Q = \frac{\pi r^4 (p_{in} - p_{out})}{8\mu_g L},$$

with the gas phase volume flux Q , the tube radius r , the inlet and outlet gas phase pressures, p_{in} and p_{out} , respectively, the gas phase dynamic viscosity μ_g and the tube length L .

Comparing this formulation to the Darcy equation Section 3.2.2, yields a representing intrinsic permeability K of the tube

$$K = \frac{\pi r^4}{8}, \quad (9.2)$$

with the hydraulic radius of the channel $r = 2A/P$, the area A and the perimeter P of the cross-sectional area. This is now applied to the rectangular channel.

In all examples, we consider isothermal conditions at a temperature of 60°C .

In the following, first, a setup with a single droplet forming at the interface between pore-network and REV domain is presented. Here, we investigate the droplet growth and compare the results to the uncoupled setup as well as the drop detachment and two-phase transport in the REV domain. Afterwards, the interaction of several droplets in a small network is considered. In the last section, we show the two-phase interaction of a pore-network representing a GDL sample with a REV domain representing a gas

distributor channel including droplet formation, growth and detachment.

9.2.1 Regular lattice network coupled with Darcy flow including single droplet interaction

For the single-droplet investigation, the same pore-network is used as for the uncoupled setup (see Figure 8.1), which allows a direct comparison of the uncoupled and coupled results. We use cubic pore shapes (pore inscribed radius $R_i = 3.745 \cdot 10^{-4}$ m, interface pore inscribed radius $R_{\text{interface}} = 0.003$ m) and pore throats with circular cross-sectional area (pore throat radius $r_{ij} = 7.5 \cdot 10^{-5}$ m, interface throat radius $r_{\text{interface}} = 1.459 \cdot 10^{-3}$ m). The pore-network is coupled with a REV domain at the interface pore, where a droplet can form. The REV domain has the following dimensions: $x = 12$ mm, $y = 10$ mm, $z = 3$ mm, with a grid resolution of $10 \times 1 \times 2$ cells. From Eq. (9.2), we get a permeability of $2.3 \cdot 10^{-3}$ m². The setup is visualized in Figure 9.19.

The pore-network is initially invaded by the non-wetting liquid phase with a pore-local saturation of 0.1 in each pore body. In the inlet pores a liquid phase saturation of 0.9 is applied to speed up the simulation time. In the REV domain initially no liquid water is present. Both domains are initialized with a gas phase pressure of 10^5 Pa. As inlet condition, a mass flux of $9.833 \cdot 10^{-8}$ kg/s is applied to each pore. The overall liquid water inflow into the pore-network equals the source flux used in the experiment and uncoupled simulation (see Section 8.1.1). In the REV domain, we apply Neumann conditions for the inlet with an influx of gas of 20 kg/(m²s) and of liquid of 0.001 kg/(m²s). At the outlet Dirichlet conditions are applied to create an outflux condition with zero liquid saturation and a gas pressure of $p_g^{\text{out}} = 10^5$ Pa. This results in a flow from front left to back right.

In Figure 9.20, the resulting drop growth is compared to the drop growth in the uncoupled setup.

We see a different behavior at the beginning of the drop formation which might result from numerical inaccuracies at the coupling with low water saturation in the interface pore. Nevertheless, the overall behavior shows a good match between the coupled and the uncoupled setup with respect to the drop growth.

In Figure 9.21, the behavior of the system after the first drop detachment is presented in three different time steps. The saturation in the REV domain is locally increased

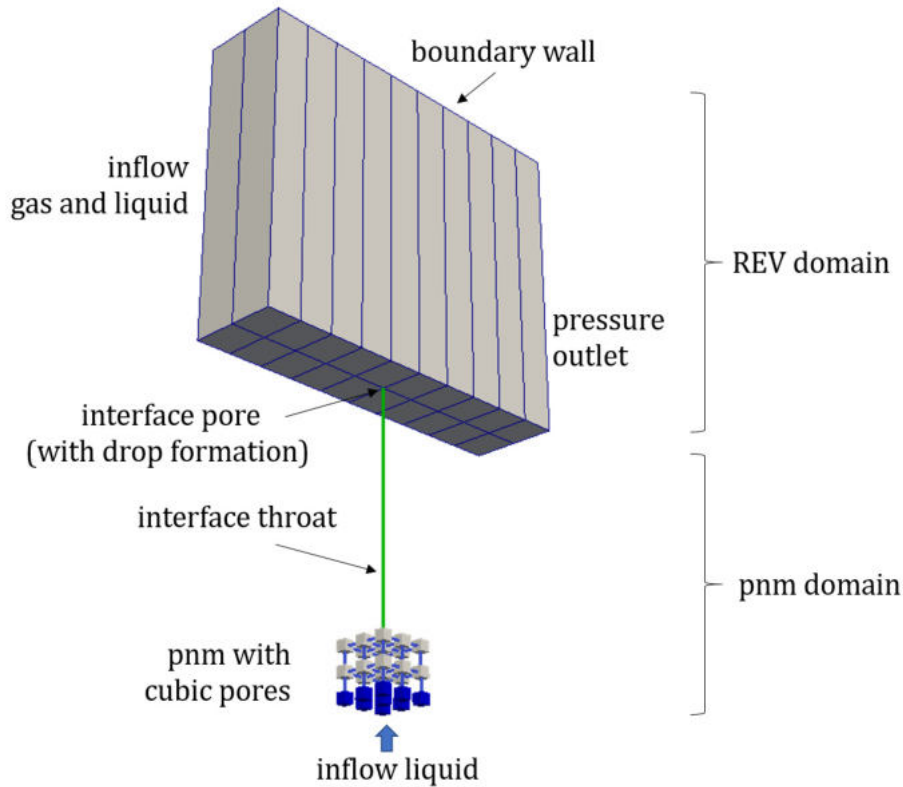


Figure 9.19: Setup to investigate the behavior of a pore-network coupled with an REV domain including droplet formation, growth and detachment. Here, only the occurrence of a single droplet is considered.

due to the liquid phase source from the drop detachment. Due to the gas flux in the channel, the liquid phase is transported out of the domain based on the relative permeabilities (see Eq. (3.33)). We also observe some spreading due to the applied capillary pressure-saturation relation.

In the pore bodies of the pore-network, the pore-local liquid phase saturation is shown. The outer pores in the top row contain low water saturation since the liquid water can easily leave the pore-network domain through the relatively wide interface throat (green) and is not pushed to the pores in the edges.

In Figure 9.22, several periods of drop formation, growth and detachment are visualized. Right after the detachment, a new drop is forming in the interface pore. Here, this is due to the very simple network and the constant inflow at the inlet pores. Since the interface throat stays invaded, the new drop radius grows fast again.

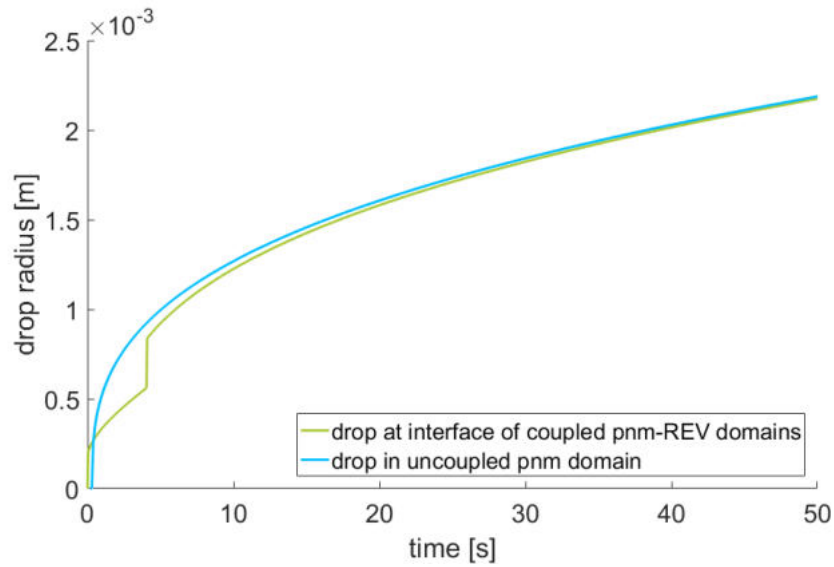


Figure 9.20: Radius of droplet forming, growing in the interface pore at the coupling interface between pore-network and REV domain compared to a droplet forming and growing in an uncoupled pnm (see Section 8.1.1 Figure 8.2). The droplet formation and growth is not influenced directly by the REV domain but the pore gas pressure is coupled with the REV domain gas pressure.

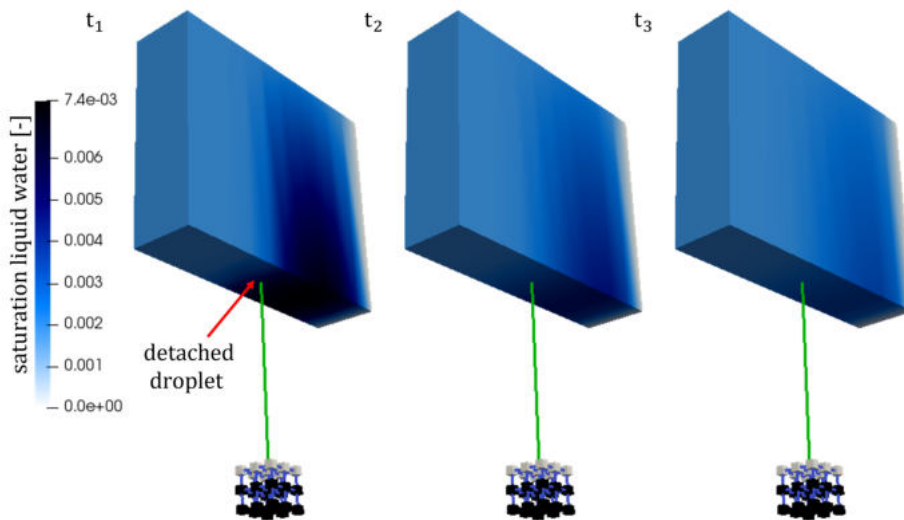


Figure 9.21: Liquid phase saturation (water) in the REV domain and the pore-network (dark pores with higher saturation than scaled) right after the detachment of a droplet which has been formed in the interface pore. The visualizations show three time steps after detachment ($t_1 = 64.5$ s, $t_2 = 65.5$ s and $t_3 = 66.5$ s).

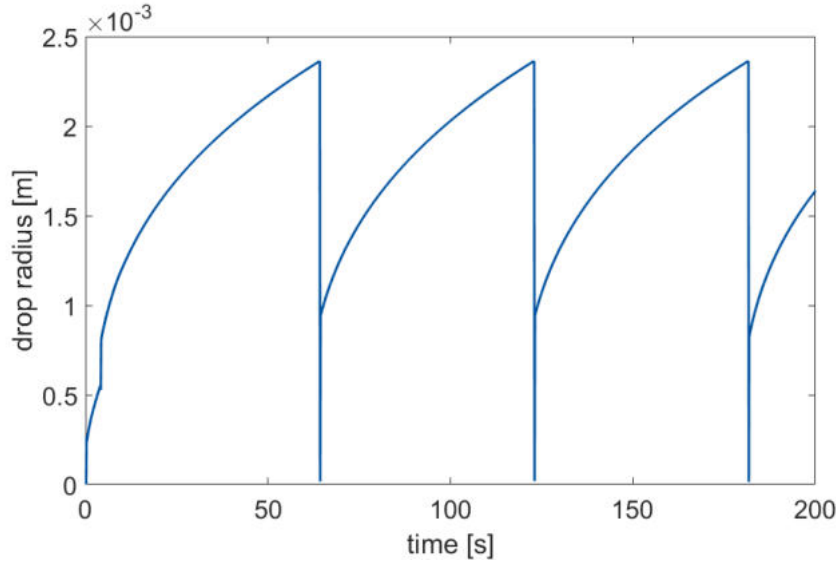


Figure 9.22: Radius of droplet forming, growing and detaching in the interface pore at the coupling interface between pore-network and REV domain. The droplet is detached based on the gas flow velocity in the REV domain.

9.2.2 Simple pore-network coupled with Darcy flow including multiple-droplets interaction

After the description and evaluation of a single droplet interaction, we apply the developed concept to a multiple-droplets setup. Here, three interface pores of a small pore-network interact with the REV domain representing a flow channel. The investigated setup is presented in Figure 9.23. The visible pore bodies have an inscribed radius of $R_i = 5 \cdot 10^{-4}$ m and pore throat radii of $r_{ij} = 5 \cdot 10^{-5}$ m. The interface pores (not visible in Figure 9.23) have an inscribed radius $R_{\text{interface}} = 0.005$ m. The three interface pores are fed by interface throats with different radii $r_{i1} = 3 \cdot 10^{-5}$ m, $r_{i2} = 2.8 \cdot 10^{-5}$ m and $r_{i3} = 2.5 \cdot 10^{-5}$ m. The numbers of the interface pores are labeled in Figure 9.23. The REV domain has the following dimensions ($x = 30$ mm, $y = 11$ mm, $z = 10$ mm) and is discretized with a resolution of $30 \times 1 \times 5$ ($x \times y \times z$) cells. The permeability is again calculated based on Eq. (9.2) and results in $k = 2.6 \cdot 10^{-3}$ m². We consider flow from right to left in the REV domain. Here, we apply Neumann conditions defining the inflow of liquid and gas (water and air), $q_{\text{liq}}^{\text{in}} = 20$ kg/(m²s) and $q_{\text{gas}}^{\text{in}} = 1$ kg/(m²s). At the outlet Dirichlet conditions are applied to create an outflux condition with zero liquid saturation ($S_{\text{liq}}^{\text{out}} = 0.0$) and a gas pressure of $p_g^{\text{out}} = 10^5$ Pa. This results in a gas flow velocity of approximately 16 m/s.

The pore-network is initially invaded by the non-wetting liquid phase with a pore-local saturation of 0.1 in each pore body. In the inlet pores, an initial liquid phase saturation of 0.95 is applied to speed up the simulation time. As a boundary condition an inflow of 10^{-4} kg/s is set. In the REV domain initially a liquid water saturation of 0.03 is present. Both domains are initialized with a gas phase pressure of 10^5 Pa. As inlet condition a mass flux of 10^{-4} kg/s is applied to each inlet pore. The overall liquid water inflow into the pore-network again equals the source flux used in the experiment and uncoupled simulation (see Section 8.1.2). The maximum time step size is set to $\max(\Delta t) = 10^{-3}$ s.

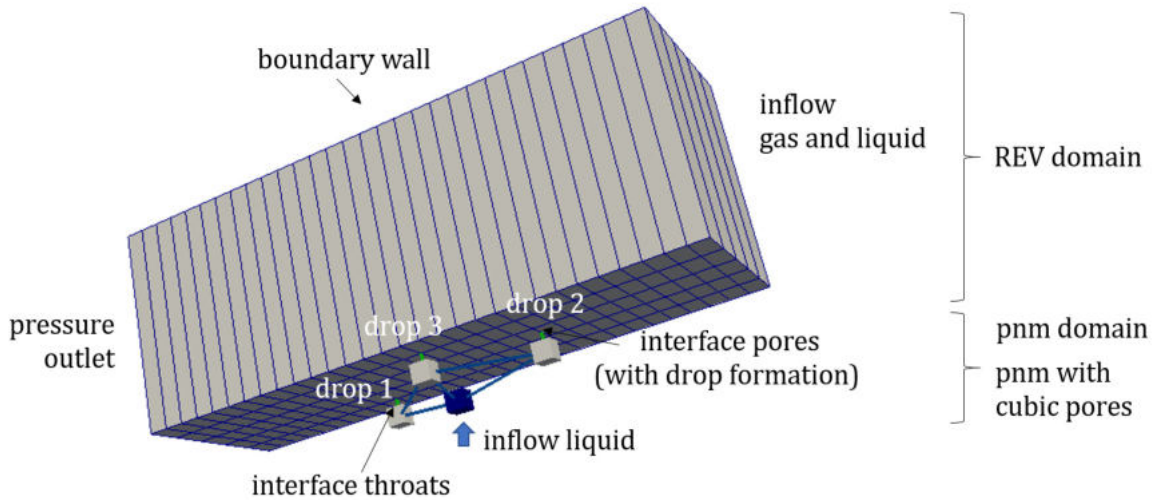


Figure 9.23: Setup to investigate the behavior of a pore-network coupled with an REV domain including droplet formation, growth and detachment at multiple interface throats. Here, the occurrence of three droplets at the interface is considered.

In Figure 9.24, the fluid configurations at six different time steps are presented. In Figure 9.25, we see the evolution of the drop radii during the simulation time. The time steps shown in Figure 9.24 are marked.

In Figure 9.24, in the channel-representing REV domain, the liquid water saturation is shown. At t_1 , we observe the initial conditions still present in the whole domain. At t_2 , droplets have been detached and we see a local increase in the liquid water saturation, which is transported out of the domain to the outlet of the channel in the back left. The time steps t_1 , t_2 , t_3 and t_4 are close together and we can observe the detailed behavior of liquid phase saturation in the channel domain after the drop detachment. At the detachment, the liquid water volume of the droplet has been transferred from the pore-network to the REV domain. However, due to the flow applied to the channel

representation (REV domain), the liquid water is transported out of the domain such that we return to the initial saturation as presented in t_6 . At t_5 , some liquid phase saturation can still be found near the outlet. Nevertheless, the time step t_6 presents a time step after which another drop detachment occurs (see Figure 9.24). Therefore, we observe a repeating behavior for this simplified setup including multiple-droplets formation, growth and detachment.

Taking a more detailed look at the drop radii of droplets occurring in the three interface pores, we realize that the droplets grow with different rates but all detach at the same simulation time for the first time. This behavior might result from pressure and flux fluctuation at the beginning of the simulation before the setup is fully equilibrated. The detachment of all droplets at the same time can also be observed in Figure 9.24, where we see a strong increase of the saturation in the REV domain at the REV nodes near the interface pores. Afterwards, the droplets detach at a certain drop size dependent on the channel flow velocity (here approx. 16 m/s). After the first detachment, the droplets detach one by one following the drop growth rates which depend on the interface throat properties. The detachment of single droplets result in a similar behavior as presented in Figure 9.24 but with an increase of the local liquid phase saturation only near one interface pore such that the overall increase in liquid phase saturation in the REV domain is less strong.

In Figure 9.25, we clearly see how drop 3 has the fastest growing rate, which results from the largest interface throat radius.

9.2.3 GDL representation coupled with gas distributor channel

In this section, we now apply the developed coupling concept to a pore-network representing a sample of a GDL structure which is exchanging fluids with a channel of a gas distributor. The gas distributor channel is represented by a REV domain. We chose an extension of the channel domain in downstream direction to be able to observe the liquid water transport after drop detachment in the channel.

First the details of the considered setup are described. A visualization of the setup is presented in Figure 9.26.

The pore-network is extracted from a MPL-free GDL sample structure generated using GeoDict®[66]. The details on pore-network generation are described in Section 3.1.4. The resulting size of the pore bodies of the pore-network is indicated by the colors in

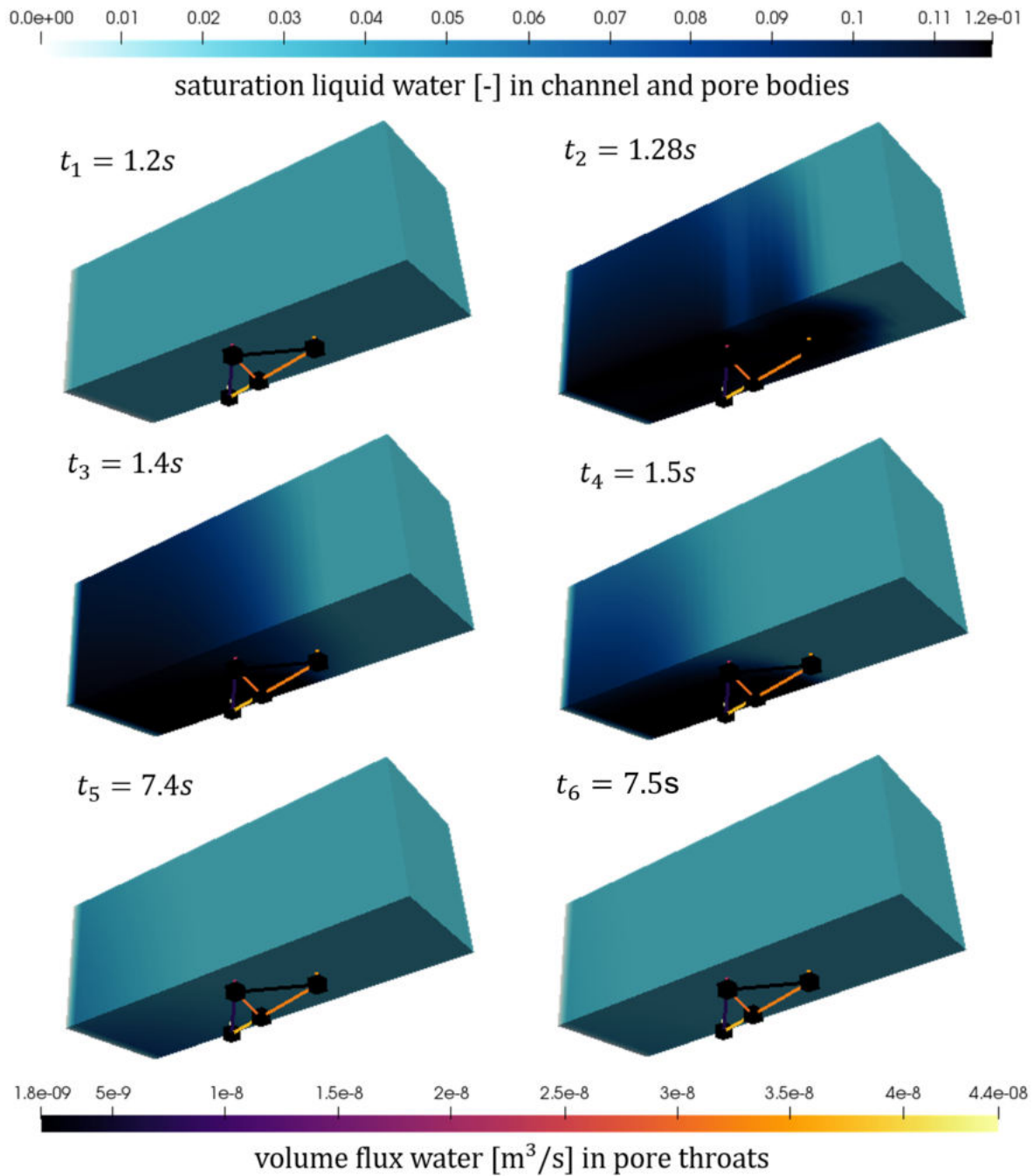


Figure 9.24: Liquid water saturation in the channel (REV domain) and the pore bodies of the pore-network. The saturation is scaled for the channel. The saturation in the network pores is approximately $s_{liq} = 0.99$. The pore throats are colored according to the volume flux of liquid water passing through them. Different time steps before and after drop detachment are shown.

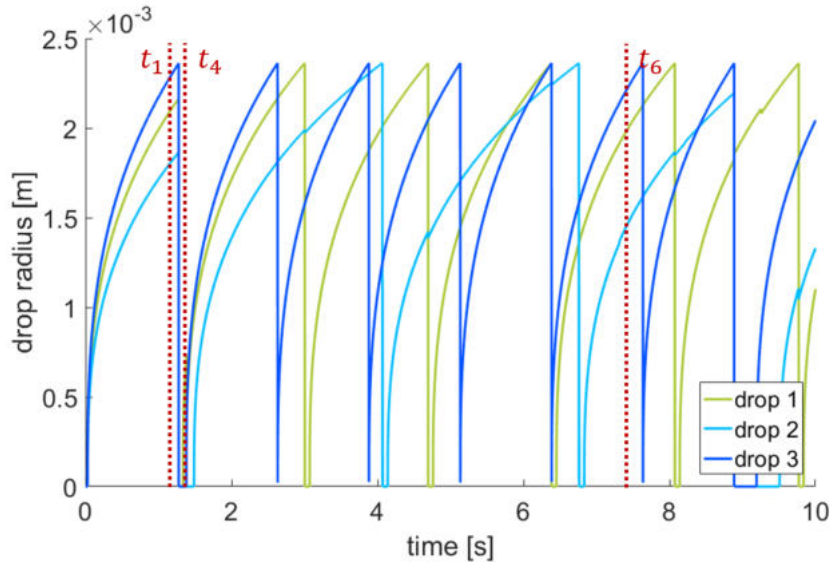


Figure 9.25: Drop radii of the three droplets forming in the interface pores. The red dashed lines refer to the time steps visualized in Figure 9.24.

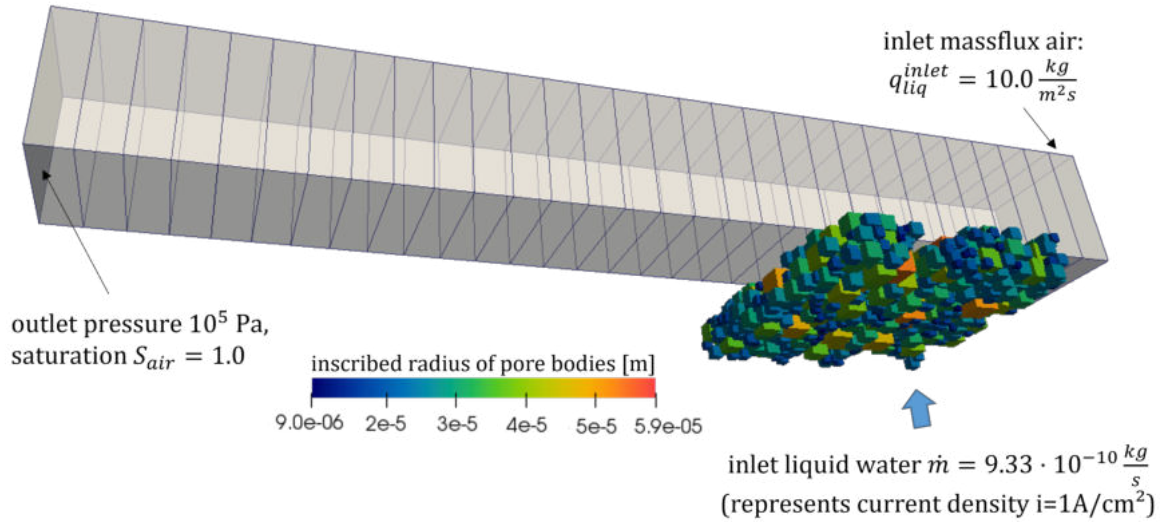


Figure 9.26: Computation setup for coupled MPL-free GDL representing pore-network and REV domain for gas distributor channel to investigate the two-phase interaction including droplet formation, growth and detachment.

Figure 9.26. The REV domain represents a channel with three dimensions ($x = 5$ mm, $y = 0.5$ mm, $z = 0.5$ mm) with a grid resolution of $(30 \times 1 \times 1)$ cells), and again, a porosity of $\Phi = 1.0$ is applied to represent an open channel. The pore-network is coupled with the REV domain through the pore bodies located at the contact area of GDL

and gas distributor channel. Here, based on the pore body inscribed radii R_i , interface throats with a length of $2 \cdot 10^{-6}$ m and throat radii of $r_{\text{interface}} = R_i - \varepsilon$ with $\varepsilon = 10^{-6}$ m are applied. The inscribed radius of the interface pore is 0.5 mm. We apply a mass flux boundary condition at the bottom of the network (blue arrow in Figure 9.26). Therefore, as in the previously described GDL representing setups, an additional boundary pore is added to the network. This inlet pore is connected to each pore at the bottom side of the pore-network. The connecting throat radii are based on the pore body sizes at the pore-network bottom ($r_{\text{inlet}} = R_i - \varepsilon$ with $\varepsilon = 10^{-6}$ m). This distributes the inlet liquid flow according to the pore bodies at the bottom of pore-network which represents a MPL-free GDL. In the pore-network, initially no liquid phase is present. In the inlet pore a liquid phase saturation of 0.981 is applied to speed up the simulation time. In the REV domain initially a liquid water saturation of 0.03 is present. Both domains are initialized with a gas phase pressure of 10^5 Pa. As inlet condition a mass flux of $9.33 \cdot 10^{-10}$ kg/s is applied to the inlet pore.

In the REV domain, we apply Neumann conditions for the inlet with an influx of gas of $10 \text{ kg}/(\text{m}^2\text{s})$ and no liquid influx. At the outlet Dirichlet conditions are applied to create an outflux condition with zero liquid saturation and a gas pressure of $p_g^{\text{out}} = 10^5$ Pa. This results in a gas flow velocity of approximately 8 m/s. The maximum time step size is $\max(\Delta t) = 10^{-2}$ s.

For this coupled GDL- gas distributor sample only one droplet is forming at the interface between the two domains. The resulting, time-dependent evolution of the drop radius in the interface pore is presented in Figure 9.27. Three of the five states, which are considered in more detail in the following, are marked.

Since we investigate a setup with constant inflow of liquid water at the bottom of the pore-network, a repeating drop occurrence, growth and detachment can be observed. The first rise of the drop radius happens quite fast. As in the previous examples, this results from the invasion of the interface throat and might also be influenced by numerical pressure fluctuations in the pore-network. Some small fluctuations also occur at the early state of drop growth starting from the third drop formation. However, the influence of these small fluctuations is negligible in the overall system behavior.

Figure 9.28 presents the state after the second droplet detachment at $t_1 = 52$ s. We see a pore-local saturation distribution of liquid water in the pore-network. The development of preferential flow paths through this heterogeneous pore-network is already known from previous investigations (see Section 7.1). In the REV domain, a local increase of the liquid phase saturation is observed due to the droplet detachment and

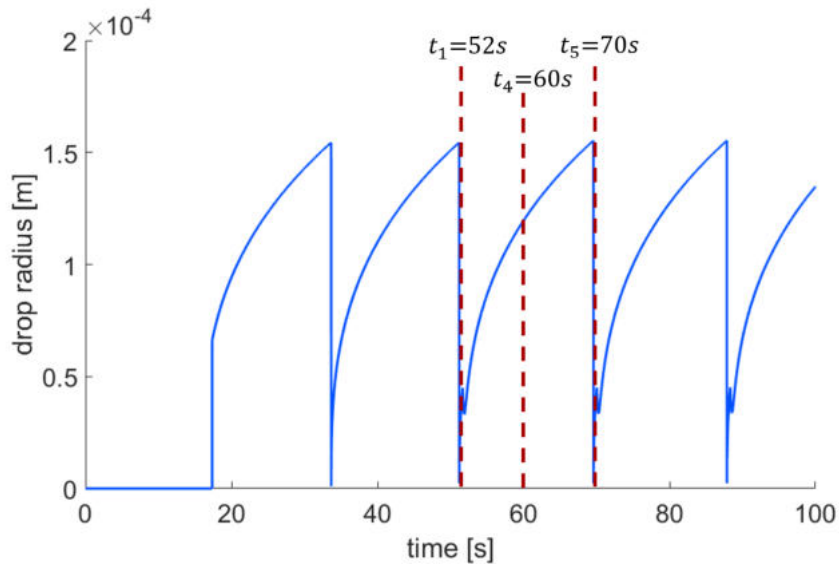


Figure 9.27: Droplet radius evolution with simulation time. Droplet forming, growing and detaching at the interface between coupled GDL representing pore-network and REV domain for gas distributor channel.

transmission of the liquid phase mass of the droplet into the REV domain.

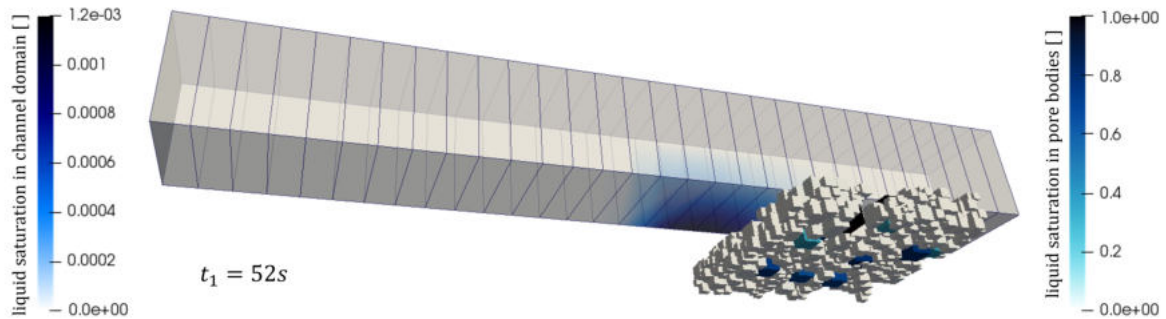


Figure 9.28: Liquid water saturation in the pore bodies of the GDL pore-network and the REV domain of the gas distributor channel at $t_1 = 52$ s.

The next time step is presented in Figure 9.29. The detached droplet is transported through the REV domain. We also observe a slight spreading of the liquid phase in the channel. In the pore-network, the configuration of liquid water does not change significantly. In the figures, the inlet side of the pore-network is shown. However, on the interface side (interface between pore-network and REV domain), we only see variations in the pore-local saturation at the formation of the first droplet. This behavior is analyzed and described in Section 8.1.

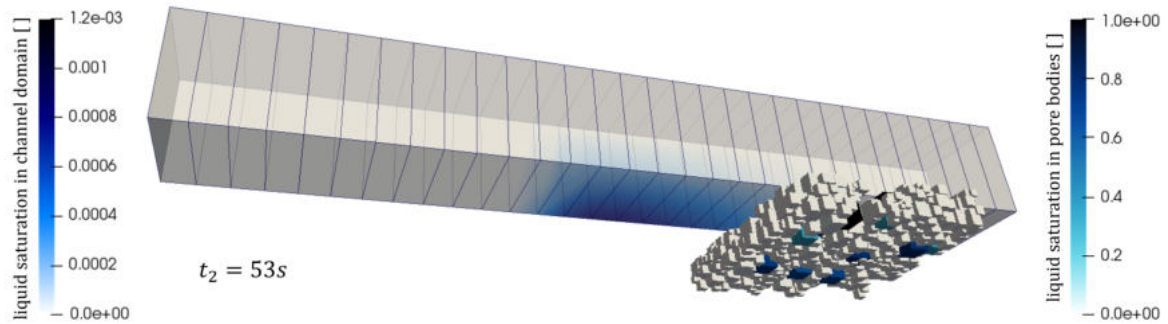


Figure 9.29: Liquid water saturation in the pore bodies of the GDL pore-network and the REV domain of the gas distributor channel at $t_2 = 53$ s.

With further progressing simulation time, the liquid water is transported more and more to the outlet of the REV domain. In Figures 9.30 and 9.31, also the spreading is visible. The liquid phase is not transported as a block but distributes locally. The applied gas phase stream acts as a shear force on the liquid phase resulting in the movement. There is no pressure gradient applied to the liquid phase. In Figure 9.32,

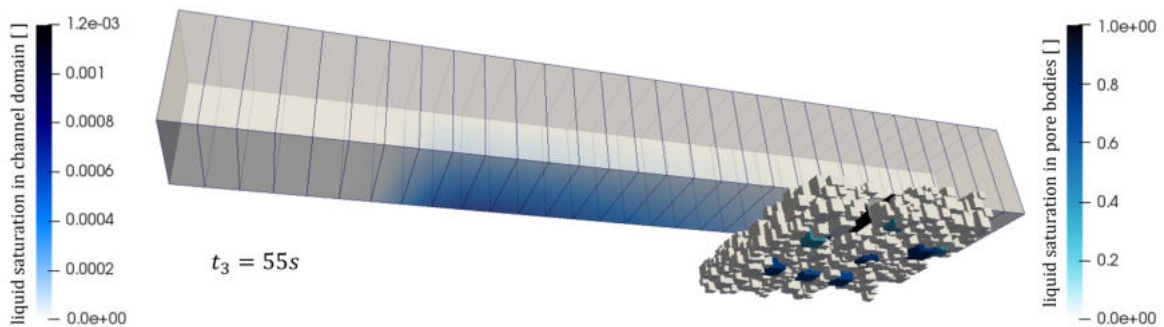


Figure 9.30: Liquid water saturation in the pore bodies of the GDL pore-network and the REV domain of the gas distributor channel at $t_3 = 55$ s.

we see the detached liquid phase volume of the next droplet which has been formed at the interface between pore-network and gas distributor. There is still some liquid phase volume from the previous drop left in the channel but the local increase in liquid phase saturation near the interface pores is clearly visible. This behavior is repeating with the constant mass flow at the inlet pores.

The presented setup shows the behavior of a small PEM fuel cell unit cell at constant operating conditions, where a current density of approximately 2 A/cm^2 is produced. Here, the excess water is produced and removed in liquid phase.

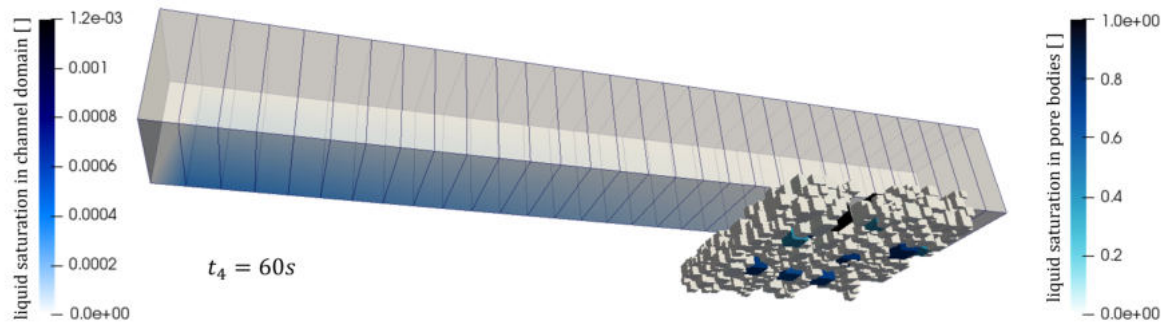


Figure 9.31: Liquid water saturation in the pore bodies of the GDL pore-network and the REV domain of the gas distributor channel at $t_4 = 60$ s.

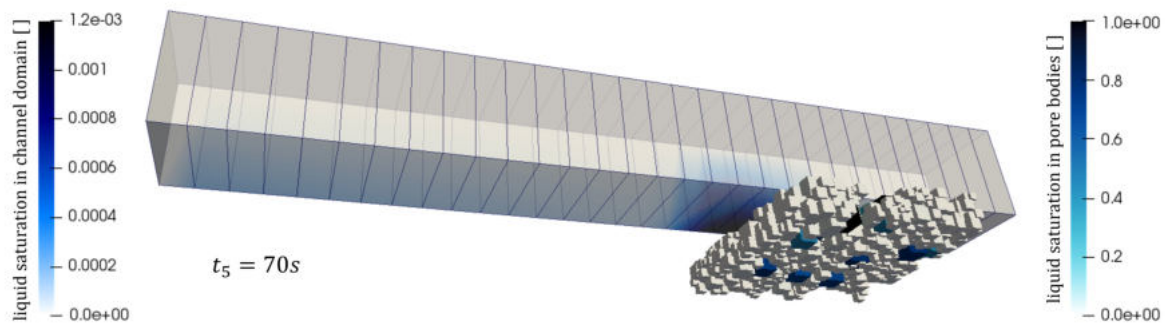


Figure 9.32: Liquid water saturation in the pore bodies of the GDL pore-network and the REV domain of the gas distributor channel at $t_5 = 70$ s.

9.2.4 Discussion

The model captures the two-phase flow interaction between a pore-network and an REV domain. The results of the model for the formation and growth of a single droplet shows good agreement with the corresponding uncoupled simulation. Also droplet detachment is captured by the presented model. In contrast to the uncoupled model which is presented in the previous section, the coupled pore-network REV model captures the drop behavior also after the detachment when the drop mass is transported away by the gas flow in the channel. The interaction of several droplets can be represented as well. As expected, this results in higher water saturation in the channel.

The two-phase implementation of pore-network and REV domain was successfully applied to a PEM fuel cell unit cell, which represents a small sample of a MPL-free GDL and a corresponding piece of the gas distributor channel.

The REV model allows an efficient representation of the two-phase flow in the channel. As described in Chapter 3, modeling two-phase flow in gas distributor channels is a special challenge. Different flow configurations can occur dependent on the local amount of liquid water and the gas flow velocity. Here, we do not focus on the details of fluid flow in the gas distributor but on the interface processes, especially droplet formation, growth and detachment. Therefore, an averaged representation of the two-phase flow in the channel is sufficient here. The Reynolds numbers of the gas phase in the channel domain Ω^{REV} in the three investigated examples (Sections 9.2.1 to 9.2.3) are $Re_1 \approx 550$, $Re_2 \approx 605$ and $Re_3 \approx 275$, such that we only consider laminar flow in all cases and we can use the Darcy based formulation for the REV domain. In Section 3.2.2, the used upscaled formulation of liquid film flow and gas flow is introduced. In Figure 9.28 to Figure 9.32, the liquid water transport through the REV channel domain is shown.

9.3 Comparison of the coupling approaches

The PNM-FF coupling model combines a pore-network model domain Ω^{PNM} , which represents a porous material on the pore-scale with a free flow domain Ω^{FF} , which represents a gas flow channel. Two-phase two-component flow (2p2c) is considered in the pore-network domain Ω^{PNM} , while single-phase two-component flow (1p2c) is solved in the free flow domain Ω^{FF} . At the interface, the advective and diffusive exchange fluxes of the components are captured as well as the formation, growth and detachment of droplets. The droplets form at liquid phase breakthrough locations at the interface due to liquid phase flow through the pore-network. We use ghost pores as part of the pore-network model to describe the droplet behavior and its influence on the flow in the pore-network Ω^{PNM} . The droplets only influence the free flow domain Ω^{FF} by evaporation from the drop surface. However, once the droplet is detached, it is no longer observed in the simulation.

The PNM-REV coupling model allows to capture two-phase flow in both computation domains, the porous domain Ω^{PNM} and the channel domain Ω^{REV} . Here, an REV-based model formulation is used to describe flow in the gas flow channels. It is assumed, that the droplets attach to the hydrophilic channel walls after detachment and form a liquid film flow at the channel walls. The REV model allows to track the detached drop volume in the channel domain without resolving the interface between the two phases in the channel. However, component transport has not been modeled to create faster results and stabilize the simulation. Additionally, considering component transfer between two multi-phase domains, it is a special challenge to formulate accurate and physical meaningful but stable interface conditions [45].

To model the interface processes between a GDL and a gas distributor channel in a PEM fuel cell cathode both models have their justification but are applicable for different operating conditions. At high relative humidities in the gas channel, e.g. downstream of a gas distributor channel in a cell, if the main focus of the investigation lies on local water contents, blockage of GDL or gas distributor channel and the water outtake occurs mainly in liquid form, the PNM-REV coupling model is more suitable. However, at intermediate humid operating conditions, e.g. front part of a gas distributor channel in a cell, if locally liquid water is present in the system but a lot of water is removed from the GDL through evaporation and the gas phase, the PNM-FF coupling model is the more accurate choice, since it allows to capture component transport in both

domains. Nevertheless, at dry operating conditions, liquid water is evaporating fast and does not occur at the interface between GDL and gas distributor. In this case, single-phase simulations are sufficient to capture advective and diffusive transport at the interface. This case is also captured by the coupled PNM-FF model.

10 Summary and Outlook

10.1 Summary

PEM fuel cell operating vehicles are a promising technique to reduce greenhouse gas emissions caused by traffic. Fuel cells drive a major part of the transformation of the mobility sector and the usage of hydrogen for energy generation. To improve the robustness and efficiency of the technology, modeling techniques are used to describe and understand the transport processes, which influence the water management in the cells. The aim of this thesis is to develop simplified model concepts for the analysis of coupled porous media - free flow models on the pore-scale. We investigate the highly dynamic interface conditions at the interface between GDL and gas distributor. We have developed and present different interface model concepts that are applied and discussed on selected examples. The developed models capture efficiently the two-phase transport in-between the porous, hydrophobic GDL and the hydrophilic gas distributor on the cathode side of a PEM fuel cell.

The occurring interface phenomena are highly complex and simplified models are necessary to represent the dynamic processes.

In this work, a model family is presented that describes the pore-local flow and transport processes at the interface between a porous GDL and a channel-structured gas distributor in the cathode of a PEM fuel cell. The coupling concept is based on the approach presented by [45] which is a further development of the sharp interface concepts developed by [101, 77, 4] applied to a pore-network model. We distinguish between different interface configuration which include the interaction between gaseous free flow and two-phase porous media flow and different interaction phenomena due to mixed-wettability at the interface between hydrophilic gas distributor and hydrophobic GDL. The developed interface conditions are applied to an uncoupled and two different coupled models.

Chapter 2 introduces the basics of modeling porous media systems with a special focus on pore-scale processes in PEM fuel cells. The centerpiece of the presented model is the pore-network model, which allows us to capture pore-scale effects in the porous GDL and at the interface between GDL and gas distributor. In Chapter 3, the conceptual and numerical models used for the single domains are discussed. Here, the details of the pore-network model representing an MPL-free GDL (fibrous GDB) are described. Additionally, two modeling concepts to describe flow in the second domain, gas distributor channels, are introduced. Chapter 4 focuses on the boundary and special interface conditions to design a model that combines flow in the MPL-free GDL and the gas distributor. The presented pore-network model has been extended to describe droplet formation, growth and detachment in the PNM context using a particularly derived pore-local capillary pressure-saturation relation. Additionally, it captures hydrophobic-hydrophilic interaction at the channel side wall using saturation thresholds and flow formulations based on the PNM principles as well as the influence of mixed-wet pores by trapping of liquid phase and an alternative capillary pressure-saturation relation. The developed interface conditions are integrated in coupling approaches, which combine the pore-network model domain Ω^{PNM} with a free flow description of the gas distributor channel flow in Ω^{FF} (see Chapter 5) and with a REV flow description of two-phase flow in the channel domain Ω^{REV} (see Chapter 6).

We use the Box method for both pore-network domain Ω^{PNM} and REV channels Ω^{REV} and a staggered-grid scheme was employed for the free-flow domain Ω^{FF} . The coupled models are implemented in the open-source simulation toolbox DuMu^x.

First, the adequate representation of a MPL-free GDL with a pore-network model is created and we evaluate the influence of structural and flow characteristics of the fibrous MPL-free GDL or GDB material in Section 7.1. We investigate the pore shapes based on the extracted network properties and the influence of contact angle variations on the global capillary pressure-saturation curve. In Section 7.2, the influence of gas distributor properties such as channel width and pressure differences between the channels is analyzed using single-phase simulations.

In Chapter 8, the developed interface conditions are applied to an uncoupled pore-network. Here, the gas distributor is roughly included by a boundary condition into the model. Each interface condition is first considered separately investigating its influence on the flow through the pore-network. Therefore, we apply each interface condition

first to a simplified pore-network and later on a pore-network representing a MPL-free GDL sample. The formation, growth and detachment of a droplet on a porous surface, applied to the pore-network model is compared to experimental data and numerical CFD investigations. The experimental data shows good agreement with the results of the pore-network model while the CFD model considers a different detachment criterion without contact angle hysteresis. This impedes the comparison but the results are discussed in detail in Section 8.1.1. The hydrophobic-hydrophilic interaction at the channel side walls is implemented using saturation thresholds. These thresholds are derived analytically and compared to numerical CFD investigations. The CFD simulations gain a better insight into the behavior at different contact angles while the analytic derivation is restricted to strongly hydrophobic pore bodies. For the analysis of the influence of mixed-wet pores at the interface between land parts of the gas distributor and GDL, stationary simulations are performed which show the accumulation based on the mixed-wet pores at the interface. In some fuel cell designs, the land parts of the gas distributor are coated hydrophobically which prevents this accumulation of liquid water. All developed interface conditions are applied together on a unit cell, which consists of a $1\text{mm}\times 1\text{mm}$ MPL-free GDL sample attached to one channel and two half-ribs (land parts) of a gas distributor. This example shows the interaction of the different interface condition and time-dependent behavior.

Chapter 9 presents the simulation results of the coupled pore-network domain Ω^{PNM} with either a single-phase free-flow domain Ω^{FF} or a two-phase REV domain Ω^{REV} , which represents a gas distributor channel, respectively. The coupled PNM-FF model includes component transport and phase change as well as droplet formation, growth and detachment at the interface between the domains Γ^{FF} . It is applied to different examples to investigate evaporation and drop formation behavior at different ambient temperatures and relative humidities. The coupled PNM-REV model considers only two-phase flow without component transport, which makes the model more efficient and numerically stable. However, it takes two-phase flow in the channel into account and allows to capture the droplet behavior in the channel after detachment from the interface Γ^{REV} between the pore-network domain Ω^{PNM} and the REV channel Ω^{REV} .

In summary, with the analysis of the different coupling concepts, we gain new understanding and knowledge that can be used for simplified coupling concepts. The analysis shows the advantages and disadvantages of the different strategies to describe droplets at the interface between porous domain and free flow and the fluid interaction

between differently wetting structures. The presented analysis enables industry research to strengthen the predictive power of their PEM fuel cell models, where detailed information of transport phenomena at the interface between GDL and gas distributor has been missing in the past. This allows to improve the water management in PEM fuel cells based on modeling results.

10.2 Outlook

PEM fuel cells are highly complex systems with a potential for further optimization. To develop a strong and robust water management and to describe the detailed transport phenomena in the cells, further research is necessary. The following aspects have been identified as key factors which are missing to improve PEM fuel cell modeling:

Overcome poor data on PEM fuel cell materials If more information on pore-local GDL properties is available, the predictive ability of the developed model can be further improved. The presented model can capture more complex pore shapes and contact angle distributions can be applied if the material data is available. Also, it is known that the GDL deforms due to the high compression of the cells after stacking of the different layers. This compression yields a deformation of the GDL in the channel-land structure of the gas distributor. At the land parts, a stronger compression is observed while the GDL is bulging into the open channels. However, to take these effects into account either a better understanding of the mechanical properties of the GDL is necessary to calculate the behavior in simulations or high resolution ct-scans of the compressed PEM fuel cell need to be used to generate the pore-network representation. The latter one is difficult due to the different reflection behaviors of carbon GDL and metal gas distributor in a ct-scan.

Statistical data of interface conditions for REV scale models Sampling of unit cells with different GDL structures and varying inflow conditions to generate statistical interface data which can be applied to an upscaled model, e.g. REV-scale models. These models can then be used to represent larger parts of a PEM fuel cell and analyse the cell behavior during different operating conditions. Currently available REV-scale models lack on accuracy of the interface condition between the layers or require several

fitting parameters to match with experimental data which are often not available. The presented model can be used to calculate representative, dynamic interface fluxes which are then applied to currently available (e.g. mortar-interface based) REV models [101, 77, 4].

Non-isothermal simulations As explained in Section 4.1, the reactions taking place in PEM fuel cells produce a noticeable amount of heat. But the materials in the cell, primarily the catalyst layers and the membrane, are sensitive to heat which favors ageing processes. Therefore, cooling channels are added in the bipolar plates, where also the gas channels are located. This results in a temperature gradient across the cell layers which needs to be taken into account for detailed predictions of fuel cell behavior. Nevertheless, several parameters influence this non-isothermal behavior. Heat is conducted not only through the void space and the fluids but the solid phase as well. Here, heat conduction coefficients of the single materials, but also many contact factors between the layers, need to be taken into account. Dual pore-networks allow to take the void and the solid parts of a porous medium with their pore-local properties into account[140]. However, in particular at the cooling channels, where humid gas is condensing, the thermal equilibrium assumption might not be fulfilled anymore.

Bibliography

- [1] R. Helmig *et al.*, *Multiphase flow and transport processes in the subsurface: a contribution to the modeling of hydrosystems*. Springer-Verlag, 1997.
- [2] J. Bear, “Dynamics of fluids in porous media,” *Soil Science*, vol. 120, no. 2, pp. 162–163, 1975.
- [3] J. T. Gostick, “Versatile and efficient pore network extraction method using marker-based watershed segmentation,” *Physical Review E*, vol. 96, no. 2, p. 023307, 2017.
- [4] K. Mosthaf, *Modeling and analysis of coupled porous-medium and free flow with application to evaporation processes*. Stuttgart: Eigenverlag des Instituts für Wasser-und Umweltsystemmodellierung, 2014.
- [5] P. K. Das, A. Grippin, A. Kwong, and A. Z. Weber, “Liquid-water-droplet adhesion-force measurements on fresh and aged fuel-cell gas-diffusion layers,” *Journal of The Electrochemical Society*, vol. 159, no. 5, p. B489, 2012.
- [6] C. Quesnel, R. Cao, J. Lehr, A.-M. Kietzig, A. Z. Weber, and J. T. Gostick, “Dynamic percolation and droplet growth behavior in porous electrodes of polymer electrolyte fuel cells,” *The Journal of Physical Chemistry C*, vol. 119, no. 40, pp. 22934–22944, 2015.
- [7] D. Niblett, A. Mularczyk, V. Niasar, J. Eller, and S. Holmes, “Two-phase flow dynamics in a gas diffusion layer-gas channel-microporous layer system,” *Journal of Power Sources*, vol. 471, p. 228427, 2020.
- [8] F. Belmer, B. Bensmann, T. Brandt, C. Cremers, M. Derflinger, R. Hanke-Rauschenbach, T. Grube, A. Heinzl, W. Horenkamp, T. Jungmann, *et al.*,

- “Brennstoffzellen-und Batteriefahrzeuge: Bedeutung für die Elektromobilität,” *VDI/VDE-Studie, VDI-GEU*, 2019.
- [9] F. Barbir, “PEM Fuel Cells: Theory and Practice,” 2005.
- [10] H. Council, “Path to hydrogen competitiveness: A cost perspective,” 2020.
- [11] N. Sammes, *Fuel cell technology: reaching towards commercialization*. Springer Science & Business Media, 2006.
- [12] D. W. Green and J. O. Maloney, *Perry’s chemical engineers’ handbook*. McGraw-Hill Education, 1997.
- [13] J. Zhou, S. Shukla, A. Putz, and M. Secanell, “Analysis of the role of the microporous layer in improving polymer electrolyte fuel cell performance,” *Electrochimica Acta*, vol. 268, pp. 366–382, 2018.
- [14] J. T. Gostick, M. A. Ioannidis, M. W. Fowler, and M. D. Pritzker, “On the role of the microporous layer in PEMFC operation,” *Electrochemistry Communications*, vol. 11, no. 3, pp. 576–579, 2009.
- [15] R. P. Ramasamy, E. C. Kumbur, M. M. Mench, W. Liu, D. Moore, and M. Murthy, “Investigation of macro-and micro-porous layer interaction in polymer electrolyte fuel cells,” *International Journal of Hydrogen Energy*, vol. 33, no. 13, pp. 3351–3367, 2008.
- [16] M. Mathias, J. Roth, J. Fleming, and W. Lehnert, “Diffusion media materials and characterisation,” *Handbook of fuel cells*, 2010.
- [17] A. Baroutaji, J. Carton, M. Sajjia, and A.-G. Olabi, “Materials in PEM fuel cells,” 2015.
- [18] A. Manso, F. Marzo, J. Barranco, X. Garikano, and M. G. Mujika, “Influence of geometric parameters of the flow fields on the performance of a PEM fuel cell. a review,” *International Journal of Hydrogen Energy*, vol. 37, no. 20, pp. 15256–15287, 2012.
- [19] J. Fimrite, B. Carnes, H. Struchtrup, and N. Djilali, “Transport phenomena in polymer electrolyte membranes: II. binary friction membrane model,” *Journal of the Electrochemical Society*, vol. 152, no. 9, p. A1815, 2005.

-
- [20] M. Eikerling, “Water management in cathode catalyst layers of pem fuel cells: a structure-based model,” *Journal of The Electrochemical Society*, vol. 153, no. 3, p. E58, 2006.
- [21] P. Carrere and M. Prat, “Liquid water in cathode gas diffusion layers of PEM fuel cells: Identification of various pore filling regimes from pore network simulations,” *International Journal of Heat and Mass Transfer*, vol. 129, pp. 1043–1056, 2019.
- [22] L. Cindrella, A. M. Kannan, J. Lin, K. Saminathan, Y. Ho, C. Lin, and J. Wertz, “Gas diffusion layer for proton exchange membrane fuel cells—a review,” *Journal of Power Sources*, vol. 194, no. 1, pp. 146–160, 2009.
- [23] M. Shams, A. Q. Raeini, M. J. Blunt, and B. Bijeljic, “A numerical model of two-phase flow at the micro-scale using the volume-of-fluid method,” *Journal of Computational Physics*, vol. 357, pp. 159–182, 2018.
- [24] D. Lakehal, M. Meier, and M. Fulgosi, “Interface tracking towards the direct simulation of heat and mass transfer in multiphase flows,” *International Journal of Heat and Fluid Flow*, vol. 23, no. 3, pp. 242–257, 2002.
- [25] P. A. García-Salaberri, J. T. Gostick, I. V. Zenyuk, G. Hwang, M. Vera, and A. Z. Weber, “On the limitations of volume-averaged descriptions of gas diffusion layers in the modeling of polymer electrolyte fuel cells,” *ECS Transactions*, vol. 80, no. 8, p. 133, 2017.
- [26] C. Qin and S. Hassanizadeh, “A new approach to modelling water flooding in a polymer electrolyte fuel cell,” *International Journal of Hydrogen Energy*, vol. 40, no. 8, pp. 3348–3358, 2015.
- [27] C. Qin and S. Hassanizadeh, “Multiphase flow through multilayers of thin porous media: General balance equations and constitutive relationships for a solid–gas–liquid three-phase system,” *International Journal of Heat and Mass Transfer*, vol. 70, pp. 693–708, 2014.
- [28] M. J. Blunt and H. Scher, “Pore-level modeling of wetting,” *Physical Review E*, vol. 52, no. 6, p. 6387, 1995.

- [29] T. Tranter, J. Gostick, A. Burns, and W. Gale, “Pore network modeling of compressed fuel cell components with OpenPNM,” *Fuel Cells*, vol. 16, no. 4, pp. 504–515, 2016.
- [30] A. Bazylak, V. Berejnov, B. Markicevic, D. Sinton, and N. Djilali, “A microfluidic pore network approach to investigate water transport in fuel cell porous transport layers,” in *ASME 2008 6th International Conference on Nanochannels, Microchannels, and Minichannels*, pp. 1335–1341, American Society of Mechanical Engineers Digital Collection, 2008.
- [31] N. Belgacem, M. Prat, and J. Pauchet, “Coupled continuum and condensation–evaporation pore network model of the cathode in polymer-electrolyte fuel cell,” *International Journal of Hydrogen Energy*, vol. 42, no. 12, pp. 8150–8165, 2017.
- [32] R. Alink and D. Gerteisen, “Modeling the liquid water transport in the gas diffusion layer for polymer electrolyte membrane fuel cells using a water path network,” *Energies*, vol. 6, no. 9, pp. 4508–4530, 2013.
- [33] J. Pauchet, M. Prat, P. Schott, and S. P. Kuttanikkad, “Performance loss of proton exchange membrane fuel cell due to hydrophobicity loss in gas diffusion layer: Analysis by multiscale approach combining pore network and performance modelling,” *International Journal of Hydrogen Energy*, vol. 37, no. 2, pp. 1628–1641, 2012.
- [34] B. Straubhaar, J. Pauchet, and M. Prat, “Pore network modelling of condensation in gas diffusion layers of proton exchange membrane fuel cells,” *International Journal of Heat and Mass Transfer*, vol. 102, pp. 891–901, 2016.
- [35] S. P. Kuttanikkad, M. Prat, and J. Pauchet, “Pore-network simulations of two-phase flow in a thin porous layer of mixed wettability: application to water transport in gas diffusion layers of proton exchange membrane fuel cells,” *Journal of Power Sources*, vol. 196, no. 3, pp. 1145–1155, 2011.
- [36] K. Khayrat and P. Jenny, “A multi-scale network method for two-phase flow in porous media,” *Journal of Computational Physics*, vol. 342, pp. 194–210, 2017.

-
- [37] Q. Xiong, T. G. Baychev, and A. P. Jivkov, “Review of pore network modelling of porous media: Experimental characterisations, network constructions and applications to reactive transport,” *Journal of Contaminant Hydrology*, vol. 192, pp. 101–117, 2016.
- [38] C. Qin, “Water transport in the gas diffusion layer of a polymer electrolyte fuel cell: dynamic pore-network modeling,” *Journal of the Electrochemical Society*, vol. 162, no. 9, p. F1036, 2015.
- [39] T. Tsuji, F. Jiang, and K. T. Christensen, “Characterization of immiscible fluid displacement processes with various capillary numbers and viscosity ratios in 3D natural sandstone,” *Advances in Water Resources*, vol. 95, pp. 3–15, 2016.
- [40] M. J. Blunt, *Multiphase flow in permeable media: A pore-scale perspective*. Cambridge University Press, 2017.
- [41] S. M. Hassanizadeh and W. G. Gray, “Thermodynamic basis of capillary pressure in porous media,” *Water resources research*, vol. 29, no. 10, pp. 3389–3405, 1993.
- [42] M. J. Blunt, B. Bijeljic, H. Dong, O. Gharbi, S. Iglauer, P. Mostaghimi, A. Paluszny, and C. Pentland, “Pore-scale imaging and modelling,” *Advances in Water Resources*, vol. 51, pp. 197–216, 2013.
- [43] V. Joekar-Niasar and S. Hassanizadeh, “Analysis of fundamentals of two-phase flow in porous media using dynamic pore-network models: A review,” *Critical reviews in environmental science and technology*, vol. 42, no. 18, pp. 1895–1976, 2012.
- [44] V. Joekar-Niasar, S. M. Hassanizadeh, and H. Dahle, “Non-equilibrium effects in capillarity and interfacial area in two-phase flow: dynamic pore-network modelling,” *Journal of Fluid Mechanics*, vol. 655, p. 38, 2010.
- [45] K. Weishaupt, “Model concepts for coupling free flow with porous medium flow at the pore-network scale: from single-phase flow to compositional non-isothermal two-phase flow,” 2020.
- [46] G. Mason and N. R. Morrow, “Capillary behavior of a perfectly wetting liquid in irregular triangular tubes,” *Journal of Colloid and Interface Science*, vol. 141, no. 1, pp. 262–274, 1991.

- [47] B. Zhao, C. W. MacMinn, B. K. Primkulov, Y. Chen, A. J. Valocchi, J. Zhao, Q. Kang, K. Bruning, J. E. McClure, C. T. Miller, *et al.*, “Comprehensive comparison of pore-scale models for multiphase flow in porous media,” *Proceedings of the National Academy of Sciences*, vol. 116, no. 28, pp. 13799–13806, 2019.
- [48] R. Lenormand, E. Touboul, and C. Zarcone, “Numerical models and experiments on immiscible displacements in porous media,” *Journal of fluid mechanics*, vol. 189, pp. 165–187, 1988.
- [49] K.-J. Lee, J. H. Nam, and C.-J. Kim, “Pore-network analysis of two-phase water transport in gas diffusion layers of polymer electrolyte membrane fuel cells,” *Electrochimica Acta*, vol. 54, no. 4, pp. 1166–1176, 2009.
- [50] S. Koshizuka and Y. Oka, “Moving-particle semi-implicit method for fragmentation of incompressible fluid,” *Nuclear science and engineering*, vol. 123, no. 3, pp. 421–434, 1996.
- [51] A. M. Tartakovsky, N. Trask, K. Pan, B. Jones, W. Pan, and J. R. Williams, “Smoothed particle hydrodynamics and its applications for multiphase flow and reactive transport in porous media,” *Computational Geosciences*, vol. 20, no. 4, pp. 807–834, 2016.
- [52] B. A. Schrefler, *The finite element method in the deformation and consolidation of porous media*. Wiley, 1987.
- [53] K. Brenner, C. Cancès, and D. Hilhorst, “Finite volume approximation for an immiscible two-phase flow in porous media with discontinuous capillary pressure,” *Computational Geosciences*, vol. 17, no. 3, pp. 573–597, 2013.
- [54] A. Q. Raeini, M. J. Blunt, and B. Bijeljic, “Modelling two-phase flow in porous media at the pore scale using the volume-of-fluid method,” *Journal of Computational Physics*, vol. 231, no. 17, pp. 5653–5668, 2012.
- [55] C. Pan, M. Hilpert, and C. Miller, “Lattice-Boltzmann simulation of two-phase flow in porous media,” *Water Resources Research*, vol. 40, no. 1, 2004.
- [56] A. K. Gunstensen, D. H. Rothman, S. Zaleski, and G. Zanetti, “Lattice Boltzmann model of immiscible fluids,” *Physical Review A*, vol. 43, no. 8, p. 4320, 1991.

-
- [57] S. Chen and G. D. Doolen, “Lattice Boltzmann method for fluid flows,” *Annual review of fluid mechanics*, vol. 30, no. 1, pp. 329–364, 1998.
- [58] G. Molaemanesh and M. Akbari, “A three-dimensional pore-scale model of the cathode electrode in polymer-electrolyte membrane fuel cell by lattice Boltzmann method,” *Journal of Power Sources*, vol. 258, pp. 89–97, 2014.
- [59] P. Meakin and A. M. Tartakovsky, “Modeling and simulation of pore-scale multi-phase fluid flow and reactive transport in fractured and porous media,” *Reviews of Geophysics*, vol. 47, no. 3, 2009.
- [60] C. Bringedal, “A conservative phase-field model for reactive transport,” 2019.
- [61] I. Bogdanov, S. Jardel, A. Turki, and A. Kamp, “Pore scale phase field model of two phase flow in porous medium,” in *Annual COMSOL Conference, Paris, France*, 2010.
- [62] V. Joekar-Niasar, “Pore-scale modelling techniques: balancing efficiency, performance, and robustness,” *Computational Geosciences*, vol. 20, no. 4, p. 773, 2016.
- [63] S. J. Paddison and K. S. Promislow, *Device and materials modeling in PEM fuel cells*, vol. 113. Springer Science & Business Media, 2008.
- [64] I. Fatt *et al.*, “The network model of porous media,” *Transactions of the AIME*, vol. 207, no. 01, pp. 144–181, 1956.
- [65] M. J. Blunt, “Flow in porous media-pore-network models and multiphase flow,” *Current opinion in colloid & interface science*, vol. 6, no. 3, pp. 197–207, 2001.
- [66] Math2Market, “Geodict software - the digital material laboratory,” 2018.
- [67] R. Schweiss, C. Meiser, T. Damjanovic, I. Galbiati, and N. Haak, “SIGRACET® Gas Diffusion Layers for PEM Fuel Cells, Electrolyzers and Batteries (White Paper),” *Sigracet*, 2016.
- [68] A. Baroutaji, J. Carton, J. Stokes, and A.-G. Olabi, “Application of open pore cellular foam for air breathing pem fuel cell,” *International Journal of Hydrogen Energy*, vol. 42, no. 40, pp. 25630–25638, 2017.

- [69] T. Wilberforce, F. Khatib, O. Ijaodola, E. Ogungbemi, Z. El-Hassan, A. Durrant, J. Thompson, and A. Olabi, “Numerical modelling and CFD simulation of a polymer electrolyte membrane (PEM) fuel cell flow channel using an open pore cellular foam material,” *Science of The Total Environment*, vol. 678, pp. 728–740, 2019.
- [70] J. Kim, G. Luo, and C.-Y. Wang, “Modeling two-phase flow in three-dimensional complex flow-fields of proton exchange membrane fuel cells,” *Journal of Power Sources*, vol. 365, pp. 419–429, 2017.
- [71] F. N. Büchi, R. Flückiger, D. Tehlar, F. Marone, and M. Stampanoni, “Determination of liquid water distribution in porous transport layers,” *ECS Transactions*, vol. 16, no. 2, pp. 587–592, 2008.
- [72] P. Kurzweil, *Brennstoffzellentechnik: Grundlagen, Materialien, Anwendungen, Gaserzeugung*. Springer-Verlag, 2016.
- [73] J. Newman and K. E. Thomas-Alyea, *Electrochemical systems*. John Wiley & Sons, 2012.
- [74] J. H. Ohs, *A Numerical and Experimental Study of Starvation Conditions in Automotive PEM Fuel Cells*. PhD thesis, RWTH Aachen, 2013.
- [75] M. Wöhr, *Instationäres, thermodynamisches Verhalten der Polymermembran-Brennstoffzelle*. VDI-Verlag, 2000.
- [76] M. Acosta, C. Merten, G. Eigenberger, H. Class, R. Helmig, B. Thoben, and H. Müller-Steinhagen, “Modeling non-isothermal two-phase multicomponent flow in the cathode of PEM fuel cells,” *Journal of Power Sources*, vol. 159, no. 2, pp. 1123–1141, 2006.
- [77] K. Baber, *Coupling free flow and flow in porous media in biological and technical applications: From a simple to a complex interface description*. Institute for Modelling Hydraulic and Environmental Systems, University of Stuttgart, 2014.
- [78] M. A. Safi, N. I. Prasianakis, J. Mantzaras, A. Lamibrac, and F. N. Büchi, “Experimental and pore-level numerical investigation of water evaporation in gas diffusion layers of polymer electrolyte fuel cells,” *International Journal of Heat and Mass Transfer*, vol. 115, pp. 238–249, 2017.

-
- [79] E. F. Medici, I. V. Zenyuk, D. Parkinson, A. Weber, and J. Allen, “Understanding water transport in polymer electrolyte fuel cells using coupled continuum and pore-network models,” *Fuel Cells*, vol. 16, no. 6, pp. 725–733, 2016.
- [80] I. V. Zenyuk, E. Medici, J. Allen, and A. Z. Weber, “Coupling continuum and pore-network models for polymer-electrolyte fuel cells,” *International Journal of Hydrogen Energy*, vol. 40, no. 46, pp. 16831–16845, 2015.
- [81] T. G. Tranter, P. Boillat, A. Mularczyk, V. Manzi-Orezzoli, P. Shearing, D. Brett, J. Eller, J. Gostick, and A. Forner-Cuenca, “Pore network modelling of capillary transport and relative diffusivity in gas diffusion layers with patterned wettability,” *Journal of The Electrochemical Society*, vol. 167, no. 11, p. 114512, 2020.
- [82] P. A. García-Salaberri, I. V. Zenyuk, J. T. Gostick, and A. Z. Weber, “Modeling gas diffusion layers in polymer electrolyte fuel cells using a continuum-based pore-network formulation,” *ECS Transactions*, vol. 97, no. 7, p. 615, 2020.
- [83] K.-J. Lee, J. H. Nam, and C.-J. Kim, “Steady saturation distribution in hydrophobic gas-diffusion layers of polymer electrolyte membrane fuel cells: A pore-network study,” *Journal of Power Sources*, vol. 195, no. 1, pp. 130–141, 2010.
- [84] K. Weishaupt, A. Terzis, I. Zarikos, G. Yang, M. de Winter, and R. Helmig, “Model reduction for coupled free flow over porous media: a hybrid dimensional pore network model approach,” *arXiv preprint arXiv:1908.01771*, 2019.
- [85] K. Weishaupt and R. Helmig, “A dynamic and fully implicit non-isothermal, two-phase, two-component pore-network model coupled to single-phase free flow for the pore-scale description of evaporation processes,” *Water Resources Research*, vol. 57, no. 4, p. e2020WR028772, 2021.
- [86] M. Grimm, E. J. See, and S. G. Kandlikar, “Modeling gas flow in PEMFC channels: Part I—flow pattern transitions and pressure drop in a simulated ex situ channel with uniform water injection through the GDL,” *International Journal of Hydrogen Energy*, vol. 37, no. 17, pp. 12489–12503, 2012.
- [87] R. Anderson, L. Zhang, Y. Ding, M. Blanco, X. Bi, and D. P. Wilkinson, “A critical review of two-phase flow in gas flow channels of proton exchange membrane fuel cells,” *Journal of Power Sources*, vol. 195, no. 15, pp. 4531–4553, 2010.

-
- [88] Z. Lu, C. Rath, G. Zhang, and S. G. Kandlikar, “Water management studies in PEM fuel cells, part IV: Effects of channel surface wettability, geometry and orientation on the two-phase flow in parallel gas channels,” *International Journal of Hydrogen Energy*, vol. 36, no. 16, pp. 9864–9875, 2011.
- [89] M. Mortazavi and K. Tajiri, “Two-phase flow pressure drop in flow channels of proton exchange membrane fuel cells: Review of experimental approaches,” *Renewable and Sustainable Energy Reviews*, vol. 45, pp. 296–317, 2015.
- [90] B. Flemisch, M. Darcis, K. Erbertseder, B. Faigle, A. Lauser, K. Mosthaf, S. Müthing, P. Nuske, A. Tatomir, M. Wolff, and R. Helmig, “Dumux: Dune for multi-phase, component, scale, physics, . . . flow and transport in porous media,” *Advances in Water Resources*, vol. 34, no. 9, pp. 1102 – 1112, 2011. New Computational Methods and Software Tools.
- [91] V. Joekar-Niasar, S. M. Hassanizadeh, and H. K. Dahle, “Non-equilibrium effects in capillarity and interfacial area in two-phase flow: Dynamic pore-network modelling,” *Journal of Fluid Mechanics*, vol. 655, pp. 38–71, 2010.
- [92] T. Patzek and D. B. Silin, “Shape factor and hydraulic conductance in noncircular capillaries: I. one-phase creeping flow,” *Journal of colloid and interface science*, vol. 236, no. 2, pp. 295–304, 2001.
- [93] P.-e. Øren, S. Bakke, and O. J. Arntzen, “Extending Predictive Capabilities to Network Models,” *SPE Journal*, vol. 3, no. 4, pp. 324–336, 1998.
- [94] T. Ransohoff and C. Radke, “Laminar flow of a wetting liquid along the corners of a predominantly gas-occupied noncircular pore,” *Journal of colloid and interface science*, vol. 121, no. 2, pp. 392–401, 1988.
- [95] D. Zhou, M. Blunt, and F. Orr, “Hydrocarbon drainage along corners of noncircular capillaries,” *Journal of Colloid and Interface Science*, vol. 187, no. 1, pp. 11 – 21, 1997.
- [96] H. Class, R. Helmig, and P. Bastian, “Numerical simulation of non-isothermal multiphase multicomponent processes in porous media.: 1. an efficient solution technique,” *Advances in Water Resources*, vol. 25, no. 5, pp. 533–550, 2002.

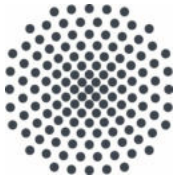
-
- [97] R. Huber and R. Helmig, “Node-centered finite volume discretizations for the numerical simulation of multiphase flow in heterogeneous porous media,” *Computational Geosciences*, vol. 4, no. 2, pp. 141–164, 2000.
- [98] Math2Market GmbH, “GeoDict 2018 GrainGeo.” <https://www.geodict.com>, 2021-08-06. Service Pack 5 Standard Edition.
- [99] J. T. Gostick, Z. A. Khan, T. G. Tranter, M. D. Kok, M. Agnaou, M. Sadeghi, and R. Jarvis, “Porespy: A python toolkit for quantitative analysis of porous media images,” *Journal of Open Source Software*, vol. 4, no. 37, p. 1296, 2019.
- [100] Z. A. Khan, T. Tranter, M. Agnaou, A. Elkamel, and J. Gostick, “Dual network extraction algorithm to investigate multiple transport processes in porous materials: Image-based modeling of pore and grain scale processes,” *Computers & Chemical Engineering*, vol. 123, pp. 64–77, 2019.
- [101] S. Ackermann, C. Bringedal, and R. Helmig, “Multi-scale three-domain approach for coupling free flow and flow in porous media including droplet-related interface processes,” *Journal of Computational Physics*, vol. 429, p. 109993, 2021.
- [102] F. H. Harlow and J. E. Welch, “Numerical calculation of time-dependent viscous incompressible flow of fluid with free surface,” *The physics of fluids*, vol. 8, no. 12, pp. 2182–2189, 1965.
- [103] H. K. Versteeg and W. Malalasekera, *An introduction to computational fluid dynamics: the finite volume method*. Pearson education, 2007.
- [104] M. Schneider, K. Weishaupt, D. Gläser, W. M. Boon, and R. Helmig, “Coupling staggered-grid and mpfa finite volume methods for free flow/porous-medium flow problems,” *Journal of Computational Physics*, vol. 401, p. 109012, 2020.
- [105] Z. Lu, M. M. Daino, C. Rath, and S. G. Kandlikar, “Water management studies in PEM fuel cells, part III: Dynamic breakthrough and intermittent drainage characteristics from GDLs with and without MPLs,” *International Journal of Hydrogen Energy*, vol. 35, no. 9, pp. 4222–4233, 2010.
- [106] C. Gerling, M. Hanauer, U. Berner, and K. A. K. Friedrich, “PEMFC model parameterization by means of differential cell polarization and electrochemical

- impedance spectroscopy,” in *ECS Meeting Abstracts*, no. 53, p. 3844, IOP Publishing, 2020.
- [107] T. E. Springer, T. Zawodzinski, and S. Gottesfeld, “Polymer electrolyte fuel cell model,” *Journal of the electrochemical society*, vol. 138, no. 8, p. 2334, 1991.
- [108] A. Theodorakakos, T. Ous, M. Gavaises, J. Nouri, N. Nikolopoulos, and H. Yanagihara, “Dynamics of water droplets detached from porous surfaces of relevance to PEM fuel cells,” *Journal of colloid and interface science*, vol. 300, no. 2, pp. 673–687, 2006.
- [109] S. Basu, K. Nandakumar, and J. H. Masliyah, “A model for detachment of a partially wetting drop from a solid surface by shear flow,” *Journal of colloid and interface science*, vol. 190, no. 1, pp. 253–257, 1997.
- [110] J. L. Plawsky, M. Ojha, A. Chatterjee, and P. C. Wayner Jr, “Review of the effects of surface topography, surface chemistry, and fluid physics on evaporation at the contact line,” *Chemical Engineering Communications*, vol. 196, no. 5, pp. 658–696, 2008.
- [111] A. Cassie and S. Baxter, “Wettability of porous surfaces,” *Transactions of the Faraday society*, vol. 40, pp. 546–551, 1944.
- [112] J. Z. Fishman, H. Leung, and A. Bazylak, “Droplet pinning by PEM fuel cell GDL surfaces,” *International Journal of Hydrogen Energy*, vol. 35, no. 17, pp. 9144–9150, 2010.
- [113] J. T. Gostick, M. W. Fowler, M. A. Ioannidis, M. D. Pritzker, Y. M. Volfkovich, and A. Sakars, “Capillary pressure and hydrophilic porosity in gas diffusion layers for polymer electrolyte fuel cells,” *Journal of Power Sources*, vol. 156, no. 2, pp. 375–387, 2006.
- [114] V. P. Carey, *Liquid vapor phase change phenomena: an introduction to the thermophysics of vaporization and condensation processes in heat transfer equipment*. CRC Press, 2018.
- [115] E. Kumbur, K. Sharp, and M. Mench, “Liquid droplet behavior and instability in a polymer electrolyte fuel cell flow channel,” *Journal of Power Sources*, vol. 161, no. 1, pp. 333–345, 2006.

-
- [116] K. S. Chen, M. A. Hickner, and D. R. Noble, “Simplified models for predicting the onset of liquid water droplet instability at the gas diffusion layer/gas flow channel interface,” *International Journal of Energy Research*, vol. 29, no. 12, pp. 1113–1132, 2005.
- [117] S. C. Cho, Y. Wang, and K. S. Chen, “Droplet dynamics in a polymer electrolyte fuel cell gas flow channel: Forces, deformation, and detachment. I: Theoretical and numerical analyses,” *Journal of Power Sources*, vol. 206, pp. 119–128, 2012.
- [118] J. T. Gostick, M. A. Ioannidis, M. W. Fowler, and M. D. Pritzker, “Direct measurement of the capillary pressure characteristics of water–air–gas diffusion layer systems for PEM fuel cells,” *Electrochemistry Communications*, vol. 10, no. 10, pp. 1520–1523, 2008.
- [119] J. T. Gostick, “Random pore network modeling of fibrous PEMFC gas diffusion media using voronoi and delaunay tessellations,” *Journal of the Electrochemical Society*, vol. 160, no. 8, p. F731, 2013.
- [120] I. Harkness, N. Hussain, L. Smith, and J. Sharman, “The use of a novel water porosimeter to predict the water handling behaviour of gas diffusion media used in polymer electrolyte fuel cells,” *Journal of Power Sources*, vol. 193, no. 1, pp. 122–129, 2009.
- [121] T. Tranter, J. Gostick, A. Burns, and W. Gale, “Capillary hysteresis in neutrally wettable fibrous media: a pore network study of a fuel cell electrode,” *Transport in Porous Media*, vol. 121, no. 3, pp. 597–620, 2018.
- [122] K. Mosthaf, K. Baber, B. Flemisch, R. Helmig, A. Leijnse, I. Rybak, and B. Wohlmuth, “A coupling concept for two-phase compositional porous-medium and single-phase compositional free flow,” *Water Resources Research*, vol. 47, no. 10, 2011.
- [123] P. Nuske, “Beyond local equilibrium: relaxing local equilibrium assumptions in multiphase flow in porous media,” 2014.
- [124] N. Wakao and S. Kagei, *Heat and mass transfer in packed beds*, vol. 1. Taylor & Francis, 1982.

- [125] J. Nordbotten, M. A. Celia, H. Dahle, and S. Hassanizadeh, “Interpretation of macroscale variables in Darcy’s law,” *Water Resources Research*, vol. 43, no. 8, 2007.
- [126] J. Nordbotten, M. Celia, H. Dahle, and S. Hassanizadeh, “On the definition of macroscale pressure for multiphase flow in porous media,” *Water Resources Research*, vol. 44, no. 6, 2008.
- [127] S. Korteland, S. Bottero, S. Hassanizadeh, and C. Berentsen, “What is the correct definition of average pressure?,” *Transport in Porous Media*, vol. 84, no. 1, pp. 153–175, 2010.
- [128] M. T. Balhoff, K. E. Thompson, and M. Hjortsø, “Coupling pore-scale networks to continuum-scale models of porous media,” *Computers & Geosciences*, vol. 33, no. 3, pp. 393–410, 2007.
- [129] M. T. Balhoff, S. G. Thomas, and M. F. Wheeler, “Mortar coupling and upscaling of pore-scale models,” *Computational Geosciences*, vol. 12, no. 1, pp. 15–27, 2008.
- [130] Y. Mehmani and M. T. Balhoff, “Bridging from pore to continuum: A hybrid mortar domain decomposition framework for subsurface flow and transport,” *Multi-scale Modeling & Simulation*, vol. 12, no. 2, pp. 667–693, 2014.
- [131] R. Schweiss, C. Meiser, T. Damjanovic, I. Galbiati, and N. Haak, “SIGRACET gas diffusion layers for PEM fuel cells, electrolyzers and batteries,” *White paper SGL Group*, 2016.
- [132] C.-Z. Qin, B. Guo, M. Celia, and R. Wu, “Dynamic pore-network modeling of air-water flow through thin porous layers,” *Chemical Engineering Science*, vol. 202, pp. 194–207, 2019.
- [133] A. Kakaee, G. Molaeimanesh, and M. E. Garmaroudi, “Impact of PTFE distribution across the GDL on the water droplet removal from a PEM fuel cell electrode containing binder,” *International Journal of Hydrogen Energy*, vol. 43, no. 32, pp. 15481–15491, 2018.
- [134] C. Lim and C. Wang, “Effects of hydrophobic polymer content in GDL on power performance of a PEM fuel cell,” *Electrochimica Acta*, vol. 49, no. 24, pp. 4149–4156, 2004.

-
- [135] J. P. Hartnett and M. Kostic, “Heat transfer to Newtonian and non-Newtonian fluids in rectangular ducts,” in *Advances in heat transfer*, vol. 19, pp. 247–356, Elsevier, 1989.
- [136] A. Bazylak, D. Sinton, and N. Djilali, “Dynamic water transport and droplet emergence in pemfc gas diffusion layers,” *Journal of Power Sources*, vol. 176, no. 1, pp. 240–246, 2008.
- [137] J. Yu, D. Froning, U. Reimer, and W. Lehnert, “Liquid water breakthrough location distances on a gas diffusion layer of polymer electrolyte membrane fuel cells,” *Journal of Power Sources*, vol. 389, pp. 56–60, 2018.
- [138] V. Konduru, “Static and dynamic contact angle measurement on rough surfaces using sessile drop profile analysis with application to water management in low temperature fuel cells,” 2010.
- [139] H. Class, *Models for non-isothermal compositional gas-liquid flow and transport in porous media*. Stuttgart: Eigenverlag des Instituts für Wasser-und Umweltsystemmodellierung, 2007.
- [140] T. Koch, K. Weishaupt, J. Müller, B. Weigand, and R. Helmig, “A (dual) network model for heat transfer in porous media,” *Transport in Porous Media*, pp. 1–35, 2021.



Institut für Wasser- und Umweltsystemmodellierung Universität Stuttgart

Pfaffenwaldring 61
70569 Stuttgart (Vaihingen)
Telefon (0711) 685 - 60156
Telefax (0711) 685 - 51073
E-Mail: iws@iws.uni-stuttgart.de
<http://www.iws.uni-stuttgart.de>

Direktoren

Prof. Dr. rer. nat. Dr.-Ing. András Bárdossy
Prof. Dr.-Ing. Rainer Helmig
Prof. Dr.-Ing. Wolfgang Nowak
Prof. Dr.-Ing. Silke Wieprecht

Vorstand (Stand 21.05.2021)

Prof. Dr. rer. nat. Dr.-Ing. A. Bárdossy
Prof. Dr.-Ing. R. Helmig
Prof. Dr.-Ing. W. Nowak
Prof. Dr.-Ing. S. Wieprecht
Prof. Dr. J.A. Sander Huisman
Jürgen Braun, PhD
apl. Prof. Dr.-Ing. H. Class
PD Dr.-Ing. Claus Haslauer
Stefan Haun, PhD
apl. Prof. Dr.-Ing. Sergey Oladyskhin
Dr. rer. nat. J. Seidel
Dr.-Ing. K. Terheiden

Emeriti

Prof. Dr.-Ing. habil. Dr.-Ing. E.h. Jürgen Giesecke
Prof. Dr.h.c. Dr.-Ing. E.h. Helmut Kobus, PhD

Lehrstuhl für Wasserbau und Wassermengenwirtschaft

Leiterin: Prof. Dr.-Ing. Silke Wieprecht
Stellv.: Dr.-Ing. Kristina Terheiden
Versuchsanstalt für Wasserbau
Leiter: Stefan Haun, PhD

Lehrstuhl für Hydromechanik und Hydrosystemmodellierung

Leiter: Prof. Dr.-Ing. Rainer Helmig
Stellv.: apl. Prof. Dr.-Ing. Holger Class

Lehrstuhl für Hydrologie und Geohydrologie

Leiter: Prof. Dr. rer. nat. Dr.-Ing. András Bárdossy
Stellv.: Dr. rer. nat. Jochen Seidel
Hydrogeophysik der Vadosen Zone
(mit Forschungszentrum Jülich)
Leiter: Prof. Dr. J.A. Sander Huisman

Lehrstuhl für Stochastische Simulation und Sicherheitsforschung für Hydrosysteme

Leiter: Prof. Dr.-Ing. Wolfgang Nowak
Stellv.: apl. Prof. Dr.-Ing. Sergey Oladyskhin

VEGAS, Versuchseinrichtung zur Grundwasser- und Altlastensanierung

Leiter: Jürgen Braun, PhD
PD Dr.-Ing. Claus Haslauer

Verzeichnis der Mitteilungshefte

- 1 Röhnisch, Arthur: *Die Bemühungen um eine Wasserbauliche Versuchsanstalt an der Technischen Hochschule Stuttgart*, und Fattah Abouleid, Abdel: *Beitrag zur Berechnung einer in lockeren Sand gerammten, zweifach verankerten Spundwand*, 1963
- 2 Marotz, Günter: *Beitrag zur Frage der Standfestigkeit von dichten Asphaltbelägen im Großwasserbau*, 1964
- 3 Gurr, Siegfried: *Beitrag zur Berechnung zusammengesetzter ebener Flächentragwerke unter besonderer Berücksichtigung ebener Stauwände, mit Hilfe von Randwert- und Lastwertmatrizen*, 1965
- 4 Plica, Peter: *Ein Beitrag zur Anwendung von Schalenkonstruktionen im Stahlwasserbau*, und Petrikat, Kurt: *Möglichkeiten und Grenzen des wasserbaulichen Versuchswesens*, 1966

- 5 Plate, Erich: *Beitrag zur Bestimmung der Windgeschwindigkeitsverteilung in der durch eine Wand gestörten bodennahen Luftschicht*, und
Röhnisch, Arthur; Marotz, Günter: *Neue Baustoffe und Bauausführungen für den Schutz der Böschungen und der Sohle von Kanälen, Flüssen und Häfen; Gestehungskosten und jeweilige Vorteile*, sowie
Unny, T.E.: *Schwingungsuntersuchungen am Kegelstrahlschieber*, 1967
- 6 Seiler, Erich: *Die Ermittlung des Anlagenwertes der bundeseigenen Binnenschiffahrtsstraßen und Talsperren und des Anteils der Binnenschifffahrt an diesem Wert*, 1967
- 7 *Sonderheft anlässlich des 65. Geburtstages von Prof. Arthur Röhnisch mit Beiträgen von*
Benk, Dieter; Breitling, J.; Gurr, Siegfried; Haberhauer, Robert; Honekamp, Hermann; Kuz, Klaus Dieter; Marotz, Günter; Mayer-Vorfelder, Hans-Jörg; Miller, Rudolf; Plate, Erich J.; Radomski, Helge; Schwarz, Helmut; Vollmer, Ernst; Wildenhahn, Eberhard; 1967
- 8 Jumikis, Alfred: *Beitrag zur experimentellen Untersuchung des Wassernachschubs in einem gefrierenden Boden und die Beurteilung der Ergebnisse*, 1968
- 9 Marotz, Günter: *Technische Grundlagen einer Wasserspeicherung im natürlichen Untergrund*, 1968
- 10 Radomski, Helge: *Untersuchungen über den Einfluß der Querschnittsform wellenförmiger Spundwände auf die statischen und rammtechnischen Eigenschaften*, 1968
- 11 Schwarz, Helmut: *Die Grenztragfähigkeit des Baugrundes bei Einwirkung vertikal gezogener Ankerplatten als zweidimensionales Bruchproblem*, 1969
- 12 Erbel, Klaus: *Ein Beitrag zur Untersuchung der Metamorphose von Mittelgebirgsschneedecken unter besonderer Berücksichtigung eines Verfahrens zur Bestimmung der thermischen Schneequalität*, 1969
- 13 Westhaus, Karl-Heinz: *Der Strukturwandel in der Binnenschifffahrt und sein Einfluß auf den Ausbau der Binnenschiffskanäle*, 1969
- 14 Mayer-Vorfelder, Hans-Jörg: *Ein Beitrag zur Berechnung des Erdwiderstandes unter Ansatz der logarithmischen Spirale als Gleitflächenfunktion*, 1970
- 15 Schulz, Manfred: *Berechnung des räumlichen Erddruckes auf die Wandung kreiszylindrischer Körper*, 1970
- 16 Mobasseri, Manoutschehr: *Die Rippenstützmauer. Konstruktion und Grenzen ihrer Standicherheit*, 1970
- 17 Benk, Dieter: *Ein Beitrag zum Betrieb und zur Bemessung von Hochwasserrückhaltebecken*, 1970
- 18 Gàl, Attila: *Bestimmung der mitschwingenden Wassermasse bei überströmten Fischbauchklappen mit kreiszylindrischem Staublech*, 1971, vergriffen
- 19 Kuz, Klaus Dieter: *Ein Beitrag zur Frage des Einsetzens von Kavitationserscheinungen in einer Düsenströmung bei Berücksichtigung der im Wasser gelösten Gase*, 1971, vergriffen
- 20 Schaak, Hartmut: *Verteilleitungen von Wasserkraftanlagen*, 1971
- 21 *Sonderheft zur Eröffnung der neuen Versuchsanstalt des Instituts für Wasserbau der Universität Stuttgart mit Beiträgen von*
Brombach, Hansjörg; Dirksen, Wolfram; Gàl, Attila; Gerlach, Reinhard; Giesecke, Jürgen; Holthoff, Franz-Josef; Kuz, Klaus Dieter; Marotz, Günter; Minor, Hans-Erwin; Petrikat, Kurt; Röhnisch, Arthur; Rueff, Helge; Schwarz, Helmut; Vollmer, Ernst; Wildenhahn, Eberhard; 1972
- 22 Wang, Chung-su: *Ein Beitrag zur Berechnung der Schwingungen an Kegelstrahlschiebern*, 1972
- 23 Mayer-Vorfelder, Hans-Jörg: *Erdwiderstandsbeiwerte nach dem Ohde-Variationsverfahren*, 1972
- 24 Minor, Hans-Erwin: *Beitrag zur Bestimmung der Schwingungsanfachungsfunktionen überströmter Stauklappen*, 1972, vergriffen
- 25 Brombach, Hansjörg: *Untersuchung strömungsmechanischer Elemente (Fluidik) und die Möglichkeit der Anwendung von Wirbelkammerelementen im Wasserbau*, 1972, vergriffen
- 26 Wildenhahn, Eberhard: *Beitrag zur Berechnung von Horizontalfilterbrunnen*, 1972

- 27 Steinlein, Helmut: *Die Eliminierung der Schwebstoffe aus Flußwasser zum Zweck der unterirdischen Wasserspeicherung, gezeigt am Beispiel der Iller*, 1972
- 28 Holthoff, Franz Josef: *Die Überwindung großer Hubhöhen in der Binnenschifffahrt durch Schwimmerhebwerke*, 1973
- 29 Röder, Karl: *Einwirkungen aus Baugrundbewegungen auf trog- und kastenförmige Konstruktionen des Wasser- und Tunnelbaues*, 1973
- 30 Kretschmer, Heinz: *Die Bemessung von Bogenstau mauern in Abhängigkeit von der Talform*, 1973
- 31 Honekamp, Hermann: *Beitrag zur Berechnung der Montage von Unterwasserpipelines*, 1973
- 32 Giesecke, Jürgen: *Die Wirbelkammertriode als neuartiges Steuerorgan im Wasserbau*, und Brombach, Hansjörg: *Entwicklung, Bauformen, Wirkungsweise und Steuereigenschaften von Wirbelkammerverstärkern*, 1974
- 33 Rueff, Helge: *Untersuchung der schwingungserregenden Kräfte an zwei hintereinander angeordneten Tiefschützen unter besonderer Berücksichtigung von Kavitation*, 1974
- 34 Röhnisch, Arthur: *Einpreßversuche mit Zementmörtel für Spannbeton - Vergleich der Ergebnisse von Modellversuchen mit Ausführungen in Hüllwellrohren*, 1975
- 35 *Sonderheft anlässlich des 65. Geburtstages von Prof. Dr.-Ing. Kurt Petrikat mit Beiträgen von:* Brombach, Hansjörg; Erbel, Klaus; Flinspach, Dieter; Fischer jr., Richard; Gál, Attila; Gerlach, Reinhard; Giesecke, Jürgen; Haberhauer, Robert; Hafner Edzard; Hausenblas, Bernhard; Horlacher, Hans-Burkhard; Hutarew, Andreas; Knoll, Manfred; Krummet, Ralph; Marotz, Günter; Merkle, Theodor; Miller, Christoph; Minor, Hans-Erwin; Neumayer, Hans; Rao, Syamala; Rath, Paul; Rueff, Helge; Ruppert, Jürgen; Schwarz, Wolfgang; Topal-Gökceli, Mehmet; Vollmer, Ernst; Wang, Chung-su; Weber, Hans-Georg; 1975
- 36 Berger, Jochum: *Beitrag zur Berechnung des Spannungszustandes in rotationssymmetrisch belasteten Kugelschalen veränderlicher Wandstärke unter Gas- und Flüssigkeitsdruck durch Integration schwach singulärer Differentialgleichungen*, 1975
- 37 Dirksen, Wolfram: *Berechnung instationärer Abflußvorgänge in gestauten Gerinnen mittels Differenzenverfahren und die Anwendung auf Hochwasserrückhaltebecken*, 1976
- 38 Horlacher, Hans-Burkhard: *Berechnung instationärer Temperatur- und Wärmespannungsfelder in langen mehrschichtigen Hohlzylindern*, 1976
- 39 Hafner, Edzard: *Untersuchung der hydrodynamischen Kräfte auf Baukörper im Tiefwasserbereich des Meeres*, 1977, ISBN 3-921694-39-6
- 40 Ruppert, Jürgen: *Über den Axialwirbelkammerverstärker für den Einsatz im Wasserbau*, 1977, ISBN 3-921694-40-X
- 41 Hutarew, Andreas: *Beitrag zur Beeinflussbarkeit des Sauerstoffgehalts in Fließgewässern an Abstürzen und Wehren*, 1977, ISBN 3-921694-41-8, vergriffen
- 42 Miller, Christoph: *Ein Beitrag zur Bestimmung der schwingungserregenden Kräfte an unterströmten Wehren*, 1977, ISBN 3-921694-42-6
- 43 Schwarz, Wolfgang: *Druckstoßberechnung unter Berücksichtigung der Radial- und Längsverschiebungen der Rohrwandung*, 1978, ISBN 3-921694-43-4
- 44 Kinzelbach, Wolfgang: *Numerische Untersuchungen über den optimalen Einsatz variabler Kühlsysteme einer Kraftwerkskette am Beispiel Oberrhein*, 1978, ISBN 3-921694-44-2
- 45 Barczewski, Baldur: *Neue Meßmethoden für Wasser-Luftgemische und deren Anwendung auf zweiphasige Auftriebsstrahlen*, 1979, ISBN 3-921694-45-0
- 46 Neumayer, Hans: *Untersuchung der Strömungsvorgänge in radialen Wirbelkammerverstärkern*, 1979, ISBN 3-921694-46-9
- 47 Elalfy, Youssef-Elhassan: *Untersuchung der Strömungsvorgänge in Wirbelkammerdioden und -drosseln*, 1979, ISBN 3-921694-47-7
- 48 Brombach, Hansjörg: *Automatisierung der Bewirtschaftung von Wasserspeichern*, 1981, ISBN 3-921694-48-5
- 49 Geldner, Peter: *Deterministische und stochastische Methoden zur Bestimmung der Selbstdichtung von Gewässern*, 1981, ISBN 3-921694-49-3, vergriffen

- 50 Mehlhorn, Hans: *Temperaturveränderungen im Grundwasser durch Brauchwassereinleitungen*, 1982, ISBN 3-921694-50-7, vergriffen
- 51 Hafner, Edzard: *Rohrleitungen und Behälter im Meer*, 1983, ISBN 3-921694-51-5
- 52 Rinnert, Bernd: *Hydrodynamische Dispersion in porösen Medien: Einfluß von Dichteunterschieden auf die Vertikalvermischung in horizontaler Strömung*, 1983, ISBN 3-921694-52-3, vergriffen
- 53 Lindner, Wulf: *Steuerung von Grundwasserentnahmen unter Einhaltung ökologischer Kriterien*, 1983, ISBN 3-921694-53-1, vergriffen
- 54 Herr, Michael; Herzer, Jörg; Kinzelbach, Wolfgang; Kobus, Helmut; Rinnert, Bernd: *Methoden zur rechnerischen Erfassung und hydraulischen Sanierung von Grundwasserkontaminationen*, 1983, ISBN 3-921694-54-X
- 55 Schmitt, Paul: *Wege zur Automatisierung der Niederschlagsermittlung*, 1984, ISBN 3-921694-55-8, vergriffen
- 56 Müller, Peter: *Transport und selektive Sedimentation von Schwebstoffen bei gestautem Abfluß*, 1985, ISBN 3-921694-56-6
- 57 El-Qawasmeh, Fuad: *Möglichkeiten und Grenzen der Tropfbewässerung unter besonderer Berücksichtigung der Verstopfungsanfälligkeit der Tropfelemente*, 1985, ISBN 3-921694-57-4, vergriffen
- 58 Kirchenbaur, Klaus: *Mikroprozessorgesteuerte Erfassung instationärer Druckfelder am Beispiel seegangsbelasteter Baukörper*, 1985, ISBN 3-921694-58-2
- 59 Kobus, Helmut (Hrsg.): *Modellierung des großräumigen Wärme- und Schadstofftransports im Grundwasser*, Tätigkeitsbericht 1984/85 (DFG-Forschergruppe an den Universitäten Hohenheim, Karlsruhe und Stuttgart), 1985, ISBN 3-921694-59-0, vergriffen
- 60 Spitz, Karlheinz: *Dispersion in porösen Medien: Einfluß von Inhomogenitäten und Dichteunterschieden*, 1985, ISBN 3-921694-60-4, vergriffen
- 61 Kobus, Helmut: *An Introduction to Air-Water Flows in Hydraulics*, 1985, ISBN 3-921694-61-2
- 62 Kaleris, Vassilios: *Erfassung des Austausches von Oberflächen- und Grundwasser in horizontalebene Grundwassermodellen*, 1986, ISBN 3-921694-62-0
- 63 Herr, Michael: *Grundlagen der hydraulischen Sanierung verunreinigter Porengrundwasserleiter*, 1987, ISBN 3-921694-63-9
- 64 Marx, Walter: *Berechnung von Temperatur und Spannung in Massenbeton infolge Hydratation*, 1987, ISBN 3-921694-64-7
- 65 Koschitzky, Hans-Peter: *Dimensionierungskonzept für Sohlbelüfter in Schußrinnen zur Vermeidung von Kavitationsschäden*, 1987, ISBN 3-921694-65-5
- 66 Kobus, Helmut (Hrsg.): *Modellierung des großräumigen Wärme- und Schadstofftransports im Grundwasser*, Tätigkeitsbericht 1986/87 (DFG-Forschergruppe an den Universitäten Hohenheim, Karlsruhe und Stuttgart) 1987, ISBN 3-921694-66-3
- 67 Söll, Thomas: *Berechnungsverfahren zur Abschätzung anthropogener Temperaturanomalien im Grundwasser*, 1988, ISBN 3-921694-67-1
- 68 Dittrich, Andreas; Westrich, Bernd: *Bodenseeufererosion, Bestandsaufnahme und Bewertung*, 1988, ISBN 3-921694-68-X, vergriffen
- 69 Huwe, Bernd; van der Ploeg, Rienk R.: *Modelle zur Simulation des Stickstoffhaushaltes von Standorten mit unterschiedlicher landwirtschaftlicher Nutzung*, 1988, ISBN 3-921694-69-8, vergriffen
- 70 Stephan, Karl: *Integration elliptischer Funktionen*, 1988, ISBN 3-921694-70-1
- 71 Kobus, Helmut; Zilliox, Lothaire (Hrsg.): *Nitratbelastung des Grundwassers, Auswirkungen der Landwirtschaft auf die Grundwasser- und Rohwasserbeschaffenheit und Maßnahmen zum Schutz des Grundwassers*. Vorträge des deutsch-französischen Kolloquiums am 6. Oktober 1988, Universitäten Stuttgart und Louis Pasteur Strasbourg (Vorträge in deutsch oder französisch, Kurzfassungen zweisprachig), 1988, ISBN 3-921694-71-X

- 72 Soyeaux, Renald: *Unterströmung von Stauanlagen auf klüftigem Untergrund unter Berücksichtigung laminarer und turbulenter Fließzustände*, 1991, ISBN 3-921694-72-8
- 73 Kohane, Roberto: *Berechnungsmethoden für Hochwasserabfluß in Fließgewässern mit überströmten Vorländern*, 1991, ISBN 3-921694-73-6
- 74 Hassinger, Reinhard: *Beitrag zur Hydraulik und Bemessung von Blocksteinrampen in flexibler Bauweise*, 1991, ISBN 3-921694-74-4, vergriffen
- 75 Schäfer, Gerhard: *Einfluß von Schichtenstrukturen und lokalen Einlagerungen auf die Längsdispersion in Porengrundwasserleitern*, 1991, ISBN 3-921694-75-2
- 76 Giesecke, Jürgen: *Vorträge, Wasserwirtschaft in stark besiedelten Regionen; Umweltforschung mit Schwerpunkt Wasserwirtschaft*, 1991, ISBN 3-921694-76-0
- 77 Huwe, Bernd: *Deterministische und stochastische Ansätze zur Modellierung des Stickstoffhaushalts landwirtschaftlich genutzter Flächen auf unterschiedlichem Skalenniveau*, 1992, ISBN 3-921694-77-9, vergriffen
- 78 Rommel, Michael: *Verwendung von Kluffdaten zur realitätsnahen Generierung von Kluffnetzen mit anschließender laminar-turbulenter Strömungsberechnung*, 1993, ISBN 3-92 1694-78-7
- 79 Marschall, Paul: *Die Ermittlung lokaler Stofffrachten im Grundwasser mit Hilfe von Einbohrloch-Meßverfahren*, 1993, ISBN 3-921694-79-5, vergriffen
- 80 Ptak, Thomas: *Stofftransport in heterogenen Porenaquifereen: Felduntersuchungen und stochastische Modellierung*, 1993, ISBN 3-921694-80-9, vergriffen
- 81 Haakh, Frieder: *Transientes Strömungsverhalten in Wirbelkammern*, 1993, ISBN 3-921694-81-7
- 82 Kobus, Helmut; Cirpka, Olaf; Barczewski, Baldur; Koschitzky, Hans-Peter: *Versuchseinrichtung zur Grundwasser- und Altlastensanierung VEGAS, Konzeption und Programmrahmen*, 1993, ISBN 3-921694-82-5
- 83 Zang, Weidong: *Optimaler Echtzeit-Betrieb eines Speichers mit aktueller Abflußregenerierung*, 1994, ISBN 3-921694-83-3, vergriffen
- 84 Franke, Hans-Jörg: *Stochastische Modellierung eines flächenhaften Stoffeintrages und Transports in Grundwasser am Beispiel der Pflanzenschutzmittelproblematik*, 1995, ISBN 3-921694-84-1
- 85 Lang, Ulrich: *Simulation regionaler Strömungs- und Transportvorgänge in Karstaquifereen mit Hilfe des Doppelkontinuum-Ansatzes: Methodenentwicklung und Parameteridentifikation*, 1995, ISBN 3-921694-85-X, vergriffen
- 86 Helmig, Rainer: *Einführung in die Numerischen Methoden der Hydromechanik*, 1996, ISBN 3-921694-86-8, vergriffen
- 87 Cirpka, Olaf: *CONTRACT: A Numerical Tool for Contaminant Transport and Chemical Transformations - Theory and Program Documentation -*, 1996, ISBN 3-921694-87-6
- 88 Haberlandt, Uwe: *Stochastische Synthese und Regionalisierung des Niederschlages für Schmutzfrachtberechnungen*, 1996, ISBN 3-921694-88-4
- 89 Croisé, Jean: *Extraktion von flüchtigen Chemikalien aus natürlichen Lockergesteinen mittels erzwungener Luftströmung*, 1996, ISBN 3-921694-89-2, vergriffen
- 90 Jorde, Klaus: *Ökologisch begründete, dynamische Mindestwasserregelungen bei Ausleitungskraftwerken*, 1997, ISBN 3-921694-90-6, vergriffen
- 91 Helmig, Rainer: *Gekoppelte Strömungs- und Transportprozesse im Untergrund - Ein Beitrag zur Hydrosystemmodellierung-*, 1998, ISBN 3-921694-91-4, vergriffen
- 92 Emmert, Martin: *Numerische Modellierung nichtisothermer Gas-Wasser Systeme in porösen Medien*, 1997, ISBN 3-921694-92-2
- 93 Kern, Ulrich: *Transport von Schweb- und Schadstoffen in staugeregelten Fließgewässern am Beispiel des Neckars*, 1997, ISBN 3-921694-93-0, vergriffen
- 94 Förster, Georg: *Druckstoßdämpfung durch große Luftblasen in Hochpunkten von Rohrleitungen* 1997, ISBN 3-921694-94-9

- 95 Cirpka, Olaf: *Numerische Methoden zur Simulation des reaktiven Mehrkomponententransports im Grundwasser*, 1997, ISBN 3-921694-95-7, vergriffen
- 96 Färber, Arne: *Wärmetransport in der ungesättigten Bodenzone: Entwicklung einer thermischen In-situ-Sanierungstechnologie*, 1997, ISBN 3-921694-96-5
- 97 Betz, Christoph: *Wasserdampfdestillation von Schadstoffen im porösen Medium: Entwicklung einer thermischen In-situ-Sanierungstechnologie*, 1998, SBN 3-921694-97-3
- 98 Xu, Yichun: *Numerical Modeling of Suspended Sediment Transport in Rivers*, 1998, ISBN 3-921694-98-1, vergriffen
- 99 Wüst, Wolfgang: *Geochemische Untersuchungen zur Sanierung CKW-kontaminierter Aquifere mit Fe(0)-Reaktionswänden*, 2000, ISBN 3-933761-02-2
- 100 Sheta, Hussam: *Simulation von Mehrphasenvorgängen in porösen Medien unter Einbeziehung von Hysterese-Effekten*, 2000, ISBN 3-933761-03-4
- 101 Ayros, Edwin: *Regionalisierung extremer Abflüsse auf der Grundlage statistischer Verfahren*, 2000, ISBN 3-933761-04-2, vergriffen
- 102 Huber, Ralf: *Compositional Multiphase Flow and Transport in Heterogeneous Porous Media*, 2000, ISBN 3-933761-05-0
- 103 Braun, Christopherus: *Ein Upscaling-Verfahren für Mehrphasenströmungen in porösen Medien*, 2000, ISBN 3-933761-06-9
- 104 Hofmann, Bernd: *Entwicklung eines rechnergestützten Managementsystems zur Beurteilung von Grundwasserschadensfällen*, 2000, ISBN 3-933761-07-7
- 105 Class, Holger: *Theorie und numerische Modellierung nichtisothermer Mehrphasenprozesse in NAPL-kontaminierten porösen Medien*, 2001, ISBN 3-933761-08-5
- 106 Schmidt, Reinhard: *Wasserdampf- und Heißluftinjektion zur thermischen Sanierung kontaminierter Standorte*, 2001, ISBN 3-933761-09-3
- 107 Josef, Reinhold: *Schadstoffextraktion mit hydraulischen Sanierungsverfahren unter Anwendung von grenzflächenaktiven Stoffen*, 2001, ISBN 3-933761-10-7
- 108 Schneider, Matthias: *Habitat- und Abflussmodellierung für Fließgewässer mit unscharfen Berechnungsansätzen*, 2001, ISBN 3-933761-11-5
- 109 Rathgeb, Andreas: *Hydrodynamische Bemessungsgrundlagen für Lockerdeckwerke an überströmbaren Erddämmen*, 2001, ISBN 3-933761-12-3
- 110 Lang, Stefan: *Parallele numerische Simulation instationärer Probleme mit adaptiven Methoden auf unstrukturierten Gittern*, 2001, ISBN 3-933761-13-1
- 111 Appt, Jochen; Stumpp Simone: *Die Bodensee-Messkampagne 2001, IWS/CWR Lake Constance Measurement Program 2001*, 2002, ISBN 3-933761-14-X
- 112 Heimerl, Stephan: *Systematische Beurteilung von Wasserkraftprojekten*, 2002, ISBN 3-933761-15-8, vergriffen
- 113 Iqbal, Amin: *On the Management and Salinity Control of Drip Irrigation*, 2002, ISBN 3-933761-16-6
- 114 Silberhorn-Hemminger, Annette: *Modellierung von Kluftaquifersystemen: Geostatistische Analyse und deterministisch-stochastische Kluftgenerierung*, 2002, ISBN 3-933761-17-4
- 115 Winkler, Angela: *Prozesse des Wärme- und Stofftransports bei der In-situ-Sanierung mit festen Wärmequellen*, 2003, ISBN 3-933761-18-2
- 116 Marx, Walter: *Wasserkraft, Bewässerung, Umwelt - Planungs- und Bewertungsschwerpunkte der Wasserbewirtschaftung*, 2003, ISBN 3-933761-19-0
- 117 Hinkelmann, Reinhard: *Efficient Numerical Methods and Information-Processing Techniques in Environment Water*, 2003, ISBN 3-933761-20-4
- 118 Samaniego-Eguiguren, Luis Eduardo: *Hydrological Consequences of Land Use / Land Cover and Climatic Changes in Mesoscale Catchments*, 2003, ISBN 3-933761-21-2
- 119 Neunhäuserer, Lina: *Diskretisierungsansätze zur Modellierung von Strömungs- und Transportprozessen in geklüftet-porösen Medien*, 2003, ISBN 3-933761-22-0
- 120 Paul, Maren: *Simulation of Two-Phase Flow in Heterogeneous Poros Media with Adaptive Methods*, 2003, ISBN 3-933761-23-9

- 121 Ehret, Uwe: *Rainfall and Flood Nowcasting in Small Catchments using Weather Radar*, 2003, ISBN 3-933761-24-7
- 122 Haag, Ingo: *Der Sauerstoffhaushalt staugeregelter Flüsse am Beispiel des Neckars - Analysen, Experimente, Simulationen -*, 2003, ISBN 3-933761-25-5
- 123 Appt, Jochen: *Analysis of Basin-Scale Internal Waves in Upper Lake Constance*, 2003, ISBN 3-933761-26-3
- 124 Hrsg.: Schrenk, Volker; Batereau, Katrin; Barczewski, Baldur; Weber, Karolin und Koschitzky, Hans-Peter: *Symposium Ressource Fläche und VEGAS - Statuskolloquium 2003, 30. September und 1. Oktober 2003*, 2003, ISBN 3-933761-27-1
- 125 Omar Khalil Ouda: *Optimisation of Agricultural Water Use: A Decision Support System for the Gaza Strip*, 2003, ISBN 3-933761-28-0
- 126 Batereau, Katrin: *Sensorbasierte Bodenluftmessung zur Vor-Ort-Erkundung von Schadensherden im Untergrund*, 2004, ISBN 3-933761-29-8
- 127 Witt, Oliver: *Erosionsstabilität von Gewässersedimenten mit Auswirkung auf den Stofftransport bei Hochwasser am Beispiel ausgewählter Stauhaltungen des Oberrheins*, 2004, ISBN 3-933761-30-1
- 128 Jakobs, Hartmut: *Simulation nicht-isothermer Gas-Wasser-Prozesse in komplexen Kluft-Matrix-Systemen*, 2004, ISBN 3-933761-31-X
- 129 Li, Chen-Chien: *Deterministisch-stochastisches Berechnungskonzept zur Beurteilung der Auswirkungen erosiver Hochwasserereignisse in Flusstauhaltungen*, 2004, ISBN 3-933761-32-8
- 130 Reichenberger, Volker; Helmig, Rainer; Jakobs, Hartmut; Bastian, Peter; Niessner, Jennifer: *Complex Gas-Water Processes in Discrete Fracture-Matrix Systems: Up-scaling, Mass-Conservative Discretization and Efficient Multilevel Solution*, 2004, ISBN 3-933761-33-6
- 131 Hrsg.: Barczewski, Baldur; Koschitzky, Hans-Peter; Weber, Karolin; Wege, Ralf: *VEGAS - Statuskolloquium 2004*, Tagungsband zur Veranstaltung am 05. Oktober 2004 an der Universität Stuttgart, Campus Stuttgart-Vaihingen, 2004, ISBN 3-933761-34-4
- 132 Asie, Kemal Jabir: *Finite Volume Models for Multiphase Multicomponent Flow through Porous Media*. 2005, ISBN 3-933761-35-2
- 133 Jacoub, George: *Development of a 2-D Numerical Module for Particulate Contaminant Transport in Flood Retention Reservoirs and Impounded Rivers*, 2004, ISBN 3-933761-36-0
- 134 Nowak, Wolfgang: *Geostatistical Methods for the Identification of Flow and Transport Parameters in the Subsurface*, 2005, ISBN 3-933761-37-9
- 135 Süß, Mia: *Analysis of the influence of structures and boundaries on flow and transport processes in fractured porous media*, 2005, ISBN 3-933761-38-7
- 136 Jose, Surabhin Chackiath: *Experimental Investigations on Longitudinal Dispersive Mixing in Heterogeneous Aquifers*, 2005, ISBN: 3-933761-39-5
- 137 Filiz, Fulya: *Linking Large-Scale Meteorological Conditions to Floods in Mesoscale Catchments*, 2005, ISBN 3-933761-40-9
- 138 Qin, Minghao: *Wirklichkeitsnahe und recheneffiziente Ermittlung von Temperatur und Spannungen bei großen RCC-Staumauern*, 2005, ISBN 3-933761-41-7
- 139 Kobayashi, Kenichiro: *Optimization Methods for Multiphase Systems in the Subsurface - Application to Methane Migration in Coal Mining Areas*, 2005, ISBN 3-933761-42-5
- 140 Rahman, Md. Arifur: *Experimental Investigations on Transverse Dispersive Mixing in Heterogeneous Porous Media*, 2005, ISBN 3-933761-43-3
- 141 Schrenk, Volker: *Ökobilanzen zur Bewertung von Altlastensanierungsmaßnahmen*, 2005, ISBN 3-933761-44-1
- 142 Hundecha, Hirpa Yeshewatesfa: *Regionalization of Parameters of a Conceptual Rainfall-Runoff Model*, 2005, ISBN: 3-933761-45-X
- 143 Wege, Ralf: *Untersuchungs- und Überwachungsmethoden für die Beurteilung natürlicher Selbstreinigungsprozesse im Grundwasser*, 2005, ISBN 3-933761-46-8

- 144 Breiting, Thomas: *Techniken und Methoden der Hydroinformatik - Modellierung von komplexen Hydrosystemen im Untergrund*, 2006, ISBN 3-933761-47-6
- 145 Hrsg.: Braun, Jürgen; Koschitzky, Hans-Peter; Müller, Martin: *Ressource Untergrund: 10 Jahre VEGAS: Forschung und Technologieentwicklung zum Schutz von Grundwasser und Boden*, Tagungsband zur Veranstaltung am 28. und 29. September 2005 an der Universität Stuttgart, Campus Stuttgart-Vaihingen, 2005, ISBN 3-933761-48-4
- 146 Rojanschi, Vlad: *Abflusskonzentration in mesoskaligen Einzugsgebieten unter Berücksichtigung des Sickerraumes*, 2006, ISBN 3-933761-49-2
- 147 Winkler, Nina Simone: *Optimierung der Steuerung von Hochwasserrückhaltebeckensystemen*, 2006, ISBN 3-933761-50-6
- 148 Wolf, Jens: *Räumlich differenzierte Modellierung der Grundwasserströmung alluvialer Aquifere für mesoskalige Einzugsgebiete*, 2006, ISBN: 3-933761-51-4
- 149 Kohler, Beate: *Externe Effekte der Laufwasserkraftnutzung*, 2006, ISBN 3-933761-52-2
- 150 Hrsg.: Braun, Jürgen; Koschitzky, Hans-Peter; Stuhmann, Matthias: *VEGAS-Statuskolloquium 2006*, Tagungsband zur Veranstaltung am 28. September 2006 an der Universität Stuttgart, Campus Stuttgart-Vaihingen, 2006, ISBN 3-933761-53-0
- 151 Niessner, Jennifer: *Multi-Scale Modeling of Multi-Phase - Multi-Component Processes in Heterogeneous Porous Media*, 2006, ISBN 3-933761-54-9
- 152 Fischer, Markus: *Beanspruchung eingeeerdeter Rohrleitungen infolge Austrocknung bindiger Böden*, 2006, ISBN 3-933761-55-7
- 153 Schneck, Alexander: *Optimierung der Grundwasserbewirtschaftung unter Berücksichtigung der Belange der Wasserversorgung, der Landwirtschaft und des Naturschutzes*, 2006, ISBN 3-933761-56-5
- 154 Das, Tapash: *The Impact of Spatial Variability of Precipitation on the Predictive Uncertainty of Hydrological Models*, 2006, ISBN 3-33761-57-3
- 155 Bielinski, Andreas: *Numerical Simulation of CO₂ sequestration in geological formations*, 2007, ISBN 3-933761-58-1
- 156 Mödinger, Jens: *Entwicklung eines Bewertungs- und Entscheidungsunterstützungssystems für eine nachhaltige regionale Grundwasserbewirtschaftung*, 2006, ISBN 3-933761-60-3
- 157 Manthey, Sabine: *Two-phase flow processes with dynamic effects in porous media - parameter estimation and simulation*, 2007, ISBN 3-933761-61-1
- 158 Pozos Estrada, Oscar: *Investigation on the Effects of Entrained Air in Pipelines*, 2007, ISBN 3-933761-62-X
- 159 Ochs, Steffen Oliver: *Steam injection into saturated porous media – process analysis including experimental and numerical investigations*, 2007, ISBN 3-933761-63-8
- 160 Marx, Andreas: *Einsatz gekoppelter Modelle und Wetterradar zur Abschätzung von Niederschlagsintensitäten und zur Abflussvorhersage*, 2007, ISBN 3-933761-64-6
- 161 Hartmann, Gabriele Maria: *Investigation of Evapotranspiration Concepts in Hydrological Modelling for Climate Change Impact Assessment*, 2007, ISBN 3-933761-65-4
- 162 Kebede Gurmessa, Tesfaye: *Numerical Investigation on Flow and Transport Characteristics to Improve Long-Term Simulation of Reservoir Sedimentation*, 2007, ISBN 3-933761-66-2
- 163 Trifković, Aleksandar: *Multi-objective and Risk-based Modelling Methodology for Planning, Design and Operation of Water Supply Systems*, 2007, ISBN 3-933761-67-0
- 164 Götzing, Jens: *Distributed Conceptual Hydrological Modelling - Simulation of Climate, Land Use Change Impact and Uncertainty Analysis*, 2007, ISBN 3-933761-68-9
- 165 Hrsg.: Braun, Jürgen; Koschitzky, Hans-Peter; Stuhmann, Matthias: *VEGAS – Kolloquium 2007*, Tagungsband zur Veranstaltung am 26. September 2007 an der Universität Stuttgart, Campus Stuttgart-Vaihingen, 2007, ISBN 3-933761-69-7
- 166 Freeman, Beau: *Modernization Criteria Assessment for Water Resources Planning; Klamath Irrigation Project, U.S.*, 2008, ISBN 3-933761-70-0

- 167 Dreher, Thomas: *Selektive Sedimentation von Feinstschwebstoffen in Wechselwirkung mit wandnahen turbulenten Strömungsbedingungen*, 2008, ISBN 3-933761-71-9
- 168 Yang, Wei: *Discrete-Continuous Downscaling Model for Generating Daily Precipitation Time Series*, 2008, ISBN 3-933761-72-7
- 169 Kopecki, Ianina: *Calculational Approach to FST-Hemispheres for Multiparametrical Benthos Habitat Modelling*, 2008, ISBN 3-933761-73-5
- 170 Brommundt, Jürgen: *Stochastische Generierung räumlich zusammenhängender Niederschlagszeitreihen*, 2008, ISBN 3-933761-74-3
- 171 Papafotiou, Alexandros: *Numerical Investigations of the Role of Hysteresis in Heterogeneous Two-Phase Flow Systems*, 2008, ISBN 3-933761-75-1
- 172 He, Yi: *Application of a Non-Parametric Classification Scheme to Catchment Hydrology*, 2008, ISBN 978-3-933761-76-7
- 173 Wagner, Sven: *Water Balance in a Poorly Gauged Basin in West Africa Using Atmospheric Modelling and Remote Sensing Information*, 2008, ISBN 978-3-933761-77-4
- 174 Hrsg.: Braun, Jürgen; Koschitzky, Hans-Peter; Stuhmann, Matthias; Schrenk, Volker: *VEGAS-Kolloquium 2008 Ressource Fläche III*, Tagungsband zur Veranstaltung am 01. Oktober 2008 an der Universität Stuttgart, Campus Stuttgart-Vaihingen, 2008, ISBN 978-3-933761-78-1
- 175 Patil, Sachin: *Regionalization of an Event Based Nash Cascade Model for Flood Predictions in Ungauged Basins*, 2008, ISBN 978-3-933761-79-8
- 176 Assteerawatt, Anongnart: *Flow and Transport Modelling of Fractured Aquifers based on a Geostatistical Approach*, 2008, ISBN 978-3-933761-80-4
- 177 Karnahl, Joachim Alexander: *2D numerische Modellierung von multifraktionalem Schwebstoff- und Schadstofftransport in Flüssen*, 2008, ISBN 978-3-933761-81-1
- 178 Hiester, Uwe: *Technologieentwicklung zur In-situ-Sanierung der ungesättigten Bodenzone mit festen Wärmequellen*, 2009, ISBN 978-3-933761-82-8
- 179 Laux, Patrick: *Statistical Modeling of Precipitation for Agricultural Planning in the Volta Basin of West Africa*, 2009, ISBN 978-3-933761-83-5
- 180 Ehsan, Saqib: *Evaluation of Life Safety Risks Related to Severe Flooding*, 2009, ISBN 978-3-933761-84-2
- 181 Prohaska, Sandra: *Development and Application of a 1D Multi-Strip Fine Sediment Transport Model for Regulated Rivers*, 2009, ISBN 978-3-933761-85-9
- 182 Kopp, Andreas: *Evaluation of CO₂ Injection Processes in Geological Formations for Site Screening*, 2009, ISBN 978-3-933761-86-6
- 183 Ebigbo, Anozie: *Modelling of biofilm growth and its influence on CO₂ and water (two-phase) flow in porous media*, 2009, ISBN 978-3-933761-87-3
- 184 Freiboth, Sandra: *A phenomenological model for the numerical simulation of multiphase multicomponent processes considering structural alterations of porous media*, 2009, ISBN 978-3-933761-88-0
- 185 Zöllner, Frank: *Implementierung und Anwendung netzfreier Methoden im Konstruktiven Wasserbau und in der Hydromechanik*, 2009, ISBN 978-3-933761-89-7
- 186 Vasin, Milos: *Influence of the soil structure and property contrast on flow and transport in the unsaturated zone*, 2010, ISBN 978-3-933761-90-3
- 187 Li, Jing: *Application of Copulas as a New Geostatistical Tool*, 2010, ISBN 978-3-933761-91-0
- 188 AghaKouchak, Amir: *Simulation of Remotely Sensed Rainfall Fields Using Copulas*, 2010, ISBN 978-3-933761-92-7
- 189 Thapa, Pawan Kumar: *Physically-based spatially distributed rainfall runoff modelling for soil erosion estimation*, 2010, ISBN 978-3-933761-93-4
- 190 Wurms, Sven: *Numerische Modellierung der Sedimentationsprozesse in Retentionsanlagen zur Steuerung von Stoffströmen bei extremen Hochwasserabflussereignissen*, 2011, ISBN 978-3-933761-94-1

- 191 Merkel, Uwe: *Unsicherheitsanalyse hydraulischer Einwirkungen auf Hochwasserschutzdeiche und Steigerung der Leistungsfähigkeit durch adaptive Strömungsmodellierung*, 2011, ISBN 978-3-933761-95-8
- 192 Fritz, Jochen: *A Decoupled Model for Compositional Non-Isothermal Multiphase Flow in Porous Media and Multiphysics Approaches for Two-Phase Flow*, 2010, ISBN 978-3-933761-96-5
- 193 Weber, Karolin (Hrsg.): *12. Treffen junger WissenschaftlerInnen an Wasserbauinstituten*, 2010, ISBN 978-3-933761-97-2
- 194 Bliedernicht, Jan-Geert: *Probability Forecasts of Daily Areal Precipitation for Small River Basins*, 2011, ISBN 978-3-933761-98-9
- 195 Hrsg.: Koschitzky, Hans-Peter; Braun, Jürgen: *VEGAS-Kolloquium 2010 In-situ-Sanierung - Stand und Entwicklung Nano und ISCO -*, Tagungsband zur Veranstaltung am 07. Oktober 2010 an der Universität Stuttgart, Campus Stuttgart-Vaihingen, 2010, ISBN 978-3-933761-99-6
- 196 Gafurov, Abror: *Water Balance Modeling Using Remote Sensing Information - Focus on Central Asia*, 2010, ISBN 978-3-942036-00-9
- 197 Mackenberg, Sylvia: *Die Quellstärke in der Sickerwasserprognose: Möglichkeiten und Grenzen von Labor- und Freilanduntersuchungen*, 2010, ISBN 978-3-942036-01-6
- 198 Singh, Shailesh Kumar: *Robust Parameter Estimation in Gauged and Ungauged Basins*, 2010, ISBN 978-3-942036-02-3
- 199 Doğan, Mehmet Onur: *Coupling of porous media flow with pipe flow*, 2011, ISBN 978-3-942036-03-0
- 200 Liu, Min: *Study of Topographic Effects on Hydrological Patterns and the Implication on Hydrological Modeling and Data Interpolation*, 2011, ISBN 978-3-942036-04-7
- 201 Geleta, Habtamu Itafa: *Watershed Sediment Yield Modeling for Data Scarce Areas*, 2011, ISBN 978-3-942036-05-4
- 202 Franke, Jörg: *Einfluss der Überwachung auf die Versagenswahrscheinlichkeit von Staustufen*, 2011, ISBN 978-3-942036-06-1
- 203 Bakimchandra, Oinam: *Integrated Fuzzy-GIS approach for assessing regional soil erosion risks*, 2011, ISBN 978-3-942036-07-8
- 204 Alam, Muhammad Mahboob: *Statistical Downscaling of Extremes of Precipitation in Mesoscale Catchments from Different RCMs and Their Effects on Local Hydrology*, 2011, ISBN 978-3-942036-08-5
- 205 Hrsg.: Koschitzky, Hans-Peter; Braun, Jürgen: *VEGAS-Kolloquium 2011 Flache Geothermie - Perspektiven und Risiken*, Tagungsband zur Veranstaltung am 06. Oktober 2011 an der Universität Stuttgart, Campus Stuttgart-Vaihingen, 2011, ISBN 978-3-933761-09-2
- 206 Haslauer, Claus: *Analysis of Real-World Spatial Dependence of Subsurface Hydraulic Properties Using Copulas with a Focus on Solute Transport Behaviour*, 2011, ISBN 978-3-942036-10-8
- 207 Dung, Nguyen Viet: *Multi-objective automatic calibration of hydrodynamic models – development of the concept and an application in the Mekong Delta*, 2011, ISBN 978-3-942036-11-5
- 208 Hung, Nguyen Nghia: *Sediment dynamics in the floodplain of the Mekong Delta, Vietnam*, 2011, ISBN 978-3-942036-12-2
- 209 Kuhlmann, Anna: *Influence of soil structure and root water uptake on flow in the unsaturated zone*, 2012, ISBN 978-3-942036-13-9
- 210 Tuhtan, Jeffrey Andrew: *Including the Second Law Inequality in Aquatic Ecodynamics: A Modeling Approach for Alpine Rivers Impacted by Hydropeaking*, 2012, ISBN 978-3-942036-14-6
- 211 Tolossa, Habtamu: *Sediment Transport Computation Using a Data-Driven Adaptive Neuro-Fuzzy Modelling Approach*, 2012, ISBN 978-3-942036-15-3
- 212 Tatomir, Alexandru-Bodgan: *From Discrete to Continuum Concepts of Flow in Fractured Porous Media*, 2012, ISBN 978-3-942036-16-0

- 213 Erbertseder, Karin: *A Multi-Scale Model for Describing Cancer-Therapeutic Transport in the Human Lung*, 2012, ISBN 978-3-942036-17-7
- 214 Noack, Markus: *Modelling Approach for Interstitial Sediment Dynamics and Reproduction of Gravel Spawning Fish*, 2012, ISBN 978-3-942036-18-4
- 215 De Boer, Cjestrir Volkert: *Transport of Nano Sized Zero Valent Iron Colloids during Injection into the Subsurface*, 2012, ISBN 978-3-942036-19-1
- 216 Pfaff, Thomas: *Processing and Analysis of Weather Radar Data for Use in Hydrology*, 2013, ISBN 978-3-942036-20-7
- 217 Lebreuz, Hans-Henning: *Addressing the Input Uncertainty for Hydrological Modeling by a New Geostatistical Method*, 2013, ISBN 978-3-942036-21-4
- 218 Darcis, Melanie Yvonne: *Coupling Models of Different Complexity for the Simulation of CO₂ Storage in Deep Saline Aquifers*, 2013, ISBN 978-3-942036-22-1
- 219 Beck, Ferdinand: *Generation of Spatially Correlated Synthetic Rainfall Time Series in High Temporal Resolution - A Data Driven Approach*, 2013, ISBN 978-3-942036-23-8
- 220 Guthke, Philipp: *Non-multi-Gaussian spatial structures: Process-driven natural genesis, manifestation, modeling approaches, and influences on dependent processes*, 2013, ISBN 978-3-942036-24-5
- 221 Walter, Lena: *Uncertainty studies and risk assessment for CO₂ storage in geological formations*, 2013, ISBN 978-3-942036-25-2
- 222 Wolff, Markus: *Multi-scale modeling of two-phase flow in porous media including capillary pressure effects*, 2013, ISBN 978-3-942036-26-9
- 223 Mosthaf, Klaus Roland: *Modeling and analysis of coupled porous-medium and free flow with application to evaporation processes*, 2014, ISBN 978-3-942036-27-6
- 224 Leube, Philipp Christoph: *Methods for Physically-Based Model Reduction in Time: Analysis, Comparison of Methods and Application*, 2013, ISBN 978-3-942036-28-3
- 225 Rodríguez Fernández, Jhan Ignacio: *High Order Interactions among environmental variables: Diagnostics and initial steps towards modeling*, 2013, ISBN 978-3-942036-29-0
- 226 Eder, Maria Magdalena: *Climate Sensitivity of a Large Lake*, 2013, ISBN 978-3-942036-30-6
- 227 Greiner, Philipp: *Alkoholinjektion zur In-situ-Sanierung von CKW Schadensherden in Grundwasserleitern: Charakterisierung der relevanten Prozesse auf unterschiedlichen Skalen*, 2014, ISBN 978-3-942036-31-3
- 228 Lauser, Andreas: *Theory and Numerical Applications of Compositional Multi-Phase Flow in Porous Media*, 2014, ISBN 978-3-942036-32-0
- 229 Enzenhöfer, Rainer: *Risk Quantification and Management in Water Production and Supply Systems*, 2014, ISBN 978-3-942036-33-7
- 230 Faigle, Benjamin: *Adaptive modelling of compositional multi-phase flow with capillary pressure*, 2014, ISBN 978-3-942036-34-4
- 231 Oladyshkin, Sergey: *Efficient modeling of environmental systems in the face of complexity and uncertainty*, 2014, ISBN 978-3-942036-35-1
- 232 Sugimoto, Takayuki: *Copula based Stochastic Analysis of Discharge Time Series*, 2014, ISBN 978-3-942036-36-8
- 233 Koch, Jonas: *Simulation, Identification and Characterization of Contaminant Source Architectures in the Subsurface*, 2014, ISBN 978-3-942036-37-5
- 234 Zhang, Jin: *Investigations on Urban River Regulation and Ecological Rehabilitation Measures, Case of Shenzhen in China*, 2014, ISBN 978-3-942036-38-2
- 235 Siebel, Rüdiger: *Experimentelle Untersuchungen zur hydrodynamischen Belastung und Standsicherheit von Deckwerken an überströmbaren Erddämmen*, 2014, ISBN 978-3-942036-39-9
- 236 Baber, Katherina: *Coupling free flow and flow in porous media in biological and technical applications: From a simple to a complex interface description*, 2014, ISBN 978-3-942036-40-5

- 237 Nuske, Klaus Philipp: *Beyond Local Equilibrium — Relaxing local equilibrium assumptions in multiphase flow in porous media*, 2014, ISBN 978-3-942036-41-2
- 238 Geiges, Andreas: *Efficient concepts for optimal experimental design in nonlinear environmental systems*, 2014, ISBN 978-3-942036-42-9
- 239 Schwenck, Nicolas: *An XFEM-Based Model for Fluid Flow in Fractured Porous Media*, 2014, ISBN 978-3-942036-43-6
- 240 Chamorro Chávez, Alejandro: *Stochastic and hydrological modelling for climate change prediction in the Lima region, Peru*, 2015, ISBN 978-3-942036-44-3
- 241 Yulizar: *Investigation of Changes in Hydro-Meteorological Time Series Using a Depth-Based Approach*, 2015, ISBN 978-3-942036-45-0
- 242 Kretschmer, Nicole: *Impacts of the existing water allocation scheme on the Limarí watershed – Chile, an integrative approach*, 2015, ISBN 978-3-942036-46-7
- 243 Kramer, Matthias: *Luftbedarf von Freistrahlturbinen im Gegendruckbetrieb*, 2015, ISBN 978-3-942036-47-4
- 244 Hommel, Johannes: *Modeling biogeochemical and mass transport processes in the sub-surface: Investigation of microbially induced calcite precipitation*, 2016, ISBN 978-3-942036-48-1
- 245 Germer, Kai: *Wasserinfiltration in die ungesättigte Zone eines makroporösen Hanges und deren Einfluss auf die Hangstabilität*, 2016, ISBN 978-3-942036-49-8
- 246 Hörning, Sebastian: *Process-oriented modeling of spatial random fields using copulas*, 2016, ISBN 978-3-942036-50-4
- 247 Jambhekar, Vishal: *Numerical modeling and analysis of evaporative salinization in a coupled free-flow porous-media system*, 2016, ISBN 978-3-942036-51-1
- 248 Huang, Yingchun: *Study on the spatial and temporal transferability of conceptual hydrological models*, 2016, ISBN 978-3-942036-52-8
- 249 Kleinknecht, Simon Matthias: *Migration and retention of a heavy NAPL vapor and remediation of the unsaturated zone*, 2016, ISBN 978-3-942036-53-5
- 250 Kwakye, Stephen Oppong: *Study on the effects of climate change on the hydrology of the West African sub-region*, 2016, ISBN 978-3-942036-54-2
- 251 Kissinger, Alexander: *Basin-Scale Site Screening and Investigation of Possible Impacts of CO₂ Storage on Subsurface Hydrosystems*, 2016, ISBN 978-3-942036-55-9
- 252 Müller, Thomas: *Generation of a Realistic Temporal Structure of Synthetic Precipitation Time Series for Sewer Applications*, 2017, ISBN 978-3-942036-56-6
- 253 Grüninger, Christoph: *Numerical Coupling of Navier-Stokes and Darcy Flow for Soil-Water Evaporation*, 2017, ISBN 978-3-942036-57-3
- 254 Suroso: *Asymmetric Dependence Based Spatial Copula Models: Empirical Investigations and Consequences on Precipitation Fields*, 2017, ISBN 978-3-942036-58-0
- 255 Müller, Thomas; Mosthaf, Tobias; Gunzenhauser, Sarah; Seidel, Jochen; Bárdossy, András: *Grundlagenbericht Niederschlags-Simulator (NiedSim3)*, 2017, ISBN 978-3-942036-59-7
- 256 Mosthaf, Tobias: *New Concepts for Regionalizing Temporal Distributions of Precipitation and for its Application in Spatial Rainfall Simulation*, 2017, ISBN 978-3-942036-60-3
- 257 Fenrich, Eva Katrin: *Entwicklung eines ökologisch-ökonomischen Vernetzungsmodells für Wasserkraftanlagen und Mehrzweckspeicher*, 2018, ISBN 978-3-942036-61-0
- 258 Schmidt, Holger: *Microbial stabilization of lotic fine sediments*, 2018, ISBN 978-3-942036-62-7
- 259 Fetzer, Thomas: *Coupled Free and Porous-Medium Flow Processes Affected by Turbulence and Roughness – Models, Concepts and Analysis*, 2018, ISBN 978-3-942036-63-4
- 260 Schröder, Hans Christoph: *Large-scale High Head Pico Hydropower Potential Assessment*, 2018, ISBN 978-3-942036-64-1
- 261 Bode, Felix: *Early-Warning Monitoring Systems for Improved Drinking Water Resource Protection*, 2018, ISBN 978-3-942036-65-8

- 262 Gebler, Tobias: *Statistische Auswertung von simulierten Talsperrenüberwachungsdaten zur Identifikation von Schadensprozessen an Gewichtsstaumauern*, 2018, ISBN 978-3-942036-66-5
- 263 Harten, Matthias von: *Analyse des Zuppinger-Wasserrades – Hydraulische Optimierungen unter Berücksichtigung ökologischer Aspekte*, 2018, ISBN 978-3-942036-67-2
- 264 Yan, Jieru: *Nonlinear estimation of short time precipitation using weather radar and surface observations*, 2018, ISBN 978-3-942036-68-9
- 265 Beck, Martin: *Conceptual approaches for the analysis of coupled hydraulic and geomechanical processes*, 2019, ISBN 978-3-942036-69-6
- 266 Haas, Jannik: *Optimal planning of hydropower and energy storage technologies for fully renewable power systems*, 2019, ISBN 978-3-942036-70-2
- 267 Schneider, Martin: *Nonlinear Finite Volume Schemes for Complex Flow Processes and Challenging Grids*, 2019, ISBN 978-3-942036-71-9
- 268 Most, Sebastian Christopher: *Analysis and Simulation of Anomalous Transport in Porous Media*, 2019, ISBN 978-3-942036-72-6
- 269 Buchta, Rocco: *Entwicklung eines Ziel- und Bewertungssystems zur Schaffung nachhaltiger naturnaher Strukturen in großen sandgeprägten Flüssen des norddeutschen Tieflandes*, 2019, ISBN 978-3-942036-73-3
- 270 Thom, Moritz: *Towards a Better Understanding of the Biostabilization Mechanisms of Sediment Beds*, 2019, ISBN 978-3-942036-74-0
- 271 Stolz, Daniel: *Die Nullspannungstemperatur in Gewichtsstaumauern unter Berücksichtigung der Festigkeitsentwicklung des Betons*, 2019, ISBN 978-3-942036-75-7
- 272 Rodriguez Pretelin, Abelardo: *Integrating transient flow conditions into groundwater well protection*, 2020, ISBN: 978-3-942036-76-4
- 273 Weishaupt, Kilian: *Model Concepts for Coupling Free Flow with Porous Medium Flow at the Pore-Network Scale: From Single-Phase Flow to Compositional Non-Isothermal Two-Phase Flow*, 2020, ISBN: 978-3-942036-77-1
- 274 Koch, Timo: *Mixed-dimension models for flow and transport processes in porous media with embedded tubular network systems*, 2020, ISBN: 978-3-942036-78-8
- 275 Gläser, Dennis: *Discrete fracture modeling of multi-phase flow and deformation in fractured poroelastic media*, 2020, ISBN: 978-3-942036-79-5
- 276 Seitz, Lydia: *Development of new methods to apply a multi-parameter approach – A first step towards the determination of colmation*, 2020, ISBN: 978-3-942036-80-1
- 277 Ebrahim Bakhshipour, Amin: *Optimizing hybrid decentralized systems for sustainable urban drainage infrastructures planning*, 2021, ISBN: 978-3-942036-81-8
- 278 Seitz, Gabriele: *Modeling Fixed-Bed Reactors for Thermochemical Heat Storage with the Reaction System $\text{CaO}/\text{Ca}(\text{OH})_2$* , 2021, ISBN: 978-3-942036-82-5
- 279 Emmert, Simon: *Developing and Calibrating a Numerical Model for Microbially Enhanced Coal-Bed Methane Production*, 2021, ISBN: 978-3-942036-83-2
- 280 Heck, Katharina Klara: *Modelling and analysis of multicomponent transport at the interface between free- and porous-medium flow - influenced by radiation and roughness*, 2021, ISBN: 978-3-942036-84-9
- 281 Ackermann, Sina: *A multi-scale approach for drop/porous-medium interaction*, 2021, ISBN: 978-3-942036-85-6
- 282 Beckers, Felix: *Investigations on Functional Relationships between Cohesive Sediment Erosion and Sediment Characteristics*, 2021, ISBN: 978-3-942036-86-3
- 283 Schlabing, Dirk: *Generating Weather for Climate Impact Assessment on Lakes*, 2021, ISBN: 978-3-942036-87-0
- 284 Becker, Beatrix: *Efficient multiscale multiphysics models accounting for reversible flow at various subsurface energy storage sites*, 2021, ISBN: 978-3-942036-88-7
- 285 Reuschen, Sebastian: *Bayesian Inversion and Model Selection of Heterogeneities in Geostatistical Subsurface Modeling*, 2021, ISBN: 978-3-942036-89-4

286 Michalkowski, Cynthia: *Modeling water transport at the interface between porous GDL and gas distributor of a PEM fuel cell cathode*, 2022, ISBN: 978-3-942036-90-0

Die Mitteilungshefte ab der Nr. 134 (Jg. 2005) stehen als pdf-Datei über die Homepage des Instituts: www.iws.uni-stuttgart.de zur Verfügung.